A Spring-Dominated Regime Design of a High Load Capacity, Electromagnetically Driven X-Y-θ Stage

by

Kuo-Shen Chen

B.S.M.E., Power Mechanical Engineering

National Tsing-Hua University

Hsinchu, Taiwan

(1989)

Submitted to the Department of Mechanical Engineering

in Partial Fulfillment of the Requirements for the degree of

Master of Science in Mechanical Engineering

at the

Massachusetts Institute of Technology

May 12, 1995

Signature of Author _____

Department of Mechanical Engineering

January, 1995

Certified by _____

Dr. David L. Trumper

Assistant Professor

Thesis Supervisor

Accepted by _____

Prof. Ain A. Sonin

Chairman, Department Committee on Graduate Students

This page is intentionally left to be blank!

A Spring Dominated Regime Design of a High Load Capacity, Electromagnetically Driven X-Y-θ Stage

by
Kuo-Shen Chen

Submitted to the Department of Mechanical Engineering at the Massachusetts Institute of Technology on May 12, 1995 in Partial Fulfillment of the Requirements for the Master of Science in Mechanical Engineering

Abstract

A three degrees of freedom magnetic actuated flexural stage has been designed and constructed as an alternative approach in atomic resolution machine design. In this system, four steel bars supply the system stiffness and a shear damper provides the required damping. The control computer reads the system positions via three capacitive probes and controls the motion of stage by six magnetic bearings.

This spring dominated regime design has excellent environment disturbance rejection. The experiment data show the system resolution is dominated by the quantization of the analog to digital (ADC) and digital to analog(DAC) converters.

Laser interfermotry is used to calibrate the capacitive probes and to find the coupling of the three controlled degrees of freedom. Experimental data shows that due to manufacturing error, the X mode and Y and θ modes are not perfectly decoupled. However, under such way of design, the three degrees of freedom are controlled simultaneously and this coupling effect can be corrected.

A nonlinear feedback compensation algorithm is implemented in this system. It consists of two feedback loops: an inner loop which utilizes feedback linearization to transform the nonlinear plant into a form that is linear and operating point invariant, and an outer loop which uses a standard linear controller to stabilize the system. A digital Proportional plus Integral (PI) control technique is applied in this loop. The sampling rate is 3 KHz. The system shows a position resolution about 0.05 microns. The bandwidth of system which can be achieved is around 90Hz.

Finally, the stage has been integrated with a stylus to allow surface roughness scanning. The maximum area of scanning is 100 μm × 100 μm. The result shows that this stage can be applied to surface measurements of dedicate samples.

Thesis Supervisor: Dr. David L. Trumper
Title: Professor of Mechanical Engineering

This page is intentionally left to be blank!

ACKNOWLEDGMENTS

I would like to express the most gratitude to my advisor, David L. Trumper, professor of Mechanical Engineering. Over the past two years, Prof. Trumper brought me into the world of mechatronics, and taught me many valuable concepts and ideas in precision design and motion control. Without his guidance, this thesis will never have be finished.

The prototype of the stage was built by Mr. Andre' Monteiro, a Ph.D. student of the University of Warwick , UK who spent time at the University of North Carolina at Charlotte. Without his work in primary design and fabrication, the project could not have been finished on time. I want to thank him here.

I also like to thank Mr. Mark. E. Williams, a Ph.D. student of Mechanicai Engineering of MIT. Mark guided me along stage design, electronics and machining during the past months. For the machine shop work, I need to thank Mr. Fred Cote' for his kindness, help, and teaching. He brought me from a beginner in machine shop to a much higher level.

During the past working period, Prof. Smith Stuart of UNCC, and Prof. Alex. Slocum of MIT gave me some valuable suggestions on precision design concepts, and these suggestions are all applied in stage modification. I want to make a special thanks to them here.

Dr. Eric R. Marsh, a former Ph.D. student of our lab and currently a professor at Pennsylvania State University helped me a lot in designing the damping mechanism . I want to thank him for his guidance on damping and structural vibration, and especially in teaching me English.

I want to express my gratitude to Dr. Maw-Kae Hor, a research fellow of Institute of Information Science, Academia Sinica, Taiwan. Dr. Hor picked me up as his research assistant in 1992 when I just demobilized from army. During that period, I learned and refreshed a lot on computer science, robotics, and system dynamics and control. It switched my major interest from thermofluid to the present field of precision design and control.

During this period, my friends and colleagues in IIS Sinica encouraged me a lot when I was down. They are Marie Hannan, Frank Chen, Jemmy Chen and his wife, Huiling Lu , Yuju Lin, Chienan Kuo, Gina Chu, Chingi Kao, Tienchun Yang, Herming Chiueh, Mingsheng Chang and his wife, Yujen Lu. Thanks for all of your help and visiting in the past two years.

Finally, I like to thank my parents for their support of the past years in my life.

This project is done under the support of Sandia National Laboratory.

This page is intentionally left to be blank!

TABLE OF CONTENTS

LIST OF FIGURES

LIST OF TABLES

This page is intentionally left to be blank!

CHAPTER 1

INTRODUCTION

1.1 Introduction to the X-Y-θ Stage

The X-Y-θ stage project is a new way to design the nano scale resolution machine by combining the feature of magnetic bearings (high precision) and flexures (high noise rejection). Current nanometric resolution machines use voice coil or piezoelectric actuators. These systems usually suffer from poor system dynamics and short motion range. Conversely, an electromagnetic actuated system can provide increased travel, nanometer resolution, and improved system dynamic performance.

For getting a clear insight for this work, I put some pictures and plots here. Figure 1.1 is a picture of our electromagnetically driven stage. The exploded draw of stage is shown in Figure 1.2. One can see the detailed components from this draw. This stage is integrated with sensors, electronics, and control subsystems to form the closed loop control. Figure 1.3 shows the schematic diagram of system integration. After setting up the whole system, we investigate the performances of the stage. The reachable resolution is 50 nanometers with dynamics range of 100 μm in both major axis. The maximum bandwith is around 90 Hz. To reach such performances, a proportional plus integral controller with nonlinear feedback is implemented in the host computer. Figure 1.4 is a schematic plot on the pratical control block diagram.

Finally, we apply this stage in surface measurement with a LVDT stylus. The experimental results shows this stage is applicable in precision measurement.

Figure 1.1 Picture of the X-Y-θ stage

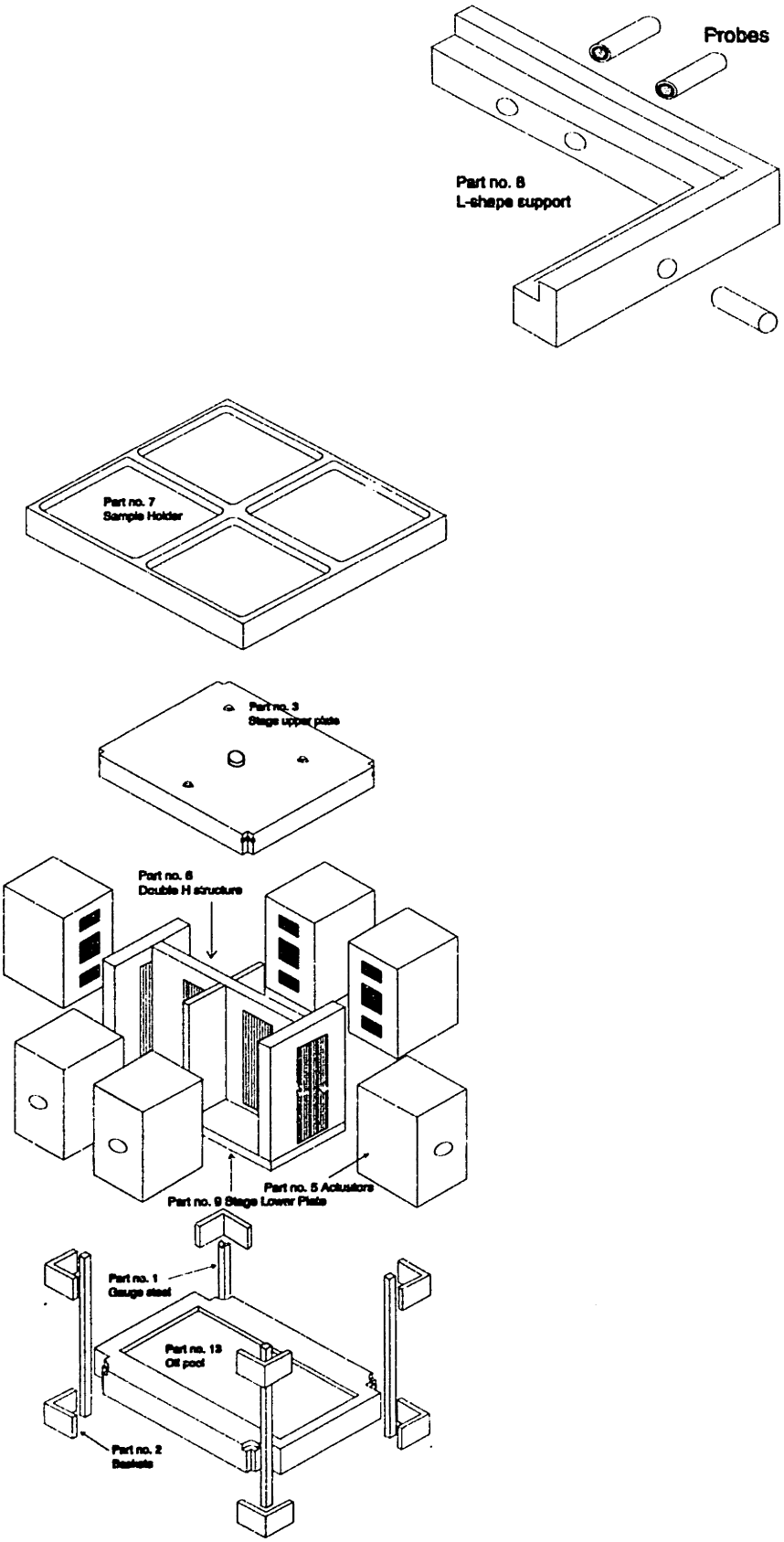

Figure 1.2 The exploded view of the X-Y-θ stage

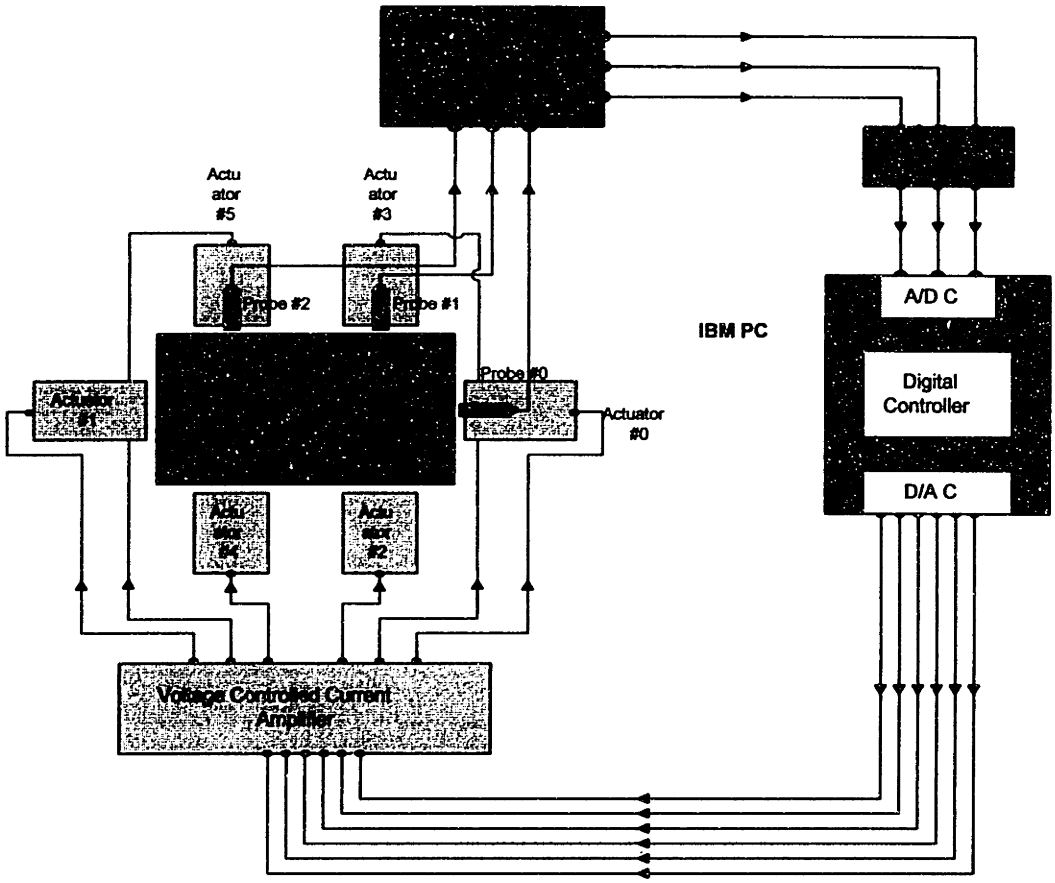

Figure 1.3 The schematic plot of the system integration

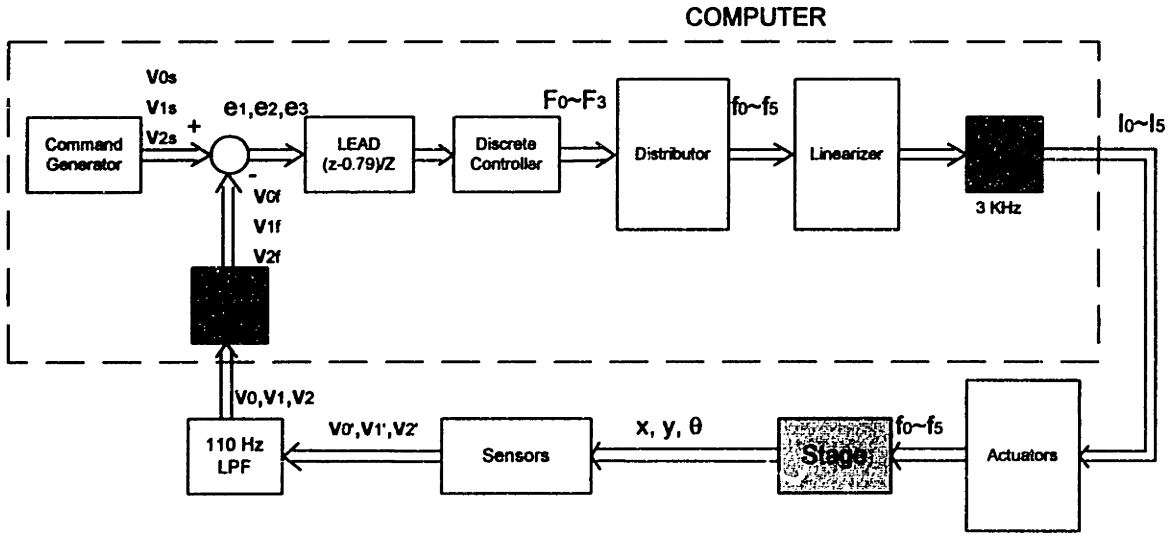

Figure 1.4 The schematic plot of real control algorithm

1.2 Review of Related Works

Among the precision engineering elements, magnetic bearings play an important role in reaching nano scale resolution. Primarily, magnetic bearings are capable of applying force and torque to a suspended object without rigidly constraining any of its degrees of freedom. The resolution of the system is limited by sensors and control electronics, and not by the mechanical system. For these reasons, magnetic bearings appear to be ideal for performing precision linear motion. Basic working principles of magnetic bearings can be found in [KaR75], [Sin87], and [WoM68].

There are numerous previous works on the application of magnetic bearings. Trumper in [Tru90] built a magnetic suspension system using seve magnetic bearings to levitate an object and to control its five degrees of freedom. Downer designed a large angle suspension in [Dow86]. Ota et.al in [OAI90] constructed a magnetic suspension system for wafer transportation. Yeh applied magnetic levitation on vibration isolation [Yeh92].

After years development, the applications of magnetic bearings are not restricted in suspending object. Higuchi et. al in [HiY93] used electromagnetic attractive forces to actuate a position servomechanism. Holmes built a stage use twelve magnetic bearings to actuate a stage as an alternative design on atomic resolution machine. For detail, see [Hol94]. Therefore, magnetic bearings can be used as actuators.

Among the various applications on magnetic bearing technologies, one of them is trying to make nano scale resolution machines by magnetic bearing directly. Traditionally, these machines are all made of piezoelectric actuators. For example, see [Bis86], [CYS92], [MoS91], and [Tzo91]. Although piezoelectric devices have intrinsic non-linearity (hysteresis, creep, and thermal susceptibility), it is possible to compensate for this by the use of local feedback, for example by using capacitive sensors incorporated in the piezoelectric transducer. This produces a very high precision displacement transducer with a reasonably high bandwidth. However, there remain two problems; the dynamic response drops with increasing range and, for high rectilinearly, the displacement needs to be guided.

Unlike piezoelectric, elastic deformation flexure stages are ideally suited for medium range translations from a few picometers up to many millimeters exhibiting smooth, rectilinear, and repeatable motion with reasonable dynamic characteristics [SmC91]. For a single degree of freedom linear translation the simple linear spring is commonly used. Building such a mechanism with symmetry in two planes should result in an actuator capable of translating in two axes x and y and if the drives are suitably designed it should also be possible to exploit the compliance about the z axis to give a further rotational control. Such a mechanism forms the basis of the design presented in this paper.

An elastic stage incorporating a symmetrical design should posses a good degree of orthogonality between the x and y translations. A typical two degrees of freedom flexure design can be found in [SCH94]. With care having been taken in the construction to avoid major distortions and pre-stresses on assembly and operated well below the elastic limit of the deflection springs, an elastic stage of the above type has been built to operate with a range of a hundred microns. With modifications to the flexures and monitoring gauges it should be possible to obtain extended range motion up to millimeter levels.

1.3 The Stage Design

As mentioned in section 1.1, this design combines the features of magnetic bearings and flexures. The feature of magnetic actuator is the non-contact, no friction and mechanical wear. As a consequence, a system can reach very high accuracy. However, a pure magnetic suspension system has very small system stiffness and low ability on noise rejection. Flexures, on the contrary, have high stiffness, therefore, high natural frequency and high ability to reduce the influence of disturbance. The design goal of the stage are: high accuracy, high bandwidth, and high noise rejection.

The stage design consists of four vertical steel flexures arranged like the legs of a table, supporting a platform that serves as both a sample holder and a kinematic mount for the position sensor surfaces. The steel flexures provide high system stiffness and

noise rejection. Fluid damping is added into the stage system to provide suitable system damping ratio by a high viscosity GE Viscosil silicone fluid. Similar designs in viscous damping are shown in [Hol94] and [KoN94]. In [Hol94], the stage was immersed in a Dow Corning Silicone fluid and keep in a natural buoyancy state. It minimized the vibration influence and provide the desired damping force. Kobayashi et. al improved the performance of some linear motion system by adding high damping Silicone fluid into system in [KoN94]. Marsh examined the frequency characteristic of some GE Viscasils in [Mar94]. These data are directly applicable in this thesis.

The performance of elastic deflection stage is a compromise between range and noise limited resolution. For a specified actuator, the higher the stage stiffness, the lower the motion range, but it will get a better noise rejection and a higher bandwidth. The driving forces for this particular design are provided by six electromagnetic actuators. These are iron core solenoids which have been optimized to provide high force with a relatively low current [WiT93]. The positions are sensed by three capacitive probes. Finally, a digital computer performs discrete control task.

1.4 System Design Methodologies

1.4.1 Spring Dominated Regime Design Approach

The stage can be treated as a second order mass-spring-damper system. The basic requirement of this stage is to minimize the influence of environment disturbance force. As a consequence of this requirement, the system should have high stiffness in mechanical structure. Combining the mechanical design, a spring dominates regime design on control also has been implemented.

Spring dominate regime design

Consider the limiting case, with a reasonable crossover frequency, when the ratio k/m >>1, (the system is very stiff) then, the system natural frequency ω_n will much higher than the crossover frequency ω_c. Under this situation, the phase margin will be large, typically, greater than 100°. This means we can use more lag compensation to increase the performance of the system and still have enough phase margin to keep the system from unstable.

Mass dominate regime design

Consider the limiting case again. Instead of high k/m ratio, now the K/m is very low, (equivalent to a soft spring support system). Under the same specification of crossover frequency ω_c, the system natural frequency ω_n will be less than the crossover frequency. From the Bode plot, the phase margin will be small, almost near zero. For maintain the stability, we must introduce phase lead compensation into the system. Unfortunately, phase lead compensators basically are differential controllers. The undesirable base vibrations and sensor noises will be amplified under such circumstance. Causing the degrading of the system performance. Therefore, under such environment, the spring dominated regime design is preferred.

1.4.2 Nonlinear compensation approach

Magnetic bearings are nonlinear devices. There are two approaches to linearize it. The traditional one is to linearize the governing equation with respect to a nominal operation point, neglecting all high order term then write down the control law based on this linearized result. The other one, nonlinear compensation, using directly position feedback to linearize the nonlinear elements in real time.

Olson in [Ols94] explored these two control techniques and made a comparison. In his conclusion, the performance of linear one degraded as the motion range increased and varied with operating point. The performance of nonlinear one, on the other side, is independent from motion range and operating point.

The control methodology of the stage, therefore, will be spring dominated regime PI control plus nonlinear feedback linearization.

1.5 Thesis Overview

There are several chapters to discuss subsystem design separately. Chapter 2 describes our design methodology - spring dominated regime design. Chapter 3 mentioned about the basic electromechanical dynamics and actuator design. Chapter 4 concerns about the mechanical part design , included stage and sample holder , and modeling the stage dynamics. Chapter 5 presents the calibration work on magnetic bearings and basic concept of nonlinear compensation. The noise modeling work is in Chapter 6. The electronic part of system, including power amplifier and capacitive probes, is presented in Chapter 7. Chapter 8 discusses the controller design, including some simulation results.

After finishing the subsystem design, the system has been integrated and can be seen on Chapter 9. Chapter 10 discusses the possible system error sources systematically. The control results are presented in Chapter 11. The application of stage in surface scan work is shown in Chapter 12. The final conclusion and suggestion of future work are written in Chapter 13.

CHAPTER 2

SPRING DOMINATED REGIME DESIGN

This chapter considers the typical classes of operation for positioning systems. These classes are spring-dominated, damping dominated, and mass dominated. The spring dominated regime design methodology is adopted for our stage design for reasons which are explained in this chapter. Section 2.1 defines the several design regimes. The performances of these designs are analyzed in the context of a single degree of freedom system in section 2.2. Several design examples are presented in section 2.3. We summarize our analysis on the different regime designs and state the reason why we choose spring dominated regime design for our stage in section 2.4.

2.1 Definitions

2.1.1 General description

Consider a one degree of freedom mass-damper-spring (or simply m, b, k for further use) system as shown in Figure 2.1. The system transfer function of displacement versus applied force can be written as

$$\frac{X_m(s)}{F_c(s)} = \frac{1}{ms^2 + bs + k} \quad \text{or} \quad \frac{X_m(s)}{F_c(s)} = \frac{1/m}{s^2 + 2\xi\omega_n s + \omega_n^2}, \qquad (2.1)$$

where $\omega_n \equiv \sqrt{\frac{k}{m}}$ is the system undamped natural frequency and $\xi \equiv b/2\sqrt{km}$ is the damping ratio. For critical damping, $\xi = 1$ and the damping is $b_c = 2\sqrt{km}$. To explore the system characteristics (2.1), we must consider the magnitude of damping ratio ξ. We discuss (2.1) in two cases, underdamped (i.e., $\xi \leq 1$) and overdamped (i.e., $\xi > 1$).

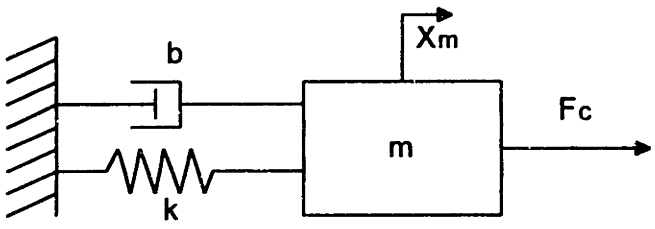

Figure 2.1 A simple mass-spring-damper system

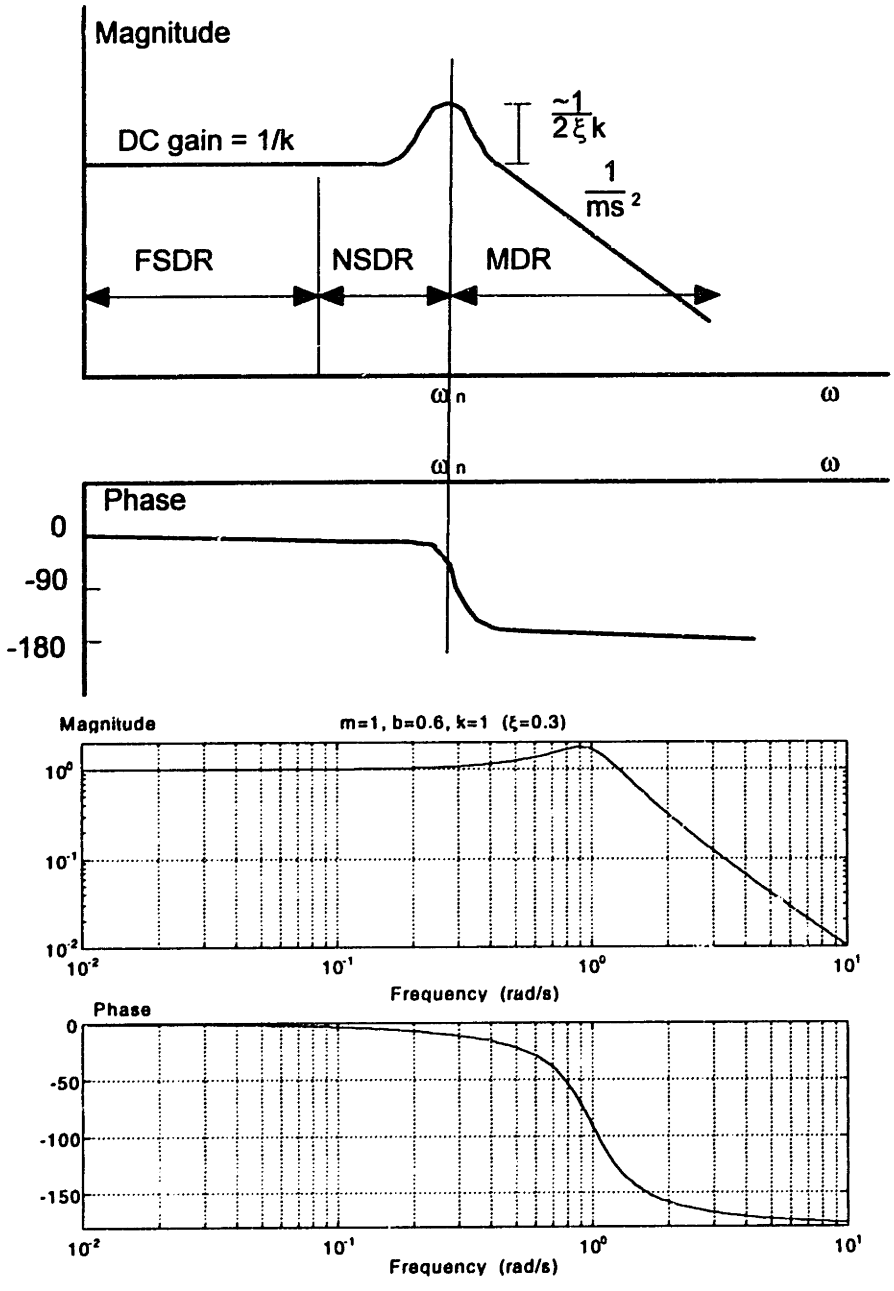

Figure 2.2a The schematic and real Bode plot of G(jω) in the underdamped case

Underdamped Case

The general frequency characteristic of (2.1) in the underdamped case is shown in Figure 2.2a. From this plot, we define some terminologies.

Far Spring Dominated Regime (**FSDR**): For excitations at frequencies much less than the resonant frequency, e.g., $\omega < 0.1\omega_n$, the inertia and damping forces are not important. The system is dominated by its stiffness. We call this region the " Far Spring Dominated Regime".

Near Spring Dominated Regime (**NSDR**):If the frequency is above the far spring dominated regime but less than its undamped system natural frequency, we call this region the " Near Spring Dominated Regime". The stage in this thesis is an example of a near spring dominated regime design. The feedback loop crossover frequency for such a system can be as high as about ω_n. For a NSDR design, in order to allow a robustly stable feedback loop, the system must have enough damping to avoid significant peaking at the system natural frequency, for reasons we explain in the subsequent sections.

Mass Dominated Regime (**MDR**): If the excitation frequency is above ω_n, the system becomes inertia force dominated. We call this the " Mass Dominated Regime".

Overdamped Case

Referring to Figure 2.2b, in the overdamped case, the plant dynamics (2.1) can be treated as the combination of two first order systems. Here we have made the assumption that $b^2 >> 4mk$, and thus that $\sqrt{1-(4mk/b^2)} \approx 1-\frac{2mk}{b^2}$. The roots of the characteristic polynomial (2.1) are

$$s_{1,2} = \frac{-b \pm \sqrt{b^2-4mk}}{2m} \approx \frac{-b}{2m}(1 \pm (1-\frac{2mk}{b^2})) \approx \frac{-b}{m}, \frac{-k}{b}. \quad (2.2)$$

Under this approximation, the associated break frequencies are $\omega_1 \approx k/b$ and $\omega_2 \approx b/m$. These break frequencies divide the Bode plot into three regimes as shown in Figure 2.2b. If $\omega < \omega_1$, the system is in the spring dominated regime. The magnitude is essentially 1/k and phase lag is about zero. If $\omega > \omega_2$, the system is the inertia dominated. In this range the transfer function is approximately $1/ms^2$.

If the frequency of interest is between ω_1 and ω_2, the system is in the *damping dominated regime* (**DDR**). In this region, the viscous damping force dominates the system behavior, and the transfer function varies as 1/*bs*.

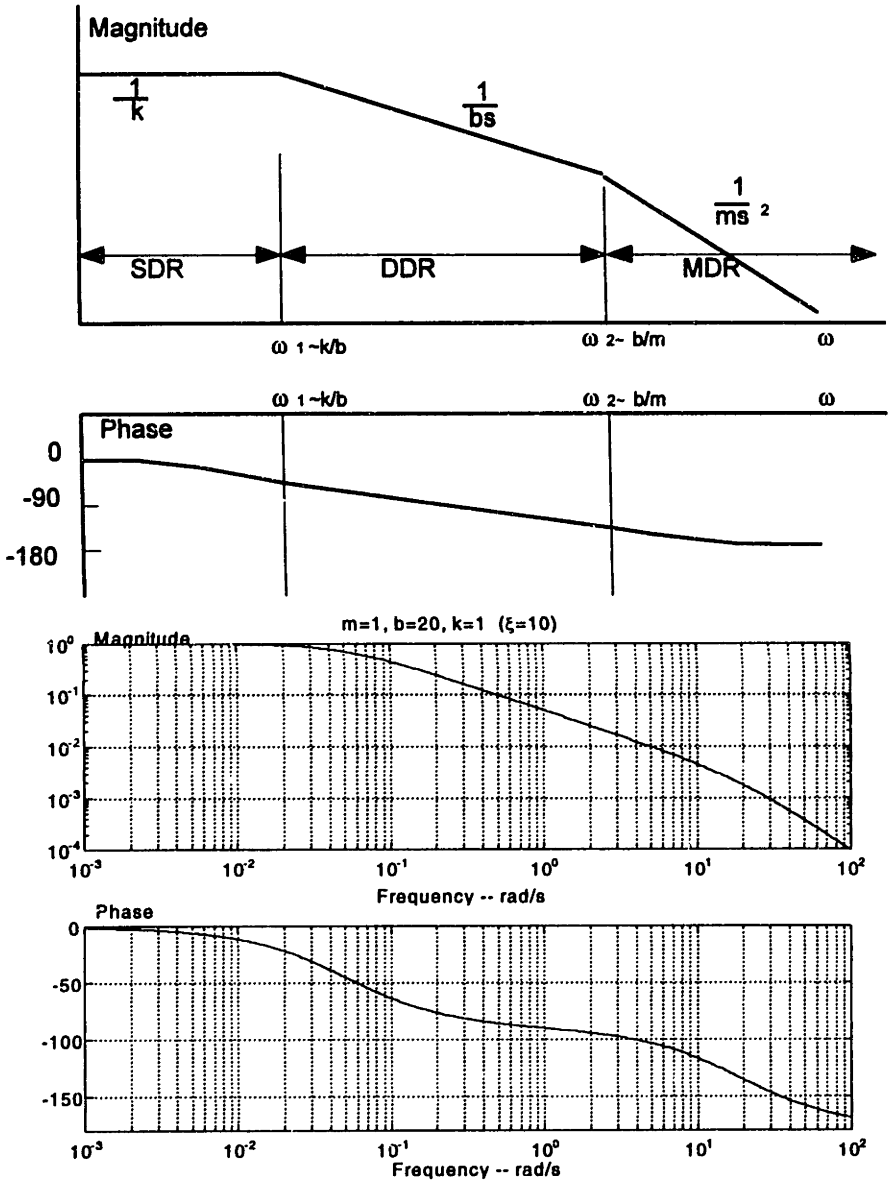

Figure 2.2b The schematic and real Bode plot of G(jω) in the overdamped case

2.1.2 Characteristic of regimes

For achieving a given set of design specifications, one usually needs to adopt a closed-loop structure. The design of such a controller for a positioning system strongly relates to

the system dynamics. That is, the relative magnitude between these system parameters (m, b, k) will determine what control law one should use and what system performance one can get. Here we state the general characteristics of each regime. A more detailed explanation is given in Section 2.2.

SDR

In SDR the system behaves like a pure spring. It is relatively insensitive to mass variation. For getting the best performance, a PI controller should be used since it eliminates steady state error, and reduces the influences of low frequency disturbances. However, if the damping ratio is too small, the system is forced to be designed in FSDR since the resonance may cause the system to be unstable. That is, we will require in all the designs herein that the loop transmission magnitude is less than unity at the resonant peak. A good feature of SDR system is in their disturbance rejection capabilities. A SDR system with PI control can attenuate low frequency disturbance. However, since a spring force grows with position, the positioning range of SDR designs is usually small. Many piezoelectric systems are designed in the SDR. Since the damping ratio of pure piezo systems is usually small they are usually designed in FSDR. Recently, however, some researchers have added some damping mechanism so they can be operated in NSDR. In addition, the stability of SDR systems is relatively insensitive to load mass changes.

MDR

In MDR, the system is inertia force dominated. In this regime, the phase lag is essentially near 180°. To control this system, it thus usually needs some amount of lead compensation to improve its stability. An integral controller is also required to improve its low frequency rejection of disturbances. However, with the integral controller, the loop may exhibit conditional instability. Since the system stiffness is essentially much smaller than in SDR, the positioning range of MDR design is usually larger than SDR's based on the same actuator capacity. However, since the lead control amplifies at high

frequencies, the MDR loop will be more sensitive to high frequency noise as compared with SDR. In addition, the system is also sensitive to the variation of system mass. Most direct drive machines such as motors and magnetic suspensions are operated in MDR.

DDR

It is hard to find a commercial design in DDR from energy consumption point of view since system velocities are limited by the high viscous drag force. However, some experimental instruments are designed by this way. An example is the stage in [Hol94] which we will discuss in more depth in the next section. A proportional controller can control the system very well since the DDR system is approximately a type 1 system. However, to eliminate steady state error, one may choose PI control. These systems have the advantage that resonant modes of the stage tend to be well-damped, and thus are suited for precise positioning tasks.

2.2 Controller Design

There are a lot of competing requirements in system performance, such as stability, bandwidth, noise rejection capability, and parameters' sensitivity. We will discuss these requirements in the context of a single degree of freedom system example in this section.

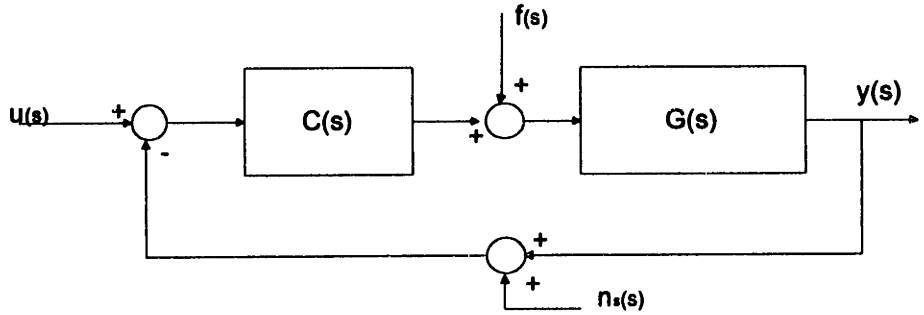

Figure 2.3 A simple feedback system

Consider the block diagram shown in Figure 2.3. A second order plant with plant dynamics (2.1) connects with a controller C(s) to form a simple closed loop feedback

system. This system is subjected to the command input u(s), an external force disturbance f(s), and a sensor noise $s_n(s)$. We assume here that the controller specifies force directly. The negative of loop transmission for each of these systems is

$$-L.T. = C(s)G(s) = \frac{C(s)}{ms^2 + bs + k}. \tag{2.3}$$

The closed loop transfer function from the command input to the output is

$$H(s) = \frac{Y(s)}{U(s)} = \frac{C(s)G(s)}{1 + C(s)G(s)} = \frac{C(s)}{ms^2 + bs + k + C(s)}. \tag{2.4}$$

The closed loop transfer function from the disturbance to the output is

$$D(s) = \frac{Y(s)}{F(s)} = \frac{G(s)}{1 + C(s)G(s)} = \frac{1}{ms^2 + bs + k + C(s)}. \tag{2.5}$$

And the closed loop transfer function from the sensor noise to the output is

$$N(s) = \frac{Y(s)}{S_n(s)} = \frac{-C(s)G(s)}{1 + C(s)G(s)} = \frac{-C(s)}{ms^2 + bs + k + C(s)}. \tag{2.6}$$

These equations will be the basis of our analysis. We find that other than a minus sign, the system behavior is the same for the command or sensor noise input, therefore, we will not discuss the system behavior subjected to sensor noise any further as a special case.

The transfer function of a PI controller is

$$C(s) = K_p(1 + \frac{1}{T_i s}). \tag{2.7}$$

Let's define L.T. as the loop transfer function. The negative of the loop transmission with a PI controller will be

$$-L.T._{PI} = \frac{\frac{K_p}{m}(T_i s + 1)}{s(T_i s^2 + 2\xi\omega_n T_i s + \omega_n^2 T_i)}. \tag{2.8}$$

The closed loop transfer function for command input will be

$$H_{PI}(s) = \frac{\frac{K_p}{m}(T_i s + 1)}{T_i s^3 + 2\xi\omega_n T_i s^2 + \omega_n^2 T_i s + \frac{K_p}{m}(T_i s + 1)}. \tag{2.9}$$

The closed loop transfer function for force disturbance input will be

$$D_{PI}(s) = \frac{\frac{T_i}{m}s}{T_i s^3 + 2\xi\omega_n T_i s^2 + T_i\omega_n^2 s + \frac{K_p}{m}(T_i s + 1)} \quad . \qquad (2.10)$$

For a PID controller

$$C(s) = K_p(1 + \frac{1}{T_i s} + K_D s). \qquad (2.11)$$

The negative of loop transmission will be

$$-L.T._{PID} = \frac{\frac{K_p}{m}(T_i s + K_D T_i s^2 + 1)}{s(T_i s^2 + 2\xi\omega_n T_i s + T_i\omega_n^2)} \quad . \qquad (2.12)$$

The closed-loop transfer function for command input will be

$$H_{PID}(s) = \frac{\frac{K_p}{m}(T_i s + K_D T_i s^2 + 1)}{T_i s^3 + 2\xi\omega_n T_i s^2 + T_i\omega_n^2 s + \frac{K_p}{m}(T_i s + K_D T_i s^2 + 1)} . \qquad (2.13)$$

The closed loop transfer function for disturbance input will be

$$D_{PID}(s) = \frac{\frac{T_i}{m}s}{T_i s^3 + 2\xi\omega_n T_i s^2 + T_i\omega_n^2 s + \frac{K_p}{m}(T_i s + K_D T_i s^2 + 1)} . \qquad (2.14)$$

In order to simplify these expressions, without loss of generality, we now normalize (2.8) through (2.14) by setting $\omega_n = 1$ and letting $K_p' = \frac{K_p}{m}$. These become

$$-L.T._{PI} = \frac{K_p'(T_i s + 1)}{s(T_i s^2 + 2\xi T_i s + T_i)}. \qquad (2.15)$$

$$H(s)_{PI} = \frac{K_p'(T_i s + 1)}{T_i s^3 + 2\xi T_i s^2 + T_i s + K_p'(T_i s + 1)}. \qquad (2.16)$$

$$D(s)_{PI} = \frac{\frac{T_i}{m}s}{T_i s^3 + 2\xi T_i s^2 + T_i s + K_p'(T_i s + 1)}. \qquad (2.17)$$

$$-L.T._{PID} = \frac{K_p'(T_i s + K_D T_i s^2 + 1)}{s(T_i s^2 + 2\xi T_i s + T_i)}. \qquad (2.18)$$

$$H(s)_{PID} = \frac{K_p'(T_i s + K_D T_i s^2 + 1)}{T_i s^3 + 2\xi T_i s^2 + T_i s + K_p'(T_i s + K_D T_i s^2 + 1)}. \quad (2.19)$$

$$D(s)_{PID} = \frac{\frac{T_i}{m} s}{T_i s^3 + 2\xi T_i s^2 + T_i s + K_p'(T_i s + K_D T_i s^2 + 1)}. \quad (2.20)$$

While algebraically correct, (2.15) through (2.20) do not give insights in how to approach the controller designs. A broader perspective can be gained by approaching the design process from a graphical frequency domain perspective. We present this approach in the next section. The relations we derive graphically are approximate but provide a perspective on how to design these systems.

PI Design in SDR

The PI controller contains a pole at s = 0 and a zero at s = -1/T_i. Using the normalized equation ω_n=1, the PI design requires $\omega_c < 1$.

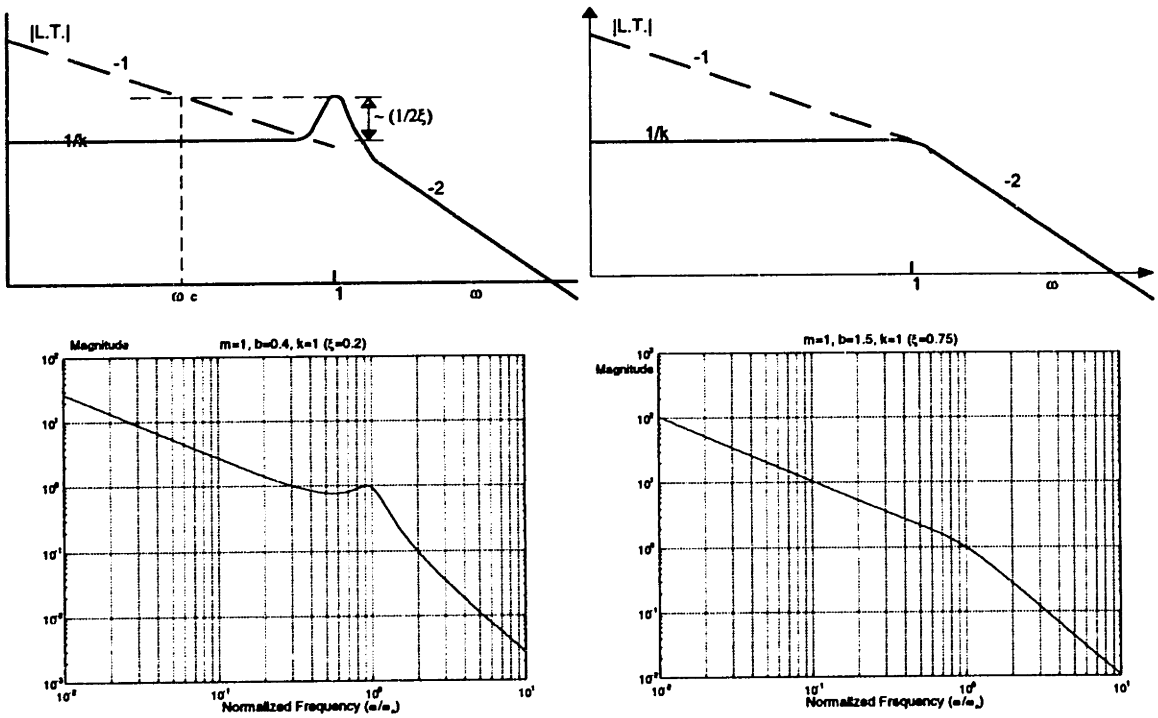

(a) (b)

Figure 2.4 Schematic and real loop transmission Bode plots of SDR PI design. (a) underdamped, (b) overdamped case

From figure 2.4, one can see that the system is essentially a first order system when the exciting frequency is below ω_c. Since the plant dynamics (2.1) is approximately a DC value below ω_c, the loop transmission is dominated by the dynamics of PI controller. The integration constant T_i in (2.7) affects the system behavior. If T_i is too small (or I-gain is too large), system will have lower stability. If T_i is too large(or, equivalently, I-gain is too small), a "long-tailed" response will happen. It increases the system settling time. Figure 2.5 shows the step responses of (2.15) with ξ equal to unity under several different T_i. From Figure 2.5, one can find that the reasonable choice is to put the PI zero at around $s = -\omega_n$, that is, $T_i = 1/\omega_n$. The system will still have enough phase margin and fast enough response under such design. Put $T_i = 1/\omega_n = 1$ and note that the magnitude of loop transmission is equal to 1 at ω_c. The magnitude of the loop transmission must be smaller than unity at the resonance frequency. One can see that the crossover frequency will be less than the system natural frequency. It depends on the system damping ratio. The smaller the damping ratio, the higher the resonance peak, and the smaller the crossover frequency. Based on the above discussion, we have the following criteria for FSDR PI design.

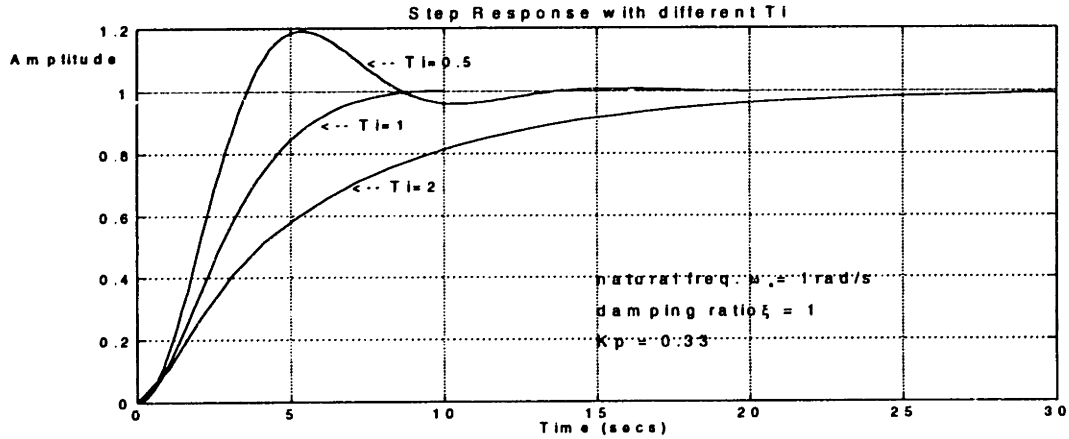

Figure 2.5 The step responses of (2.15) under different T_i

$$T_i = 1/\omega_n. \tag{2.21a}$$

$$K_p = 2\xi k. \tag{2.21b}$$

$$\omega_c < \frac{2\xi}{T_i}\frac{1}{\sqrt{1-4\xi^2}} \quad \text{for } \xi < 0.5. \tag{2.21c}$$

If $\xi > 0.6$, we can let system crossover near ω_n. About choosing the integration constant T_i, for underdamped case, we put $T_i = 1/\omega_n = 1$ by the same reason as above. Note that the allowable values of K_p and ω_c decrease with ξ, and the gain $1/T_i$ increases with ω_n. Thus the best performance is achieved with a system with near critical damping and with as large as ω_n as possible. For the overdamped case, depending on the design specs, the criteria can be extended to put zero between ω_1 andω_2 for increasing system performance. If the zero is put beyond ω_2, the phase margin may be not enough and the system may become conditional unstable. The followings are the design criteria for SDR PI design.

$$\frac{1}{T_i} \geq \omega_n. \tag{2.22a}$$

$$K_p = k. \tag{2.22b}$$

$$\omega_c = \omega_n. \tag{2.22c}$$

Figure 2.6 shows the effect of zero location by loop transmission Bode and root locus plots. The damping ratio of the loop transmission (2.15) is 1.5. There are three poles at s = 0, -0.5, and -2 respectively. Both cases are crossover at 1 rad/sec (i.e., ω_n). The zero is put in s = -1 for case I and s = -4 for case II. Both cases shows about 55° phase margin. However, from root locus, we know case II is easier to go unstable.

Effect on disturbance rejection

Figure 2.7 shows the schematic Bode plot of (2.5), (2.10) or (2.20). Below crossover, where the loop transmission magnitude is large, the transfer function $\frac{Y(s)}{F(s)} \approx \frac{1}{C(s)}$. Above crossover, this transfer function is roughly equal to G(s), since the loop transmission magnitude is small in this region. If the system is well damped (that is, no resonance peak at resonance frequency), the system can crossover at $\omega_c = 1$. If the system is not well damped, the crossover will be given approximately at (2.21c). The magnitude of the transfer function of position output versus disturbance force input should be as

small as possible. Comparing Figure 2.7a and 2.7b, the poorly-damped damped system transfer function has higher magnitude at low frequency compared to the well damped one. Therefore, the poorly-damped system will lose a certain amount in disturbance rejection ability as indicated by the meshed area in Figure 2.7b. Therefore, to achieve the best performance, proper damping is very important in SDR PI design. It will both increase the system bandwidth and its disturbance rejection.

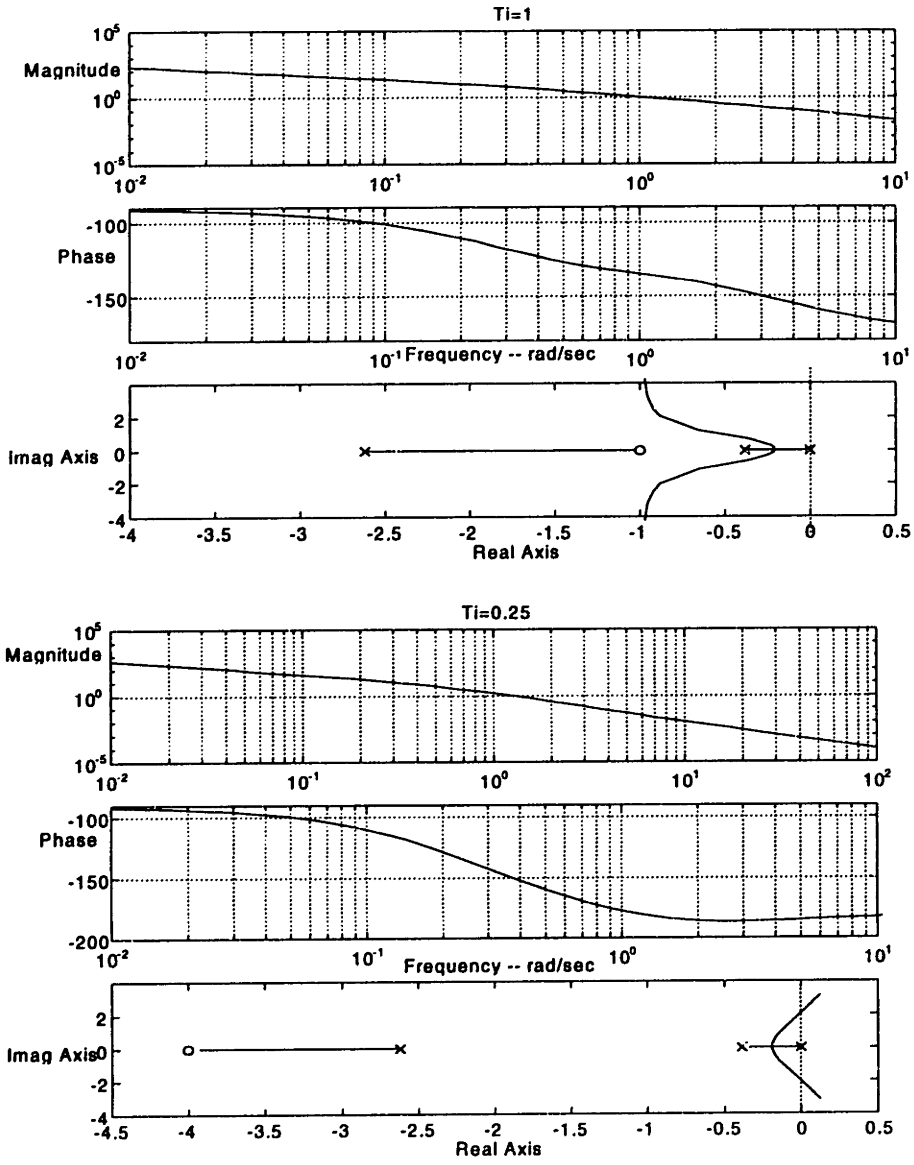

Figure 2.6 Bode and root locus plots for different Ti in SDR design

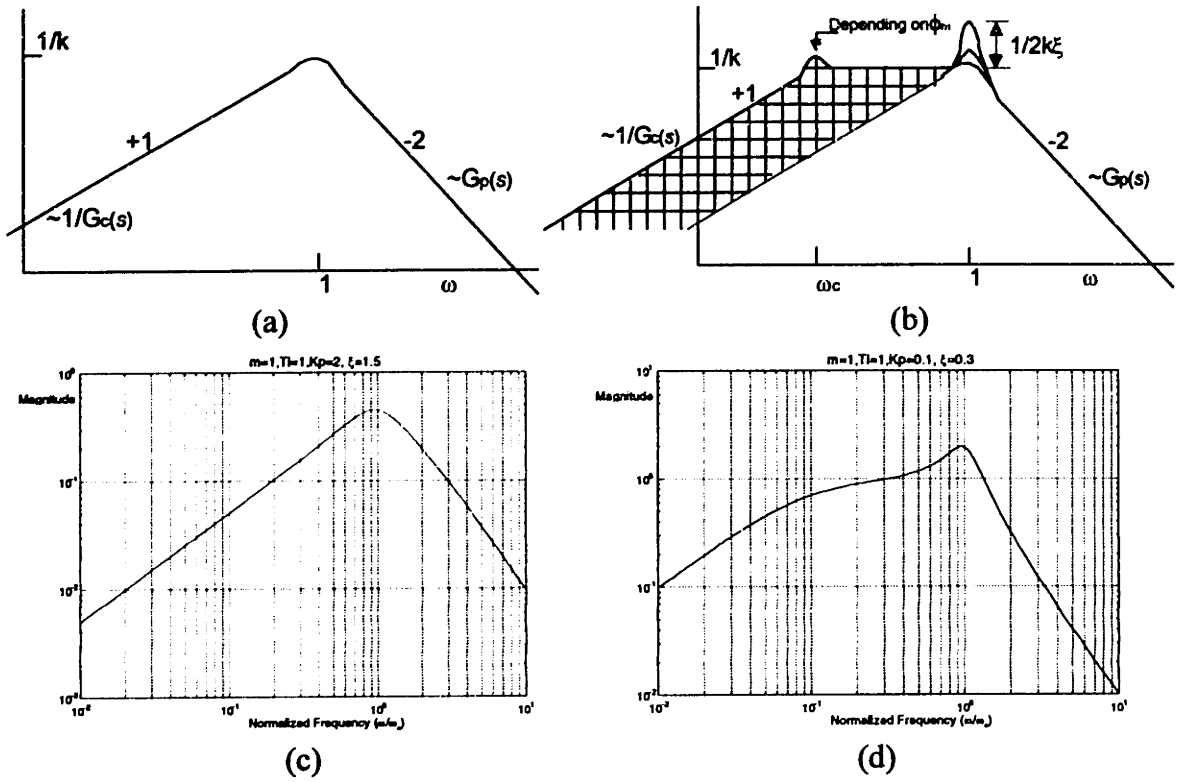

Figure 2.7 Schematic and real SDR PI design Bode plot for system response to disturbance input. (a)(c) overdamped case. (b)(d) underdamped case. Shaded area shows performance loss if the system is underdamped. The magnitude of the peak at ω_c depends upon the loop phase margin.

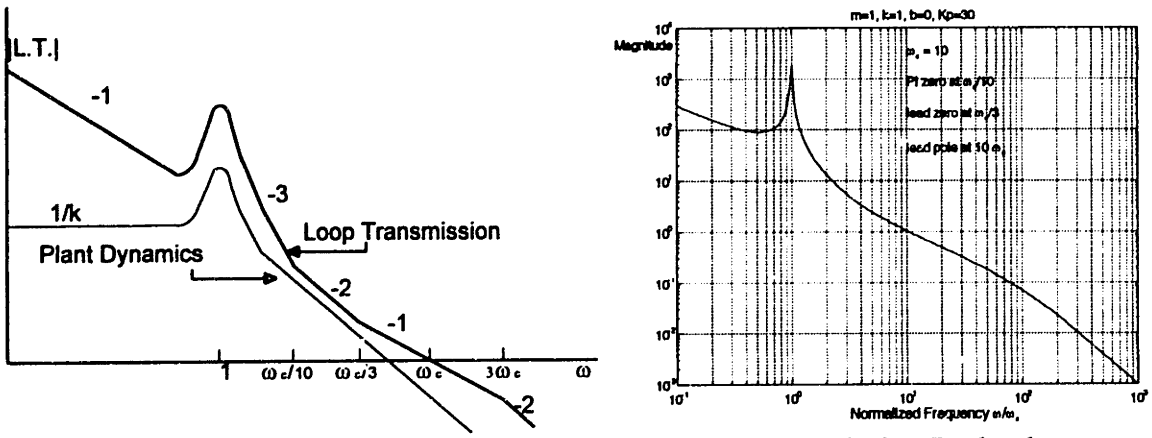

Figure 2.8 Schematic and real MDR PID loop transmission Bode plot

PID Design in MDR

For MDR design, a PID controller is usually applied. Figure 2.8 shows the loop transmission Bode plot. A PID controller has one pole at s=0 and two zeros, which are located at $s \approx -1/T_i$ and $s \approx -1/K_d$. For a real implementation, one more pole is

required, and the D controller is replaced by a lead compensator. The lead pole is typically placed 10 times farther to the left than the lead zero. The system crossover frequency will be much larger than system natural frequency. Under such circumstance, the uncompensated phase lag is nearly 180° and the system needs additional phase compensation. For a general MDR design, the zero of the I controller is placed at equal or less than $\omega_c/10$ to get good performance at low frequency and without dangering the stability. The zero of lead should be placed closer to the crossover frequency, that is, put the zero at ω_c/α, where α is around 3 or 4. The lead pole is located at $\alpha\omega_c$ to get the maximum phase compensation at ω_c. To determine the proportional gain, note that (2.12) is approximately to $-L.T._{PID} \approx K_p \frac{(1+K_d s)}{ms^2}$ in MDR(the stiffness and damping are not important in MDR). Setting the magnitude of the loop transmission equals to 1 at the crossover frequency ω_c yields $K_p \approx \frac{m\omega_c^2}{\sqrt{1+K_d^2\omega_c^2}}$.

In summary, for MDR PID design, we have the following criteria

$$\omega_c >> \omega_n. \tag{2.23a}$$

$$T_i \geq \frac{10}{\omega_c}. \tag{2.23b}$$

$$K_d = \frac{\alpha}{\omega_c} \quad \text{where } \alpha \text{ is around 3.} \tag{2.23c}$$

$$K_p \approx \frac{m\omega_c^2}{\sqrt{1+K_d^2\omega_c^2}}. \tag{2.23d}$$

The damping of the system resonance is not important in MDR design since in the vicinity of the crossover only the mass has a significant effect. However, if $1/T_i$ is significantly greater than ω_n, the system may go unstable if the proportional gain is decreased since the phase curve will drop below -180° below crossover. Another important issue is the system bandwidth. Although the system has its crossover at ω_c, in terms of settling time, the PI pole and zero will dominate the system response, that is, the real system settling time may be about 10 times slower than that which should be predicted from ω_c. The phase lead compensator also amplifies high frequency noise.

Figure 2.9 shows the effect of zero location in PID controller through loop transmission Bode and root locus plots. The damping ratio of loop transmission (2.18) is 1.5. The system is crossovers at 10 rad/sec (i.e., $10\omega_n$). K_d in both cases is equal to 0.1. In case I, the loop transmission has 55° phase margin with a T_i=0.6. This phase margin decreases as T_i decreases. In case II, the system has 30° phase margin only and exhibits conditional instability.

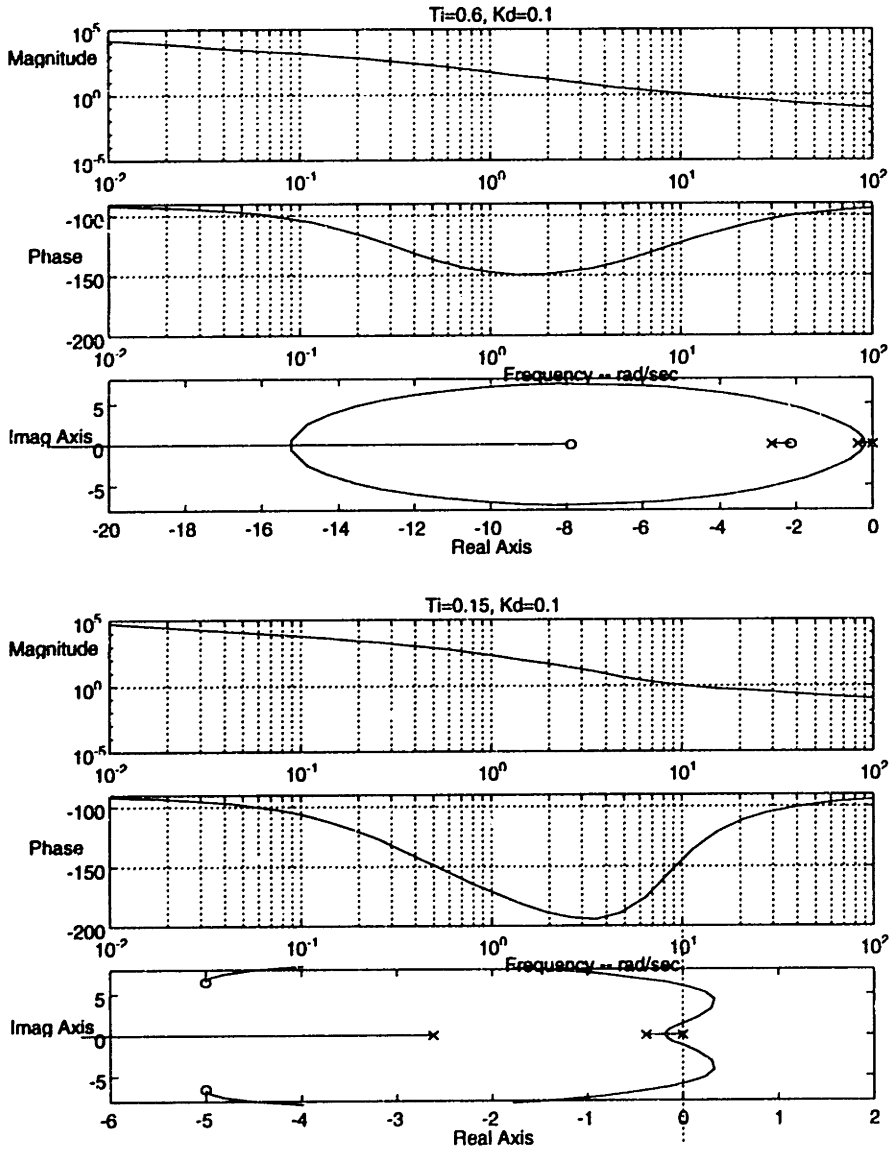

Figure 2.9 Bode and root locus plots for different K_d and T_i in MDR design

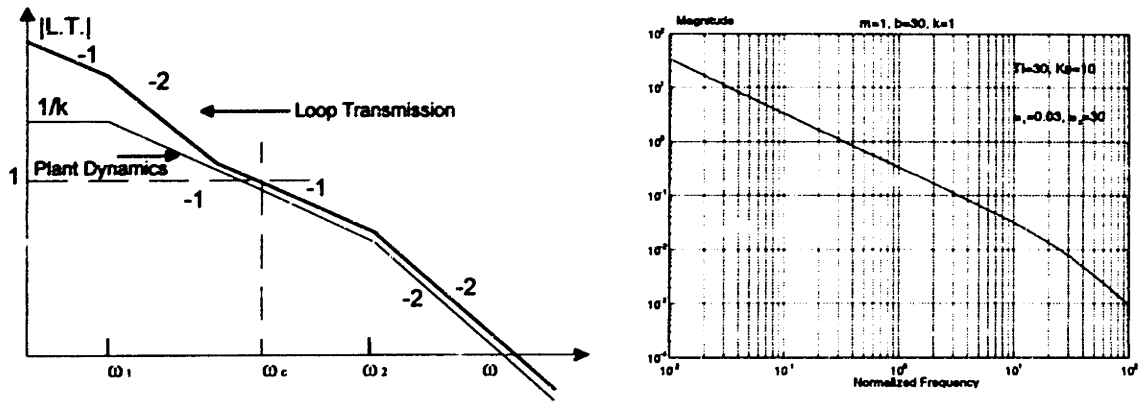

(a) (b)

Figure 2.10 (a)A schematic DDR PI loop transmission Bode plot. (b)A DDR PI design example by putting PI zero at ω_1

PI Design in DDR

For a PI controller design in DDR, the situation is similar to a PI design in SDR. However, in DDR design, the system crossover frequency ω_c is between the two break frequencies ω_1 andω_2. The zero of the PI compensator, as in SDR design, should be put below ω_2 for stability concern. One possible design is shown on the right of Figure 2.10. In this design, the PI zero is placed at ω_1. Alternatively, to achieve better disturbance rejection, we can locate the PI controller zero breakpoint at a frequency only slightly below crossover. For the purposes of discussion, we can set the zero breakpoint at $\omega_c/4$. Since the PI zero is at $-1/T_i$, this design choice gives $T_i=4/\omega_c$.

We can choose the value of Kp as follows. In the region $\omega_1 < \omega < \omega_2$, the plant transfer function (2.4) $\approx$ 1/bs. Further, in the vicinity of ωc, the PI controller gain is approximately Kp. Given our earlier choice of Ti, these values are summarized below:

$$\omega_1 < \omega_c < \omega_2. \tag{2.24a}$$

$$T_i \approx \frac{4}{\omega_c}. \tag{2.24b}$$

$$K_p \approx b\omega_c. \tag{2.24c}$$

The free parameter ω_c is set according to the balance of bandwidth versus sensor noise rejection. The design choice of ω_c will thus depend upon the application.

Figure 2.11 shows the effect of different T_i by Bode and root locus plots. In this example, the damping ratio of the two real axis plant poles is 5. There are thus three loop transmission poles at s =0, -0.101, and s= -9.9 respectively. Both cases crossover at 3 rad/sec. In the first case, follow (2.24b), the zero is located at s = -1. It results in a 60° phase margin. However, in the second case, the zero is put at s= -11. It results a phase margin near 0° and shows conditional instability.

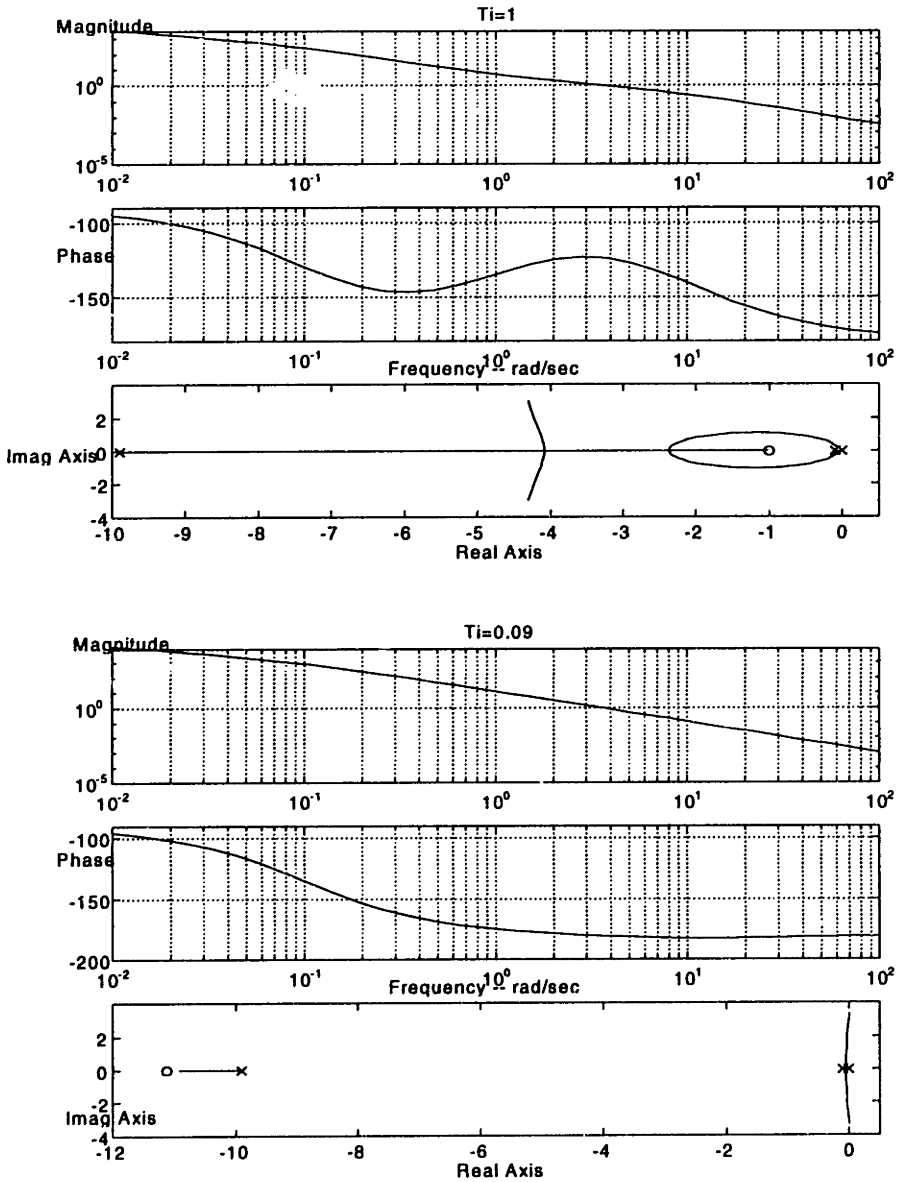

Figure 2.11 Bode and root locus plots for different T_i in DDR design

2.3 Design Examples

Mass Dominated Regime Design

Consider a system [Ols94] with effective mass m = 0.53 Kg, stiffness k=1340 N/m, and essentially no damping (i.e., b ≈ 0). This system has a natural frequency ω_n = 8 Hz. However, the desired bandwidth is 100 Hz. The system dynamics can be written as

$$G_m(s) = \frac{1}{0.53s^2 + 1340}. \qquad (2.25a)$$

The Bode plot of Eq.(2.25a) is shown in Figure 2.12a.

As mentioned in Section 2.1, this system needs a lead compensator to increase its phase margin. Let's introduce a phase lead controller here. It can be written as

$$C_{Lead}(s) = \frac{K_P(1 + s/\omega_o)}{1 + s/\omega_p} \qquad \omega_o < \omega_p. \qquad (2.25b)$$

Now Eq(2.3), (2.4), and (2.5) become

$$-L.T = \frac{(K_P/\omega_o)s + K_p}{(0.53/\omega_p)s^3 + 0.53s^2 + (1340/\omega_p)s + 1340}. \qquad (2.25c)$$

$$H(s) = \frac{(K_P/\omega_o)s + K_p}{(0.53/\omega_p)s^3 + 0.53s^2 + (1340/\omega_p + K_p/\omega_o)s + 1340 + K_p}. \qquad (2.25d)$$

$$D(s) = \frac{s/\omega_p + 1}{(0.53/\omega_p)s^3 + 0.53s^2 + (1340/\omega_p + K_p/\omega_o)s + 1340 + K_p}. \qquad (2.25e)$$

The loop transmission, system closed loop responses subjected to command and disturbance inputs are shown in Figure 2.12b and 2.13 a,b respectively.

From Figure 2.12b. Choosing ω_p = 1200 rad/s, ω_o = 30 rad/s, and K_p=11500, one can get a crossover frequency at around 650 rad/s with 60° phase margin. From Figure 2.13, one can find that the system gain is a little bit less than 1 but it increases when frequency increases. It has a maximum gain at around 500 rad/s. The system response will be amplified when the frequency of input signal is in 100 - 600 rad/s. This is due to the lead compensator since it is a derivative based controller.

Damping Dominated Regime Design

Consider a system [Hol94] with effective mass m=3 Kg and a damping coefficient b = 200,000Ns/m and no stiffness. The desired system bandwidth is around 1 Hz. The system dynamics can be written as

$$G_h(s) = \frac{1}{s(3s + 2\times 10^5)}. \tag{2.26a}$$

The system transfer function is shown in Figure 2.14. Due to the high damping, the inertia term can almost be neglected. Therefore, the system's behavior is similar to a pure integrator.

The proportional controller can be expressed as

$$G_P(s) = K_p. \tag{2.26b}$$

Eq.(2.3),(2.4),and (2.5) can be re-written as

$$-L.T. = \frac{K_p}{s(3s + 2\times 10^5)}. \tag{2.26c}$$

$$H(s) = \frac{K_P}{3s^2 + 2\times 10^5 s + K_P}. \tag{2.26d}$$

$$D(s) = \frac{1}{3s^2 + 2\times 10^5 s + K_p}. \tag{2.26e}$$

The loop transmission Bode plot, closed loop Bode plots for command and disturbance inputs are shown in Figure 2.14 and 2.15, under Kp = 1,200,000 N/m. One can get a crossover frequency around 6.3 rad/s with a phase margin around 90°. The system closed loop behaviors for command input and disturbance input is the same except the DC gain. The system does not amplify the high frequency input signals. For ultra precision machine, its disturbance rejection is not enough. It needs some auxiliary design. The stage in [Hol94] was designed as floating in oil and it is carefully manufactured such that its equivalent density is equal to the ambient fluid. Under such neutral buoyancy, the base disturbance is essentially rejected.

Spring Dominated Regime Design

And finally, consider a system with effective mass m=1Kg, damping coefficient b = 1500 Ns/m and stiffness k=7×10^5. The system dynamics can be written as

$$G_k(s)=\frac{1}{s^2+1500s+7\times10^5}. \qquad (2.27a)$$

Its Bode plot is shown in Figure 2.16. The system natural frequency is 840 rad/s. The PI controller can be expressed as (2.7). Eq.(2.2),(2.3),and (2.5) are written as

$$-L.T.=\frac{K_Ps+1/T_i}{s^3+1500s^2+7\times10^5 s}. \qquad (2.27b)$$

$$H(s)=\frac{K_P(s+1/T_i)}{s^3+1500s^2+(7\times10^5+K_p)s+K_P/T_i}. \qquad (2.27c)$$

$$D(s)=\frac{s}{s^3+1500s^2+(7\times10^5+K_p)s+K_P/T_i}. \qquad (2.27d)$$

Figure 2.16 and 2.17 are the Bode plots for Eq.(2.32), (2.33),and (2.34) respectively. Under K_p=600,000 and T_i=1/550. One can get a crossover frequency at 550 rad/s with a 70° phase margin. Figure 2.17 shows a very important characteristic of spring dominated system under PI controller. It has a great attenuation of disturbance response at low frequency.

Parameter Sensitivity

In general, the final objective of stages is for carrying samples for some purposes, e.g., scanning samples, wafer transporting, etc. The stiffness of the system is essentially unchanged. The damping of system can be treated as a constant if the temperature does not vary a lot. However, the system mass is usually not a constant since the mass of samples changed each by each. In mass dominated design, it is sensitive to the change of mass. However, in both spring and damping dominated design, the sensitivity is essentially much lower than the mass dominated design. For this reason, the stage which is designed in the spring dominated regime can be used for carrying heavy loads.

2.4 SDR PI Design of Stage

For control a system to achieve the required performance, the system dynamics and design specs determine what control law one should use. Table 2.1 is a brief summary of the above analyses.

If the plant has enough damping, the SDR PI system bandwidth can be equal to the plant natural frequency. The ability in disturbance rejection will be increased too. In our flexure based stage design, a damper is introduced into the system. It created enough damping force such that no resonance at resonance frequency. This admits us to design our system bandwidth much closer to the system natural frequency. The final design shows the achievable system bandwidth is about 70% of system natural frequency. Compare the electromagnetically actuated stage system and traditional piezoelectric driven system, although piezo based systems can add damping to increase their performances too, their dynamic range is too small and with some nonlinearity. Comparing to piezo system, electromagnetic based system can have much higher dynamic range and the nonlinearity can be eliminated by proper control algorithm. These are the unique features of our system.

Table 2.1 A brief summary of three parameter dominated systems

	Mass Dominated	Damping Dominated	Spring Dominated
Bandwidth (BW)	BW is usually larger than the system mode	BW is usually small	BW is usually smaller than the system mode
Control law	PID or PD Control	PI or P Control	PI Control
Noise rejection	Will amplify the high frequency disturbance	No special attenuation or amplification	Will attenuate the low frequency disturbance
Parameter (mass) sensitivity	Larger	Smaller	Smaller
Influence of system damping	Not important whatever system is overdamped or underdamped	Not sensitive since the damping ratio is very high	Important for system performance
Typical applications	MEGLEV,Air bearings Direct driving system		Piezo related systems

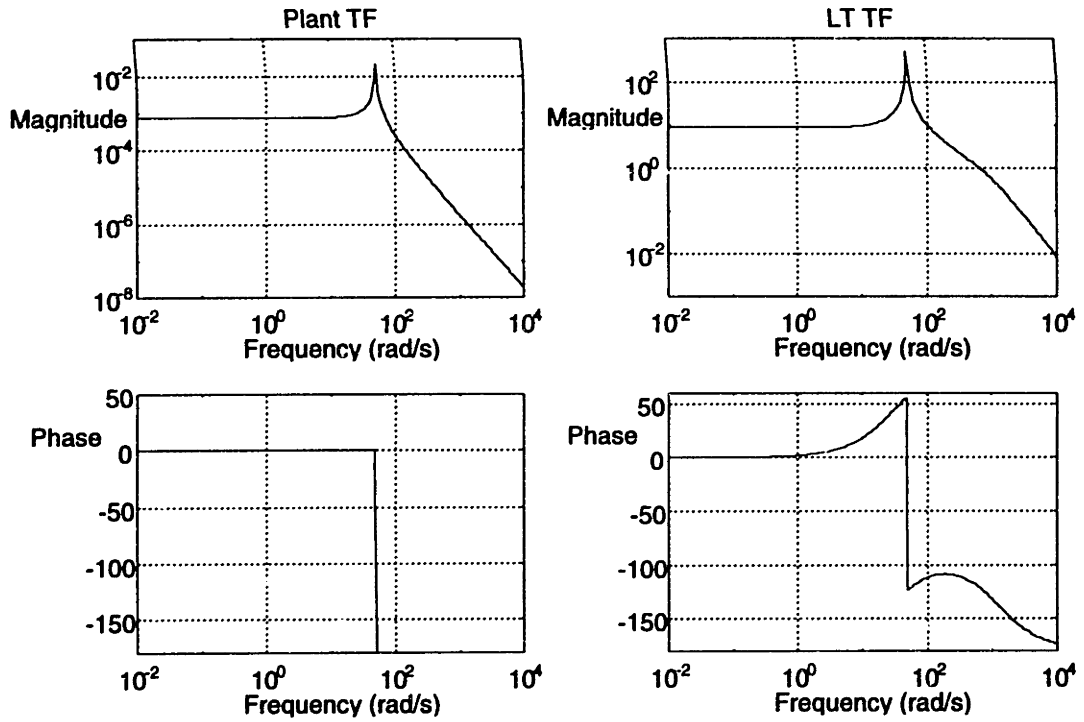

Figure 2.12(a,b) The system and loop transmission Bode plot of the MDR example

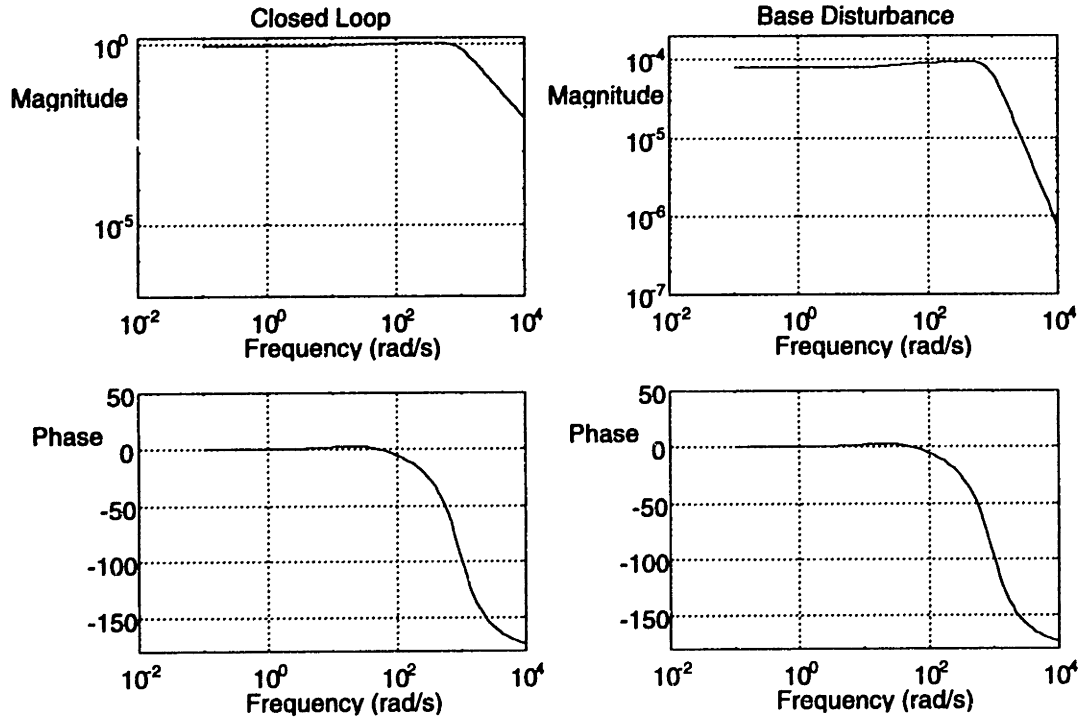

Figure 2.13 The closed loop Bode plot of the MDR example

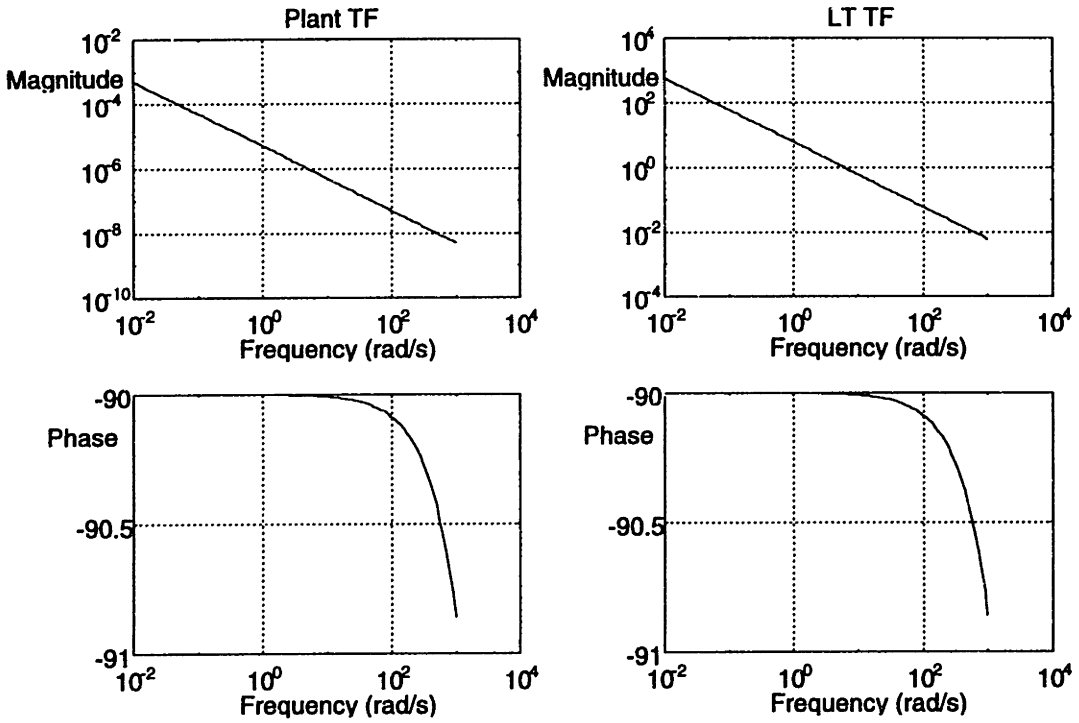

Figure 2.14 The system and loop transmission Bode plot of the DDR example

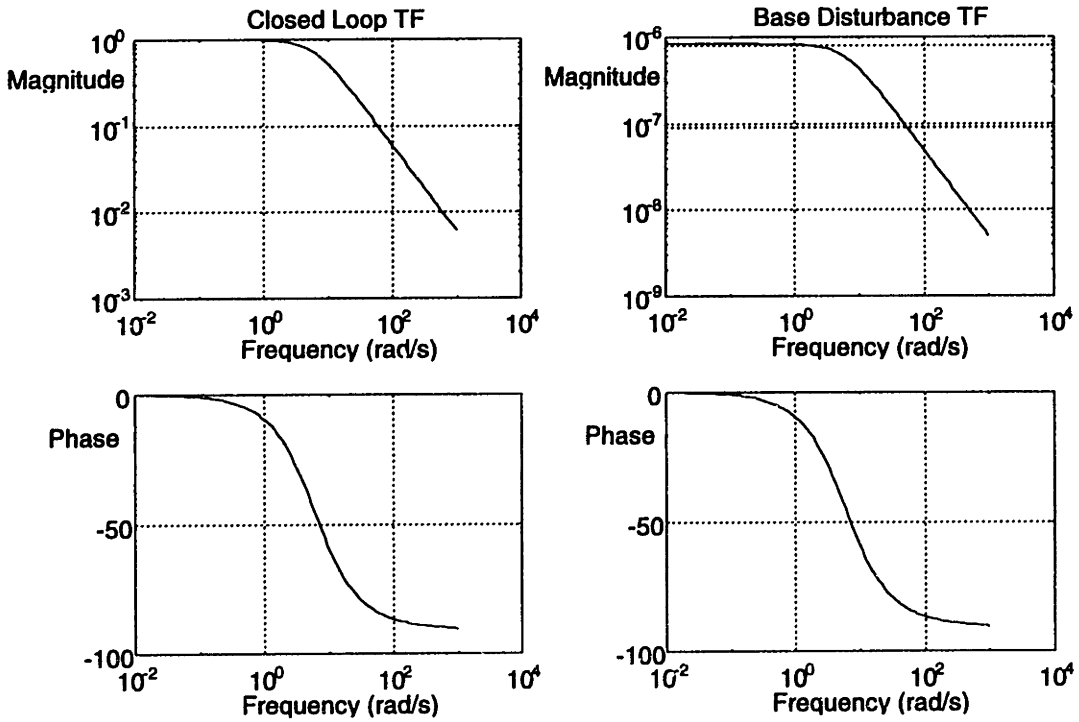

Figure 2.15 The closed loop Bode plot of the DDR example

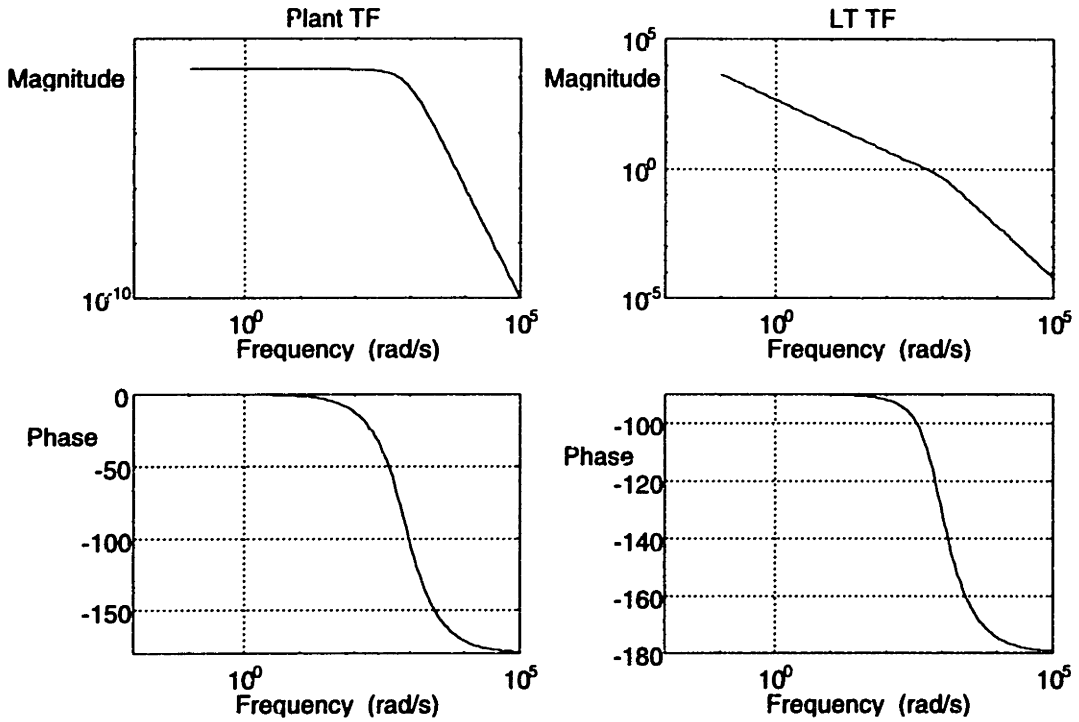

Figure 2.16 The system and loop transmission Bode plots of the SDR example

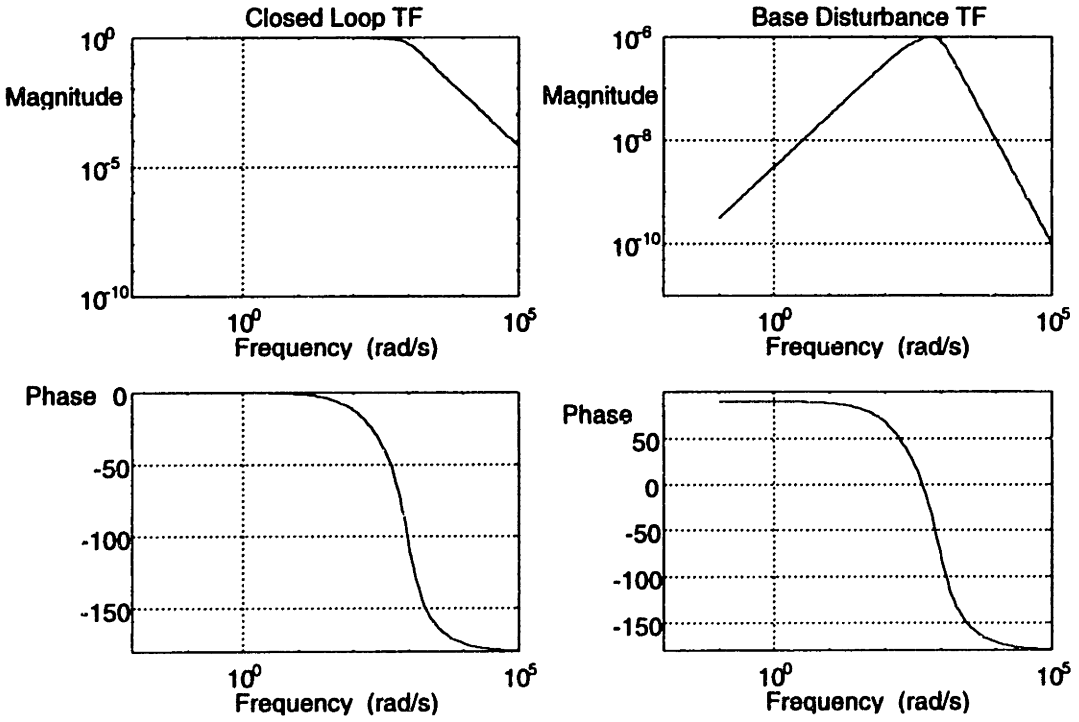

Figure 2.17 The closed loop Bode plots of the SDR example

CHAPTER 3

BASIC ELECTROMECHANICAL DYNAMICS

This chapter discusses the basic electromechanical dynamics. Section 3.1 presents basic concepts and terminology on the electromagnetics. An electromechanical coupling example which is extremely similar to the current case is discussed on section 3.2. Finally, section 3.3 concerns the electromagnetic actuator design. Detailed mechanical drawings of the actuators are shown in Appendix I.

3.1 Basic Electromagnetic

3.1.1 Definition

The following are some important definitions in electromagnetics which will be used in electromechanical dynamics analysis and actuator design. For more detail, refer to [Zor89] and [WoM68].

Magnetic flux

Magnetic flux φ is a characteristic of the magnetic field. Magnetic flux density B may be thought of as representing the line of force between a north magnetic pole and a south magnetic pole. In the SI system of units, flux is measured in the unit of Webers(Wb).

Magnetic flux density

Magnetic flux density is defined as the ratio of the magnetic flux φ divided by the area perpendicular to the flux, A. Thus,

$$B = \frac{\varphi}{A}, \quad \text{or} \quad \varphi = \int B dA. \tag{3.1}$$

The flux density of a material is a measurement of its magnetization, which reveals the magnetic status of the material. The unit of magnetic flux density is Tesla.

Magnetomotive force

The magnetomotive force (mmf) $\mathcal{J}$or the magnetic potential of a coil, is given by the product of the winding current (i) times the number of turns (N), that is, mmf = Ni. The unit of the mmf in the SI system of units is ampere-turns (A).

Magnetic field intensity

The magnetic field density H for a given magnetic circuit driven by a coil with N turns is equal to the ratio of the mmf divided by the length of the mean magnetic path, thus,

$$H = \frac{Ni}{l}\text{,, or } Ni = \int Hdl. \qquad (3.2)$$

It is often referred to as the magnetizing force. The unit of magnetic field intensity is A/m. Magnetic field intensity is related to flux density by

$$\mu = \frac{dB}{dH}. \qquad (3.3)$$

where μ represents the permeability of the material. In a magnetically linear material, this relation reduces to B=μH.

Permeability

Permeability is a measure of how easily a material can be magnetized. Magnetizing a material means aligning all microscopic magnetic forces or moments within the material in the direction of the externally applied field. It is an intrinsic property of all materials and is designated by the Greek letter μ. The actual permeability of a magnetic material is given by $\mu = \mu_0\mu_r$, where μ_r is the relative permeability and μ_0 is the permeability of free space which equals $\mu_0 = 4\pi \times 10^{-7}$ H / m. For good ferro magnetic materials, μ_r is typically on the order of 1,000 to 10,000.

Reluctance

In analogy to the case of resistance in electric circuits, the reluctance is defined as the ratio of the applied magneto motive divided by the flux through the magnetic path under consideration. Mathematically,

$$R = \frac{NI}{\varphi}\ (\frac{\text{A}}{\text{Wb}}). \qquad (3.4)$$

The B-H Curve and Hysteresis Loop

The intrinsic properties of a magnetic material are revealed by the material's B-H curve. The intrinsic properties and B-H curve of a magnetic material depend on the orientation of its magnetic moments which are caused by the spinning and orbiting of an atom's electrons. A typical B-H curve is shown in Figure 3.1. It forms a close-looped curve known as "Hysetresis Loop" of this material. Since the flux density B is proportional to the voltage V and the field intensity H is proportional to the current i, therefore, the area enclosed by the curve is proportional to the power loss of the material per circuit around the hysteresis loop. There are two major issues on magnetic material selection for actuators. The first one is the saturation of the electromagnets. Actuators are expected to work in the unsaturated region, therefore, the higher the saturation limit, the higher current we could input to get a higher force. The other issue is the hysteresis consideration. The area of the enclosed hysteresis loop should be as small as possible in order that the relationship between current and actuator force is one-to-one. This allows the accurate inversion of the actuator nonlinearity. This subject is treated in detail in Chapter 5.

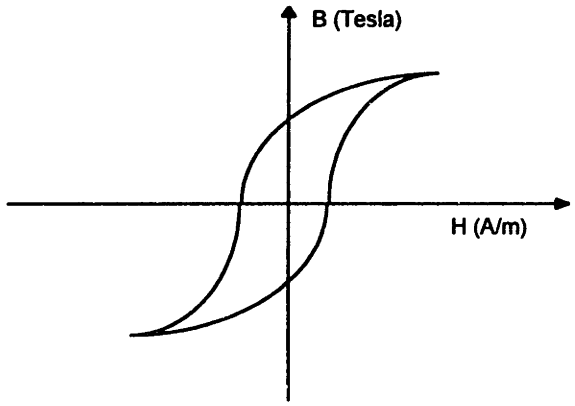

Figure 3.1 A typical B-H curve and hysteresis loop

3.1.2 The Force Relationship of the Electromagnetic Actuator

The theoretical analysis of our magnetic actuator is addressed via standard magnetic circuit calculations such as those in [WoM68]. As shown in Figure 3.2, we use an E-

shaped electromagnet with pole face width w in the center face and w/2 in the side faces. The depth of these faces are all d. The number of turns is N. The current which passes through the coil is i. The air gap between the electromagnet and the steel target is x.

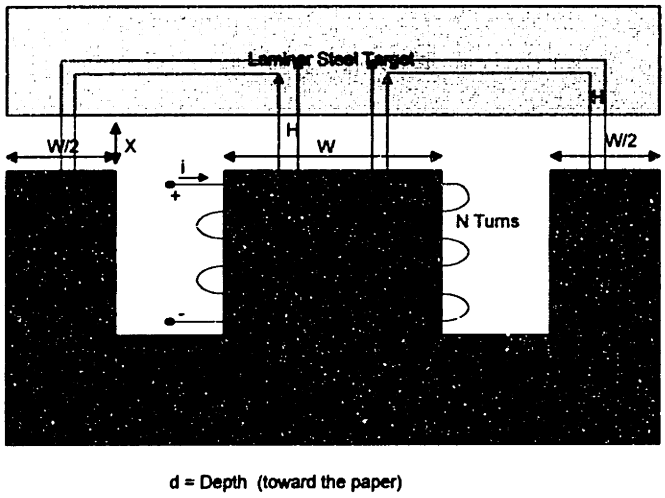

Figure 3.2 The electromagnets - target pair

The permeability μ of the iron core is much greater than the permeability of air. Thus the field intensity H can be assumed to be zero in the iron. That is, all mmf drops are in the part of the path which crosses the air gap. From $\oint H \cdot dl = \int_s J_f \cdot nds$, we have

$$2Hx = Ni. \tag{3.5}$$

Thus the flux crossing the central air gap is wdH, or

$$\varphi = \mu_0 H(wd) = \frac{wd\mu_0 Ni}{2x}. \tag{3.6}$$

and the flux linked by the N-turn coil is

$$\lambda = N\varphi = \frac{wd\mu_0 N^2 i}{2x}. \tag{3.7}$$

Then, under the assumption of no iron saturation, since $\lambda = L(x)i$, we have the actuator inductance as

$$L(x) = \frac{wd\mu_0 N^2}{2x}. \tag{3.8}$$

Since magnetic coenergy $W_m' = \frac{Li^2}{2}$ (3.9)

and

$$F(x) = -\frac{dW_m'(x)}{dx} \tag{3.10}$$

therefore,

$$F(x,i) = \frac{wd\mu_0 N^2}{4}\left(\frac{i}{x}\right)^2. \tag{3.11}$$

Define C $\equiv \frac{wd\mu_0 N^2}{4}$, called the force constant here. Using this notation, we have the final desired equation

$$F(x,i) = C\left(\frac{i}{x}\right)^2. \tag{3.12}$$

Theoretically, if there is no flux leakage or saturation, the force constant C is a function of the number of windings N and the pole face area only. However, due to flux leakage and saturation, one will not get exactly this value. The actual force constant value is a function of many other effects, i.e., such as finite iron permeability, bias current level, signal frequency, material, etc. For getting the exact constitution curve of the actuators, we have performed the electromagnet calibration which is discussed in Chapter 5.

3.2 An Introductory Example

In this section, we consider a mass-spring-damper system driven by a force which exerted by an electromagnet as shown in Figure 3.3. This example is a one-degree of freedom analogue for the X-Y stage design which forms the focus of this thesis. The following is adapted from [WoM68]. Since the relation between electromagnet force, coil current, and air gap is nonlinear, the forcing term is position dependent. We will consider this issue and try to linearize the system dynamics.

3.2.1 Governing Equation:

Here we define x as the air gap. The governing equation for this electromechanical coupling device is

$$m\ddot{x}+b\dot{x}+kx=-F_{magnetic}+f_d \qquad (3.13)$$

where f_d is the disturbance force and $F_{magnetics}=C(\frac{i}{x})^2$.

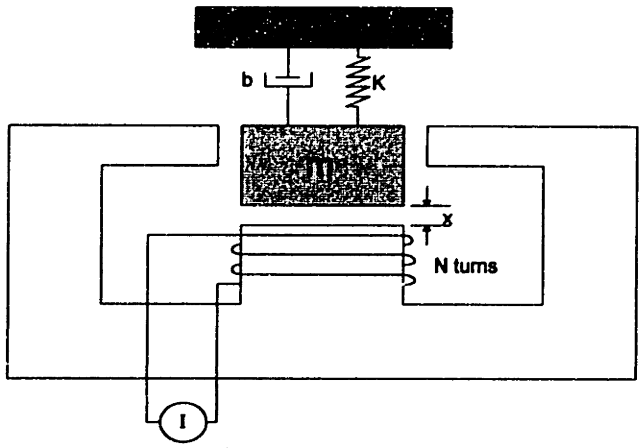

Figure 3.3 An electromechanical coupling system

At equilibrium position, the velocity is equal to zero. We assume in this position, the elongation of the spring is d, the electrical current is I_d, the air gap between electromagnet and object is X_d, and the disturbance force is F_d. Then

$$kd=-C(\frac{I_d}{X_d})^2+F_d. \qquad (3.14)$$

3.2.2 State-Space Form and Linearization

Let $x = x_1$ and $\dot{x} = x_2$, we have the following state space equation

$$\begin{aligned}\dot{x}_1 &= x_2\\ \dot{x}_2 &= \frac{1}{m}(-bx_2-k(d+x_1)+C(\frac{i}{x_1})^2)+\frac{f_d}{m}.\end{aligned} \qquad (3.15)$$

We are interested in the system behavior near the equilibrium point. Therefore, the air gap, input current, and the disturbance force can be expressed as $x = X_d+\hat{x}$, $i = I_d+\hat{i}_d$,

and $f_d = F_d + \hat{f}_d$. Where $\hat{x}$, $\hat{i}$, and $\hat{f}_d$ are the small varied signals. Using Taylor series expansion to linearize $(\frac{i}{x})^2$ in the neighborhood of the equilibrium position I_d, X_d, and F_d. Neglecting higher order terms, we get

$$(\frac{i}{x_1})^2 = (\frac{I_d}{X_d})^2 + 2X_d^{-3}I_d^2\hat{x}_1 + 2X_d^{-2}I_d\hat{i}. \tag{3.16}$$

The final linearized equation will be:

$$\begin{aligned} \dot{\hat{x}}_1 &= \hat{x}_2 \\ \dot{\hat{x}}_2 &= \frac{1}{m}(-b\hat{x}_2 - k\hat{x}_1) + \frac{C}{m}(\frac{2I_d^2}{X_d^3}\hat{x}_1 - 2\frac{I_d}{X_d^2}\hat{i}) + \frac{\hat{f}_d}{m}. \end{aligned} \tag{3.17}$$

3.2.3 System Transfer Function

Taking a Laplace transform on (3.17), we can get

$$s^2\hat{x}(s) = \frac{1}{m}(-bs\hat{x}(s) - k\hat{x}(s)) + \frac{C}{m}(\frac{2I_d^2}{X_d^3}\hat{x}(s) - \frac{I_d}{X_d^2}\hat{i}(s) + \frac{\hat{f}_d(s)}{m}. \tag{3.18}$$

or

$$[s^2 + \frac{b}{m} + (\frac{k - \frac{2CI_d^2}{X_d^3}}{m})]\hat{x}(s) = \frac{-C}{m}\frac{I_d}{X_d^2}\hat{i}(s) + \frac{\hat{f}_d}{m}. \tag{3.19}$$

the transfer function of X(s) versus I(s) will be

$$\frac{\hat{x}(s)}{\hat{i}(s)} = \frac{\frac{-CI_d}{X_d^2}}{(ms^2 + bs + k - \frac{2CI_d^2}{X_d^3})}. \tag{3.20}$$

and the transfer function of $\hat{x}(s)$ versus disturbance $\hat{f}_d$ will be

$$\frac{\hat{x}(s)}{\hat{f}_d(s)} = \frac{1}{(ms^2 + bs + k - \frac{2CI_d^2}{X_d^3})}. \tag{3.21}$$

We can get the pole location by the characteristic polynomial of Eq(3.20) and (3.21). Examining the characteristic polynomial, one can find

If $k - \frac{2CI_d^2}{X_d^3} > 0$: System will be open-loop stable since all poles are in left half plane (LHP).

If $k - \frac{2CI_d^2}{X_d^3} < 0$: System will be open-loop unstable since one pole is in right half plane (RHP).

The above analysis shows this task is an open loop stable system if the bias current does not exceed a critical value related to the spring rate. This is the major difference between this project and other magnetic suspension systems. The term $(-2CI_d^2 / X_d^3)$ can be treated as a negative spring constant and the system stiffness is the summation of the positive spring constant(k) and this negative spring constant. When the summation is zero, the system is in the critical state, i.e., no stiffness. To show the effect of bias, we let $C = 4 \times 10^{-6} Nm^2 / A^2$, $k = 6 \times 10^5 N / m$, and $X_d = 250\mu m$. These values are close to the final design specifications as will be shown in later chapters. The critical bias current will be 1.08 Ampere. If the bias current exceeds 1.08A, the system will become open loop unstable.

The other important result of the above analysis is that the bias current will reduce the system stiffness. Once the system stiffness is reduced, the system natural frequency, noise rejectability will be reduced too. This feature is an unfavorable situation for spring dominated design methodology. However, this problem can be addressed by linearizing the actuator in real time as described in Chapter 5.

3.3 Actuators Design[1]

The actuators are composed of a core wound with magnet wire. The core metal is laminated to reduce the eddy current effect. It is stacked by layers of E-shaped

[1] The analysis, design, and fabrication of actuator were done by Mr. Mark Williams, a Ph.D student in Mechanical Engineering at MIT. The author would like to acknowledge Mr. Williams's assistance here.

laminations with thickness of 0.013 inch (or 0.33 mm in SI units). Selection of the core material is an important consideration in the design of high precision magnetic bearing actuators. A good material will posses low magnetic loss and coercive force, along with high permeability and high saturation flux. In [WiT93], several kinds of alloy sheet steels are considered, including 80% nickel steel, 49% nickel steel, silicon steel, and cobalt iron. From the electromagnet calibration data shown in Figure 3.4, the cobalt iron material demonstrated high flux levels. However, it exhibited higher electromagnetic hysteresis and coercive force than the acceptable limit in this application. This material is also very expensive.

The silicon steel showed a moderately high saturation limit and a moderate hysteresis loop. The 80% nickel steel has very low hysteresis, but its saturation level is reduced significantly and thus this actuator can not produce the necessary force. Finally, the 49% nickel steel is chosen for the core material since it has small hysteresis and a moderately high saturation limit. Table 3.1 shows a brief comparision between actuators which formed by these four core materials. Their dimensions are the same and are shown in Figure 3.5 with N = 240 turns.

Table 3.1 A brief comparison of actuators performance with different core materials

	Cobalt iron	Silicon steel	80%Ni-Fe	49% Ni-Fe
Max. Reachable Force (N) at gap=80μm and I = 1.6A	~480	~280	~58	~220
($F_{forward}$ - $F_{backward}$)(N) at I = 0.6A, gap=100 μm	~25	~10	<0.5	<2
($Force_{650\mu m}$/$Force_{80\mu m}$) I=1.6A	~5%	~10%	~35%	~10%

The following design analysis is adapted from [WiT93]. Forces produced by the actuators are expressed by Eq.(3.11), with pole face area A_p= wd. Since actuator power is $P = i^2R$, we obtain the force-power relation

$$F = \frac{\mu_0 A_p N^2 P}{4x^2 R}. \qquad (3.22)$$

The number of coil turns N, is equal to the area of the core window multiplied by a package factor constant. We can reduce N to the window area in terms of pole width (W), lamination length (L), and height (h). These parameters are shown in Figure 3.5.

$$N = A_w = 2w^2 - (4h + L)w + 2hL \qquad (3.23)$$

where A_w is the window area. If the average coil turn diameter is in the middle of the core window, the average turn length will be approximately equal to 2L. Since the coil resistance is the product of the average turn length *2L*, the number of turns *N*, and the material resistivity *1/ρ*, the coil resistance can be written as

$$R = 2LN / \rho = aLA_w. \qquad (3.24)$$

Where a is a proportional constant. Substituting (3.23), (3.24) into (3.22) and eliminating all constants. Under constant power consumption, we get

$$F_u = 2w^4 - (4h + L)w^3 + 2hLw^2. \qquad (3.25)$$

where F_u is force per unit pole face. Differentiating (3.25), we get the criteria for maximum force under constant power.

$$8w^2 - 3(4h + L)w + 4hL = 0. \qquad (3.26)$$

Commercially available EI laminar steel sheet is selected for building the actuators to reduce the cost. Eq.(3.26) provided a criterion for dimension determination. Figure 3.5 shows the dimension of the laminar core of actuator. The real photo of the actuator is shown in Figure 3.6. In such a design, one can get 50 N force under normal operation, i.e., at 250 micron air gap and 1A current input. Based on the different requirement for X and Y motion, we use the same core materials but a different size and number of turns on magnet wire winding. The Y-direction actuators use #22 wire with 550 turns. The X-direction actuators use #26 wire and 550 turns. Table 3.2 shows some important design parameters of X and Y actuators. By Eq(3.11) and Table3.2, , the theoretical force constant for X-direction actuators is $5.1 \times 10^{-5}\ Nm^2 / (Amp)^2$. For Y direction actuators, this value will be $.17 \times 10^{-5} Nm^2 / (Amp)^2$. The design of actuator is shown in Appendix I.

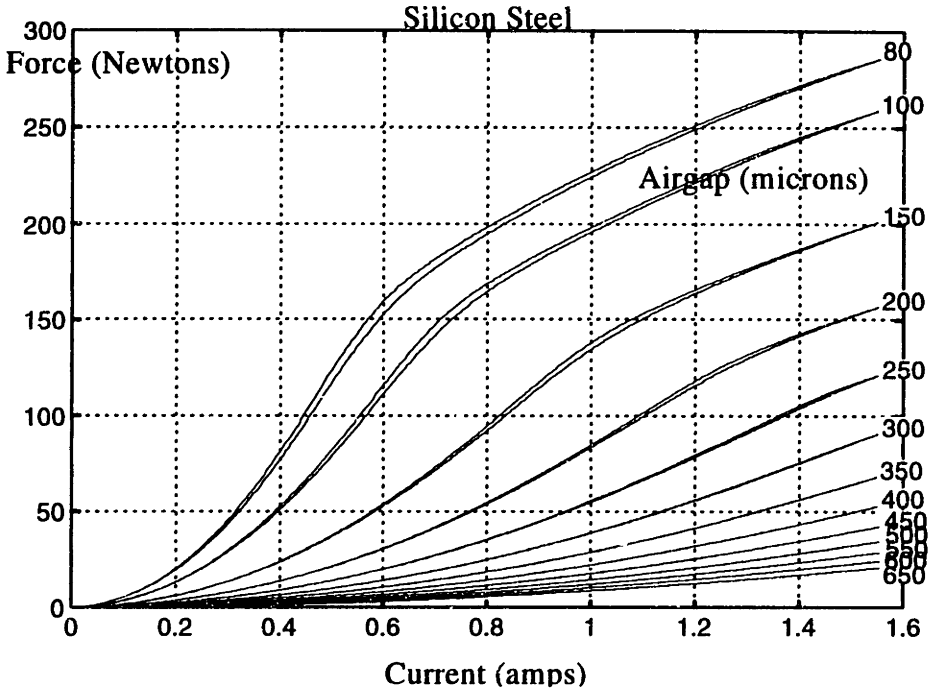

Figure 3.4a: Silicon-steel force curves. (Adapted from [WiT93])

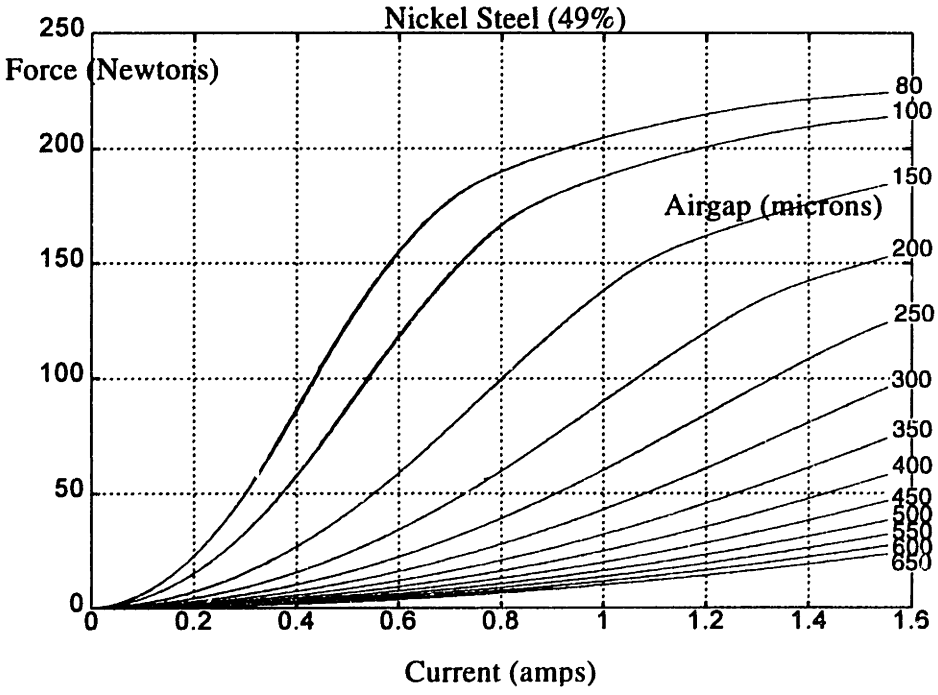

Figure 3.4b: 49% Nickel-steel force curves. (Adapted from [WiT93])

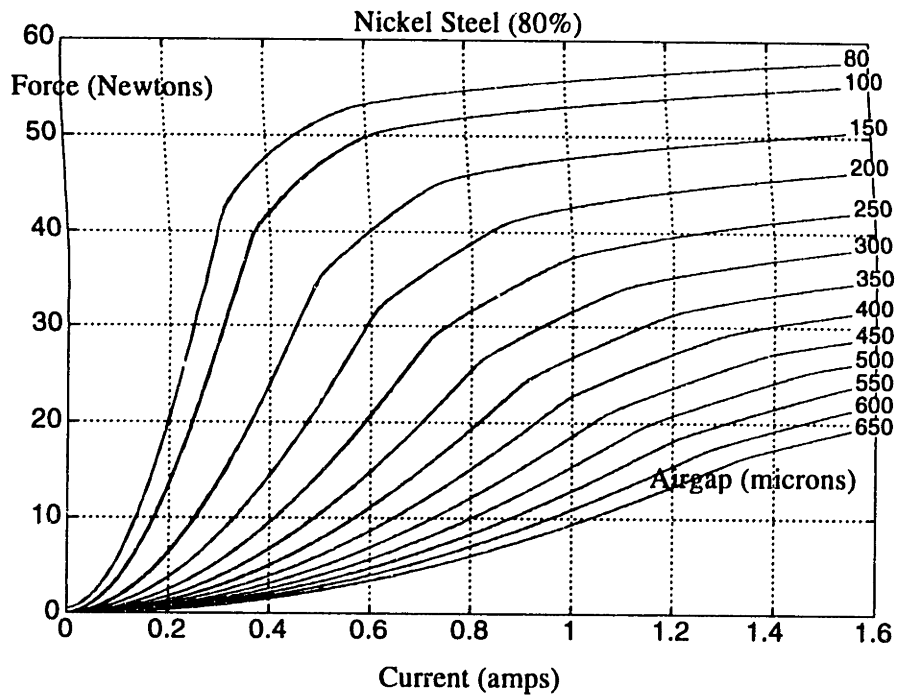

Figure 3.4c: 80% Nickel-steel force curves. (Adapted from [WiT93])

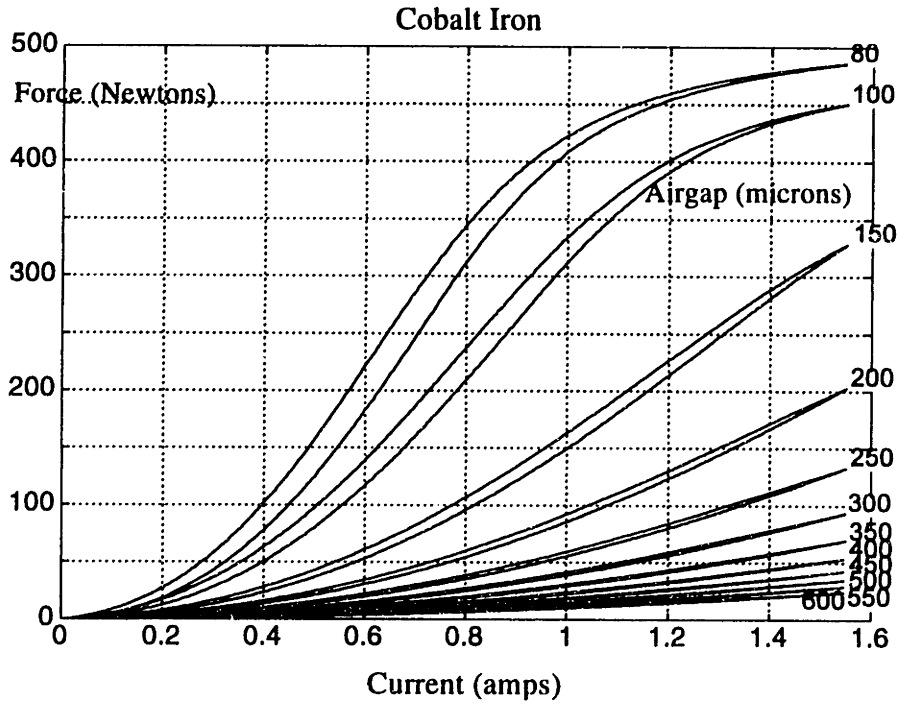

Figure 3.4d: Co-V-Fe force curves. (Adapted from [WiT93])

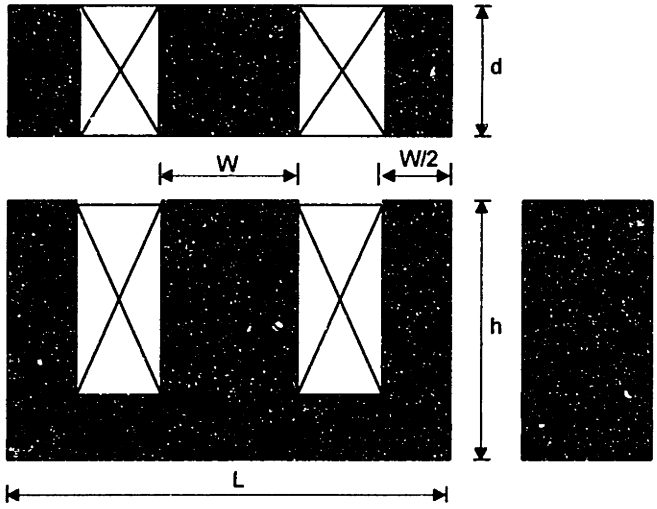

Figure 3.5 Electromagnet core sizing plot

Table 3.2 The design parameter of actuators

	Actuators of Figure 3-4 a - d	X - Actuators (49% Ni)	Y - Actuators (49% Ni)
L (inch)	1.6	1.6	1.6
W (inch)	0.5	0.5	0.375
h (inch)	1.0	1.0	1.0
d (inch)	0.5	0.5	0.5
N (turns)	240	550	550
$\mathbf{C}_{\text{theoretical}}$ (Nm^2/A^2)		1.53×10^{-5}	1.18×10^{-5}

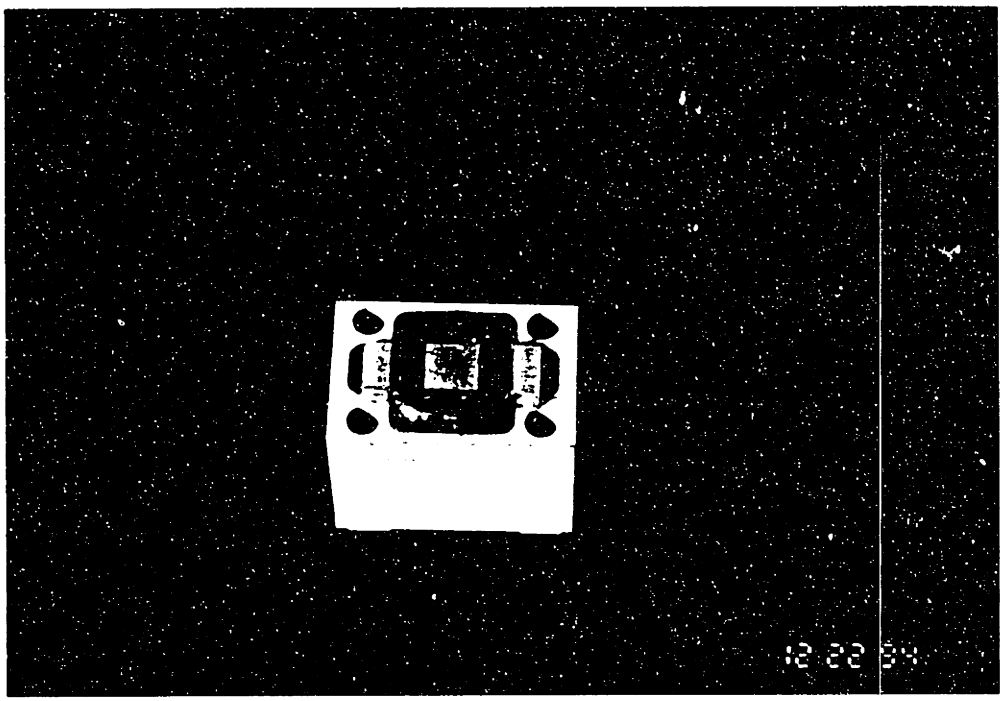

Figure 3.6 Photo of electromagnetic actuator

CHAPTER 4

THE MECHANICAL DESIGN

This chapter presents the mechanical design issues associated with our system. The design approach is presented in section 4.1. Section 4.2 discusses the stage design based on solid and fluid mechanics. After calculating the stage parameters, section 4.3 deals with the second order system modeling. The issue of kinematic coupling design of the sample holder is explained in section 4.4. Finally, combining the theoretical modeling and experiment data, we present the system dynamics in section 4.5. Detailed drawings of the stage and actuator designs are shown in Appendix I.

4.1 General Design[1]

For a short range, high precision stage with high noise rejection, the concept of spring dominated regime (SDM) design has been introduced in Chapter 2. In this design approach, the mass of stage should be as small as possible and the stiffness, on the other hand, should be as high as possible, in order to achieve a high system resonant frequency. There will be a compromise between the mass and stiffness of the system, the capacity of actuators, the material, and the dimensions.

For rejecting the low frequency base vibration and reducing the steady state error, a PI control scheme is used. As the integrator is introduced into the controller, this will tend to reduce the system stability. A viscous damping mechanism, therefore, should be added into the stage for stabilizing the system under closed loop control.

---

[1] Most of the design and fabrication of the prototype were done by Mr. Andre' Monteiro, a Ph.D student of University of Warwick, U.K, working under the guidance of Prof. Stuart Smith. The author wishes to acknowledge Mr. Monteiro's contribution here here.

Two matching rectangular aluminum blocks connected by four steel legs made of chrome-vanadium gage steel are used as the two-axes flexure stage (Figure 3.1a). One of these plates is bolted down to a larger base plate, while the other becomes the moving stage platform (Figure 3.1b). Around the two plates are six electromagnetic force actuators which are optimized to produce high forces at low currents (Figure 3.1c). Four of them act parallel to the y axis and the other two are positioned orthogonal and constituted the x axis drives. Rigidly fixed to the underside of the top table is an aluminum webbed frame (of horizontal cross section like a double 'H') containing iron core targets to be attracted by the electromagnets (Figure 3.1c). For optimum rectilinearly the targets are centered halfway between top and bottom plates [Pla56].

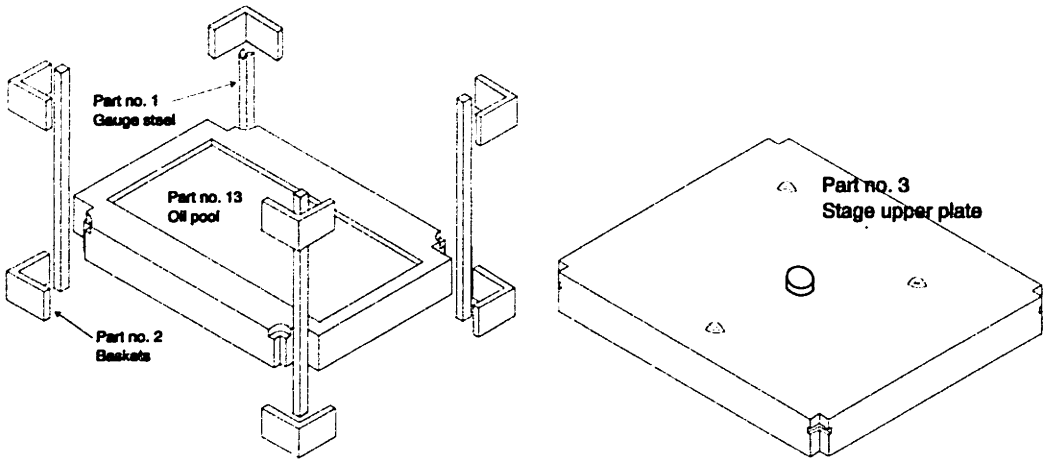

(a) (b)

Figure 3.1(a) A isometric draw of stage components -- steel flexures and viscous oil pool (b) The upper plate of stage and the kinematic coupling elements

Kinematically mounted on the top plate is a sample holder with three kinematic coupling elements (Figure 3.1d). On this frame four precision ground orthogonal flat surfaces have been produced. Among the four surfaces, two are used as the target ground plane electrode for three capacitance position sensing gauges, the other two, however, will be used for attaching a plane mirror for laser calibration. Around two sides of this frame and bolted to the base plate is an L-shaped datum bracket holding three capacitive gauges (Figure 3.1e). The probe electrodes are arranged with two placed in parallel along the longer lengths of the frame, one at the other end. The third is positioned centrally on a short side and is orthogonal to the other two. These three sensors are capable of

detecting the relative displacements between the stage and the sides of the L-shaped mount (that is bolted onto the larger base plate) which therefore forms the datum. Yaw is monitored as the difference between the two parallel sensors on the same side by dividing their mean separation. Bolted at the bottom of the double H structure below the moving platform is a thin damping plate which is parallel, and in near proximity, to the stationary bottom plate of the stage (See Figure 3.1a and 3.1c). Viscous damping of the stage's translation can be achieved by filling an appropriate fluid into this gap. The amount of damping can be controlled by both of the viscosity of the fluid used and the gap separation.

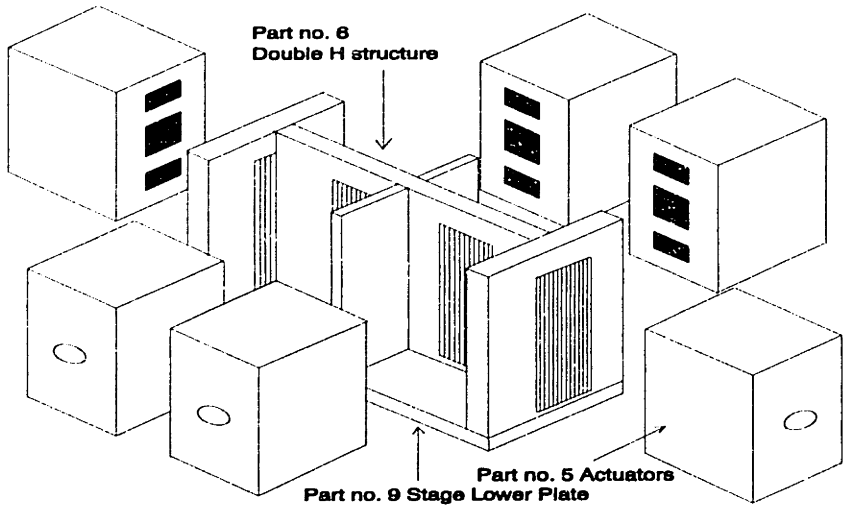

Figure 4.1c The double H structure of stage which used for interaction with six actuators and the stage bottom plate, which used for getting viscous damping. There are six magnetic actuators surround them.

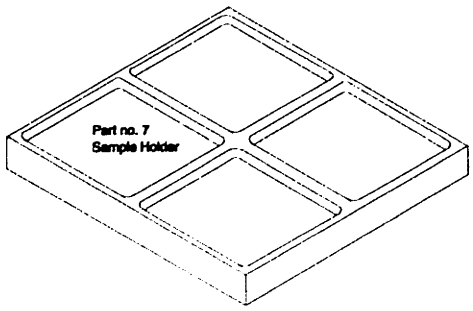

(d)

Figure 4.1d The stage sample holder.

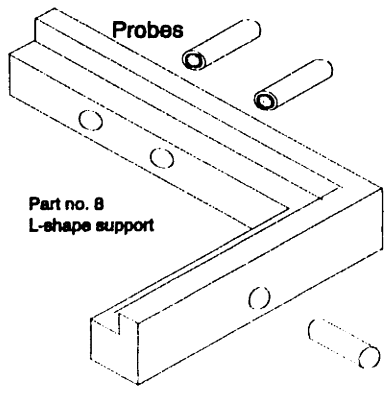

(e)

Figure 4.1e The L shaped bracket and sensors

The prototype of the stage was designed and produced by Andre' Monteiro, a Ph.D. student of University of Warwick, U. K. staying at the University of North Carolina at Charlotte during the summer of 1993. In general, it follows the above principles but this prototype had a lot of problems. First, it used wax to provide dry friction as the system damping. It is not suitable. Thus, a new base plate was made by the author for replacing the old design for adding viscous damping. Second, all the lag connections at the top and bottom plates were reworked to ensure that the legs are firmly attached, and thus to prevent mechanical hysteresis. Third, the kinematic coupling sample holder was redesigned. Finally, due to the change in sensor dimensions, the L- shaped mount, the sample holder, and some support blocks were redesigned and manufactured.

4.2 The Stage Design

4.2.1 Stiffness modeling from elementary beam theory

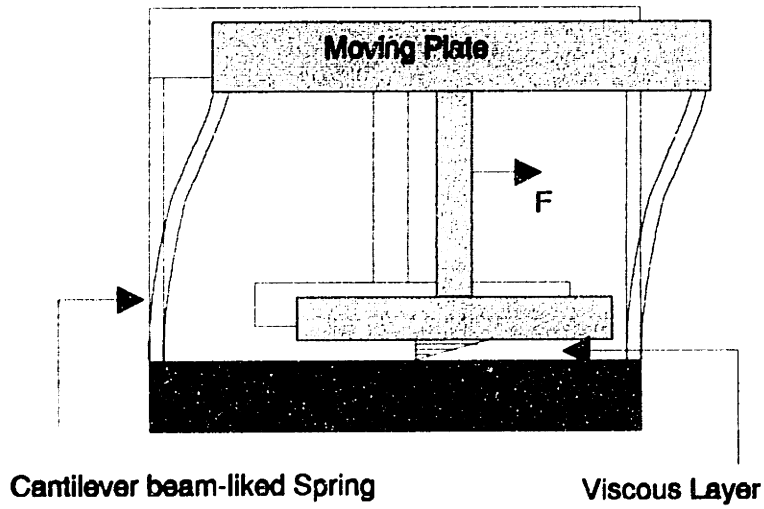

Figure 4.2 The idea of the stage motion

Stiffness of translation mode

The four steel legs supply the stiffness of the stage since the steel rods deflect when the stage undergoes attractive force. There exists a relationship between the loading F and the displacement x. The stiffness then is defined as $K = \frac{F}{x}$. From Figure 4.2, it can be found that the steel rods of the stage can be modeled as cantilever beams, therefore, the result of beam theory can be directly applied for modeling the stage stiffness. Considering the case in Figure 4.1, the stiffness of each rod λ can be found in [TiG72],

$$\lambda = \frac{12EI}{L^3}. \tag{4.1}$$

The total linear stiffness of the complete flexure in one axis as seen by the drive actuator will be $K_{total} = 4\lambda$. Here E is the Young's modules of the metal, L is the effective length of the beam and I is the second moment of area of the cross section of the beam.

If the same bending stiffness is used for both the x and y directions, a square cross section can be employed. This is likely to introduce minimal crosstalk between axes (ultimately, a circular cross section being optimal since it eliminates any possibility of warping effects). For a beam of square cross section the moment of inertia is

$$I = \frac{a^4}{12}. \tag{4.2}$$

where a is the side length of the cross section.

To model each linear degree of freedom of the system as a simple second order harmonic oscillator its natural undamped resonant frequency, f_n, is given by

$$f_n = \frac{1}{2\pi}\sqrt{\frac{K}{m_e}}. \tag{4.3}$$

where m_e is the effective mass of the system.

To maximize the stiffness while keeping the structure light the stage is built out of aluminum while the cantilever legs are of chrome vanadium gage steel stock. The maximum stiffness that can be used is limited by the force of the drivers and the maximum range required. The maximum force available from each actuator is approximately 50 N under normal operation, and a displacement of approximately 150 μ

m peak to peak is the requirement. Using the following parameters: a = 4 mm, L = 70 mm, E = 207 Gpa, we get $K_{total} = 6.37 \times 10^5 N/m$. The effective mass of stage m_e being 940 g, yields a natural frequency of 135 Hz with a range of ±80 μm.

Stiffness of rotation mode

There are two major contributions in stiffness of rotational motion. The first one is the torsion of steel rod T_t, the other is the resultant moment which caused by the translation motion of whole four steel legs T_l.

Since the steel beams of the stage are not circular types, formulas of elementary mechanics of materials can not be applied. However, the exact solution of rectangular cross-sectional beam can be found in the theory of elasticity [TiG70].

$$T_t = 0.1406 G\theta (2a)^4. \tag{4.4}$$

where a is the width of the cross-section of the beam, G is the torsion rigidity of steel which equals 70 GPa. Using Eq(4.4), with width a = 4 mm, the torsional stiffness is $K_{\theta t} = \frac{T_t}{\theta} = 45.7 N \cdot m/rad$. The other effect, using the stiffness matrix method, assumes on infinitesimal displacement. Omitting the detail of the derivation, by a first order approximation. The result is

$$K_{\theta l} = \frac{48EIa^2}{L^2}. \tag{4.5}$$

Using the design data, it can be found that $K_{\theta l} = 2744 N \cdot m/rad$. The total stiffness of rotational mode is then

$$K_\theta = K_{\theta l} + K_{\theta t} = 2927 N \cdot m/rad.$$

It is difficult to estimate the polar moment of inertia of the stage due to the complicated configuration. For simplicity, we just treat the stage as a combination of several rectangular plates. Using the definition of the polar moment of inertia and the parallel axes theorem, the estimated polar moment of inertia is $J = 1.8 \times 10^{-3} Kg \cdot m^2$. (This combines with the sample holder which will be mentioned in section 4.4)

The natural frequency of rotational motion then is given by

$$f_{\theta n} = \frac{1}{2\pi}\sqrt{\frac{K_\theta}{J}}. \qquad (4.6)$$

In this case, $f_{\theta n}$ is around 200 Hz and the range of rotational motion is ±2.2 mrad.

Vertical Motion

As shown on Figure 4.2, a small vertical motion will be associated with on X or Y direction motion. The amount of change in Z direction can be approximated by

$$\Delta z \approx L(1-\cos\theta). \qquad (4.7)$$

Using L=70 mm, maximum motion range to one side equals 50 μm. From this, one can get a maximum angle of 0.71 mrad and thus the maximum vertical displacement Δz = 17.8 nm. This mode is an undesirable but at about 18 nm, it is ignoble for most applications. However, for example, when the stage work with piezo based STM head, since the STM probe is sensitive to the vertical gap change, one should control the piezo actuator motion to compensated this error motion.

4.2.2 The Viscous Damping Calculations

Modeling the stage as a classical second order system with viscous damping, the equation of motion for each linear freedom q_n is

$$m_e\frac{d^2q_n}{dt^2} + b\frac{dq_n}{dt} + Kq_n = F. \qquad (4.8)$$

where b is the damping force per unit velocity of the system.

To avoid long setting times produced by an over-damped system it is better to go for a slightly under damped condition with optimal value being in the region 0.6 - 0.8 in the closed loop control system. A closed loop damping ratio of ξ=0.7 will be desirable. However, a closed loop PI control will tend to decrease system damping. Therefore, a higher damping ratio in the design is required. The amount is depends on the magnitude of these control gains. These can be verified from the root - locus plot of systems as shown in Chapter 8.

Damping of translation motion:

The damping ratio is defined by

$$\xi = (\frac{b^2}{4m_e K})^{1/2}. \qquad (4.9)$$

solving for b yields

$$b = \xi\sqrt{4m_e K}. \qquad (4.10)$$

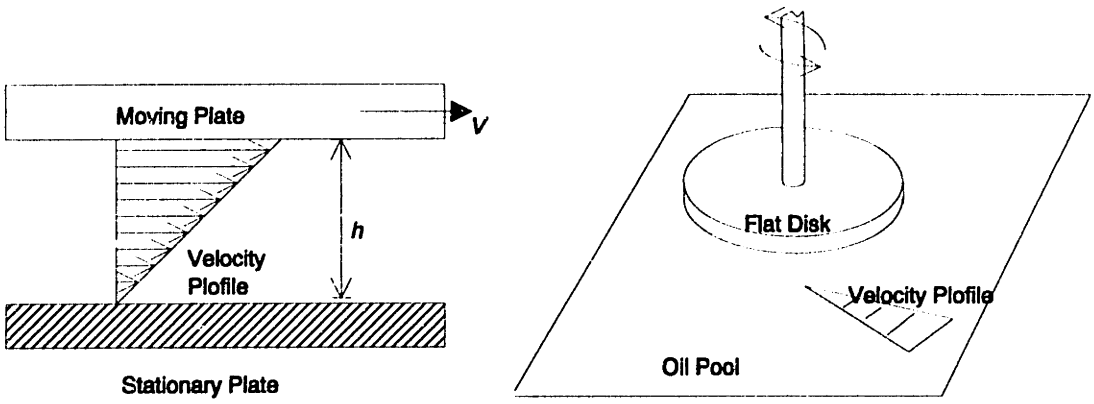

Figure 4.3 Damping in translation (4.3a) and rotation motion (4.3b)

Choosing the ξ = 1 and using the former data of m_e and K_{total}. Eq(4.10) yields a desired damping coefficient of $b = 1553$ Ns m^{-1}. Considering Figure 4.3a, we assume the laminar flow conditions between the damping plate and the base. The viscous reaction force between the stationary base and the adjacent damping plate is then

$$F = \frac{\mu VA}{h} \qquad (4.11)$$

where μ is the dynamic coefficient of viscosity of the fluid employed, V the velocity of the plate over the fluid, A the area of the plate and h is the thickness of the intervening fluid. For laminar condition, $b = F/V$ and thus

$$h = \frac{\mu A}{b} \qquad (4.12)$$

or for the desired value of b,

$$h = \frac{\mu A}{2\xi\sqrt{Km_e}}. \qquad (4.13)$$

Damping of rotational motion:

Consider the ideal situation shown in Figure 4.3b, where a torsional motion occurs in the bar and disk system. The disk contacts with the damping fluid. Using the classical dynamics, assume a circular disk performs a torsional motion in a viscous pool. The friction torque will be

$$T = \frac{\pi\mu}{2h}\omega R^4 \quad \text{and thus} \quad b = \frac{\pi\mu}{2h}R^4. \qquad (4.14)$$

where T is the friction torque, R the radius of circular disk. In this case, the "disk" is not circular, but rectangular, therefore, instead of R, an effective radius R* should be used.

The desired damping ratio may not be reached by translation and rotation modes simultaneously. Since the translation will play a much more important role in stage motion and the stage rotation is merely for fine adjustment, the translation mode damping should be given first priority. Since b has already been chosen by previous design constraints and A, the area of the friction plate cannot be increased significantly, we are left with the fact that μ has to be very large in order to increase the gap h by around two orders of magnitude. The best choice of high viscosity fluid will be the Viscasil (Silicone Fluid). The final choice is GE Viscasil with kinematics viscosity = 600,000 cSt (centi-stokes). The density of Viscasil is roughly equal 1000 Kg/m^3. Then, put the data on Eq(4.13), we can get h = 1.83 mm for ξ=1. Although Viscasil works obey the definition of Newtonain fluid, i.e., $\tau = \mu\frac{du}{dx}$, its viscosity is a function of the rate of shear (frequency). Marsh in [Mar94] measured the characteristics of GE Viscasil 600,000 cSt fluid and did curve fitting. He found that its viscosity can be represented by the following equation.

$$\mu(f) = 1300 f^{-0.72} \qquad f > 10 \text{ Hz.} \qquad (4.15)$$

and μ decreases linearly from 800 to 250 poises if f smaller than 10 Hz. Figure 4.4 shows this result. This frequency dependent property brings some troubles in system modeling. The gap h is initially designed based on the nominal viscosity, however, when put into

control, the system performs as if there were very little damping. Therefore, I reduced the gap until the damping ratio is increased enough to meet the requirement at the system resonant frequency. However, under such a situation, the damping force will be too large if working at a lower shear rate.

4.3 The system Modeling

System modeling with base excitation

The stage can be treated as a decoupled three degree of freedom system. Its behavior can be described by Eq(4.8). However, under the influence of environmental disturbances, we need to modify Eq(4.8) to a more general case.

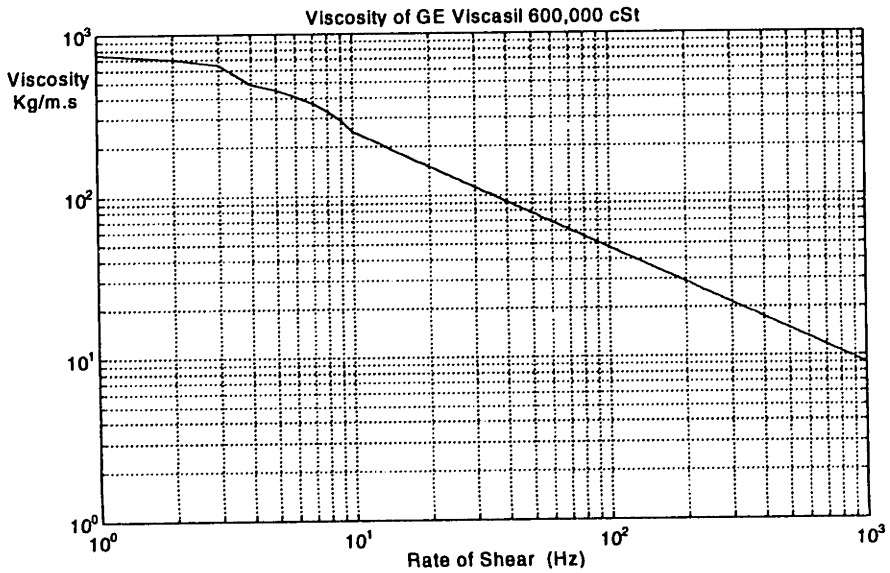

Figure 4.4 The characteristic of GE Viscasil 600,000 cSt [Mar94]

Consider the system plotted on Figure 4.5. The system has included the influence of base excitation. The situation is similar to the working principles of vibration measurement instruments such as vibrometer and accelerometer [Rao85]. Consider a mass-spring-damper system with a vibration of reference base.

The equation of motion of the system will be:

$$m\ddot{x} + b(x - y) + K(x - y) = 0. \tag{4.16}$$

or

$$m(\ddot{x}-\ddot{y})+b(\dot{x}-\dot{y})+K(x-y)=-m\ddot{y}. \tag{4.17}$$

where y is the displacement of base vibration.

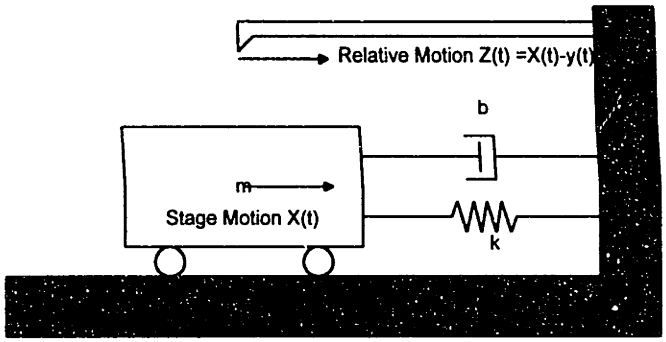

Figure 4.5 Schematic for Stage Motion

Let z = x-y, we have

$$m\ddot{z}+b\dot{z}+Kz=-m\ddot{y}. \tag{4.18}$$

Assume $y=Y_b\sin\omega t$, or in general $y=\sum_{i=1}^{\infty}Y_b\sin\omega_i t$, then

$$m\ddot{z}+b\dot{z}+Kz=\omega^2 Y_b\sin\omega t. \tag{4.19}$$

and

$$z(t)=Z\sin(\omega t-\phi). \tag{4.20}$$

Where

$$Z=\frac{mY\omega^2}{\sqrt{(k-m\omega^2)+(b\omega^2)}}=\frac{Y(\frac{\omega}{\omega_n})^2}{\sqrt{[1-(\frac{\omega}{\omega_n})^2+(\frac{2\xi\omega}{\omega_n})^2}}. \tag{4.21}$$

$$\tan\phi=\frac{\omega_c}{K-m\omega^2}=\frac{2\xi(\frac{\omega}{\omega_n})}{1-(\frac{\omega}{\omega_n})^2}. \tag{4.22}$$

X is taken as the absolute displacement of the stage. However, since the results of all position measurement instruments are based on the vibrated reference base, all one can measure will be z -- the relative motion between stage and vibrated base. Figure 4.6 shows the frequency response of (4.19), where we take acceleration $\omega^2 y_b$ as the input.

System transfer function

The system transfer function of the output z(t) versus the base vibration input y(t) can be written as follows:

$$H_1(s) = \frac{Z(s)}{-Y(s)} = \frac{ms^2}{ms^2 + bs + K}. \tag{4.23}$$

or, using base acceleration as system input, we have

$$H_2(s) = \frac{Z(s)}{-s^2 Y(s)} = \frac{m}{ms^2 + bs + K}. \tag{4.24}$$

Eq(4.24) will be used as the governing equation of noise modeling in Chapter 6.

In the general case, the force term involves two items, one is the control input and the other is the base vibration disturbance. To solve the equation, one may solve them separately and use linear combination to get the total effect.

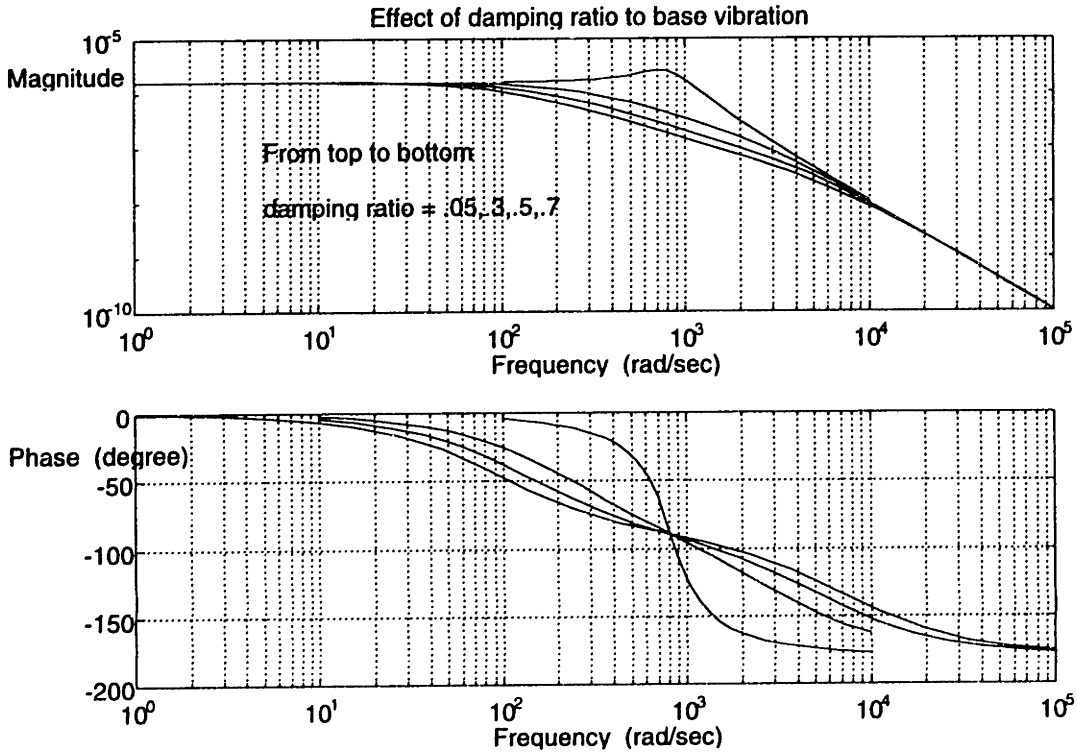

Figure 4.6 Stage response to base vibration input

4.4 Sample Holder Design

In this design, the stage system design is separated into two major parts. One is made for interaction with actuators and has been discussed in the previous sections. The other part is used for carrying testing samples and for position sensing. It is called the sample holder.

Sample holder design considerations

There are some basic requirements for the sample holder design. The sample holder should be attached to the stage firmly under a definite pre-load. The surface finish in the target area should be reached to a certain level for interaction with capacitance probes. The squareness of this sample holder is critical since the stage Cartesian coordinates will are based on the three probes as referred to the target surfaces. The three probes will establish the coordinate of the whole system. The degree of parallelism is also critical since this is required for sensor calibration by laser. Furthermore, the weight should be as light as possible in order to keep the natural frequency as high as possible. The structural damping should also be reasonable high to avoid the undesired vibrations of sample holder. Those vibration will be detected by sensors and this contaminated feedback signal will influence the system control and degrade the overall performance.

A piece of aluminum is cut carefully to remove mass as much as possible. After cutting work, precision grinding can grant the surface smoothness and squareness to a certain level, depending on the accuracy of grinder and gages. For avoiding the residual stress causing distortion, thermal cycling may be necessary on the aluminum part, although we did not take this step here.

After finishing the above procedures, the structural damping is very low. By structural testing, the damping ratio ξ is only around 0.01~0.02. It should be increased since the stage motion may excite the structural mode and the position signal which sensed by probes may contain some undesirable structural noise. There are two common ways to

increase the structure damping, one is the mass damper and the other is the shear damper. They have been discussed in [Slo92].

The mass damper is impractical in this case since it requires the introduction of additional mass which will reduce the system performance. Therefore, the shear damper will be the only method to be considered.

The basic principle of shear damper is introducing a third material as a layer between two pieces of the primary material. Their material parameters are different. When the "composite material" vibrates, related shear occurs on the boundary which dissipates some vibration energy and thus increases the structural damping. The epoxy which used for gluing the kinematics coupling element which will be discussed in the next section plays a certain contribution on shear damping but it's still not enough. The remaining requirement will be reached by attaching a sound attenuation on the surface of sample holder. After these efforts, the structural damping is increased to $0.05 \sim 0.1$.

The Kinematic coupling design

Consider a contact between two rigid bodies. Since there are six degrees of freedom of a rigid body in free motion, i.e., three translations and three rotations, there exists a relationship between the resulting degrees of freedom f and the number of independent contact points n.

$$f = 6 - n. \tag{4.25}$$

Therefore, if one can make a proper six-points contact, the motion of a rigid body will be totally constrained. Several design examples can be found in [Slo92] and [SmC91].

The final design is shown in Figure 4.7. There are three kinematic coupling elements in this sample holder as shown in Figure 4.8. Each element is composed of a piece of aluminum and two steel rollers to make a groove for two-point contact. These rollers are glued by epoxy to the aluminum to form the element. These elements are then glued to the sample holder.

On the upper face of stage, three steel hemispheres form the other half of the kinematic coupling pairs. Each hemisphere makes contact with two groove rollers. Therefore, with

three such pairs, a six-point contact is formed. The reason for choosing steel for the couplings is its stiffness. In prototype designs, the kinematic coupling elements in the sample holder were made of aluminum alloy which were deformed a little bit and formed an over-determined contact during the preloading process.

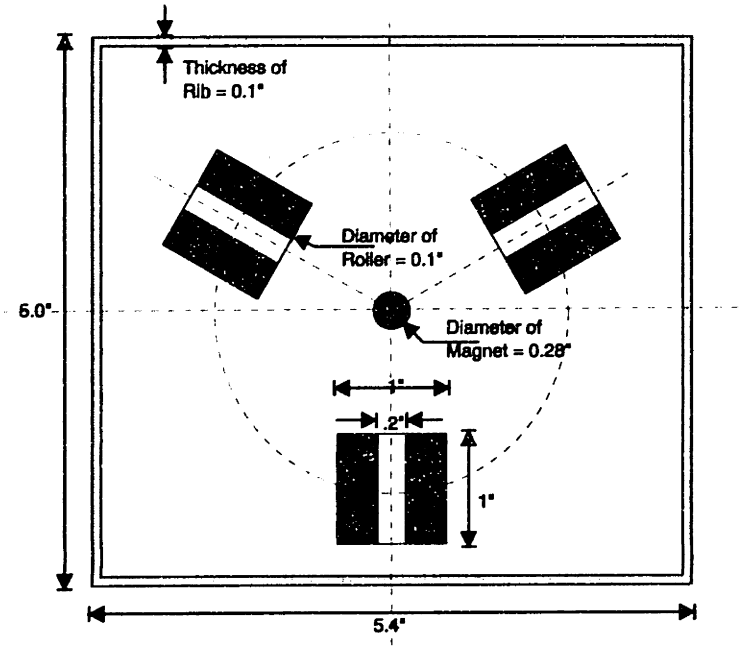

Figure 4.7 The kinematic coupling design of sample holder

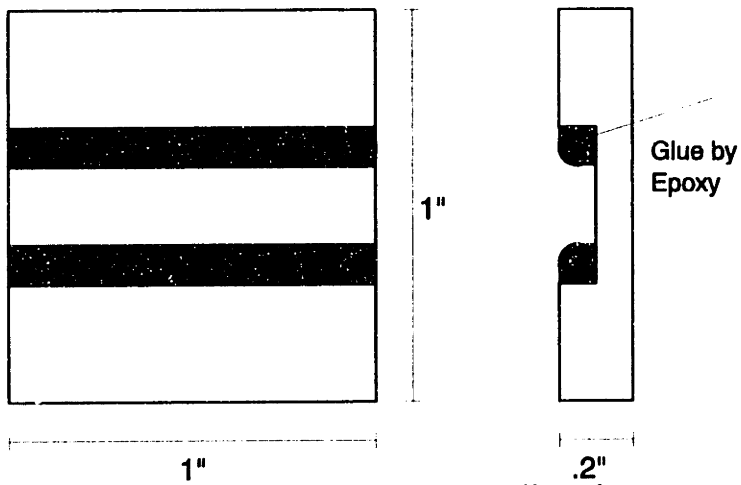

Figure 4.8 The kinematic coupling element

The size of the rollers, hemispheres, and the space between two rollers are carefully calculated to get a 120° angle between two contacting normal forces on the hemispheres to guarantee the stability.

The preload of the kinematic coupling system is provided by the attraction between two rare-earth based permanent magnets. One is glued on the stage, the other, on the sample holder. Note that the shorter the gap between these magnets, the higher the preload force, however, the two magnets cannot contact with each other since it will destroy the six-point kinematics contact condition.

4.5 Dynamics Testing of Stage

An experiment for finding the true system parameters is necessary since the theoretical calculation of stiffness and damping can only offer a rough estimation. The assembly work can vary the stiffness a lot from the theoretical value. The non-Newtonian characteristics, frequency-dependent viscosity, the manufacturing error on the parallelism between stationary base plate and the lower surface of stage, and the difficulty to get the exact gap all contribute to the uncertainty of damping ratio modeling. These effects will be discussed in chapter 10.

Natural frequency test

After finishing the stage assembly and before introducing viscous damping, the damping ratio of the stage is very low. One can find the modes of the stage by a hammer test. The result is plotted in Figure 4.9a. The power spectrum diagram shows two major peaks. One is at 125 Hz, which is close to the theoretical calculation on translation mode natural frequency. The other one, showing smaller amplitude, is located at 200 Hz. It's believed to be the rotation mode.

Once the shear damper has been introduced, due to the strong damping force, one cannot perform the hammer test again. On the other side, one can use electromagnets which exert some random pulses with width = 1 ms and an amplitude of approximate 15 N. The stage response is shown in Figure 4.9b. A HP35665A dynamic analyzer is used

to find the frequency response. The mode of linear motion is again about 125 Hz for translation mode.

Damping ratio test

Since both the structural mode has been found, one may apply Eq(4.15) for f = 125 and 200 Hz, one gets the effective viscosities of 40.2 and 33.1 poises respectively, about 1/20 and 1/24 of nominal viscosity. A simple way to find the system damping ratios is in the follows. Instead of finding the damping ratio at those frequencies, we try to find the damping ratio at very low shear rate. Under such shear rate, the viscosity is nearly to the nominal value. Once the damping ratio has been found, one can get the damping ratio under certain frequency by multiplying a factor. Since a nearly critical damping is preferred, and the effective viscosity is only 1/20 or 1/24 of nominal viscosity, one should predict that a huge damping ratio will be got by this test.

To find the damping ratio, the actuator is set to exert a constant force to drive the stage to a certain position or angle then turned off power. The stage will be pulled back by its own stiffness. Recording the position, the experiment data shows that both modes are highly overdamped. Using the known system natural frequencies and some damping ratios to fit, one can find that the damping ratio is about 20 ~ 24 in translation mode and 12~14 in rotation mode. These results are based on the nominal viscosity. For real application, the damping ratio of translation mode will be 1.1 ~ 1.2 and 0.5 ~ 0.6 in rotation mode. Figure 4.10 shows the test result. Since the natural frequency and damping ratio of both modes have been found, the plant dynamics of translation can be written down as

$$G_x(s) = G_y(s) = \frac{1}{0.94s^2 + 1771s + 6.37 \times 10^5}. \qquad (4.26)$$

For rotational mode

$$G_\theta(s) = \frac{1}{1.84 \times 10^{-3} s^2 + 2.6s + 2910}. \qquad (4.27)$$

The system transfer functions are plotted on Figure 4.11 and 4.12 respectively.

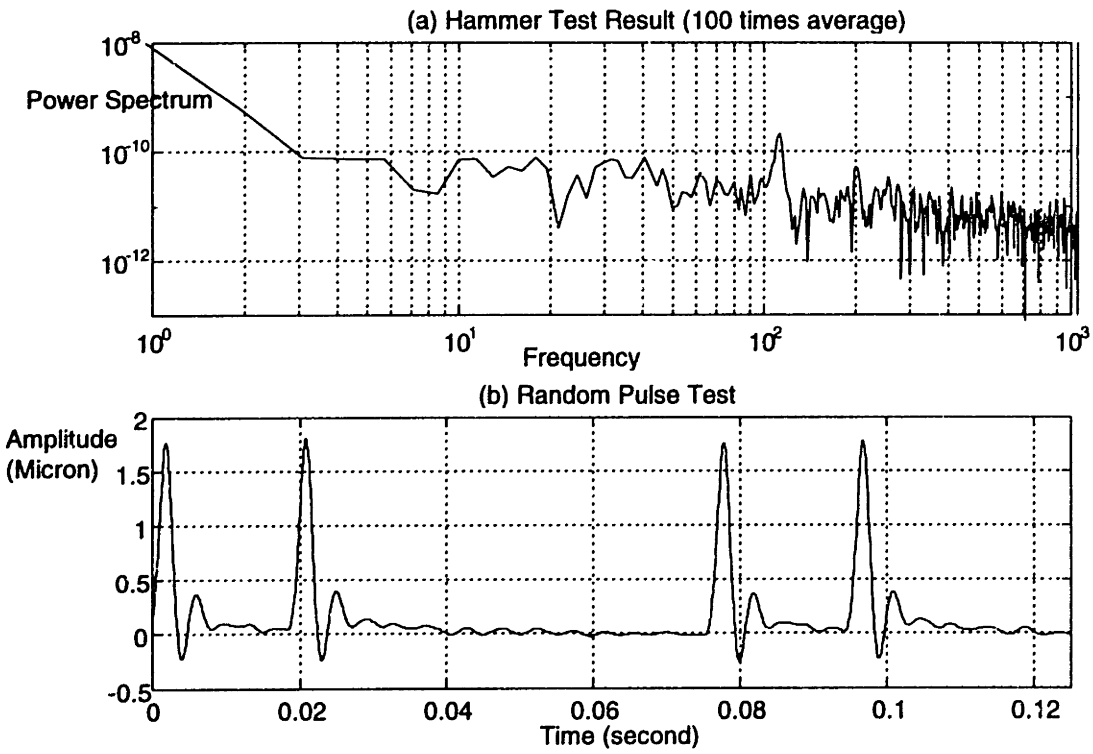

Figure 4.9 Result of frequency test

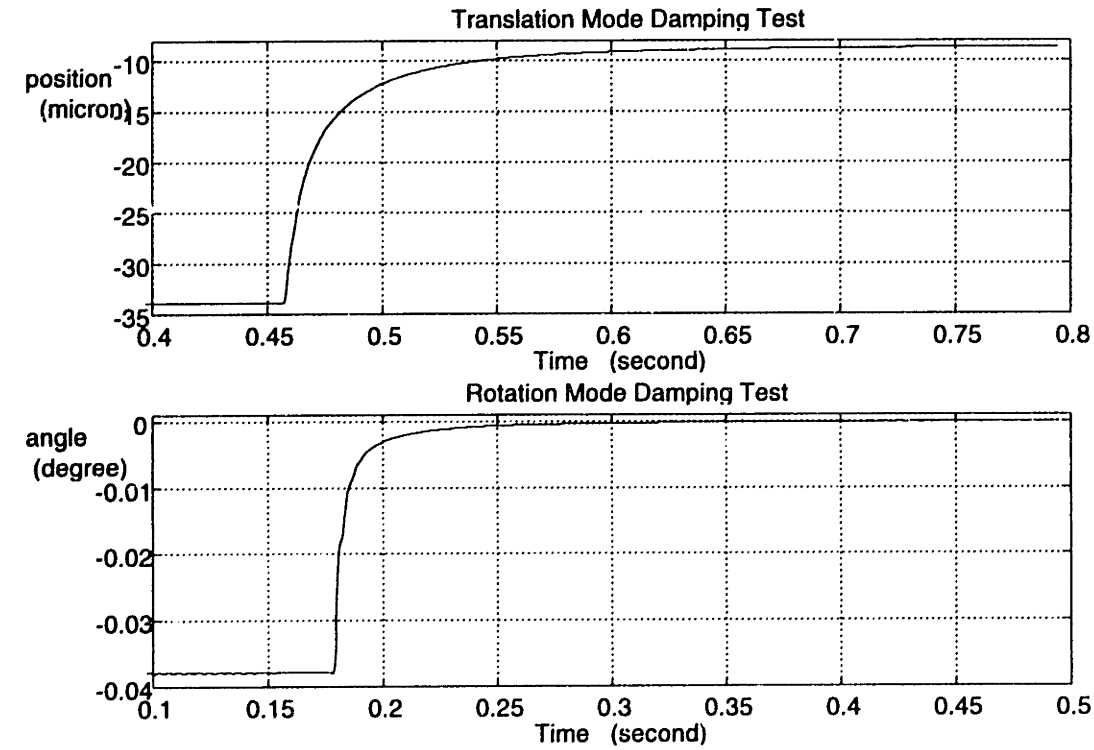

Figure 4.10 Result of damping test

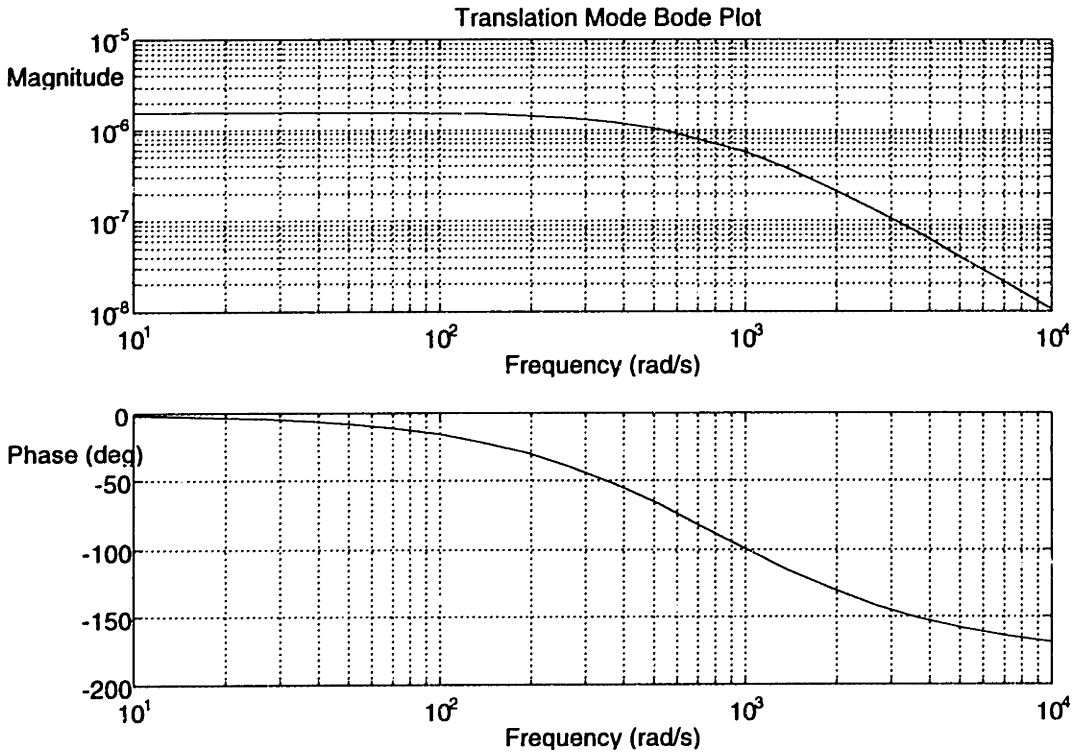

Figure 4.11 Bode plot of translation mode (Eq 4.26)

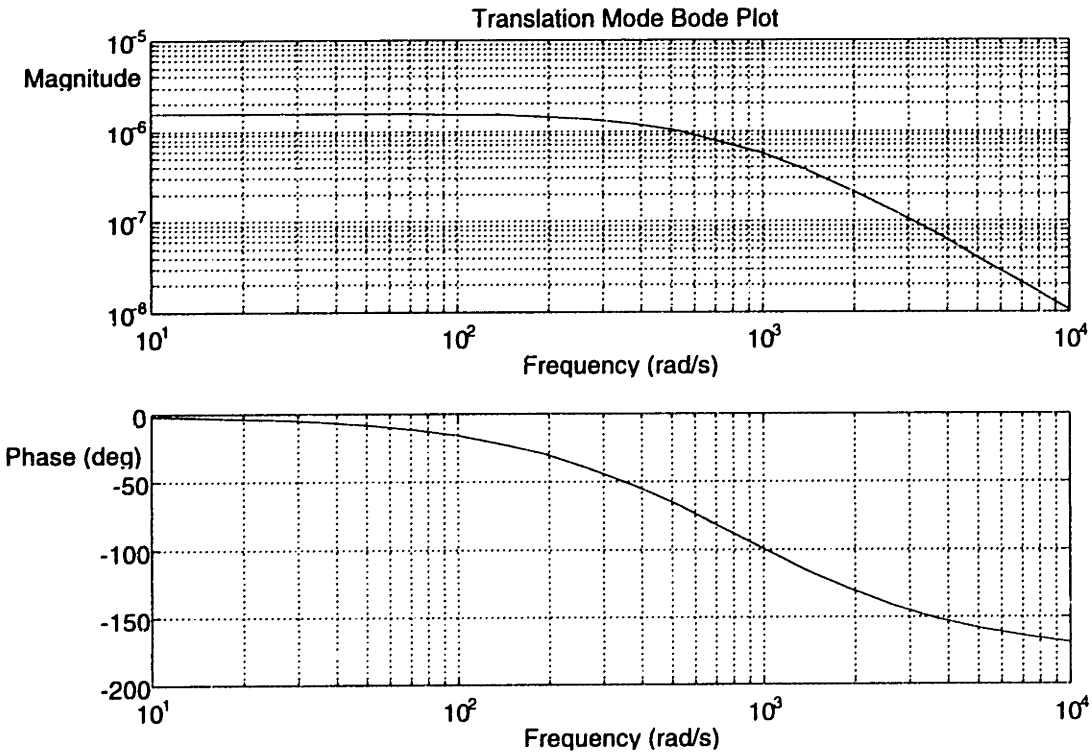

Figure 4.12 Bode plot of rotation mode (Eq 4.27)

CHAPTER 5

CALIBRATION AND NONLINEAR COMPENSATION OF ACTUATORS

This chapter deals with the issues of further identification and modeling of the actuators. Section 5.1 describes the electromagnet calibration principles and results. Section 5.2 describes the general principle of feedback linearization. We use such an approach to linearize the actuators in our system.

5.1 Electromagnets Calibration

Theoretically, as shown in section 3.2, the force exerted by electromagnets are a function of current, gap, number of coils, the permeability of air, and the area of the pole face. It means that the force constant which defined in Eq.(3.12) should be a constant and is independent with the core metal, however, due to the leakage and the characteristics of core metal, the result do not match theory. A calibration system was therefore built by Poovey and Trumper to get the exact force-current-gap relationship. and is shown in Figure 5.1, which is adapted from [PHT94]. Three capacitive probes are used for determine the air gap. Three load cells are used for measuring the electromagnetic force. Three gothic arch and hemisphere ball pairs which are made by silicon carbide form a kinematic coupling contact between the target and the main body of fixture. A geometric transformation relationship has been established between the locations of three capacitive probes and the target center.

[1]The test procedure is shown in Figure 5.2. The user first initializes the actual air gap between the electromagnet face and target using a software-assisted procedure. Then, through a digital-to-analog converter, the test software outputs a ramp control voltage which goes from zero to ten volts and back to zero. This signal is fed to a power

[1] Poovey, a graduate student of University of North Carolina at Charlotte, designed and made the whole calibration device and procedures. The author like to acknowledg his contribution here.

amplifier which outputs a current proportional to the input voltage. The power amplifier output drives the electromagnet which applies a corresponding force to the target platen. The force $f(I,G)$ is a function of input current I and target separation gap G. Load cells transduce this force into a proportional charge which is amplified and converted to a voltage by the charge amplifier. Both the electromagnet current and the load cell output voltage are logged into the 386-based computer via analog-to-digital converters for storage. After data is taken for one separation gap, the gap is adjusted to a new value and the test procedure is repeated. Following this, we may collect these data by several different gaps then calculate the force constant C.

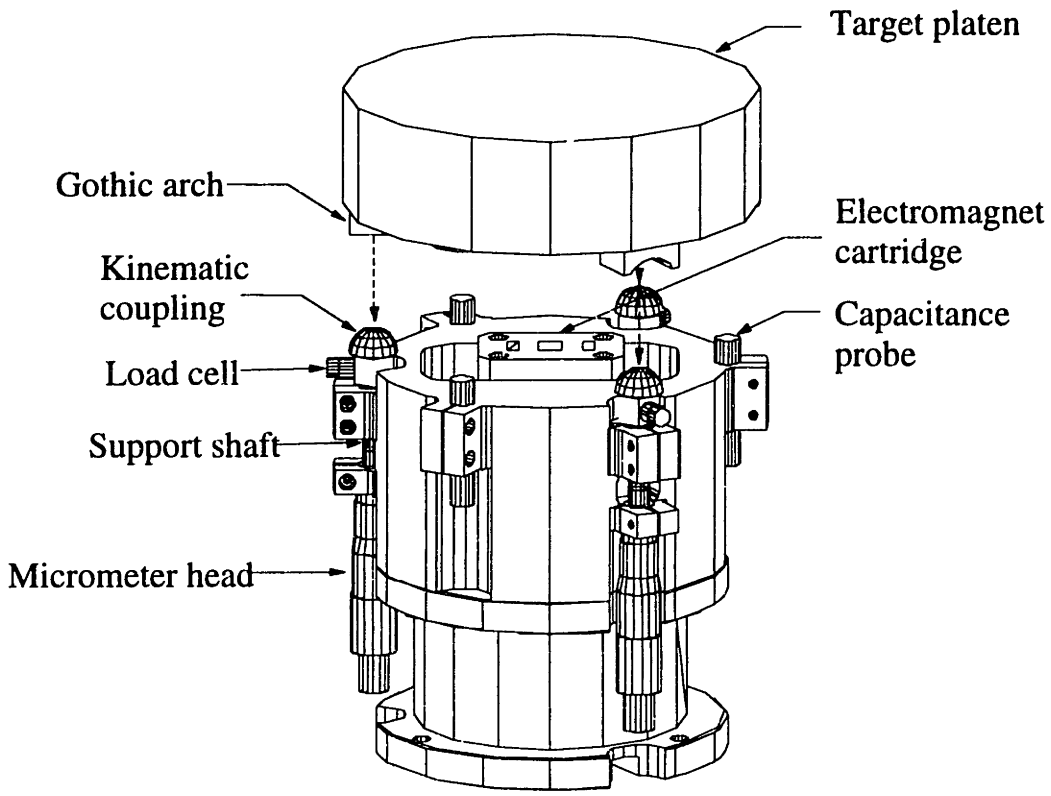

Figure 5.1 The electromagnets calibration fixture

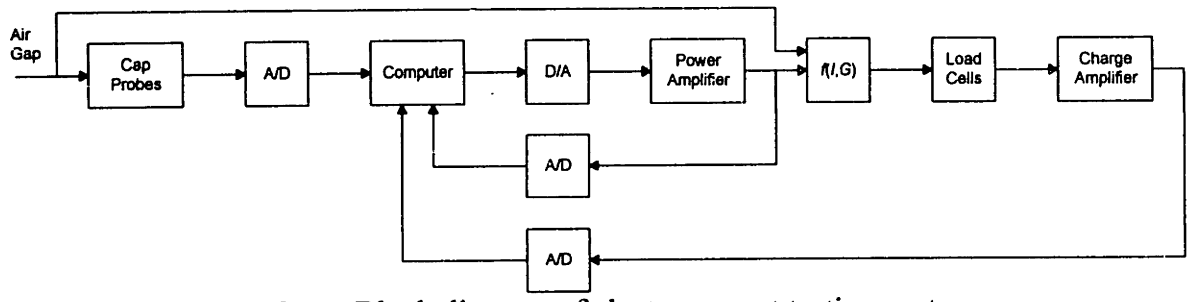

Figure 5.2 Block diagram of electromagnet testing system

The physical dimension of our electromagnetic actuator is shown in Table 3.2. The calibration results of X actuators are shown in Figure 4.3a~d. The calibration results of Y actuators are shown in Figure 4.4a~d.

There are four kinds of plot based on the same calibration data. In Figure a, the actuator force is the Y axis and the input current is the abscissa. By theoretical formula, there should be a parabolic-like relationship between force and current. In Figure b, we use $C = Fx^2/i^2$ as the Y axis and the current is the abscissa. One can observe this value varies when current change, however, for a wide region, the variation is very small and it can be treated as a constant. For figure c, we use a current - air gap relationship under constant force to interpret the experiment data. The slope of fitted i-x line is $\sqrt{F/C}$. In figure d, we plot the relationship between force constant C and attracting force F. That is, $C = F/a^2$, where a is the slope of the i-x curves in Figure c.

From Figure 5.3a and Figure 5.4a, we can find that the maximum reachable force for the X and Y actuators is around 200 N and 120 N for an 150μm air gap. From Figure 5.3b and 5.4b, one can find the a great variation in force constant when applied current is small. Which maps to the region from $i = 0$ to 0.1 amperes in Figure 5.3a, 5.3b, 5.4a, and 5.4b. It is an extremely numerical sensitive region since we define $C=Fx^2/i^2$. When both the numerator and denominator are small, a tiny experiment data fluctuation will cause a lot change in the quotient. That's the reason why C changes randomly in this region. Beyond this region, the variation of C becomes much smaller. It can be found that the i-C curve becomes nearly flat if the gap is greater than 250 μm. If the current increases again, the value of the force constant will become continuously decreasing again which is caused by the saturation effect. The smaller the gap, the earlier the saturation occurs.

Based on the result in figure 5.3b and 5.4b, the nominal separation between the actuator pole face and target surface has been set as 250 μm. This is a compromise between the power consumption and variation of force constant. The lower the gap, the lower the power consumption but the higher the variation of force constant and difficulty of control. And the higher the gap, the easier the control but the higher the power consumption.

The theoretical model Eq(3.11) has another defect since it predict an infinite attractive force when the air gap is zero, which is impossible. For a better model, one may modify Eq(3.11) to

$$f = C\frac{i^2}{(x+g_0)^2} \qquad (5.1)$$

then, a finite force results when air gap is zero. Figure 4.3c and 4.4c are used for to find the constant g_0. Using least square fitting and extrapolating, we can find g_0 in the modified model $f = C\frac{i^2}{(x+g_0)^2}$. The slope of the fitting line equals $\sqrt{\frac{f}{C}}$. We may also find the force constant in the region in which we have interest. From Figure 4.3c, the constant g_0 is around 35μm for the X-direction actuators, and its force constant C From Figure 5.4c, the corresponding data for the Y-direction actuators are 30μm for g_0. Since the actuators are designed to supply a force within 50N under normal operation, we have interest to find the correspondence force constant under this region. Figure 5.3d and Figure 5.4d show these. The X actuator's force constant C is around 1.5×10^{-5} N-m^2/amp^2 in average. The force constant of Y actuators is 1.15×10^{-5} N-m^2/amp^2 in average. Both results shows a perfect match with theoretical result (see Table 3.2). However, as shown in Figure 5.3b and 5.4b, the unsaturated force constant of X actuators is around 1.3×10^{-5} N-m^2/amp^2. For Y actuator, this value is about 0.98×10^{-5} N-m^2/amp^2. Both shows 90% of the theoretical value. This is due to the flux leakage. We will use these two value to design our controller. Table 5.1 summarizes the calibration results.

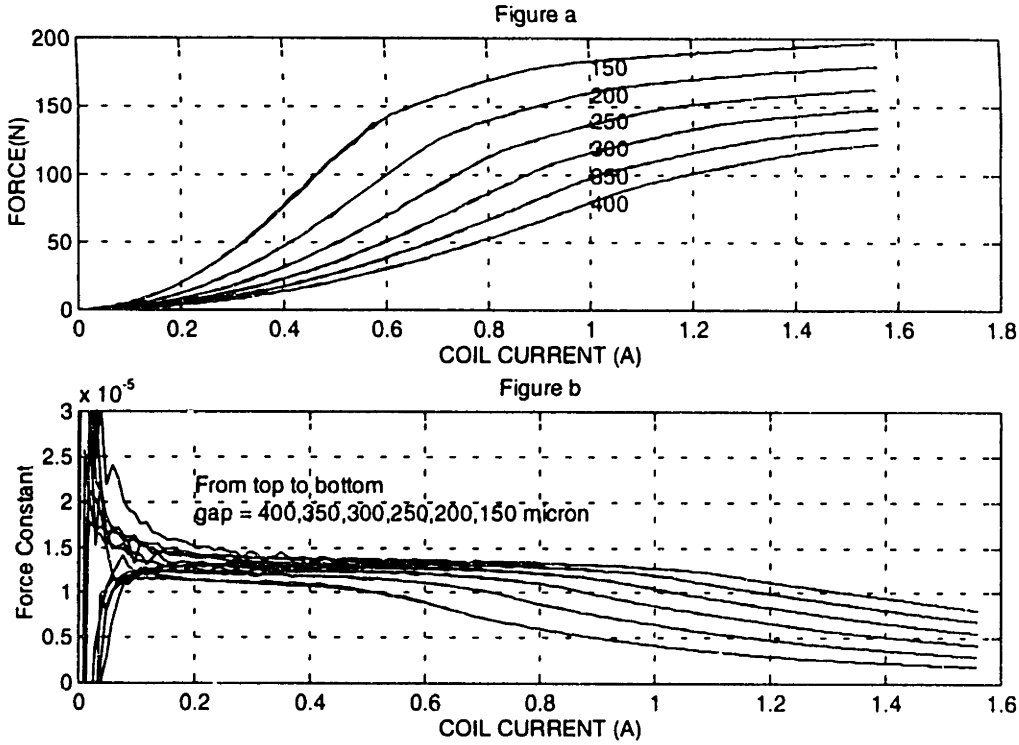

Figure 5.3a,b The force-current plot for X-direction actuators

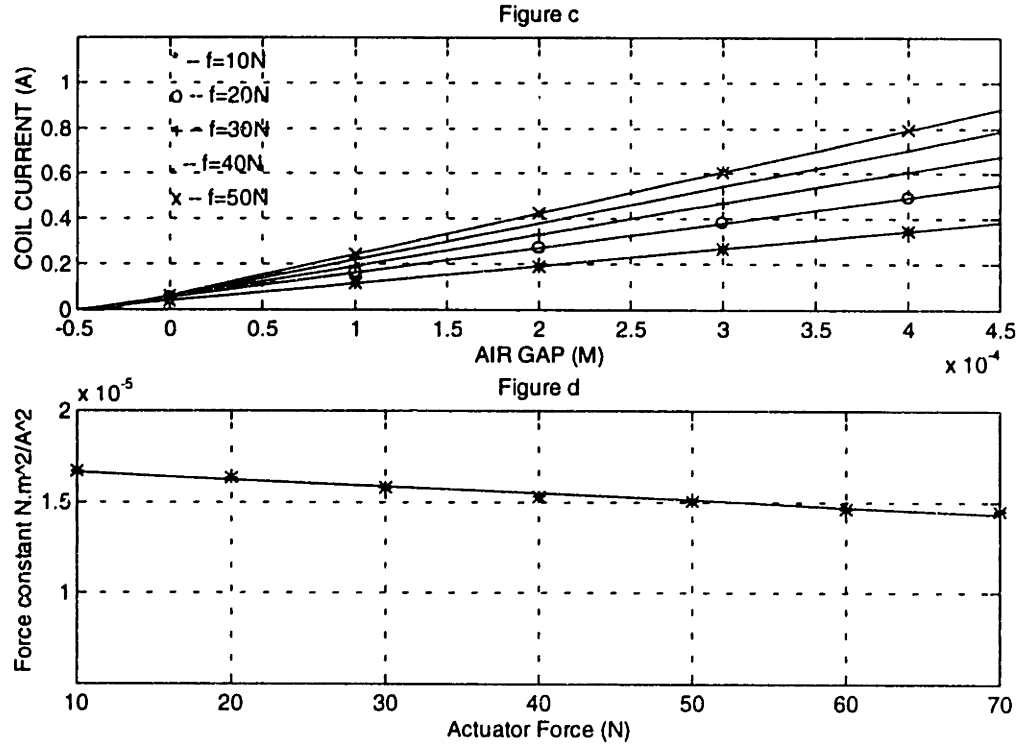

Figure 5.3c,d The C-i and current-gap plot for X-direction actuators

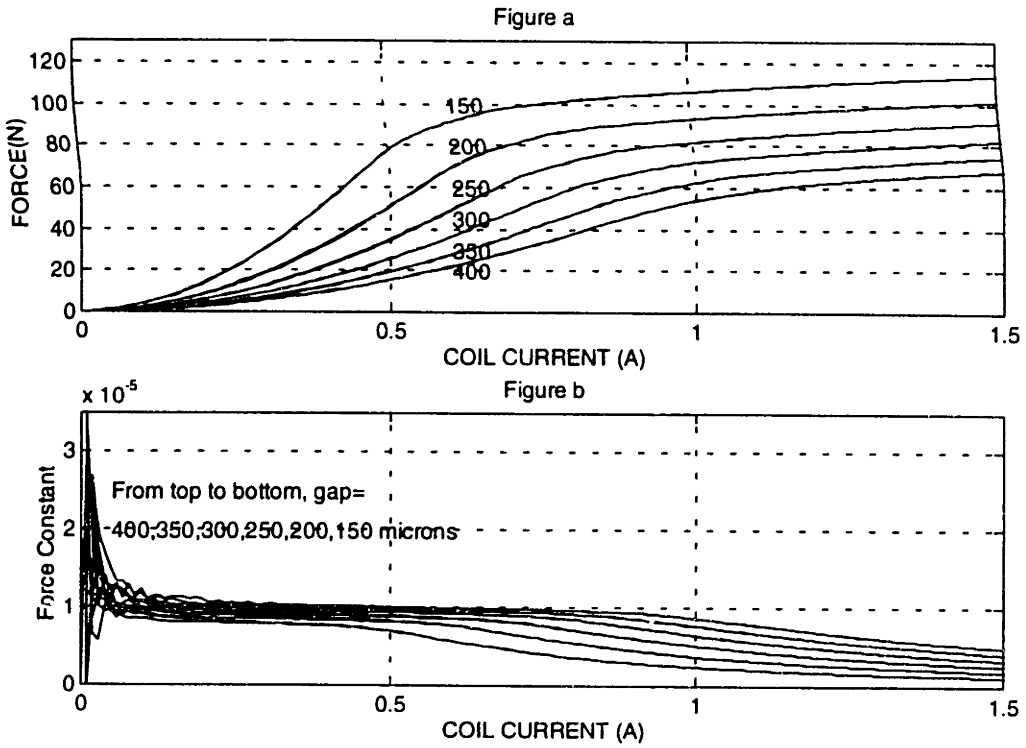

Figure 5.4a,b The force-current plot for Y-direction actuators

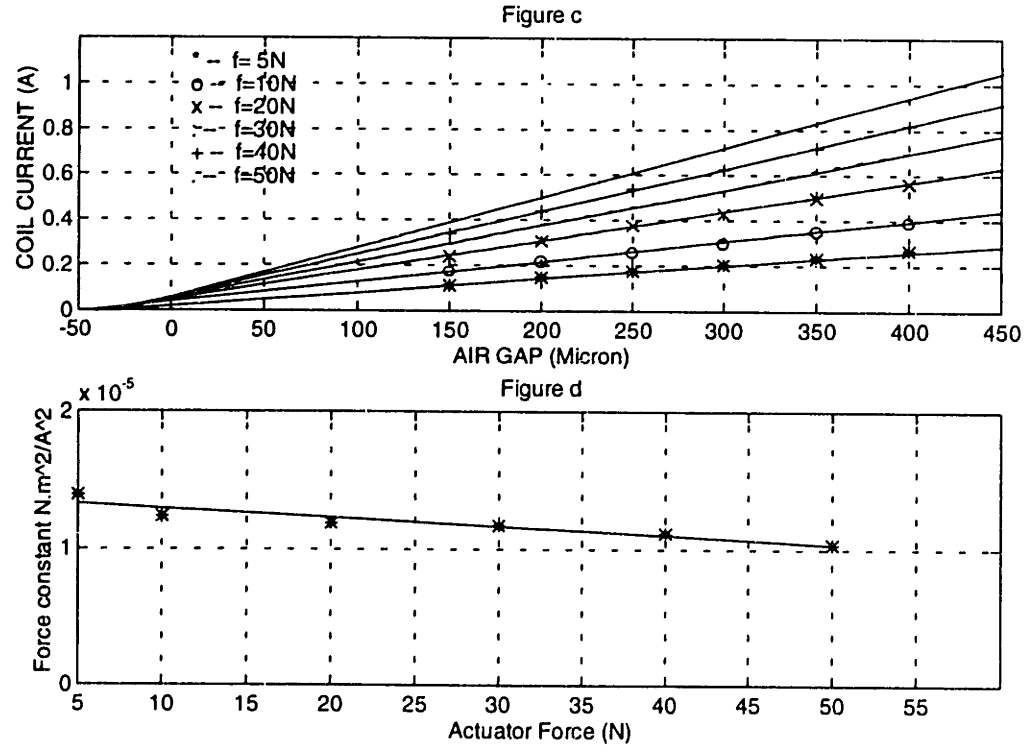

Figure 5.4c,d The C-i and current-gap plot for Y-direction actuators

Table 5.1 A brief summary of actuators calibration

	X - Actuators	Y- Actuators
Maximum Force (N)	200@150μm	120@150μm
g_0 (μm)	35	30
$C_{theoretical}$ (Nm^2/A^2)	1.53×10-5	1.17×10-5
C_{actual} From(5.3 and 5.4d)	1.5×10-5	1.15×10-5
C_{actual} From(5.3 and 5.4b)	1.3×10-5	0.98×10-5

5.2 Feedback Linearization

Feedback linearization is an approach to non-linear control design for algebraically transforming nonlinear system dynamics into linear ones so that linear control techniques can be applied. It is achieved by exact state transformations and feedback, rather than by linear approximations of dynamics. This has been applied to robotics research and in other areas including magnetic bearings, [SpV89], [SlL91], [TSN91]. In our cases, such linearization can be represented as shown in Figure 5.5.

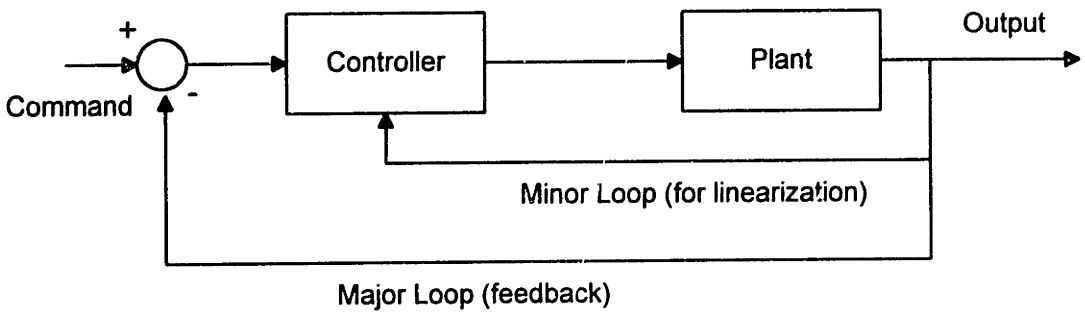

Figure 5.5 The basic structure of feedback linearization

The magnetic actuated stage control problem is nonlinear, since the force is proportional to the square of current and inverse square of the gap between the pole face and the target, i.e., $F = C\frac{i^2}{x^2}$.

In this system, the control output voltage V drives a power amplifier to generate a current i on the actuator, and thereby produce a force on the plant. The control loop can be treated as Fig. 5.6. and the problem statement is in the following:

Can we achieve a controller output in order that the output of the actuator(F) will be independent from gap x and current i by the feedback linearization method?

The issue can be solved. Assume the gain of power amplifier is K. If the desired force is $F_s = C\frac{i^2}{x^2}$, and we let the control output be

$$u = \frac{x}{K}\sqrt{\frac{F_s}{C}} \tag{5.2}$$

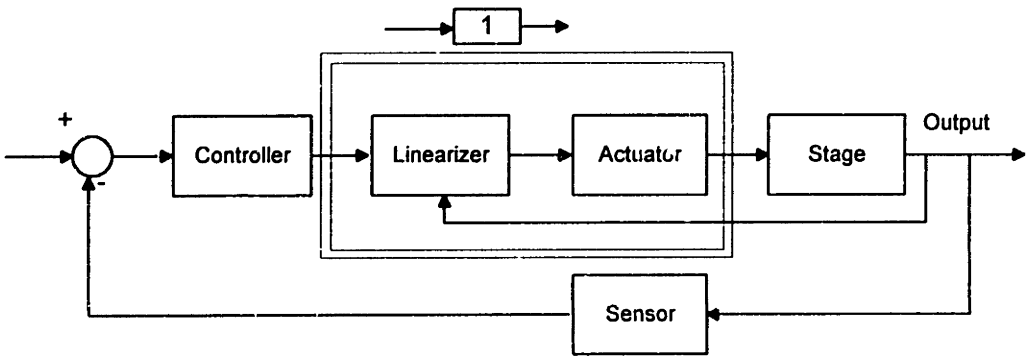

Figure 5.6 Feedback linearization of stage control system

then,

$$i = x\sqrt{\frac{F_s}{C}} \tag{5.3}$$

thus, we can get the final result $F = F_S$.

The whole block group between controller and actuator in Fig. 5.6 can be treated as a pure gain after exactly canceling the nonlinear effect of the system.

There are several reasons why we like to choose the nonlinear compensation. The first is the system stiffness consideration. For a linear controller design, one needs to apply a bias current to the electromagnetic coils. According the analysis result of Chapter 3, this bias current will decrease the system stiffness, system natural frequency, and the capability on noise rejection.

The second reason is the power consumption consideration. The bias current will increase the power consumption. This power will convert to heat eventually, cause the distortion of stage and actuators, and thereby degrade the accuracy.

The third reason is the overall performance. Olson in [Ols94] made a comparison between linear compensation and nonlinear feedback linearization algorithms. In his conclusion, the nonlinear controller was found to give more consistent performance independent of the air gap operating point. Conversely, the performance of the linear controller degraded as the operating point was varied.

Based on the above reasons, nonlinear compensation is used in this X-Y stage control. In the real world, it is impossible to get an exact elimination by this way. Since the force constant C is a function of x and i, we use a constant to approximate it just to perform this technique. The computational delay and zero order hold of D/A causes the sensed gap values to be not equal to the gap value at the right time. However, there are many factors which make contribution on the system's nonlinearity such as quantization of A/D and D/A, non-idealism of damping fluid, and the mis-alignment during fabrication. Of course, the major source of nonlinearity comes from the characteristic of the electromagnetic force. After performing the feedback linearization, although we cannot eliminate the nonlinearity of electromagnetic force exactly, the residual nonlinearity is small enough compared to the effect of other nonlinearity sources. The influence of other error sources will be discussed in Chapter 10.

CHAPTER 6

NOISE MODELING

An important issue in precision motion control is the disturbance influence on system output. There are several disturbance sources actually on the stage. These are base vibration, sensor noise, and the quantization of the A/D and D/A converters. Beside those, careful shielding and grounding on all signal cables is required for reducing electrical noise pickup. There are fundamental trade-offs between the conflicting objectives of reducing sensitivity to disturbances and parameter uncertainty on the one hand, and the filtering out of any internal generated noise on the other. To design a low-noise control system, an analysis of the disturbances and their mathematical model is required.

Section 6.1 deals with measurement of base vibration noise. Section 6.2 discusses some noise sources in the feedback loop. Finally, in section 6.3, the effect of quantization is added into the whole system. The simulation result shows that at present quantization dominates the system noise.

6.1 Base Vibration

6.1.1 Effect of plant stiffness to vibration noise

Base vibrations are contributed by the shaking of the building due to outside traffic and to the vibration of air handling equipnment in a room adjacent to our laboratory. These sources contribute a force disturbance to the system. Consider a second order

system with the transfer function (2.1). The open loop block diagram on Figure 6.1. The transfer function for plant P to control input U and disturbance input D are

$$G_u(s) = \frac{P(s)}{U(s)} = \frac{1}{ms^2 + bs + k}. \qquad (6.1)$$

and

$$G_d(s) = \frac{P(s)}{D(s)} = \frac{m}{ms^2 + bs + k} \quad . \qquad (6.2)$$

respectively.

The DC gain for $G_u(s)$ and $G_d(s)$ are *1/k* and *m/k* respectively. One can find that the increasing of stiffness will decreases the sensitivity of the plant output to the control input and disturbance in the same time. In close loop case, which shown on Figure 6.2, the transfer function of output Y(s) to the command input U(s) and disturbance input D(s) will be (2.4) and (2.5) respectively.

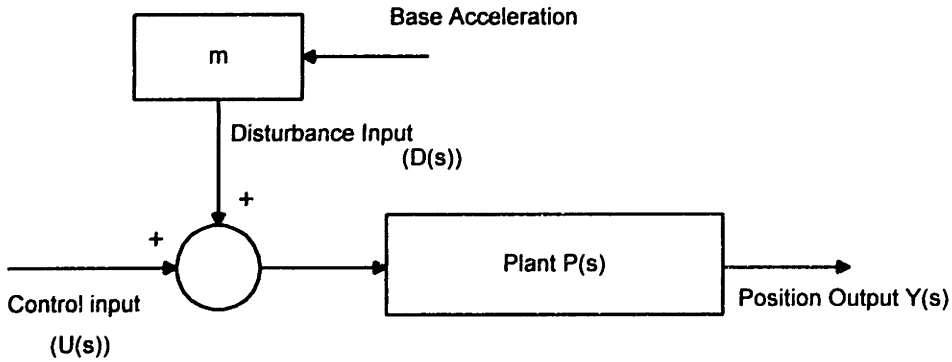

Figure 6.1 An open loop position control system

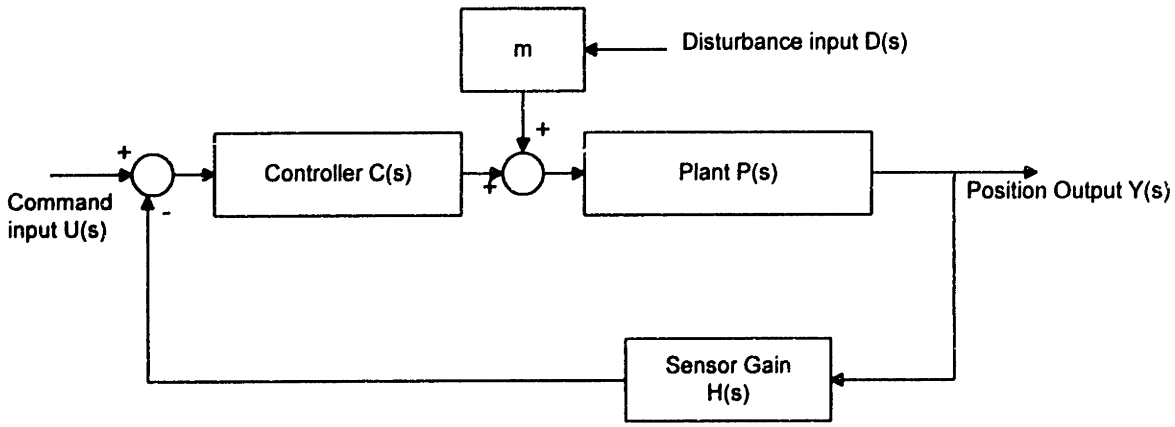

Figure 6.2 A closed loop position control system

One may choose a big G(s)H(s) to reduce the response due to disturbance D(s). Actually, a closed loop PI control will eliminate steady state error and attenuate the response by the low frequency disturbance force, the effect of PI control law on disturbance attenuation is discussed in section 2.2 and 8.3.

6.1.2 Base Vibration Modeling

There are some important definition on random variable should be mentioned in the first. Assume a plant G with input signal u and output signal x. Here, we define the mean square value of signal x:

$$\bar{x}^2 = \lim_{T\to\infty} \frac{1}{2T} \int_{-T}^{T} x^2(t)dt. \tag{6.3a}$$

That is the average power o signal x.

The RMS value of signal x:

$$RMS = (\bar{x}^2)^{1/2} = (\lim_{T\to\infty} \frac{1}{2T} \int_{-T}^{T} x^2(t)dt)^{1/2}. \tag{6.3b}$$

The auto correlation function of signal x:

$$R_x(\tau) = \lim_{T\to\infty} \frac{1}{2T} \int_{-T}^{T} x(t)x(t+\tau)dt. \tag{6.3c}$$

The cross-correlation function of signals x and u:

$$R_{xu}(\tau) = \lim_{T\to\infty} \frac{1}{2T} \int_{-T}^{T} x(t)u(t+\tau)dt. \tag{6.3d}$$

Let $S_X(\tau)$ denote the Fourier transform of R_X. Thus

$$S_x(\omega) = \int_{-\infty}^{\infty} R_x(\tau)e^{-j\omega\tau}d\tau;$$

$$R_x(\tau) = \frac{1}{2\pi} \int_{-\infty}^{\infty} S_x(\omega)e^{j\omega\tau}d\omega; \tag{6.3e}$$

$$\bar{x}^2(t) = R_x(0) = \frac{1}{2\pi} \int_{-\infty}^{\infty} S_x(\omega)d\omega.$$

The function $S_X(\omega)$ is called the power spectral density of the signal x.

The followings are several relations between correlation functions and spectral densities of the input and output signals. For its proof, see [BeP71].

1. Relation between the cross-correlation function of u and x and auto correlation function of input signal u

$$R_{ux}(\tau) = \int_{-\infty}^{\infty} g(\alpha) R_u(t + \tau - \alpha) d\alpha . \qquad (6.4)$$

2. Relation between the auto correlation functions of the input and output signal

$$R_x(\tau) = \int_{-\infty}^{\infty} d\alpha \int_{-\infty}^{\infty} g(\alpha) g(\lambda) R_u(\tau + \alpha - \lambda) d\lambda . \qquad (6.5)$$

3. Relation between the spectral densities of the input and output signals

$$S_x(\omega) = |G(j\omega)|^2 S_u(\omega) . \qquad (6.6)$$

Eq(6.4)~(6.6) have an important physical meaning. That is, one may obtain the system transfer function sudjected to the disturbance input by calculating the power spectrum density of the system input and output. It is a system identification process. In this chapter, however, we will not try to find the system transfer function subjected to noise input, but use experimental data and idealized block diagram to find the noise influence on stage output. For future work, this system identification process will be involved.

The procedure of noise analysis is the followings:

1. Disturbance data collection
2. Frequency Analysis on disturbance data
3. From 2, try to model the vibration disturbance
4. Use the noise data which are collected on 1 as the input to the system block diagram to see the noise influence on plant output.
5. Use different control gain on 4 to see the disturbance rejection effect.

The stage will run on an optical table for the high frequency vibration reduction and using PI control for the low frequency disturbance attenuation. For collecting the

vibration data of optical table, we use a PCB 393C seismic type accelerometer and HP 35665A Dynamic analyzer. After collecting, we change the format to ASCII code and use MATLAB to do the time and frequency domain analysis. Figure 6.3 shows the whole process from data acquisition to analysis.

6.1.3 Base vibration noise data of workbench

Figure 6.5 is a typical table vibration noise data plot. The peak to peak of base vibration is roughly $0.008 m/s^2$ and the standard deviation is $1.64 \times 10^{-3} m/s^2$. From the power spectrum density plot we can find there are some vibration modes, they are 11 Hz, 56 Hz, and 120 Hz. The 120 Hz one should be the AC noise. The 56 Hz one is due to the air conditioner of our building. After putting the data set into SIMULINK, we make analysis on simulation result of system response. The standard deviation of the output is 1.4 nanometers, and the peak to peak is about 8 nanometers. Note that the stiffer the stage, the lower the noise response. The power spectrum of output shows the high frequency will be attenuated since the stage is basically a second order system, but the low frequency influence still plays an important role. The contribution of low frequency noise does not attenuate at all. As mentioned before, that's the reason why introduce PI controller in since it can reduce the low frequency disturbance.

To simulate the effect of different control gains, the data which gotten from accelerometer are input into SIMULINK as the command input. For simulating the continuous case, using the block diagram of Figure 6.2. A typical response is shown in Figure 6.6. Note that from the power spectrum density plot, the intensity of low frequency part has been reduced by an order of 10 or larger. After trying several PI combinations, the result is shown in Figure 6.7. For digital case, using the block diagram of Figure 6.4 and a typical response is plotted in Figure 6.8. The overall relationship between control gains and noise attenuation is shown in Figure 6.9. From these simulations, we can find that the higher the controller gain, the higher in noise response reduction. However, if the PI gain is too large, it will cause the instability of the closed loop system, therefore, the noise influence effect will spring back.

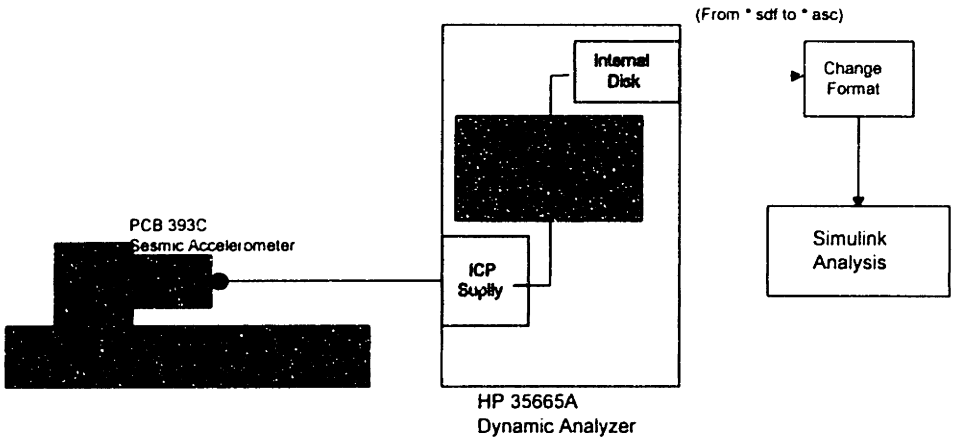

Figure 6.3 Overall process to get vibration data for SIMULINK analysis

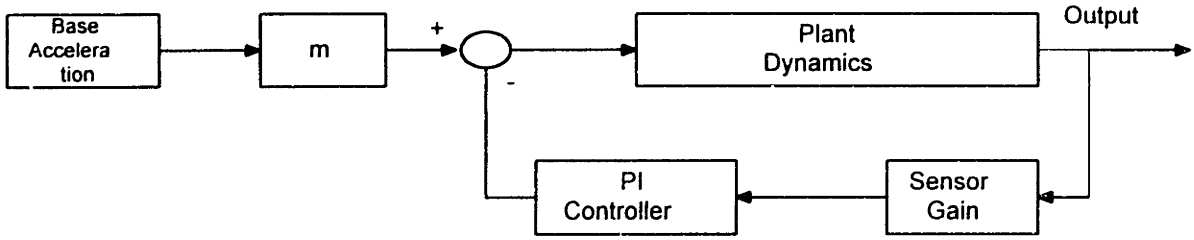

Figure 6.4 SIMULINK analysis for the system response to base vibration

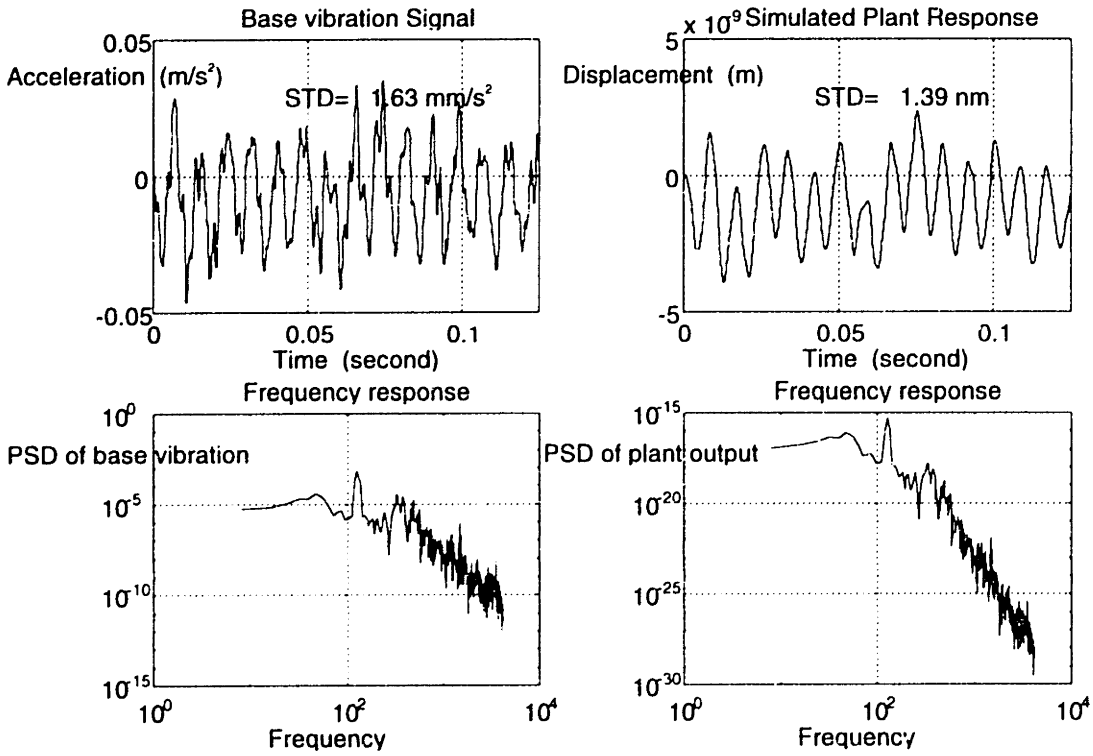

Figure 6.5 Typical base vibration noise and its influence on stage

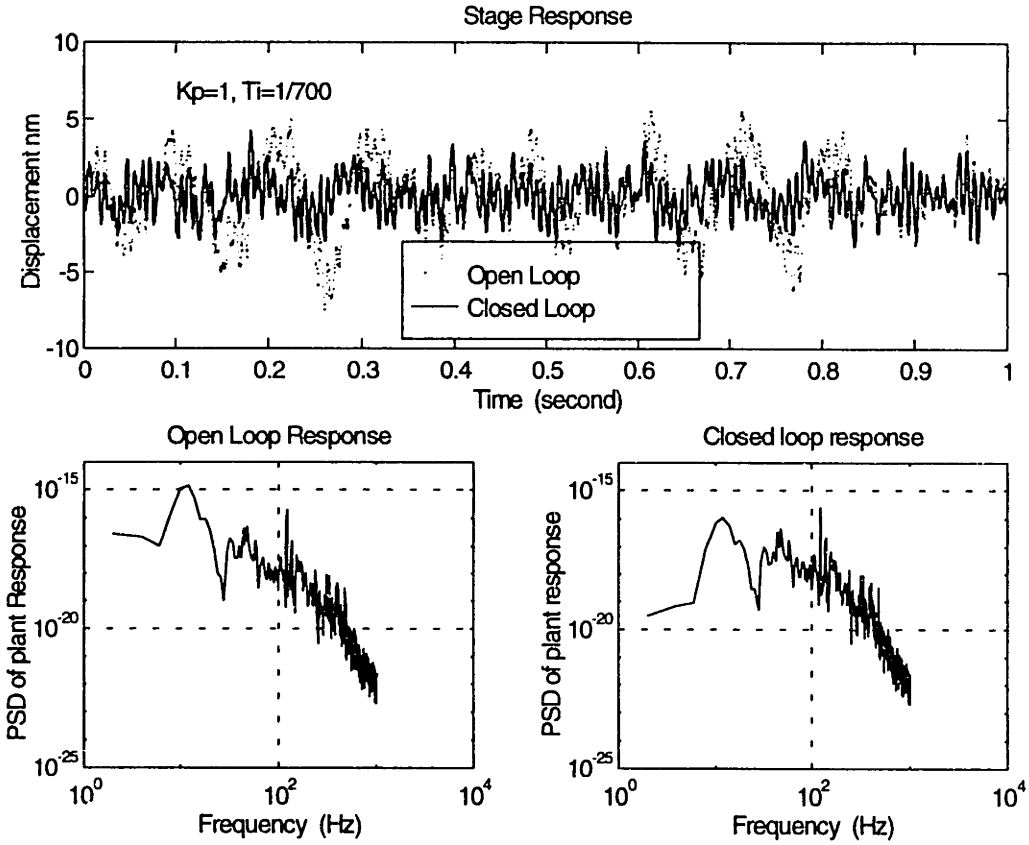

Figure 6.6 The stage response to a noise input under continuous PI control

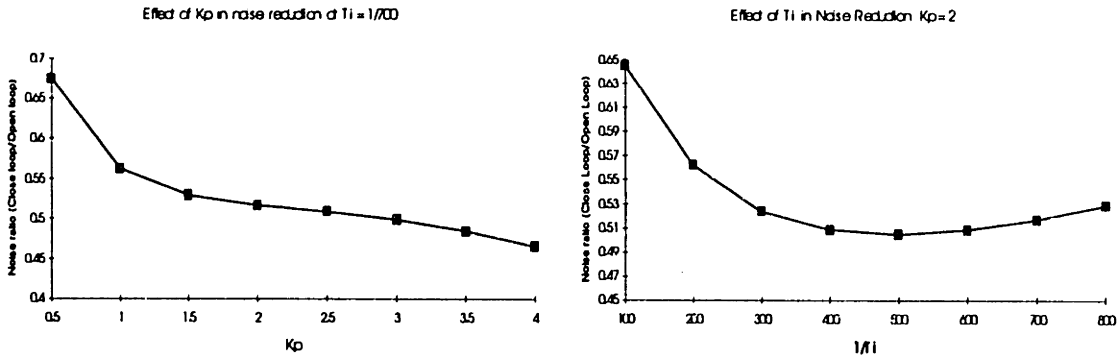

Figure 6.7 a, b : Continuous Case- The effect of K_p and Ti in noise reduction

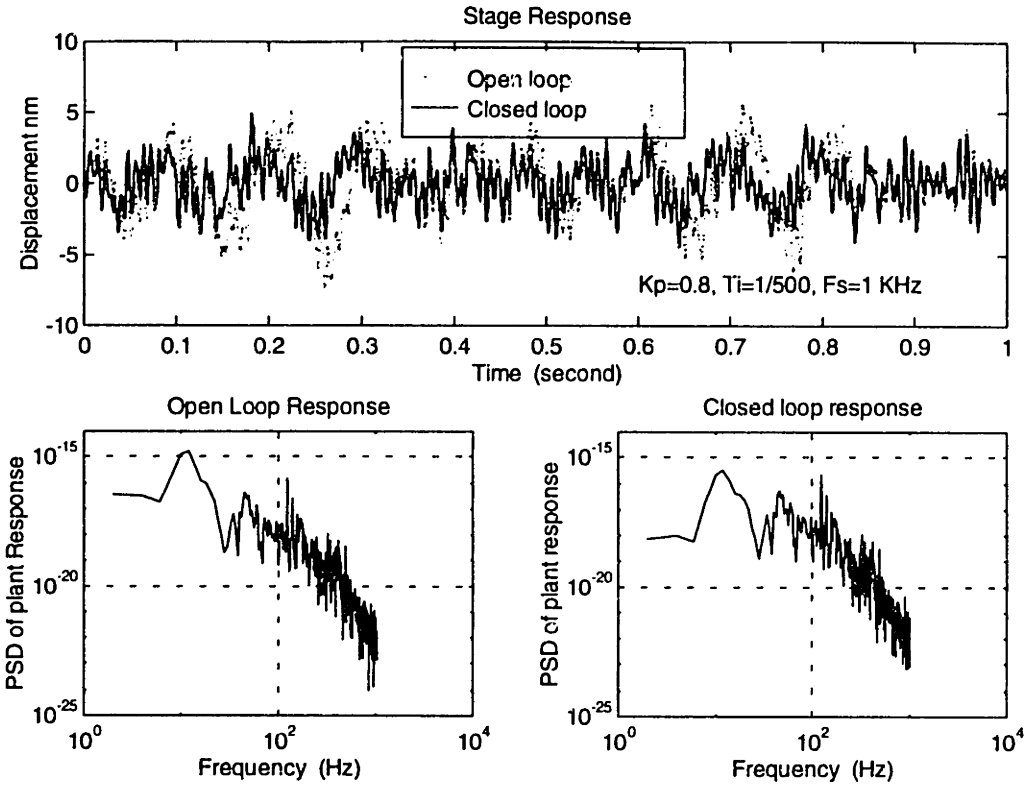

Figure 6.8 The stage response to a base vibration input under discrete time PI control (Assume no quantization)

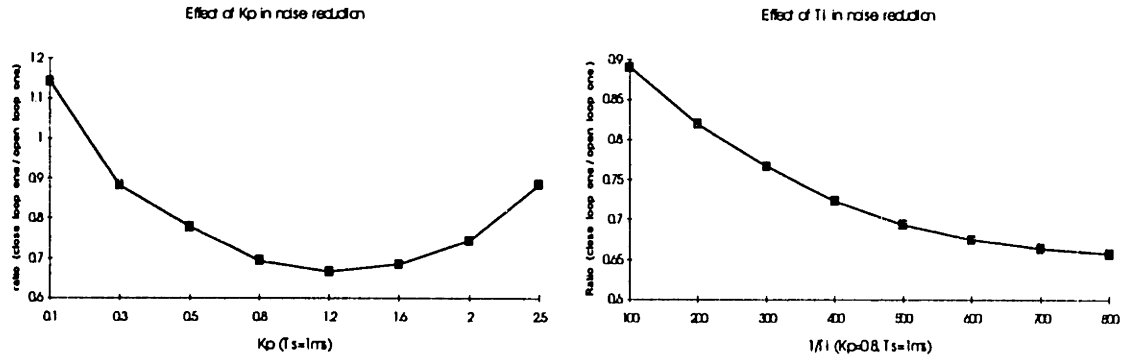

Figure 6.9 a,b: Discrete Case - The effect of K_p and T_i in noise reduction

6.2 Noise of feedback path

The feedback loop contains position sensors and some signal cables. These cables should be shielded and grounded carefully to reduce the influence of electric and magnetic field as much as possible. Low pass anti-aliasing filters are necessary to filter undesirable high frequency signals before computer accesses the feedback information. For more information, see [Ott76] and [Mor86]. Figure 6.10 shows the schematic diagram of feedback path.

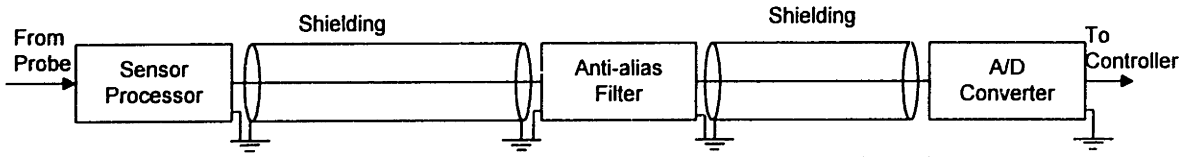

Figure 6.10 Signal transmission in feedback path

There are several possible noise sources existing in the feedback path. The power supply and the light source contain some 60 Hz and its harmonic signals called the AC noise. When we do the power spectrum analysis of sensors and accelerometers, there are some obviously peaks at 60, 120, 180, 240 Hz, etc. In our experiment, with proper shielding, the standard deviation can be reduced from 0.027 mV (without shielding) to 0.002 mV(with shielding).

The sensors themselves are another noise source. Figure 6.11 shows experimental data of the sensor noise. These data are collected by an HP35665 Dynamics Analyzer with a sampling rate 2K. Since the test environment is not well-isolated from external electrical noise, one can find some odd harmonics of AC signal, i.e., 60, 180, 300 420Hz. These likely come from the external AC power source and not the sensor itself, however, these signals do indeed influence the sensor response. Its peak-to-peak value is roughly equal to 0.12 mV, or 0.6 nanometers by position. The power spectrum shows that the disturbance frequency is evenly distributed noise as if white noise in our interested range. The driving frequency of these sensors is 1.2 MHz. The block diagram of sensor noise influence is shown on Figure 6.12, the effect of sensor noise N in Figure 6.12 on the output is shown by (2.6)

Although the magnitude of sensor noise is very small, however, we should note that it appears on the system output via the same transfer function as the command input. This means that the controller cannot recognize which part is the position setpoint signal, and which part is the sensor noise. i.e., the sensor noise is involved into the major loop and no control strategy can reduce its effect on position error. See [FPE86]. The only way to attenuate its influence is by selecting a sensor whose noise frequency range is much higher than the system roots, thus, attenuated by the plant and system dynamics. The influence of feedback path noise can be simulated by SIMULINK too. A file in our simulation contains the sensor noise as measured experimentally

To avoid aliasing of the signal due to sampling, anti-aliasing low pass filters are necessary in digital control. The circuits of anti-aliasing filters are simple in this case. Three RC circuits are built in a shielding box with 1/RC = 680 rad/s. The bandwidth thus is 110 Hz. Figure 6.13 shows the circuit of anti-aliasing filter. A 15KΩ resistor and a 0.1μF capacitor form a simple low pass filter. For avoiding the disturbance of environment, these filter are located in a shielded environment.

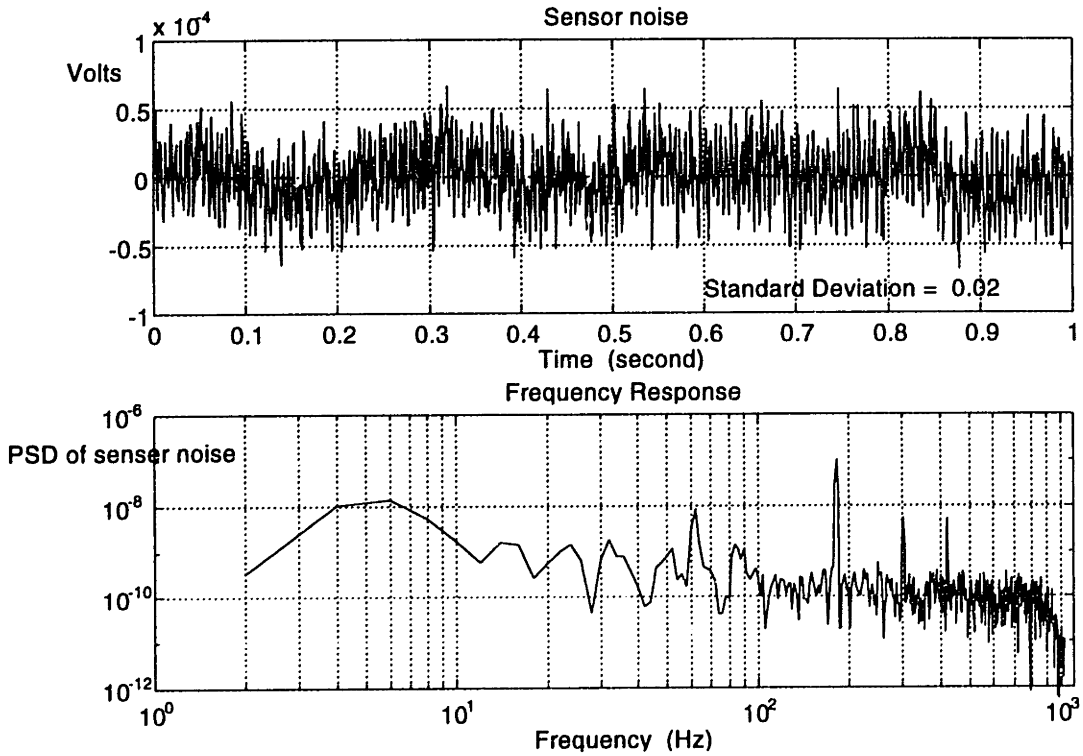

Figure 6.11 Typical sensor noise data

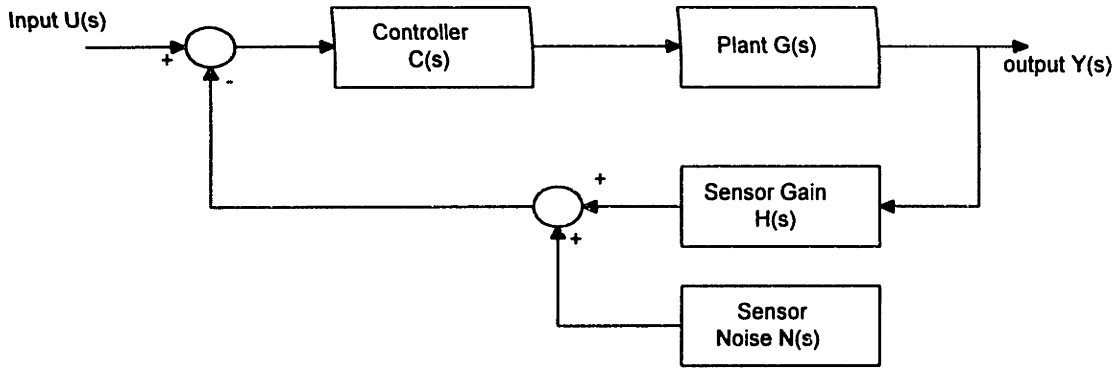

Figure 6.12 The block diagram for simulating sensor noise effect

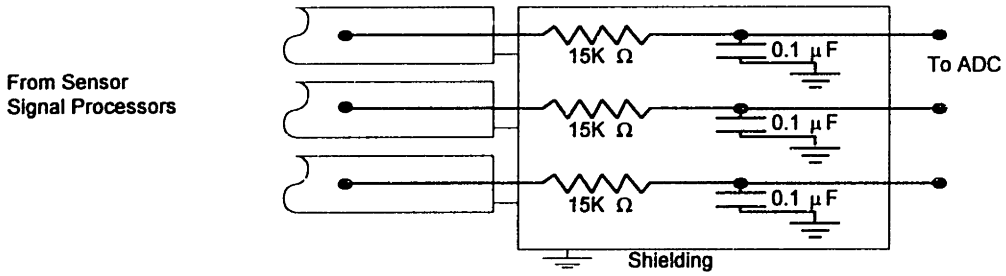

Figure 6.13 Anti-aliasing filters

6.3 Quantization of Digital Interfaces

Another source of undesirable signal is the quantization of the digital devices, including the round off and truncation off of computer calculation, A/D and D/A quantization and saturation. Such quantization makes things worse and much more complicated to analyze since it adds nonlinearity to the system [OpS89]. Figure 6.14 shows the effect of quantization. Here X is the input signal, X_q is the signal after quantization.

Among these, compared to the quantization of A/D and D/A, the computational aspect can be neglected if overflow does not occur. In this experiment, the A/D converter is a National Instrument® AT-MIO 16L DAQ board. It's a 12-bit ADC, therefore, the

resolution is $1/2^{12} = 1/4096$. Using the bipolar 10V to -10V configuration, the quantization level is 4.9 mV. The D/A converter in this experiment is a DATEL 422 DAQ board. It is a bipolar -10V to 10V configuration too. It has 12 bits and thus has same resolution with ADC.

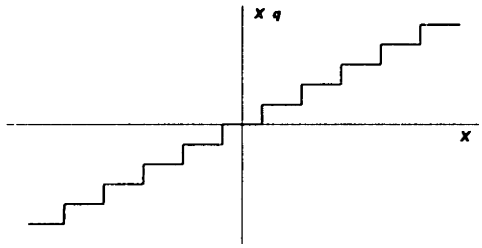

Figure 6.14 Round-off quantization error

The environmental disturbance on forward loop, the sensor and electronic noise on feedback loop, and the quantization of digital equipment are the three major contributions to disturb the system. The most important one among these three are varied under different environments, controllers, and equipment. In this case, from Figure 6.5 and 6.6, the maximum position error due to the base vibration is less than 14 nanometers peak-to-peak. The sensor's contribution is even less. However, the minimum quantization level of the A/D is 4.9mV or 24.8 nanometers per least count. This is thus the dominate effect. The quantization error combines with the contribution of the base vibration and sensor noise to yield a system noise level of about 50 nanometers.

Figure 6.15 is the block diagram for SIMULINK® simulation of combining the three noise effects. When the quantizer is 12 bit, whatever one chooses any P gain and I gain, no any noise attenuation is found since the quantization effect dominates the system response completely. However, as the number of bits increase, for example, to 16 bits, the quantization level will decrease to $1/2^{16}$ or 1.75 nanometer in this case. In this case, since the quantization level is smaller than the influence of the base vibration disturbance, the effect of our PI control law in noise attenuation start to reveal. Figure 6.16 is the simulation result if one replace the 12 bit quantizer by 16 bit one. It shows the effect of noise reduction under various Kp and Ti by comparing the standard deviation of the position output with and without control.

The above analysis shows that due to the spring dominated design approach, the vibration disturbance has been lower to a small level. Its influence is even can not appear under current digital devices. The position accuracy is dominated by the digital devices. Thus, it is possible to increase the position resolution by changing the digital devices without making modification on system design.

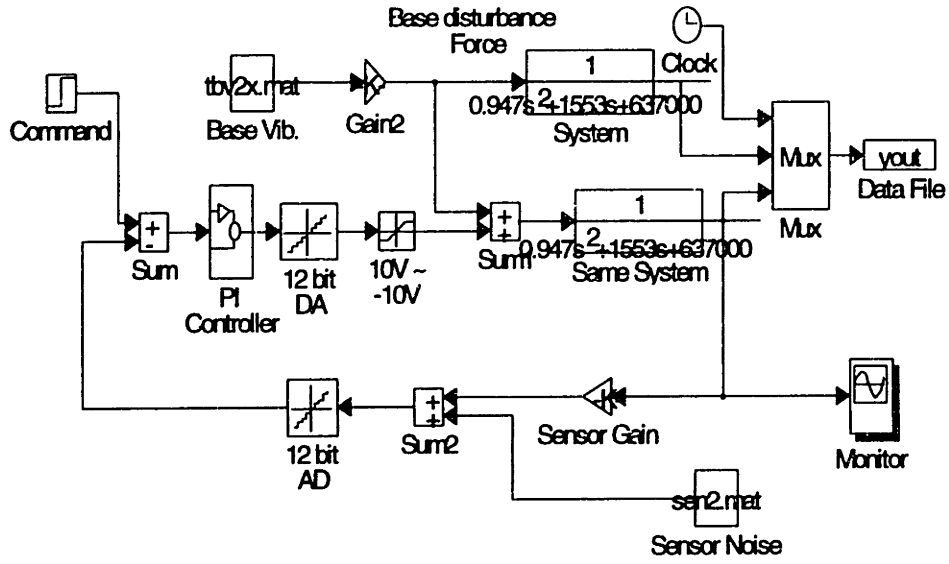

Figure 6.15 The SIMULINK block for analyzing the quantization, base vibration, and sensor noise

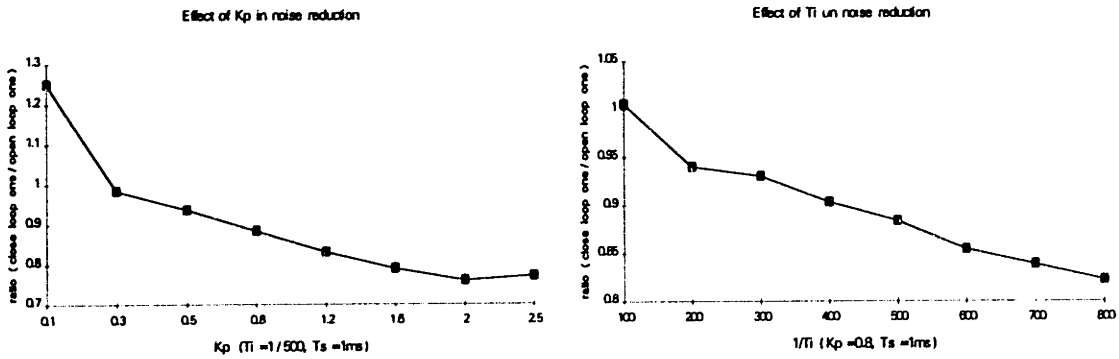

Figure 6.16 Effect of Kp and Ti in noise reduction with 16bit Quantizer

CHAPTER 7

ELECTRONICS SYSTEM DESIGN

In addition to the mechanical system and control system design, the electronics design is also an important issue. There are two main parts included in this chapter. One is the design of power amplifiers and the other is selection and calibration of feedback sensors. Section 7.1 discusses the power amplifier. Section 7.2 presents the basic working principles of the feedback sensor. The sensor calibration results are shown in section 7.3.

7.1 Power Amplifiers

The host computer outputs a control effort via D/A converter in the form of voltage, which drives power amplifiers to convert the control setpoint from voltage to current since the attraction force is a function of current, not voltage.

The transfer function of voltage controlled current amplifier is

$$I = K(\omega)V. \qquad (7.1)$$

Here K is the gain of this amplifier. For an ideal case, this gain should be unchanged through the whole span of frequency domain. In real world, one can never get such an amplifier. Real amplifiers act like a low pass filter with a certain bandwidth. When frequency of signal is beyond this bandwidth, the output will be attenuate.

Another important issue should be considered is that the amplifiers should contain a flyback circuit. Since the actuators are basically inductors, any abrupt change in magnetic flux will induce a back emf and cause the instability of amplifier or damage it. Flyback circuits are designed for eliminating such effect.

In this experiment, the amplifiers are adapted from those in [Tru90] with some small modifications. Each original amplifier contains a lead circuit for getting extra phase

margin. In this work, this network is taken out since the phase margin is good enough. In addition, lead compensation will amplify noises since it's basically a differential compensator.

The voltage dividers are also changed to get a higher gain. The original resistor is 10K Ω, and the gain K is 715/(715+10K) = 0.066. After changing from 10KΩ to 6.8KΩ, the gain will be increased to 0.095, which is suitable for this work.

Figure 6.1a and 6.1b are the circuit diagrams of the two kinds of power amplifiers I used in this work. There are four floated load type and two grounded load type. Figure 6.2 shows the frequency response of a floated load type amplifier. The bandwidth of these systems is near 5 KHz. For this experiment, this bandwidth is good enough and the amplifier can be treated as just a constant gain K without any other dynamics.

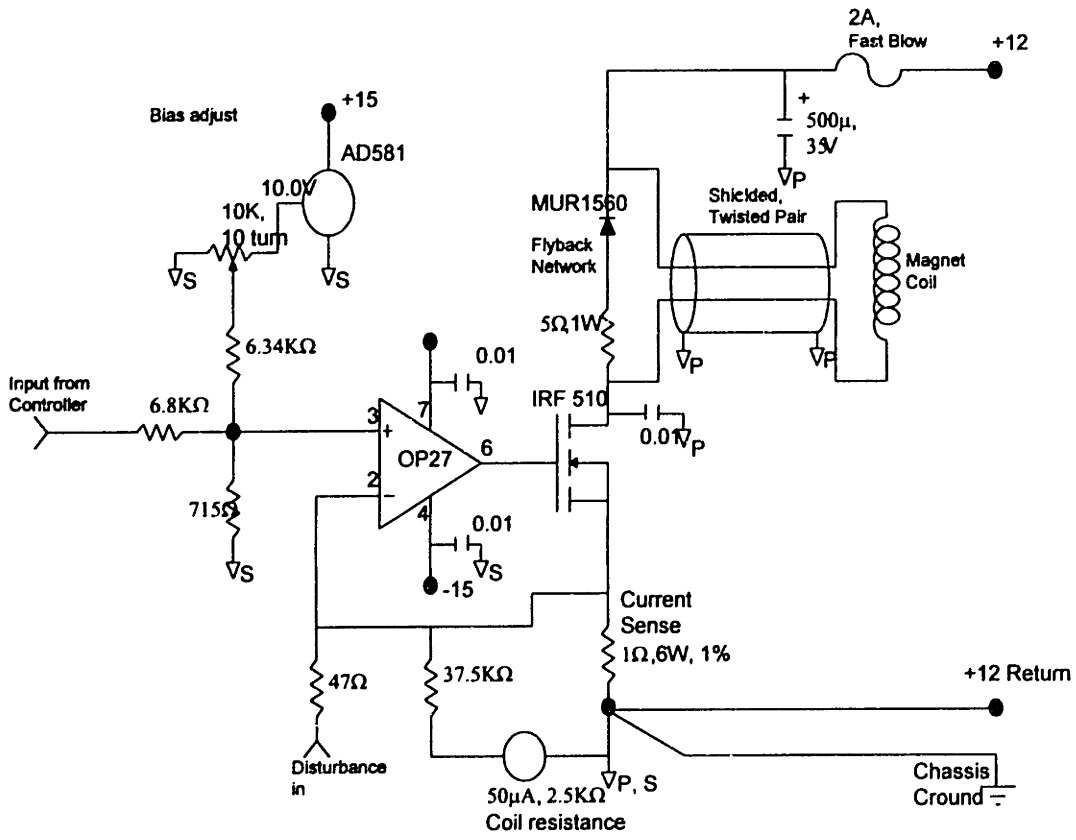

Figure 7.1a The power amplifier for floated load (Adapted from [Tru90])

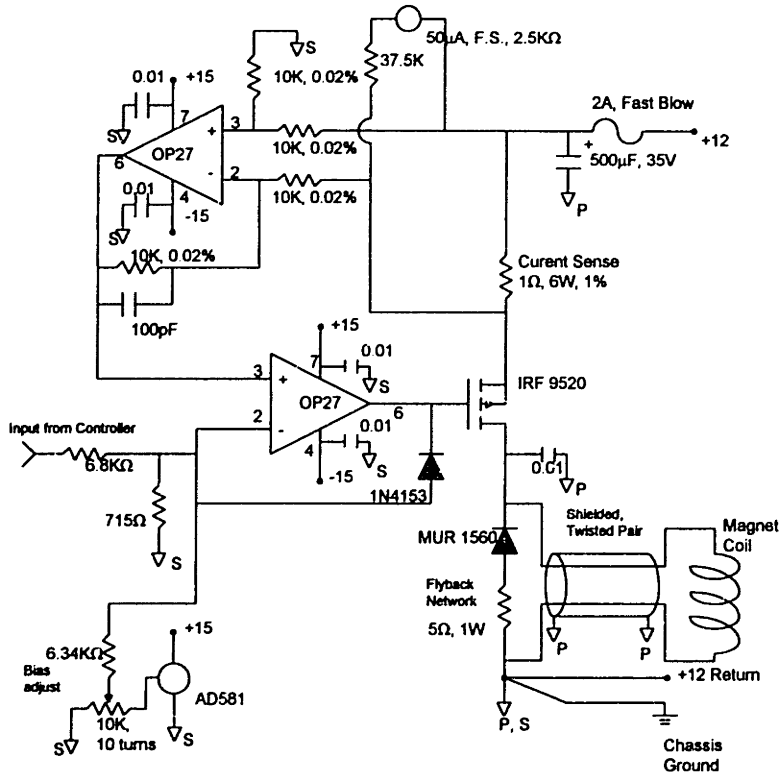

Figure 7.1b The power amplifier for grounded load (Adapted from [Tru90])

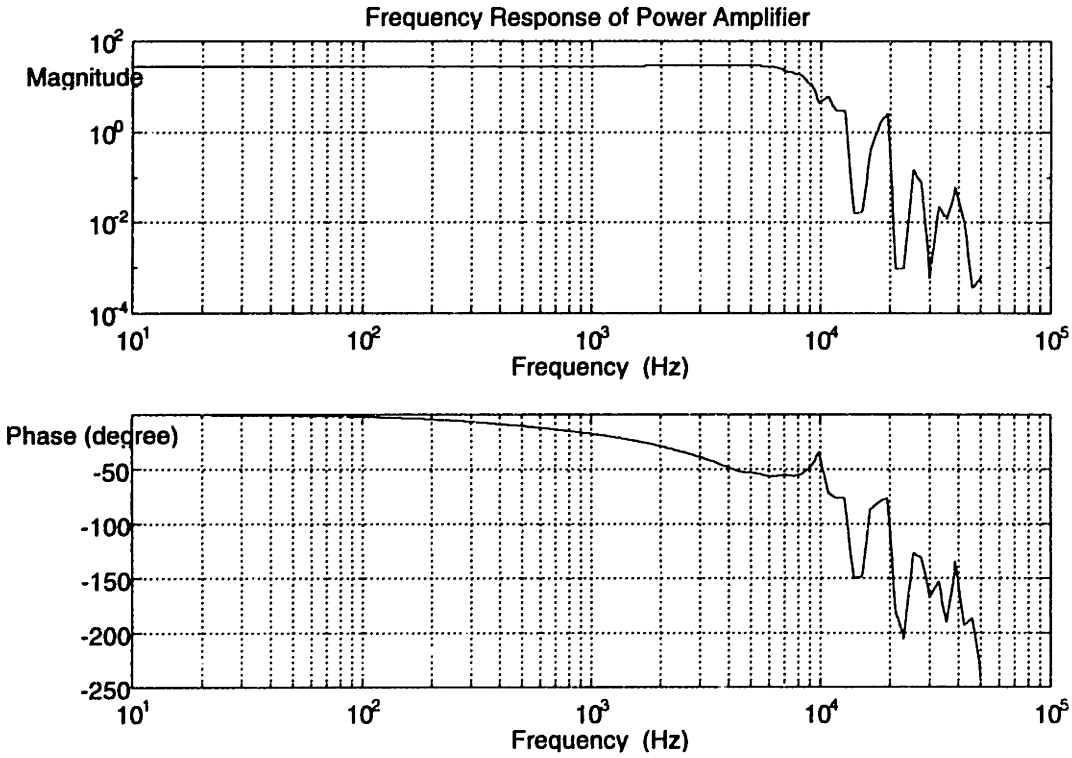

Figure 7.2 The frequency response of floated load power amplifier

7.2 Position Sensors

We use capacitive type sensors for position feedback in this task. Capacitive sensor has a very high position resolution. The basic capacitive transducer consists of two conducting plates separated by a dielectric. In general, transduction is affected by the following factors.

1. Change of distance between plates.

2. Change of plate area.

3. Chemical or physical changes in the dielectric.

There are a lot of applications of this kind of sensor, such as position sensing, pressure sensing, and water level sensing. A brief discussion of the working principle of non-contact sensing can be found from [McR87].

Two conductive plates separated by a dielectric material form an electrical capacitor. The capacitance C depends on total plate area A, distance between plates y, and the dielectric constant K. The relationship is expressed by

$$C = \frac{\varepsilon A}{d}. \qquad (7.2)$$

Where ε is the permittivity (Newton/m)

When an alternating voltage V is connected across a capacitor, an alternating current I_C flows through the circuit. Their relationship is the following:

$$I_c = \frac{V}{X_c}, \quad \text{and} \quad X_c = \frac{1}{2\pi fC}.$$

where f is the signal frequency and X_c is the system impedance. Therefore

$$I_c = \frac{2\pi fV\varepsilon A}{d}. \qquad (7.3)$$

Thus, if f, A, V, and K are held constant, Ic is a measure of capacitor-plate separation. Equation (7.3) is the basic principle of non-contact sensing.

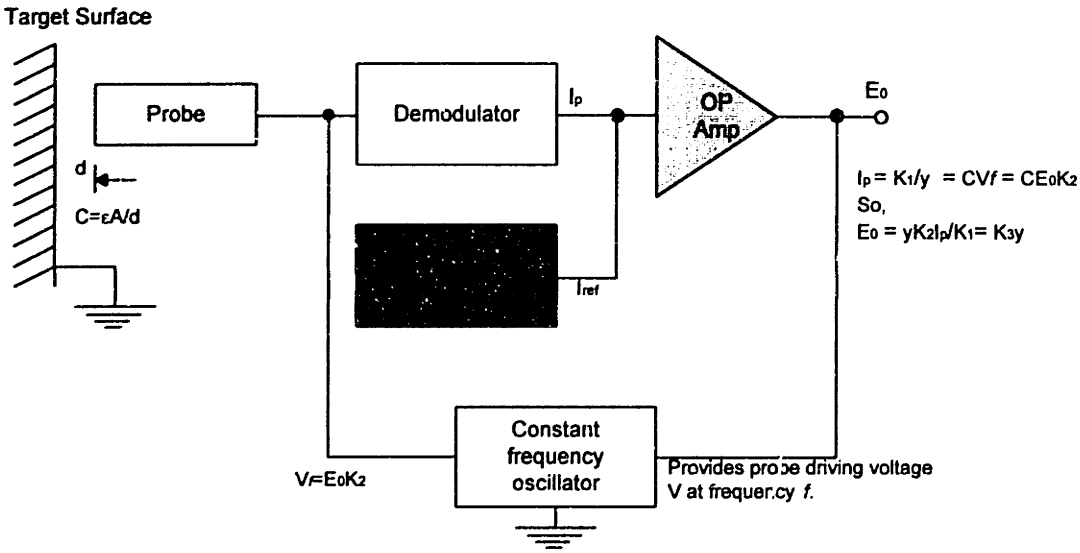

Figure 7.3 Converting probes signal to distance

Capacitance probes need at least three pieces of signal-processing equipment:

1. *Oscillator-driver:* The oscillator provides excitation energy for the probe. In this case, the driving frequency is 1.2 MHz.
2. *Demodulator-linearizer:* This unit converts the probe signal to a voltage proportional to the gap between the probe and target.
3. *Signal conditioners:* Once a signal is made proportional to distance, signal conditioning circuit modules transform the signal into required information by filtering the signal and thus reducing the noise.

Figure7.3 shows the converting of probe current to distance. Probe systems use an operational amplifier to convert rectified probe current, I_p to an output voltage E_o. Amplifier output varies the amplitude of the oscillator output voltage to the probe to make I*p* always equal to a constant reference current I_{ref}. Thus E_o varies as required to maintain a zero amplifier input voltage and is a linear function of the target distance y.

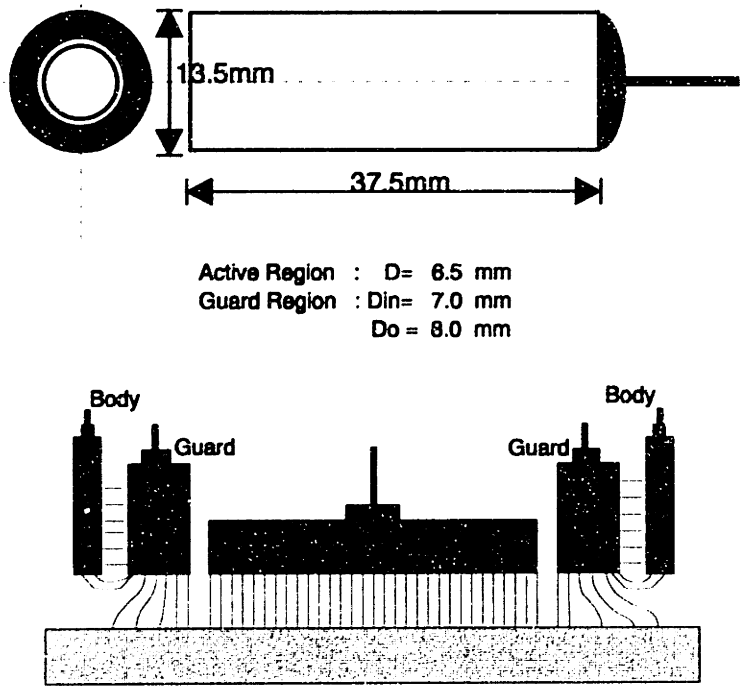

Figure 7.4 The concept of guarding and the mechanical layout of the probe

7.3 Sensors Calibration

In this work, three Pioneer capacitance probes are used for position sensing. The dimensions of this kind probe are shown in Figure 7.4. Note that in the above section, the fringing effect of the electric field is neglected since it is assumed that the plate is infinite. However, in a practical system, the dimension of the probe is finite and one must add a guard ring to prevent this effect. Figure 7.4 also shows the principle of guard concept. For keeping the electric field uniform, it is necessary to put a guard ring on the outside of the sensor. The bandwidth of these sensors are around 10 Khz. Comparing to the desired bandwidth, their dynamics can be neglected.

Before using these probes, it is necessary to make a rough calibration on each probes to find their gain. The experiment is simple and the schematic diagram is shown in Figure 7.5 Probes are mounted on a structure which is screwed onto an optical table. A

flat face target is mounted on a precision micrometer which is screwed on the table too. The resolution of micrometer is 2 μm. After setting the calibration environment, one records both the readouts of the micrometer and multimeter. Finally, a least square technique is used to fit a straight line. The gains on position sensors vary but all are close to 200,000 V/m or 0.2V/μm. Table 7.1 is a brief summary. The experimental result, however, contains the structural dynamics of the supporting fixture. Without changing the gap, just recording the fluctuation of signal and using a HP35665A dynamics analyzer to do the power spectrum analysis, one can see the frequency response. Figure 7.6 shows the experimental result on sensor gain and power spectrum density. About the power spectrum density, the low frequency portion is contributed by the structure mode. The signal is attenuated rapidly after frequency over 200 Hz. The power spectrum density is almost constant when the signal frequency is greater than 2000Hz. This is the real signal of sensor noise.

It still needs to do further calibration for higher accuracy. The peak to peak value of sensor noise, as mentioned on Section 7.2, is about 2 mV or 10 nm equivalently. The only thing that can calibrate it in our lab is a laser interferometer with a resolution of 5 nm.

Table 7.1 The micrometer calibration result

Probe number	**Sensor gain**
Probe #1	206.4 mV/μm
Probe #2	202.9 mV/μm
Probe #3	208.3 mV/μm

Figure 7.7 shows the basic working principle of plane mirror type laser interferometer [Zyg91]. A laser source emits a source beam. It is split to two beams (reference beam and measurement beam) after passing splitter, then, passing retroreflector, they come together finally and enter the receiver where a photo detector and circuit convert the light intensity change into counts. In our system, the least count is 5 nm.

Figure 7.8 shows the experiment setup for sensor calibration. The computer outputs a series of control efforts. After passing power amplifier, it is converted to current and used to generate force on actuators for moving the stage. We collect laser reading and probe reading simultaneously. Finally, we can get a curve between laser and probe reading. Then, using least square fitting, the sensor gains of capacitive probes can be gotten. They are shown in Figure 7.9 ~ Figure 7.11. Table 7.2 is a brief result. From Figure 7.9~7.11, one can observe the relationship between force (in terms of displacement, since F = kx) and current(in terms of DA output since current proportional to the control effort) is a square-like law. The laser calibration has very high resolution at low current input. After curve fitting the data, we find the sensor gain is around 200 mv/μm but they are always smaller than the corresponding value of micrometer test. The standard deviations between fitting line and experimental data are 38mv, 12mv, and 36mv for probe0,1,2 respectively. Note that the probe #1 has smallest difference between the two calibration result and a smallest standard deviation. A possibility is that the alignment of probe #1 in stage is closer to its alignment on micrometer calibration. In chapter 10, the alignment error of capacitive probe will be discussed. The higher the tilt angle, the lower the sensor gain will be. That is a possible reason why the result by laser calibration is always less than by micrometer.

Table 7.2 The laser calibration result

Probe Number	**STD Deviation** (Deviation ≡ Fitting value-Experiment value)	**Sensor Gain**
Probe #0	38 mv	202.34 mV/μm
Probe #1	12 mv	201.57 mV/μm
Probe #2	36 mv	200.42 mV/μm

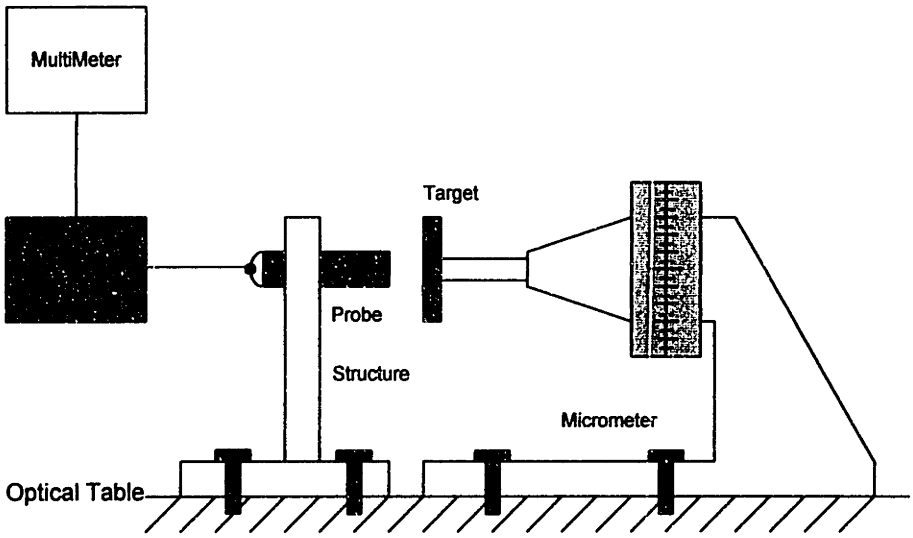

Figure 7.5 A simple probe calibration device

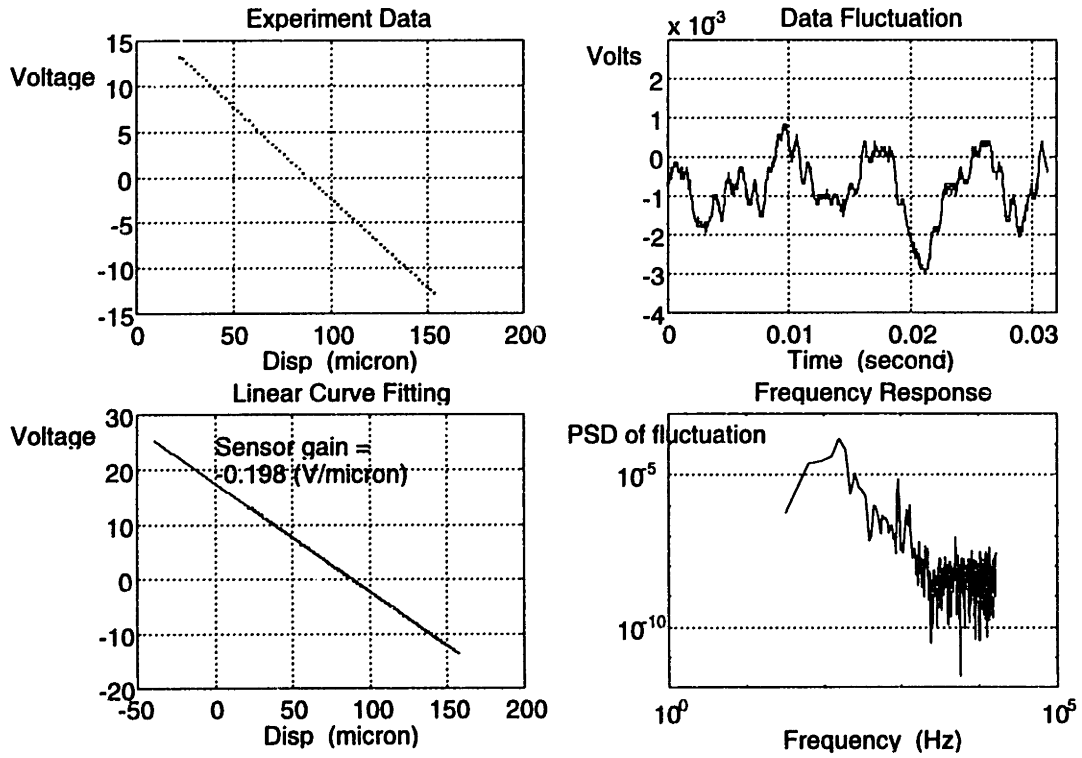

Figure 7.6 Sensor calibration result using micrometer

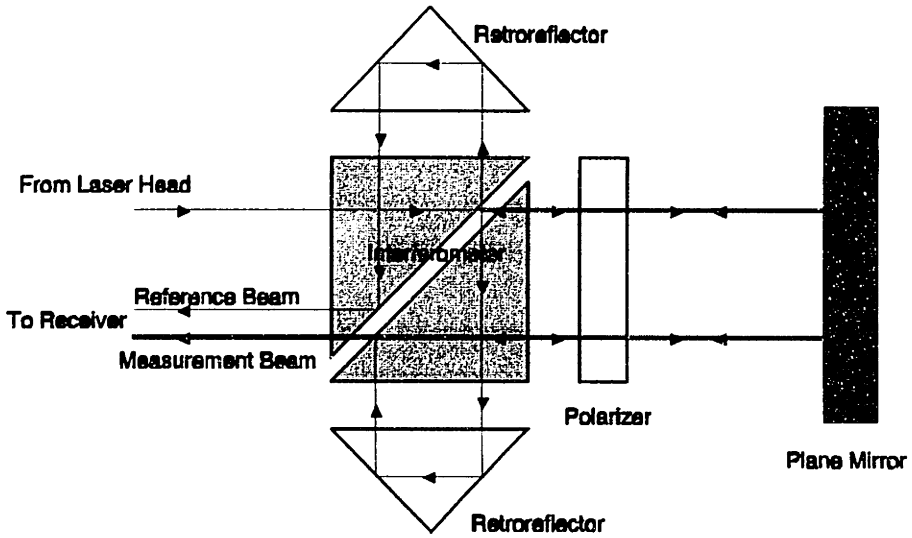

Figure 7.7 Principle of Plane Mirror Laser Interferometer

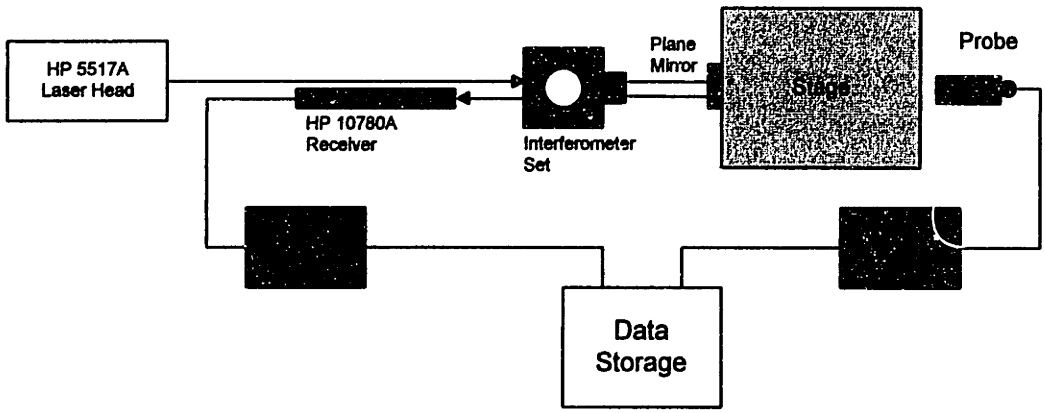

Figure 7.8 Experiment set up for probe calibration by laser

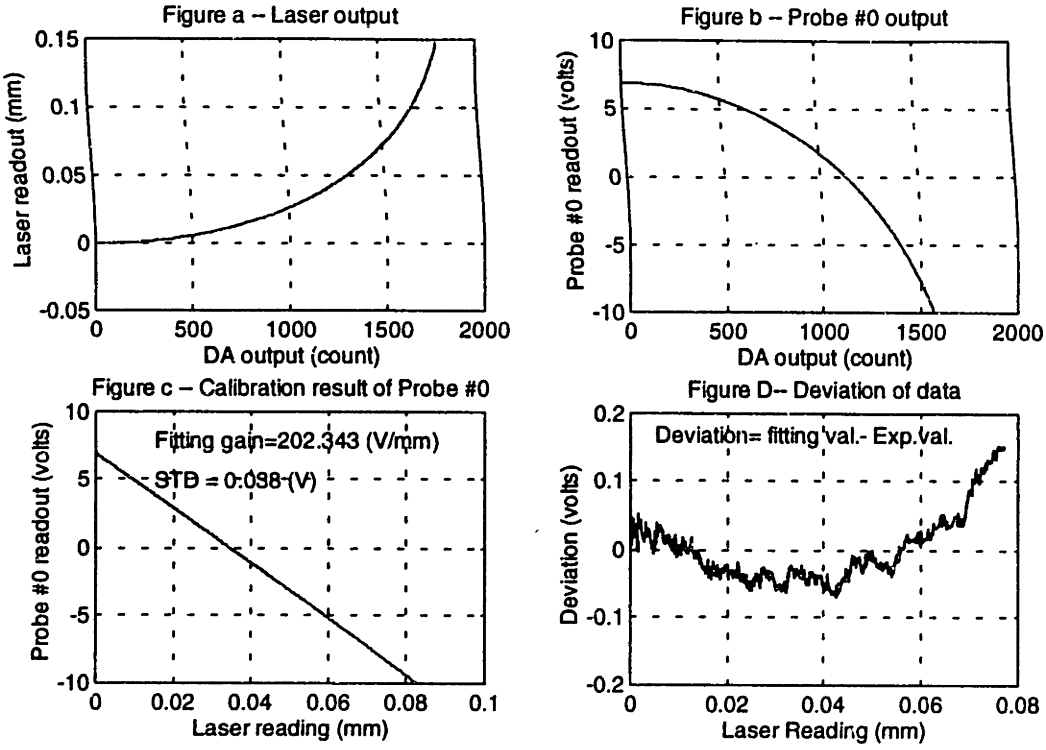

Figure 7.9 The laser calibration result of probe #0

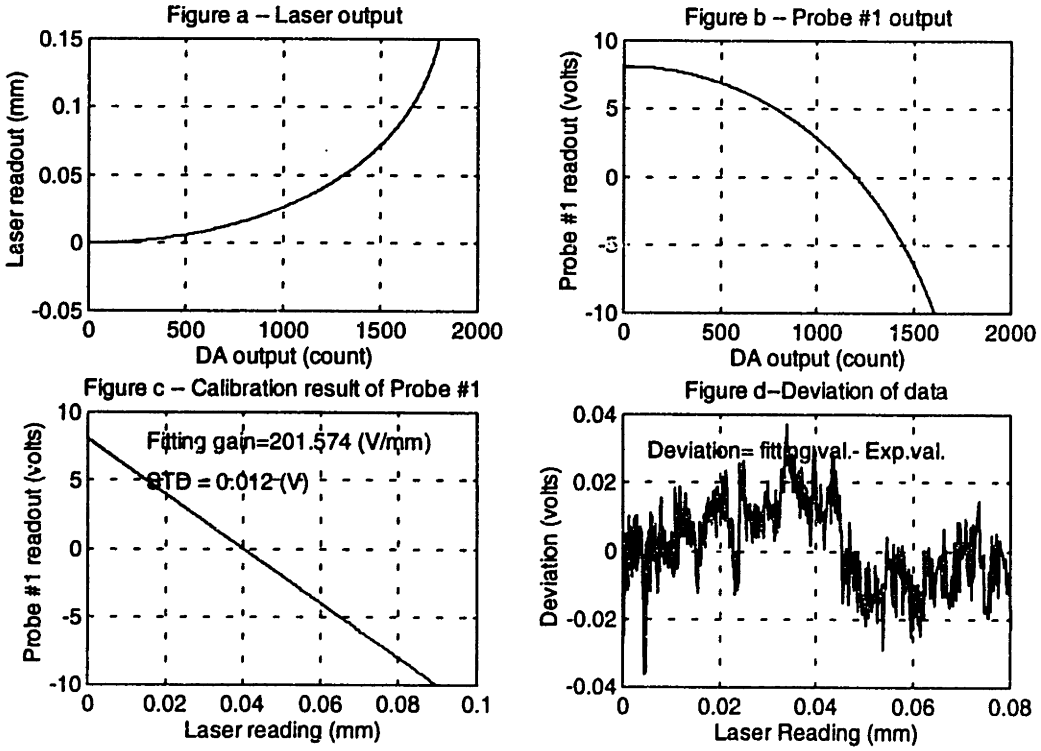

Figure 7.10 The laser calibration result of probe #1

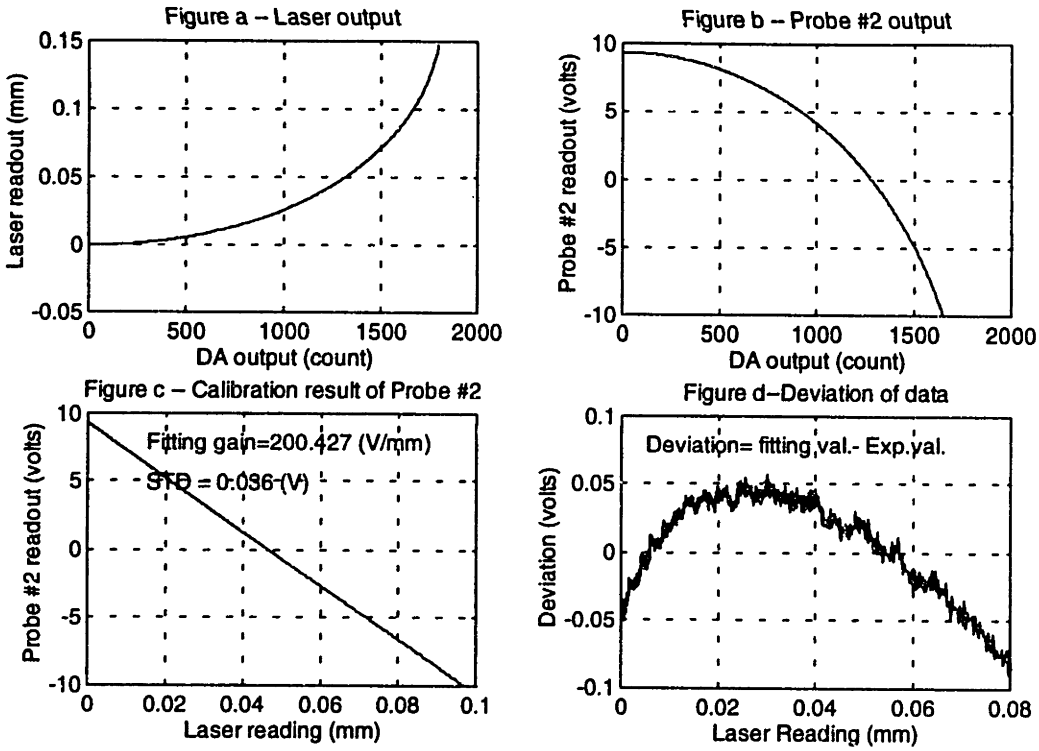

Figure 7.11 The laser calibration result of probe #2

CHAPTER 8

CONTROLLER DESIGN

In this chapter, we develop the controller by a linear system approach. That is, assuming the feedback linearization performs perfectly, the whole nonlinear block can be represented by just a constant gain K. The viscosity of Viscasil is assumed constant under the motion modes of the natural frequencies. Furthermore, the saturation and quantization effects are also ignored at this time. After finishing the linear analysis, we design the digital controller directly. Finally, we account for all nonlinear effects such as saturation and quantization by making computer simulations to verify the system performance.

Section 8.1 discusses the design considerations, including both the time and frequency domain viewpoints. Section 8.2 discusses the characteristics of the system transfer functions under PI control. Section 8.3 deals with the concept of the design the single degree of freedom system in the s-domain. Section 8.4 shows the single degree of freedom discrete controller design. The multi-degree of freedom controller design and SIMULINK simulation is presented in section 8.5.

8.1 Design Consideration

A lot of performance requirements should be specified based on the characteristics of the plant and actuators. Based on the discussions in the previous chapters, a PI control law is selected for zeroing the steady state error and for low frequency noise attenuation. These specifications give the designer some restrictions in controller design.

Moving range: The maximum moving range will be ± 80μm based on the actuator's maximum output. However, the probes can only detect ± 60μm and we need some margin for fine adjustment. Therefore, based on the above considerations, the maximum moving range will be restricted within ± 50μm.

Accuracy: As shown in Chapter 6, the dominant noise will be the quantization of the DAQ devices. Therefore, the best resolution that can be reached will be two ADC units or 49 nanometers based on current devices (12 bit ADC). The base vibration and sensor noise have just a little effect under this circumstance. However, it may still cause the resolution worse than ±2 ADC unit if the noise is too strong. Therefore, the control law should attenuate the base vibration readily to keep the accuracy in the best situation. It means 50 nanometers will be the desired goal for resolution.

Bandwidth: The bandwidth is restricted by the natural frequency of mechanical plant and by the design approach. The spring dominated design indicates that a cross-over frequency less than the system natural frequency will be necessary. However, on the other side, if the bandwidth is too low, the performance will be degraded and the application will be restricted. After compromising, a bandwidth nearly 500 rad/s should be a reasonable choice. To get optimum specification, one must go through Bode analysis.

Disturbance rejection: The influence of environment disturbance should be attenuated as much as possible. Especially the low frequency disturbance. To achieve this requirement, the controller should contain a integral part and avoid to use differential related controller (e.g., PD or lead controller).

Steady state error: The steady state error should be zero for desired position control. To reach this goal, the controller should contain integrator.

The design procedures are the following:

1. Understanding plant characteristics.
2. Determine the sampling rate and get the ZOH equivalent system transfer function.
3. From the desired specs, determine the crossover frequency, gain and phase margin in Bode plot. Also from root locus, one can convert the time domain specs to Z plane, that is, all system poles should be located in a specified region.
4. Determine all control gains and verify the control result by step response.

We use the modeling results (4.26) and (4.27) as the plant dynamics for controller design. We select PI control to control the stage. Rather than doing the continuous design

first, then doing the emulation, we make the digital design directly since there are several realistic issues that will happen in digital control but never in the continuous domain. There are the A/D, D/A quantizations, which were discussed in Chapter 6, and a computational delay in the digital computer.

In addition to the above considerations, anti-aliasing low pass filters with bandwidth of 110 Hz are introduced into the system and they increase phase lag (See Section 6.2). For eliminating its effect, one should put a zero on the corresponding pole location. Since one can not get a zero alone, a lead compensator is used for this goal. If the pole location in lead is much far away from zero, their effect will be almost equal although it is better to include the anti-alias filter into the plant model and then compensate it via controller design. In controller design, we assume that the lead can perfect cancel the low pass filter effect as well as that the nonlinearlity of actuator can be canceled out by feedback linearization. Therefore, the whole system for design, as shown on Figure 8.1, will be a series combination of PI controller, a unit time delay, and the plant.

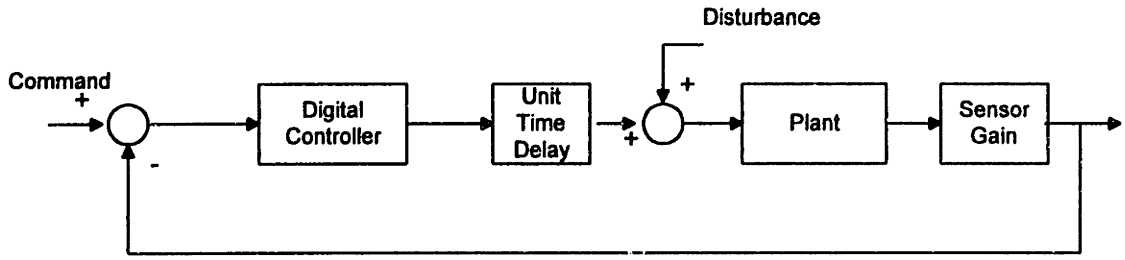

Figure 8.1 The block diagram which used for controller design

8.2 System Transfer Function Under PI Control

The stage translation mode is designed to have enough phase margin. This eliminates the requirement for additional phase compensation, i.e., the system does not need the phase lead compensator. That means no differential terms will be included in the loop and henceforth reduce the chance of high frequency noise amplification. In addition, since the system has springs to provide its stiffness, an integration term is necessary to force the system to follow the command and zero the steady state error. Moreover, from the analysis in Chapter 6, the PI control will reduce the low frequency vibration noise.

Here, defining the Proportional plus Integral (PI) controller in continuous domain as (2.7), where Kp is the proportional gain and T_i is the integration constant. Figure 8.2 shows the schematic Bode plot of the PI controller. The gain decreases by a -1(-20dB) slope when ω is below $1/T_i$, and approach to a constant gain K_p when ω is above this value. The initial phase lag is -90° and decreases to zero as ω increases. The negative of the loop transmission of the system is -LT(s) = C(s)G(s), where G(s) is the plant transfer function.

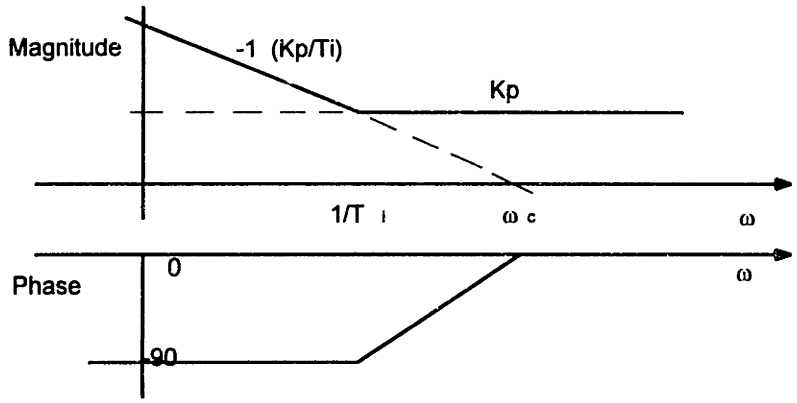

Fig. 8.2 The Schematic Bode plot of PI control

The negative of the loop transmission of the whole system will be (2.8). The loop transmission plot of Eq(2.8) is shown in Figure 8.3a for translation mode with K_p=2.5, T_i=1/330 and in Figure 8.3b for rotational mode with K_p=0.18, T_i=1/330. Note that the proportional gain in rotational mode is much smaller than that in the translation mode. That is due to the higher DC gain of the rotation mode.

The closed loop transfer function between position output and the input is (2.4). Or, substituting from Eq.(2.8)

$$H(s) = \frac{K_p K_s (s + \frac{1}{T_i})}{ms^3 + bs^2 + (k + K_p K_s)s + \frac{K_p K_s}{T_i}} \qquad (8.1)$$

in terms of stage parameters.

By the same way, one can find the closed loop transfer function between position output and the base acceleration $\ddot{y}$ (2.17), or in terms of stage parameters,

$$D(s) = \frac{Z(s)}{-\ddot{y}(s)} = \frac{m}{ms^2 + bs + (k + K_p K_s) + \frac{K_p K_s}{T_i s}}. \qquad (8.2)$$

Figure 8.4 and 8.5 are typical closed loop bode plots for transfer function H(s) and D(s), respectively. Where K_p=2.5, T_i=1/330 for translation mode and K_p=0.18, T_i=1/330 for rotation mode. Note that under PI control, by Eq.(8.2), the influence of low frequency base vibration will be greatly attenuated. The reason is that we can treat the integrator as a spring and its spring constant is proportional to the inverse of frequency. At low frequency, the stiffness will be very high and the magnitude of D(s) is reduced.

For the rotation mode of the stage, we can also apply PI controller on it initially. However, since its damping is not enough, the phase margin may not be enough. From Figure 8.3b, the magnitude plot is flat between 200 - 1000 rad. It is not good if we like the system crossover in this region since a little change in K_p will change crossover frequency a lot. For low frequency motion of stage, the PI law is still good for rotation mode. If we desire a high crossover frequency in rotation mode, a lead compensator should be introduced into the controller. Therefore, we decide to use a PI and Lead controller to control the rotation mode.

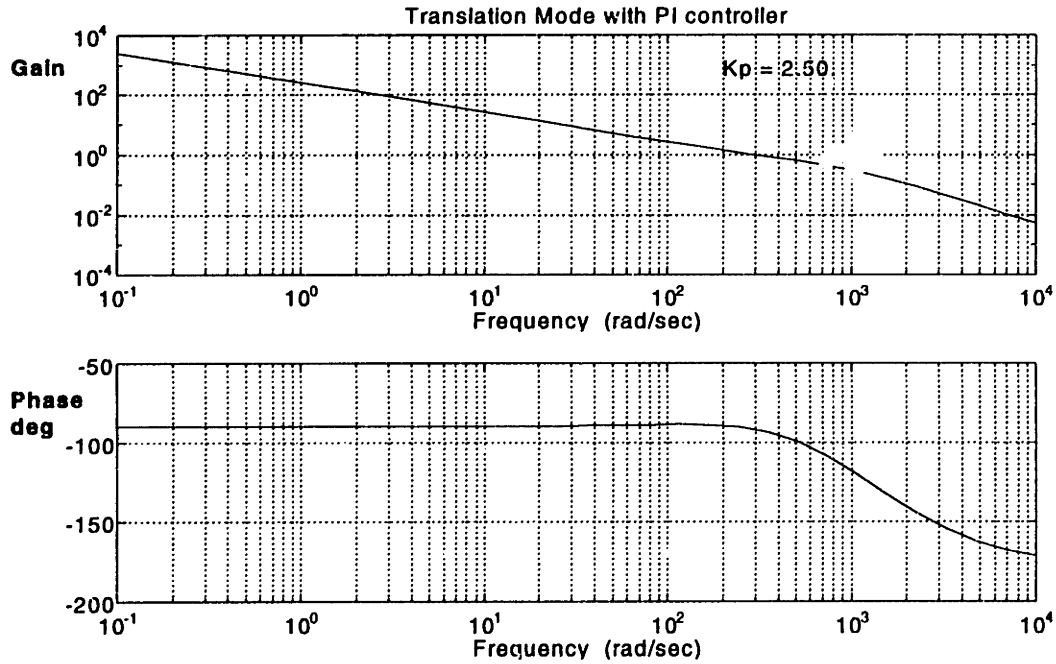

Figure 8.3 a The Bode plot of translation mode under PI control

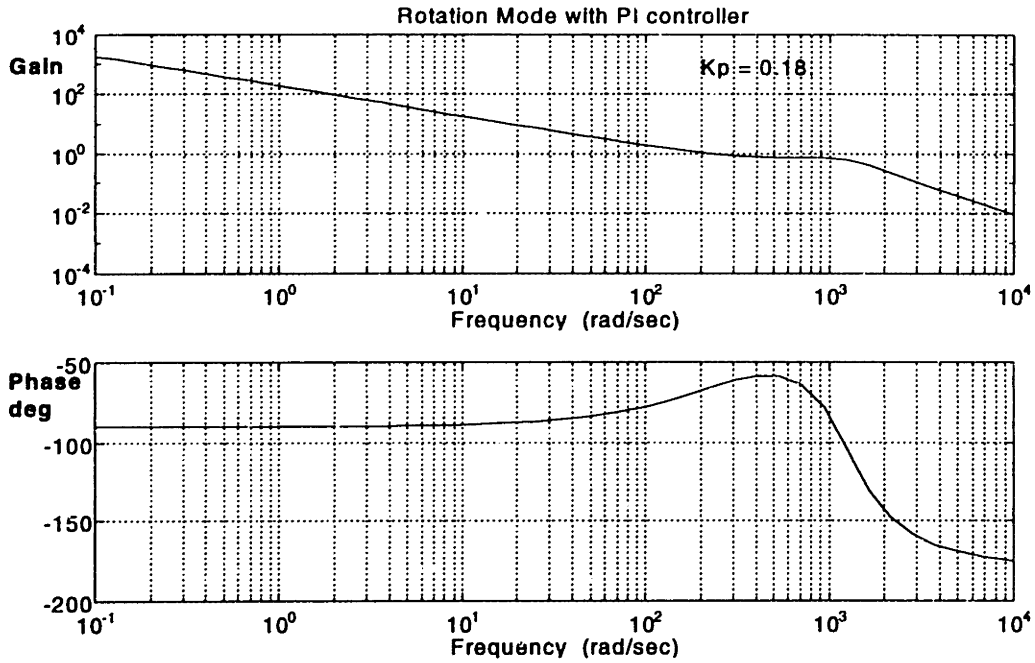

Figure 8.3 b The Bode plot of rotational mode under PI control

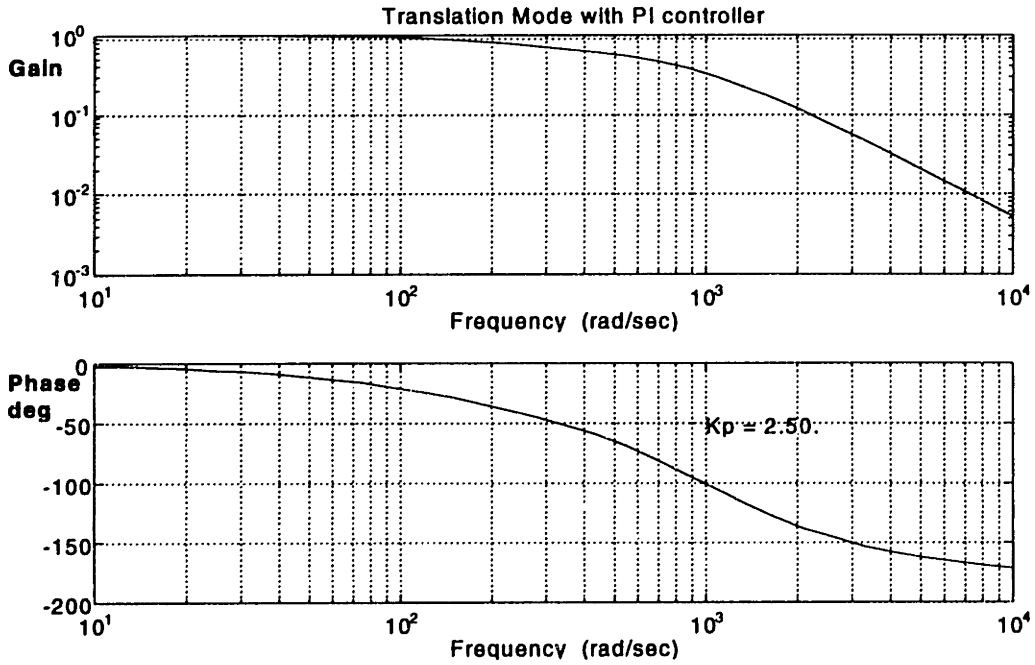

Figure 8.4 a Translation mode closed loop Bode plot w.r.t command input

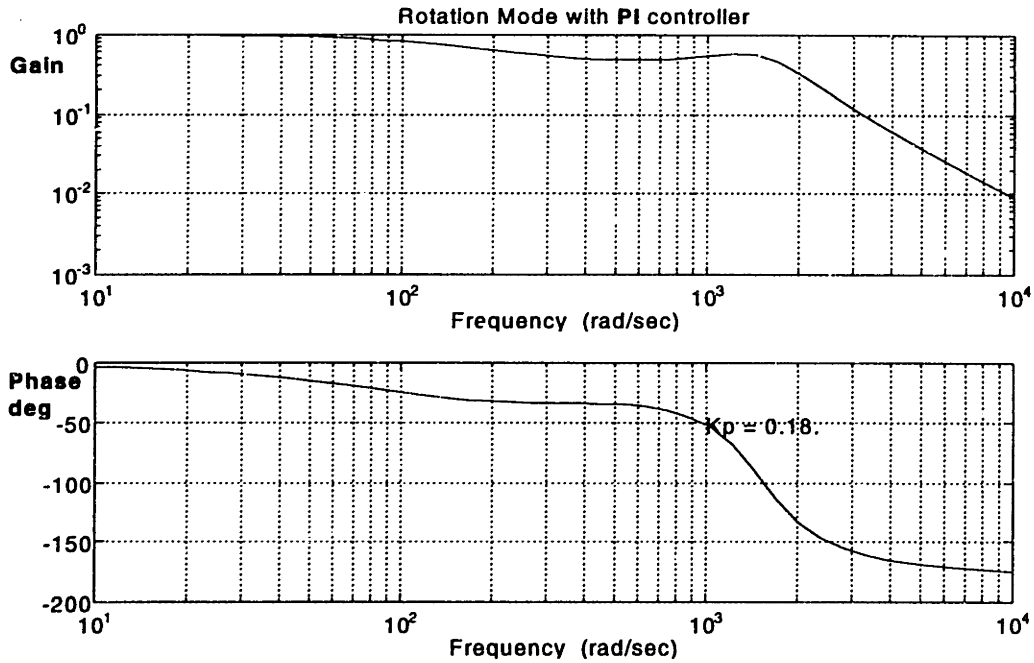

Figure 8.4 b Rotation mode closed loop Bode plot w.r.t. command input

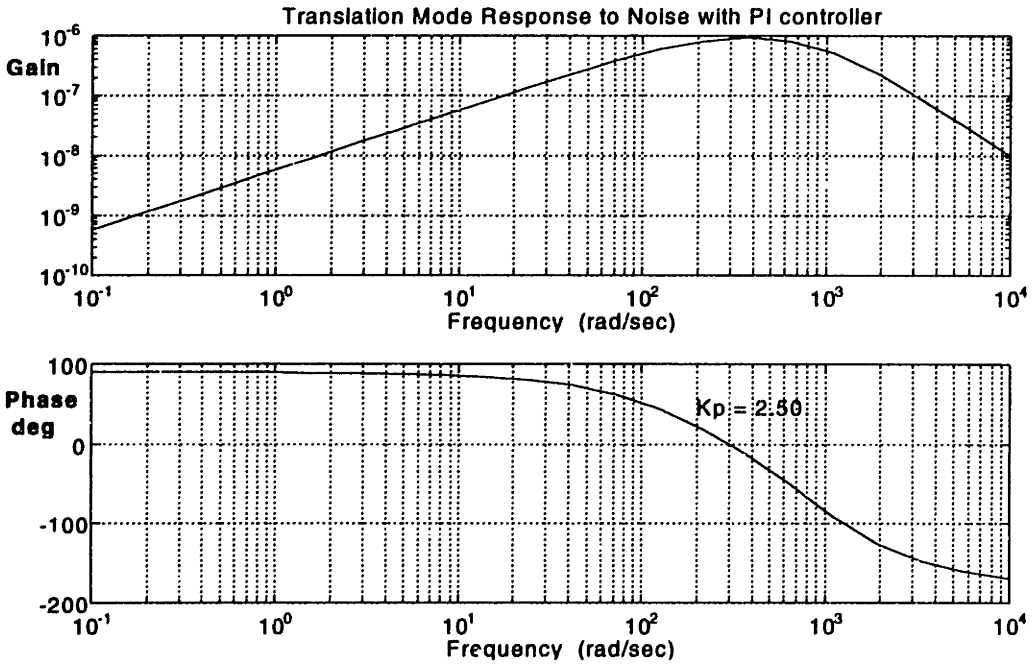

Figure 8.5 a Translation mode Bode plot w.r.t. base vibration noise input

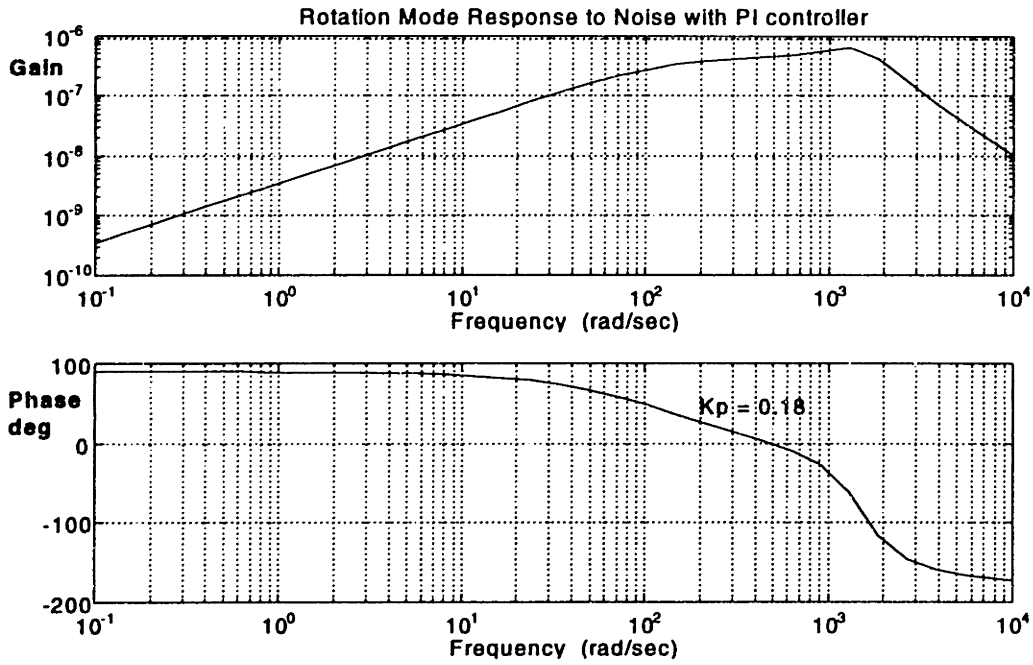

Figure 8.5 b Rotation mode Bode plot w.r.t. base vibration noise input

8.3 Continuous Analysis of Single Degree of Freedom System

Root Locus Analysis
Translation mode

The open loop poles of the stage are located at s=-1400 and s=-460. The first step in the controller design is to select a suitable integration constant T_i. A PI controller will add a pole at origin and a zero at s= $-1/T_i$ in the s-plane. Therefore, how to put this zero will be the first issue of the design procedure. Figure 8.6a shows several root locus plots for different locations of the zero. There are three different situations. Considering Figure 8.6a (I), the zero is located between the pole at s=0 and s=-460. It determines the location of the system dominated pole. Too large of a T_i value (typically 1/100) caused a slow response of system (Case I). If T_i is too small, such as T_i=1/1600, it will force a pole pair toward s=0, thus, not only get slow response but huge oscillation too (Case II). Placing zero between two plant poles or in the case of Case I but very near the pole at s=-460 will be a good choice for getting a reasonable bandwidth and damping ratio.

Rotation mode

The rotation mode root loci are shown in Figure 8.6b. It is underdamped with open loop pole s = 614 ± 1097 *j*. Figure 8.6b suggests that the integration constant T_i should not greater than 1/600, since the system damping ratio will be reduced more comparing to the case T_i larger than 1/600. It will decrease system phase margin. It corresponds to a problem in placing PI zero in FSDR design and has been discussed in Chapter 2.

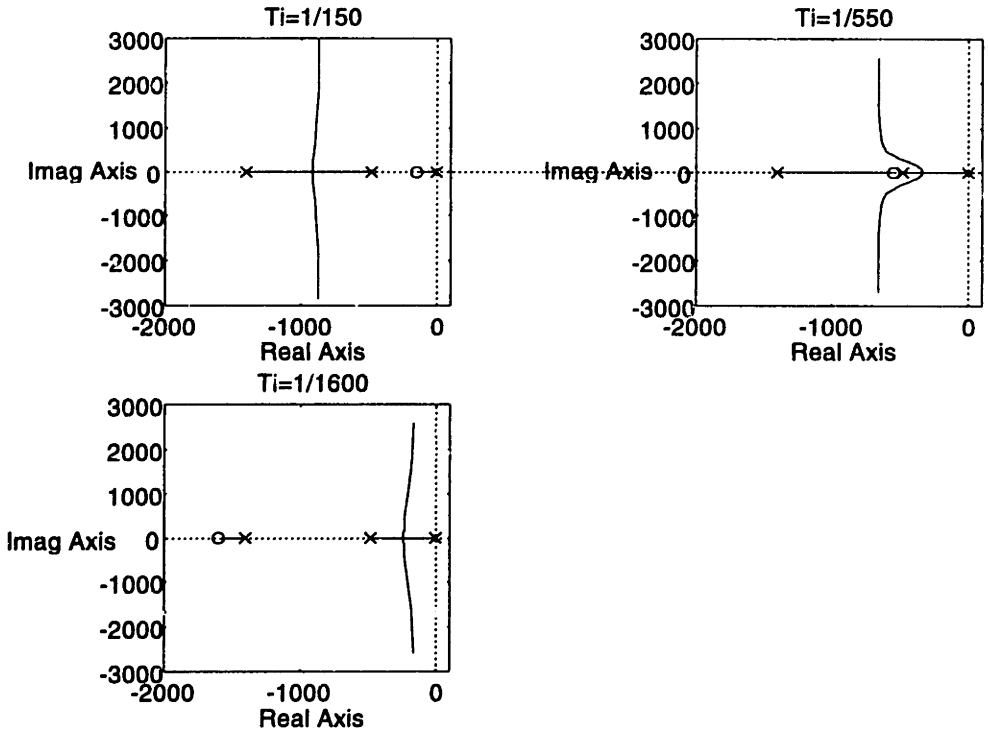

Figure 8.6 a Translation mode root loci under different T_i

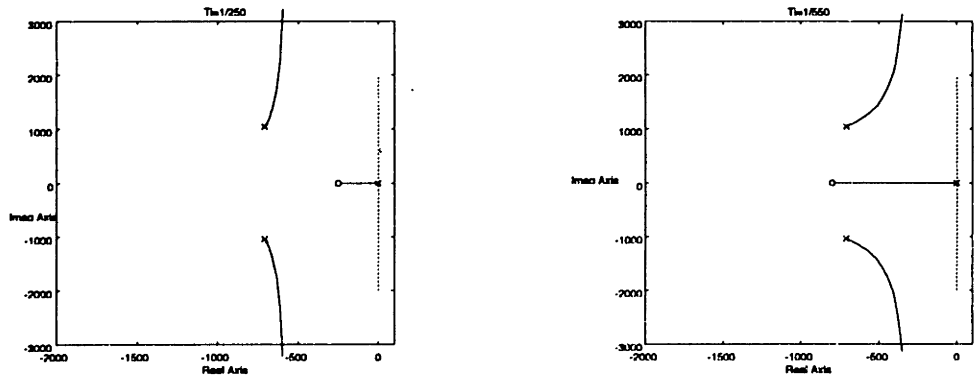

(a) T_i=1/250 (b)T_i=1/550

Figure 8.6 b Rotation mode root loci under different T_i

Bode Plot Analysis

From the perspective developed in Chapter 2, a schematic bode plot for the loop transmission of Eq.(2.8) is shown in Figure 8.7. The magnitude decreases by a -1 slope until $\omega = 1/T_i$, from $\omega=1/T_i$ to $\omega=\omega_n$, it keeps constant, and again decreased by a -2 slope beyond. For fast attenuating of the undesired signal in this flat region, one should reduce this flat region to as small as possible. By this reason, the value of T_i will be designed between 1/400 and 1/800. Since there exists an approximate relationship between damping ratio ζ and phase margin ϕ_m,

$$\zeta \cong \frac{\phi_m}{100} \qquad (8.3)$$

therefore, the phase margin should be in the region of 65° to 75° for get the system damping ratio around 0.7. For the rotational degree of freedom, one cannot get such damping ratio due to its system characteristics, it needs a PID controller.

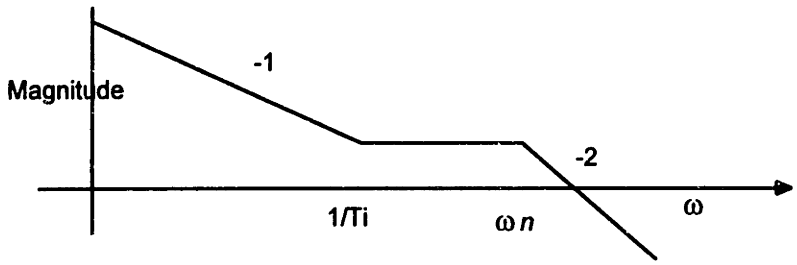

Figure 8.7 The schematic loop transmission plot

8.4 Digital Design of Single Degree of Freedom System

Formulation of discrete systems

Unlike continuous domain, discrete systems will be modeled by the Z-transform. The PI controller of (2.8) can be approximately by the following representation if we choose the backward difference approach.

$$C(z) = K_p\left(1+\frac{T_s z}{T_i(z-1)}\right) \qquad (8.4)$$

where T_S is the sampling period.

The computer need to spend some times on control effort computation and feedback linearization. The unit time delay makes thing even worse. Although this computation time may not exceed one sampling period, it is better to model the controller with unit time delay for a conservative design. The unit time delay can be expressed by

$$D(z) = \frac{1}{z} \qquad (8.5)$$

Finally, the zero order hold (Z.O.H) equivalent of sensor gain Q and stage transfer function (2.1) will be

$$G_{h0}(z) = (1-z^{-1})Z\left\{\frac{G(s)}{s}\right\} \qquad (8.6)$$

The loop transmission of discrete system will be the series combination of the above three blocks as shown in Figure 8.1.

Root Locus Design

Translation mode

From the discussion in Section 8.3 and 8.4, we start to design the controller. Selecting T_i = 1/500 and 1/330 for translation and rotation mode respectively. The sampling rate is 3K Hz. The root locus of the translation mode is shown in Figure 8.8a. Note that the pole at z=1 initially dominated the bandwidth of the system. The pole at z=0 is contributed by the unit time delay in the controller.

Figure 8.8b shows the step response for different K_p under T_i = 1/500 and various T_i under K_p = 5. It shows that K_p=3 and T_i=1/500 result a system rising time smaller than 10 samples and overshoot smaller than 10%. This thus represents a good choice for the translation mode design.

Rotation mode

Figure 8.9a shows the root locus of rotation mode with PI control. The Bode plot shows either the system crossover is at low frequency with enough phase margin or it is at a high frequency without enough phase margin. The corresponding step response is shown in Figuure 8.9c. We find that the step responses are not good whatever choosing

the K_p and T_i value. Either results a huge oscillation or slow response. That is due to the leak of decoupling of this mode in mechanical design. Now, we will pay some price for this. To increase the system damping by control, we put a lead compensator in the control. As shown in Figure 8.9c, a lead network

$$L(z) = 3.3\frac{z-0.7}{z} \tag{8.7}$$

is added into the system. The root locus after PI and lead compensation is shown in Figure 8.9d. Figure 8.9e shows a Bode plot with T_i=1/1200. The system has crossover at 1000 rad/sec with 50° phase margin. From Figure 8.9f, we know the system responses are better. Although lead compensator can improve the system damping, however, it increases the possibility of high frequency noise disturbance. Fortunately, based on the noise analysis, we know the quantization dominates the system resolution and effect of high frequency noise is not very important.

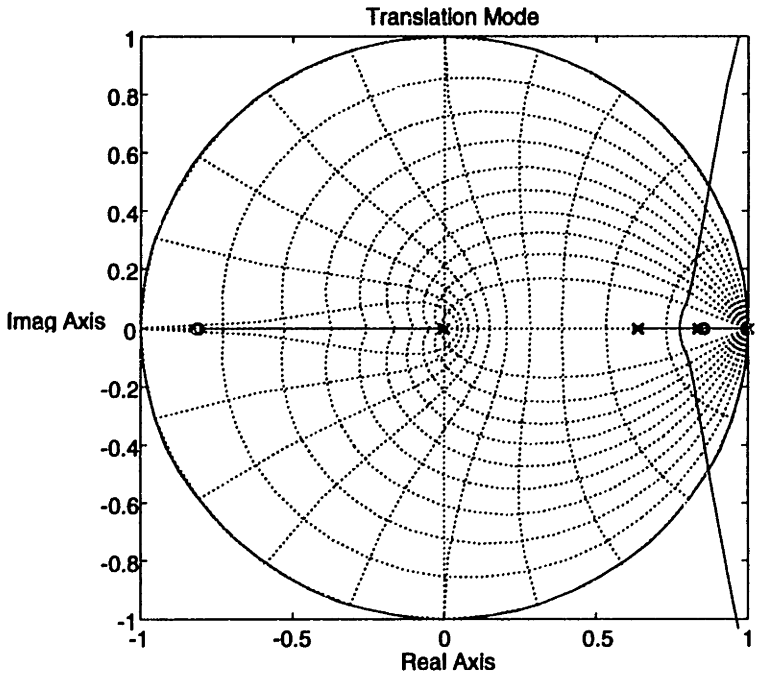

Figure 8.8a Root locus of translation mode (T_i=1/500, T_s=0.33 ms)

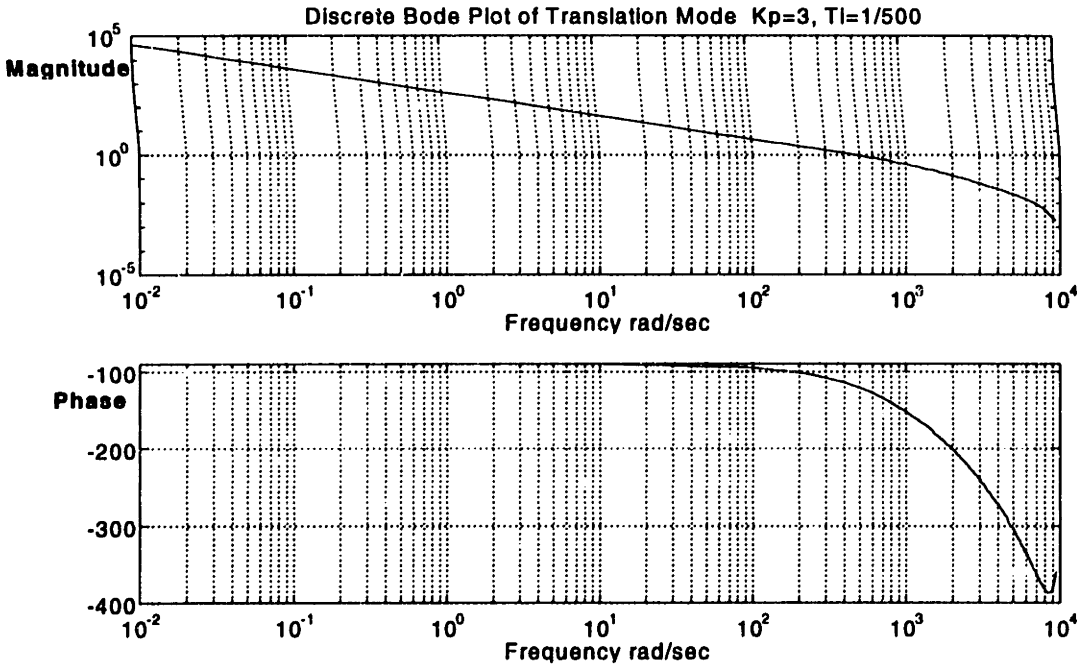

Figure 8.8b Discrete Bode plot of translation mode (T_i=1/500, T_s=0.33 ms)

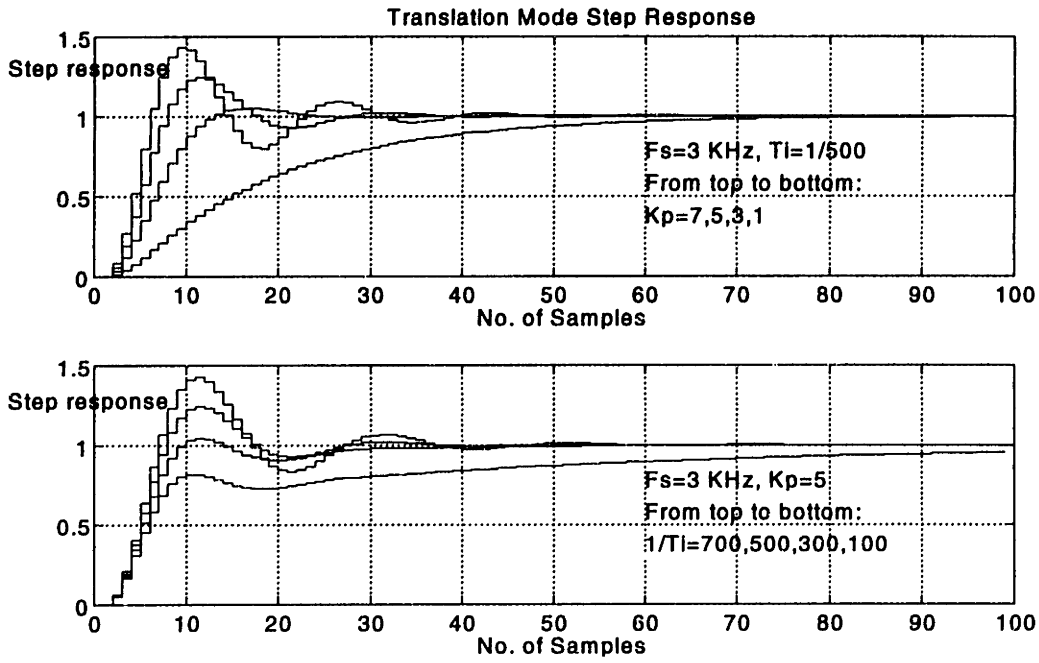

Figure 8.8c Translation mode step response

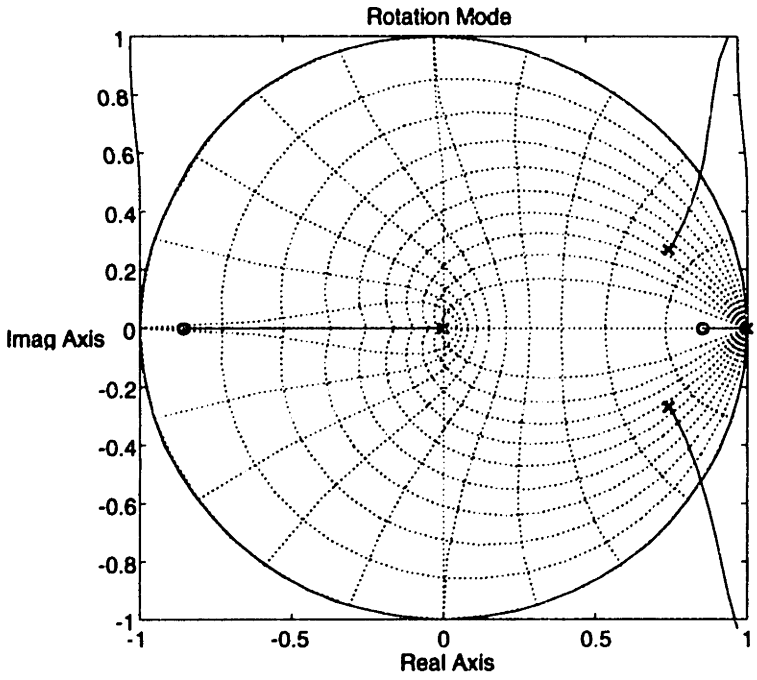

Figure 8.9a Root locus of rotation mode under PI control (T_i=1/500, T_s=0.33 ms)

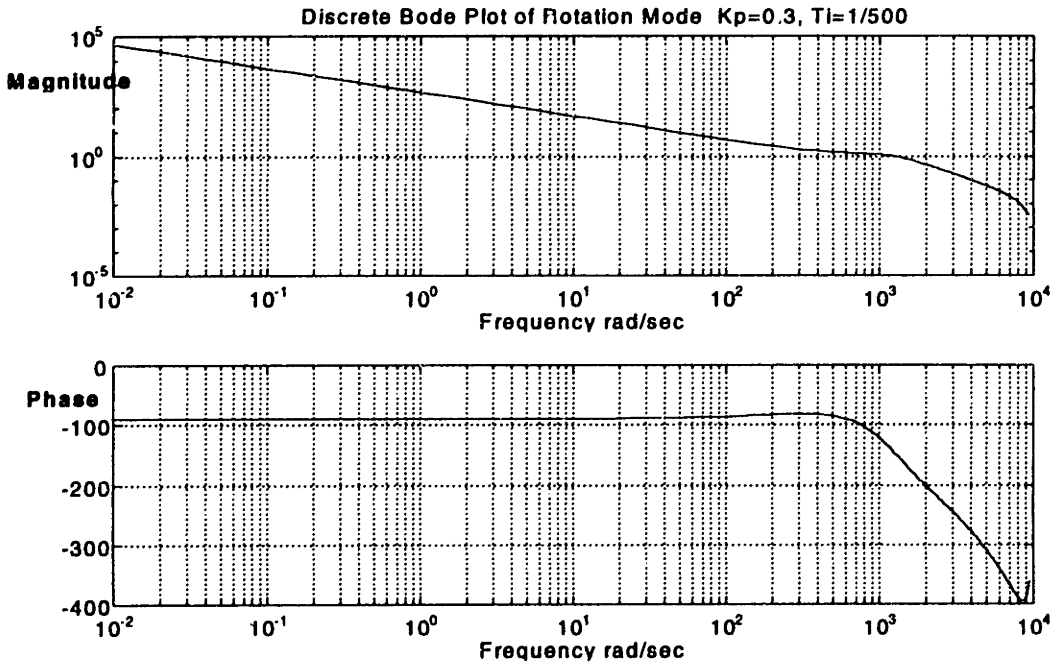

Figure 8.9b Discrete Bode plot of rotation mode under PI control

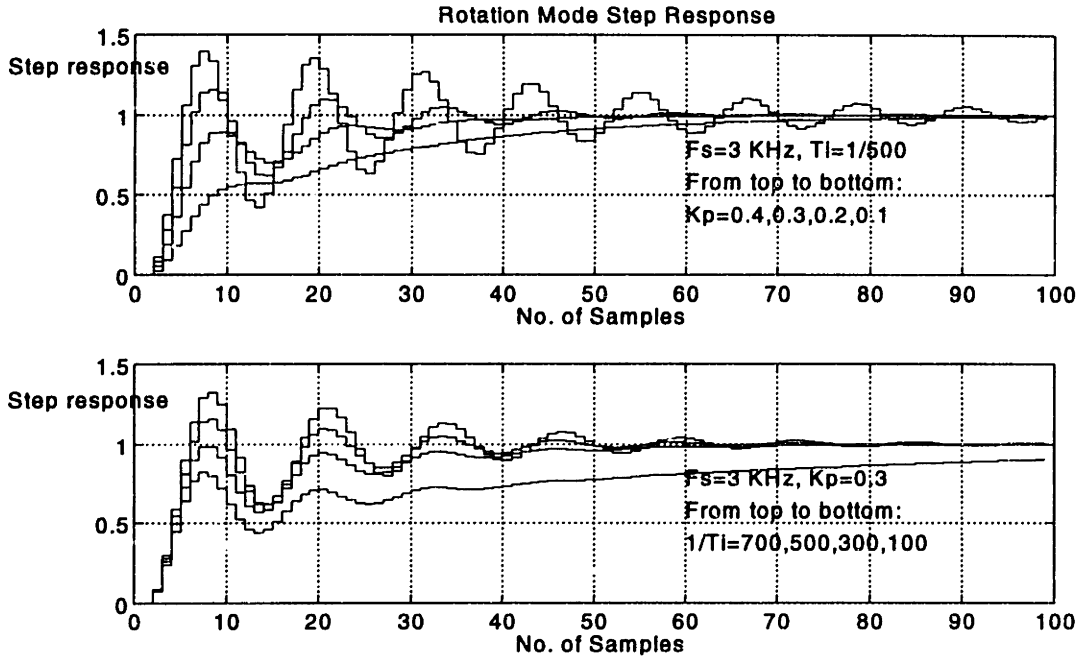

Figure 8.9c Rotation mode step responses under PI control

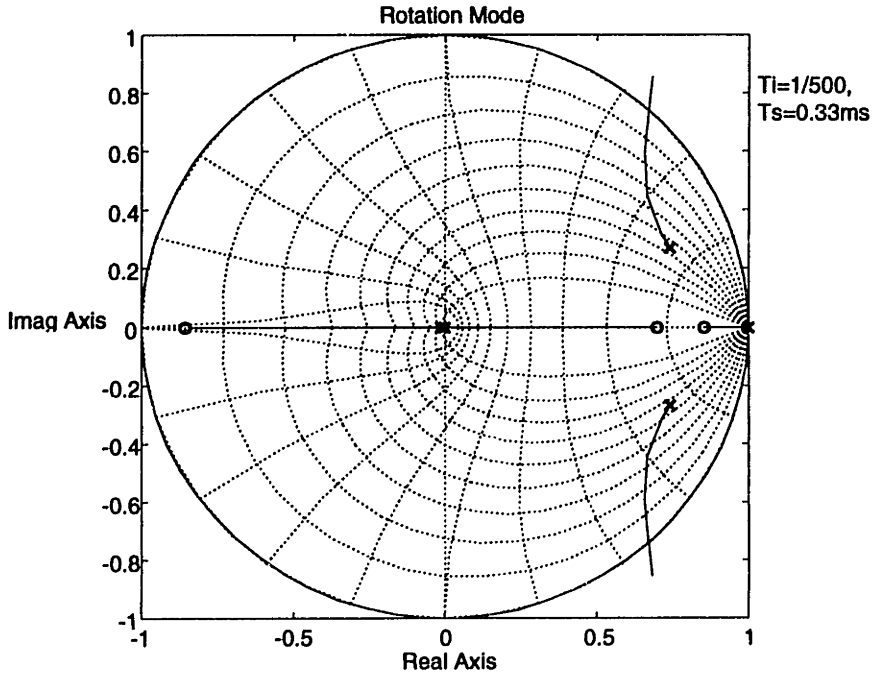

Figure 8.9d Root locus of rotation mode with PI and lead compensator

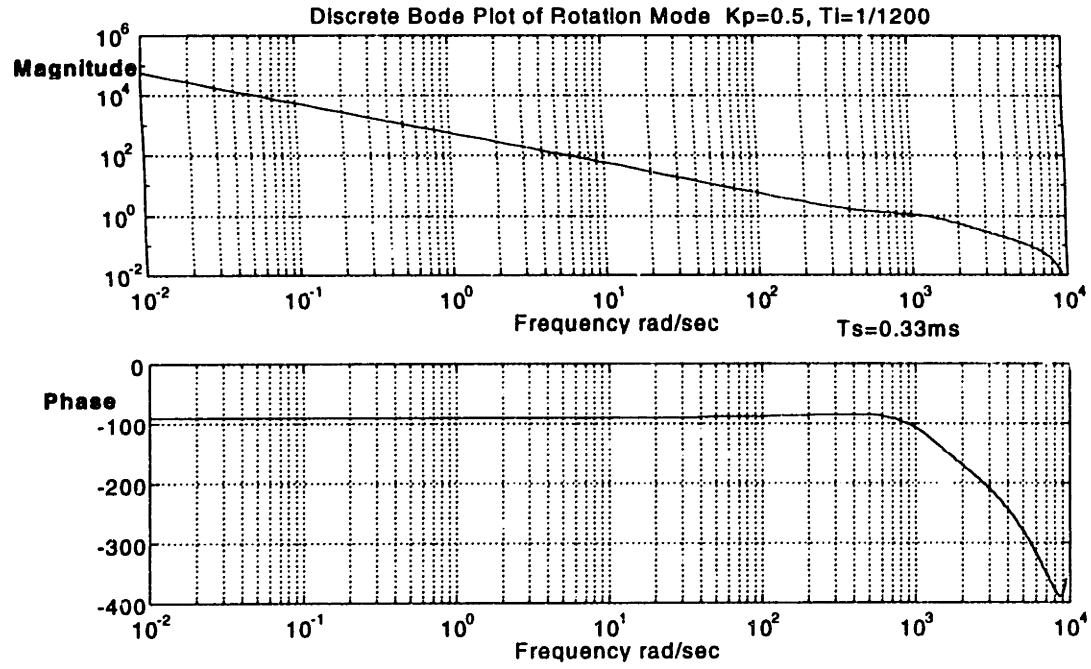

Figure 8.9e Discrete Bode plot of rotation mode with PI and lead compensator

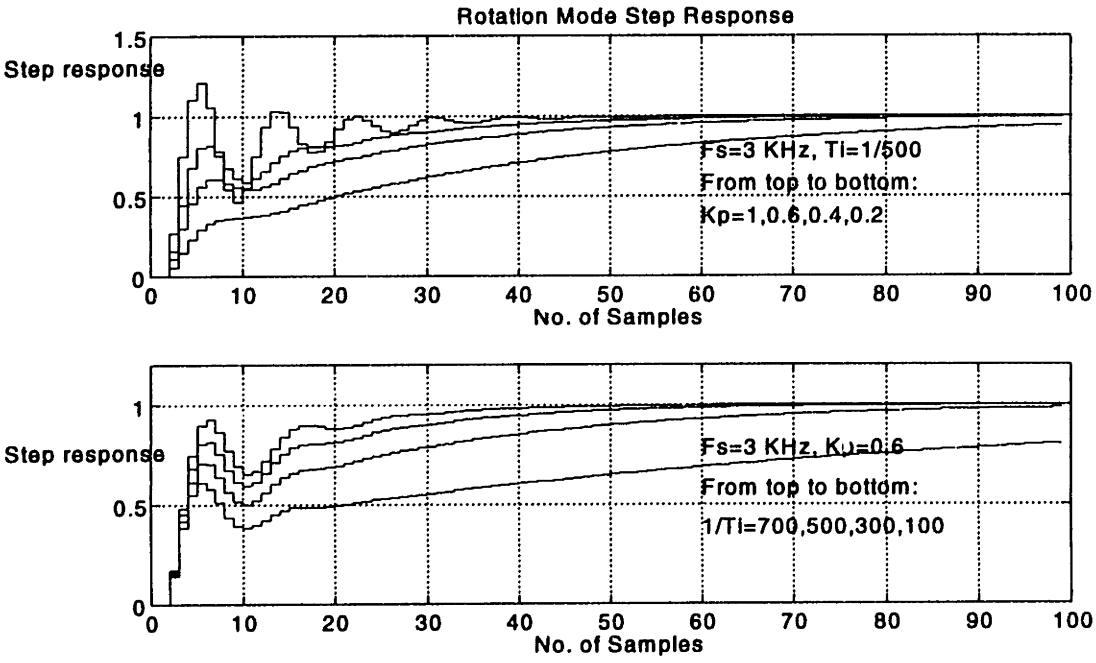

Figure 8.9f Rotational step response after PI and lead compensation

8.5 Decoupling Digital Design of Three-Degree of Freedom System

The design principle of three degrees of freedom using six actuators is basically the same with the single degree of freedom design. However, a simple coordinate transformation between the output of probe #1, #2 , the real displacement of Y-axis and $_z$ should be established since the system outputs are voltage of probes, not displacements. Furthermore, the electromagnets can only exert attraction force. Basically, a pair of actuators is necessary per degree of freedom. A force distributor must be built into the control code for distributing the control effort to six actuators.

Under the assumption of small rotations and with reference to Figure 8.10, the relationship between the probe readings and the stage position output is given by the following linear transformations.

$$X = K_0 V_0$$
$$Y = \frac{(K_1 V_1 + K_2 V_2)}{2} \qquad (8.8)$$
$$\theta_z = \frac{(K_1 V_1 - K_2 V_2)}{2R}$$

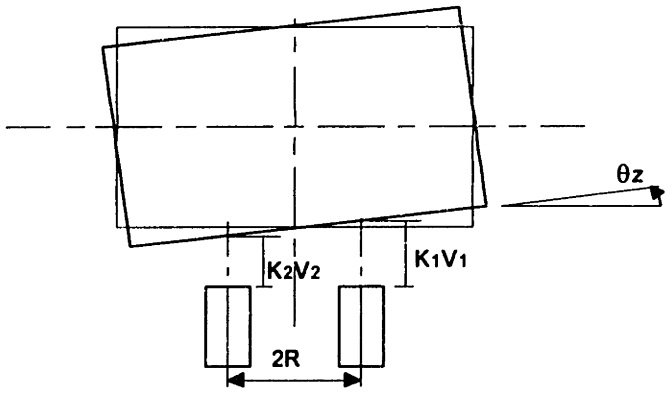

Figure 8.10 The schematic plot of stage rotation

where K_0, K_1, K_2 are the position gain of the sensors which are gotten from the sensor calibration work described on Chapter 7. R is the separation between the two lateral probes. A brief SIMULINK system block diagram of multi-degrees of freedom design is shown in Figure 8.15. The details of this block diagram can be seen is in Appendix II.

The controller design is based on the second order modelling. There are some unmodeled dynamics and some error sources. These effects are discussed in Chapter 10.

The SIMULINK simulation block diagrams are shown in Appendix II. A number of simulations on stage control have been made before running the stage. Figure 8.11 shows the step response. Figure 8.12 shows the sinusoidal responses of the single degree of freedom system based on the same controller parameters respectively.

Apply the same control parameters on the decoupling multi-degrees of freedom design. We expect that the X-axis control should be unchanged and, the Y-axis output should be the same characteristic with that of the X-axis since there is no difference in their plant dynamics. Figure 8.13 is the simulation result in which the Y command is a step and θ command is zero. Figure 8.14 is the result in which θ command is a step while Y command is zero. It shows a small oscillation in steady state whatever the control gain is.

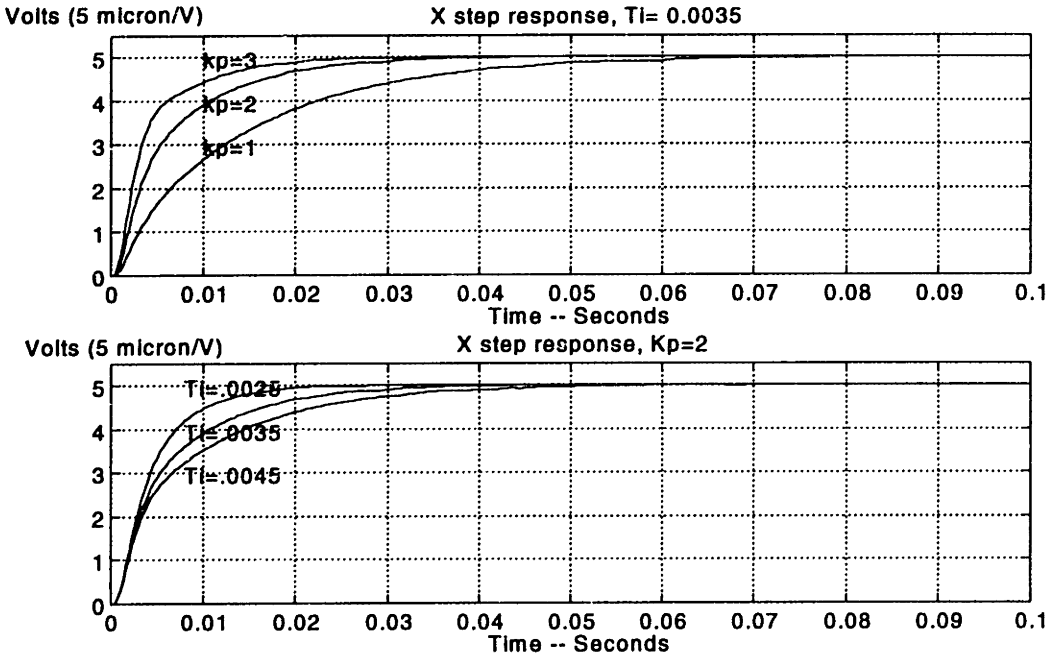

Figure 8.11 Single degree of freedom simulation result (Step response)

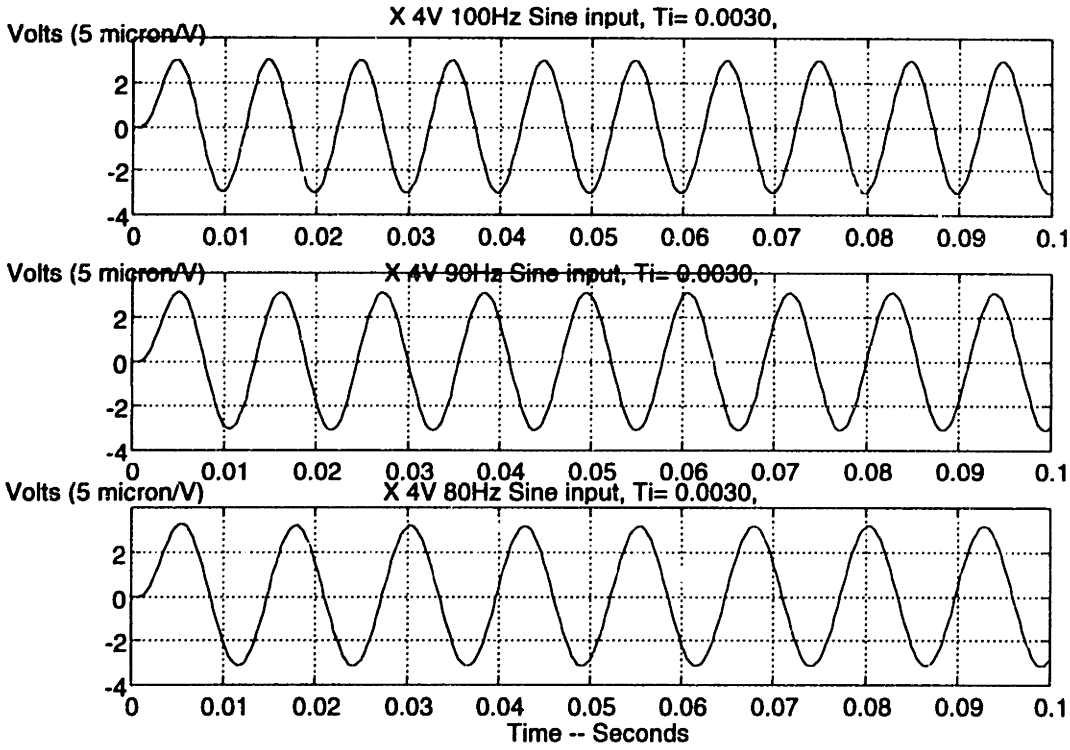

Figure 8.12 Single degree of freedom simulation result (Sinusoidal response)

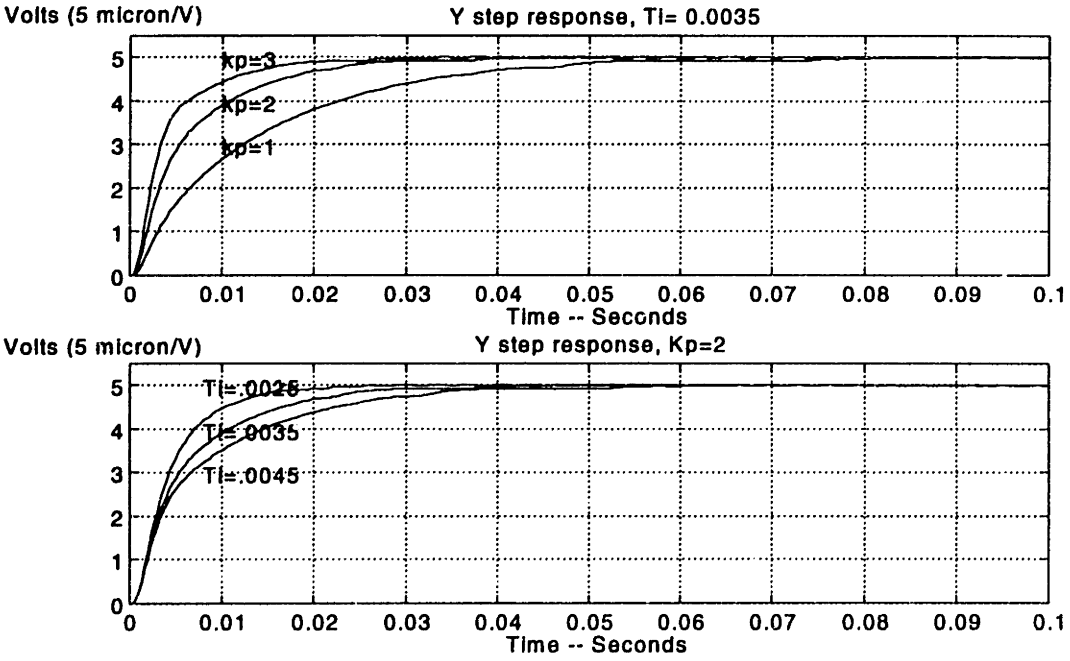

Figure 8.13 Multi degrees of freedom simulation result (Y step response, $\theta_c \equiv 0$)

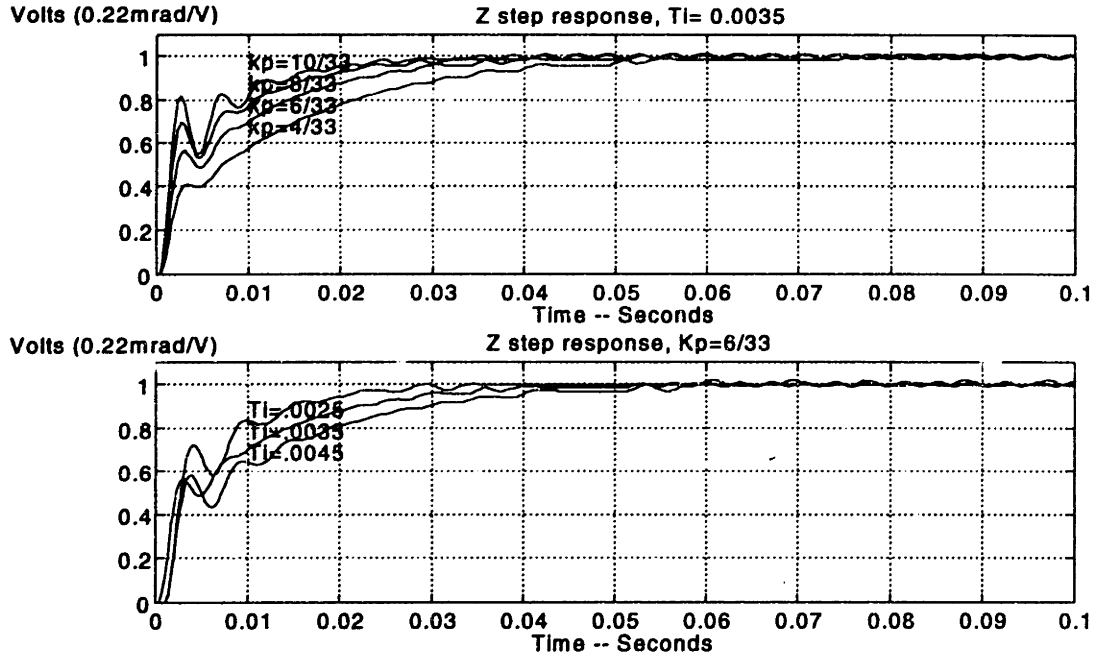

Figure 8.14 Multi degrees of freedom simulation result (θ step response, $Y_c \equiv 0$)

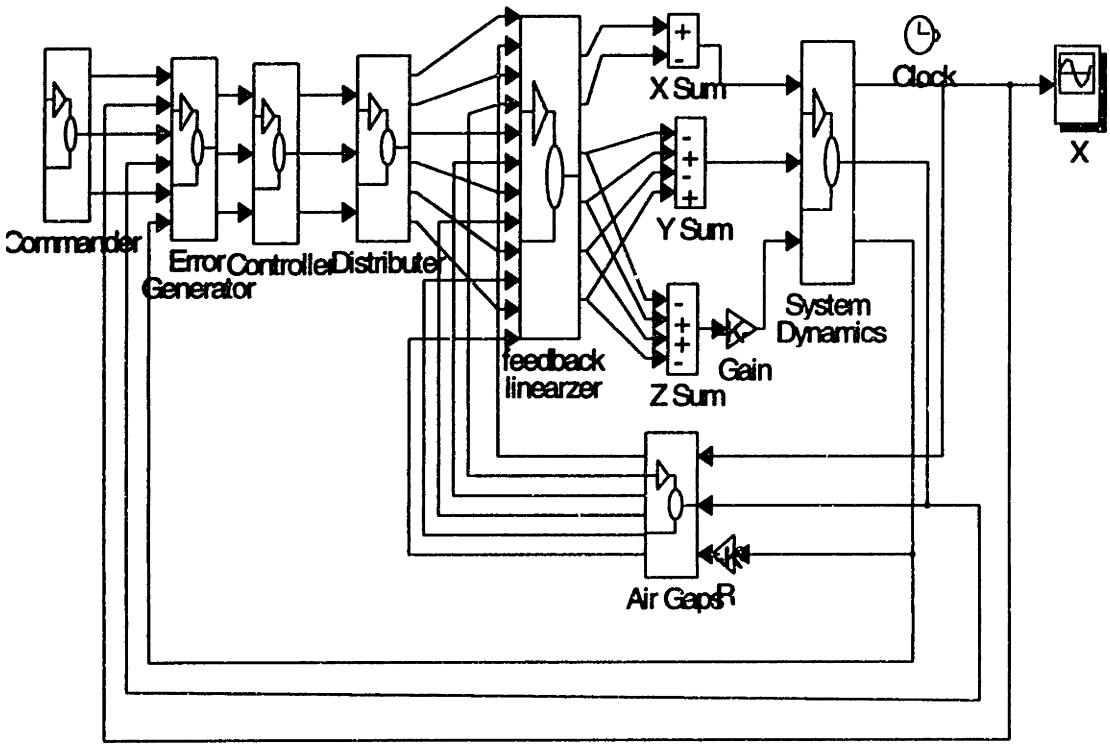

Figure 8.15 The overview of SIMULINK simulation in multi-control of stage

CHAPTER 9

SYSTEM INTEGRATION

The previous sections have considered the design of the mechanical, electrical, and control systems. In this chapter we discuss the integration of these sub-systems. A schematic system plot is shown in Figure 9.1.

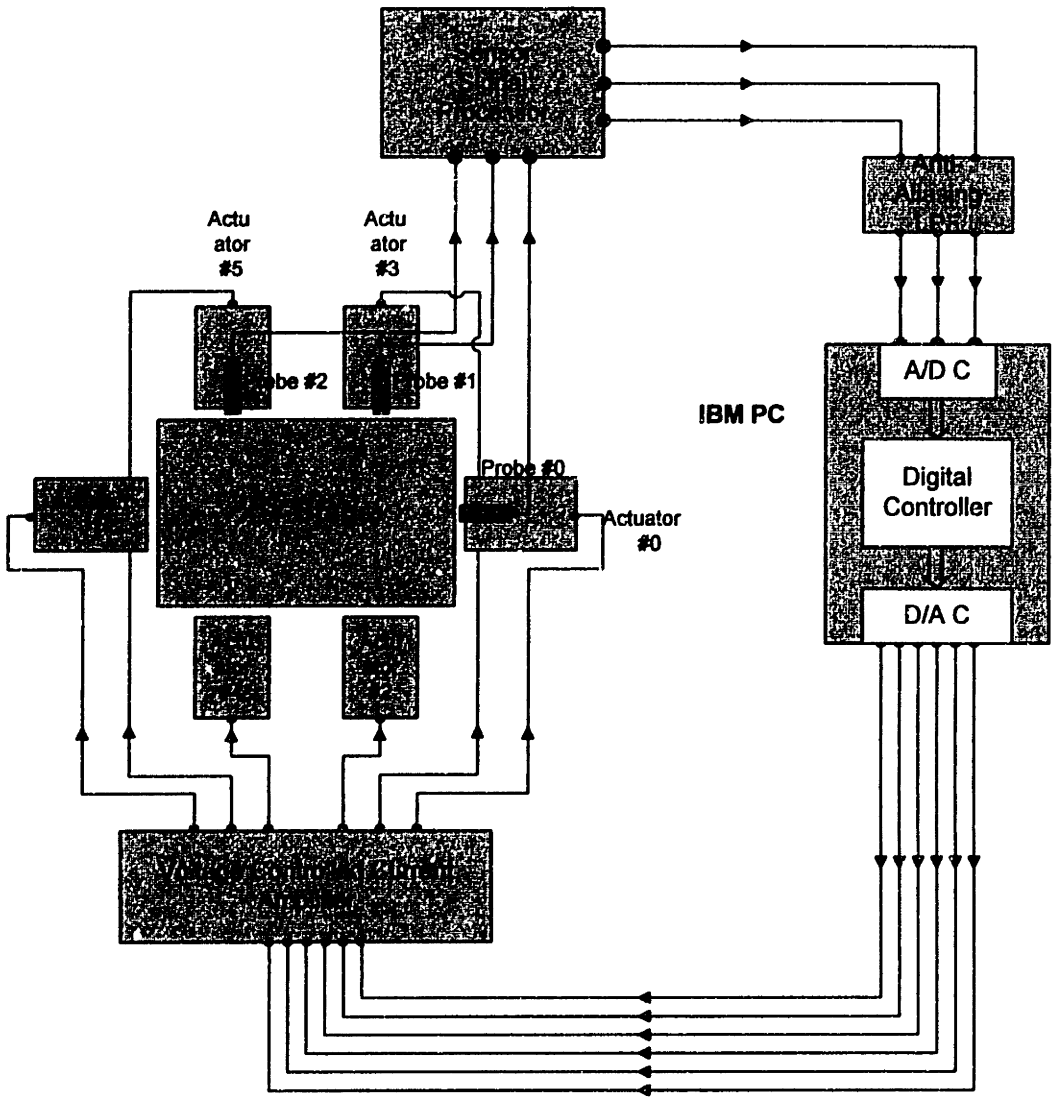

Figure 9.1 The Overview of the whole System

Figure 9.2 shows a photo of the stage. Figure 9.3 shows a photo of the stage with actuators and sensors. Figure 9.4 shows the sample holder. Figure 9.5 shows the whole system of stage, sensors, actuators, and the sample holder. Figure 9.6 shows the host computer. Figure 9.7 shows the electronics cabinet which contains power amplifiers and position sensor electronics. Figure 9.8 shows the laser calibration work. Figure 9.9 shows the integration of stage with a TALYSURF surface profiler head for surface measurment which will be discussed in Chapter 12.

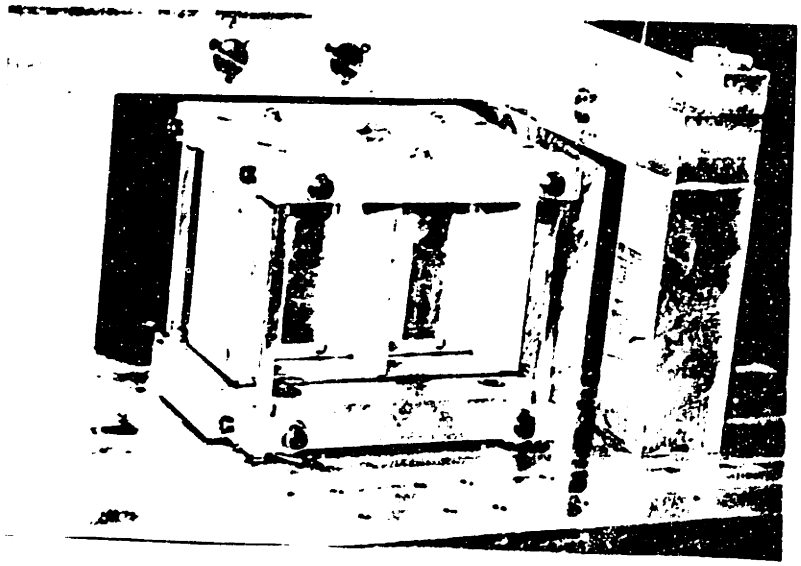

Figure 9.2 The photo of stage

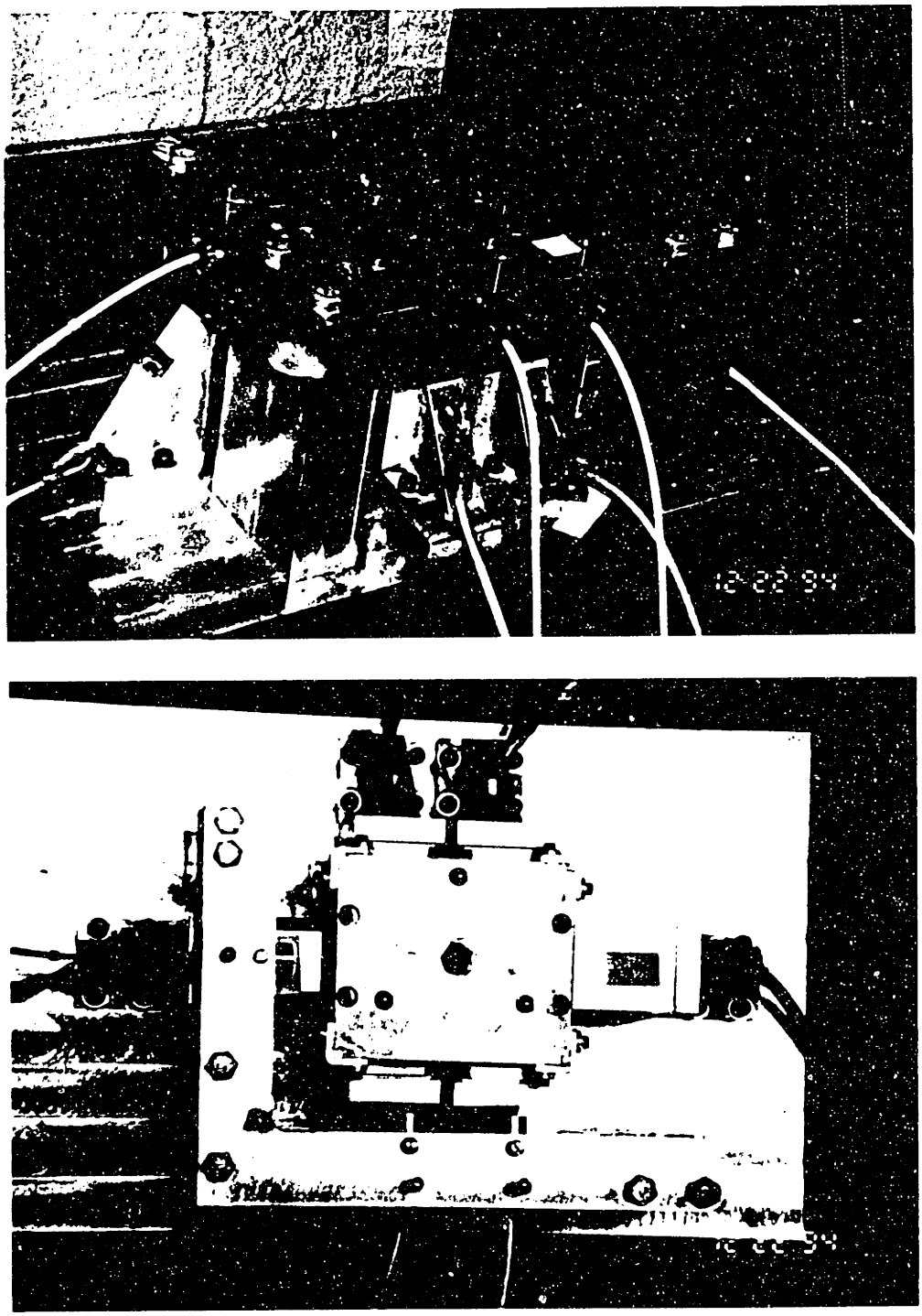

Figure 9.3 The photos of stage, sensors, and actuators subsystem

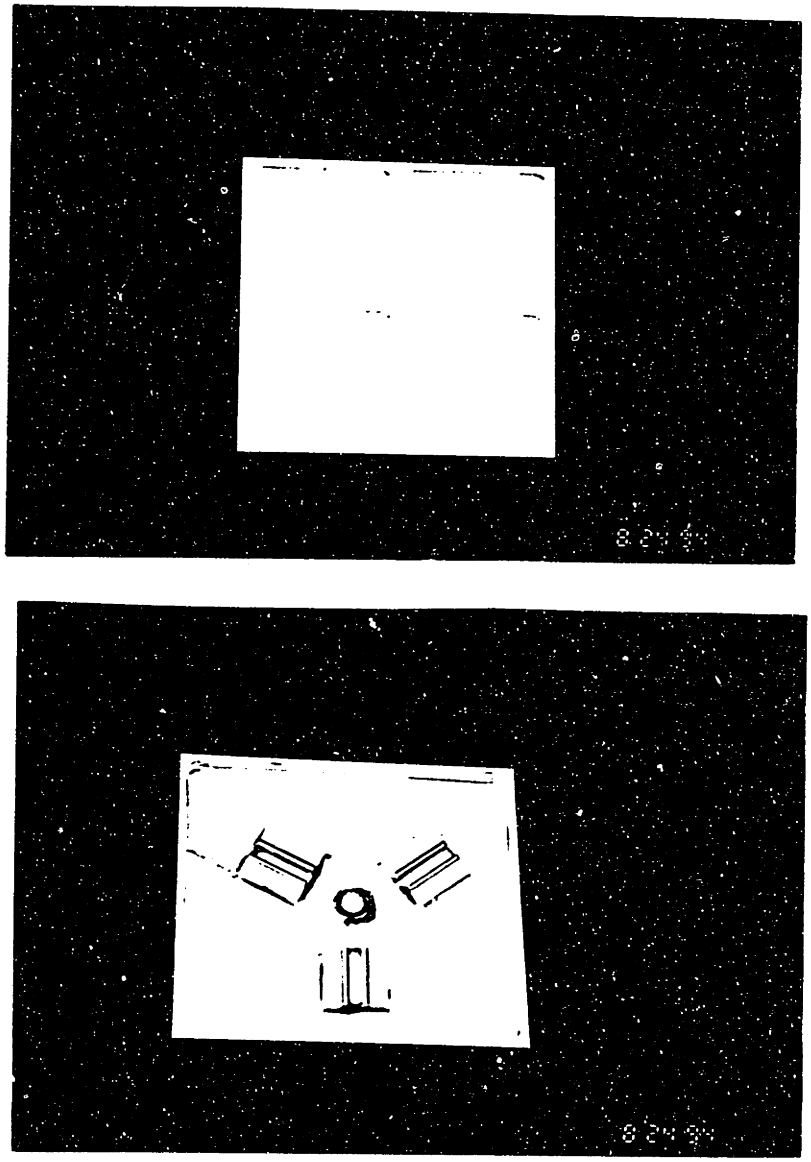

Figure 9.4 The photos of the sample holder

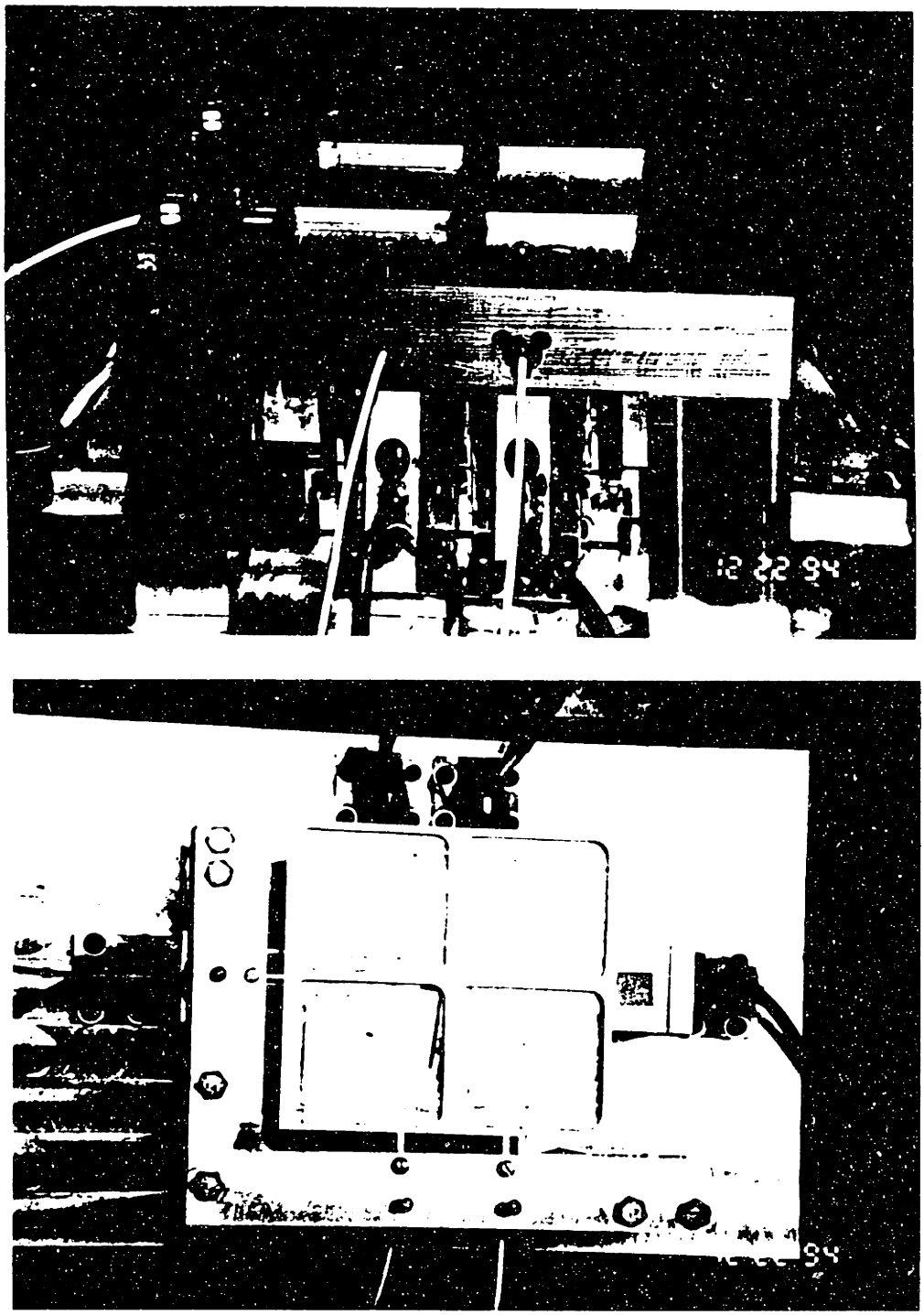

Figure 9.5 The photos of the stage, sample holder, sensors, and actuators subsystem

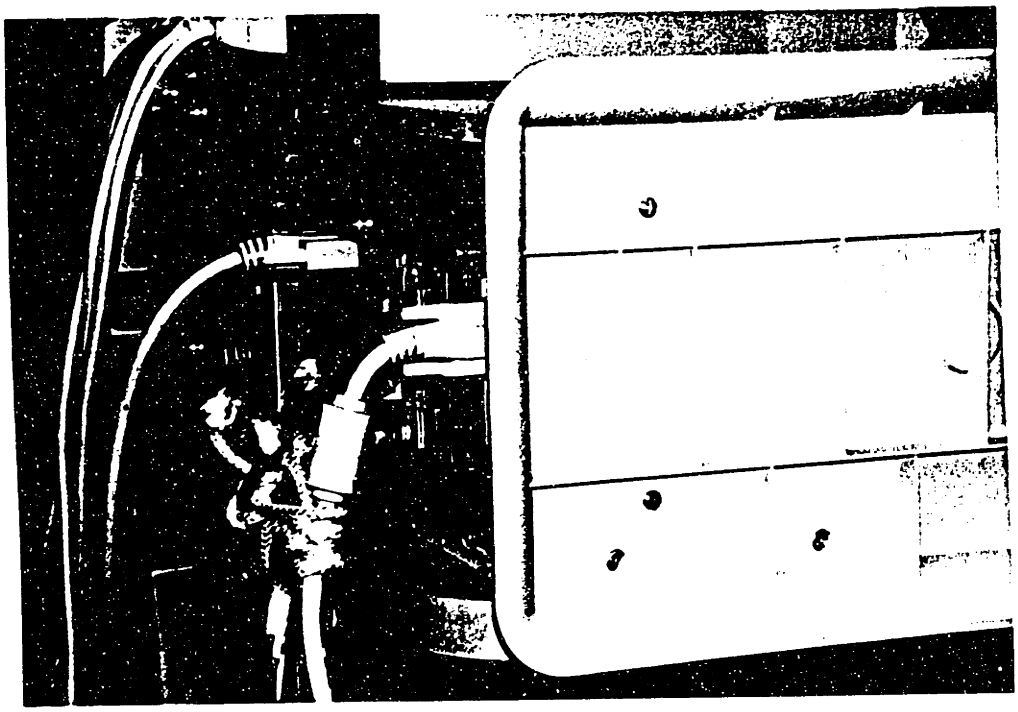

Figure 9.6 The host computer

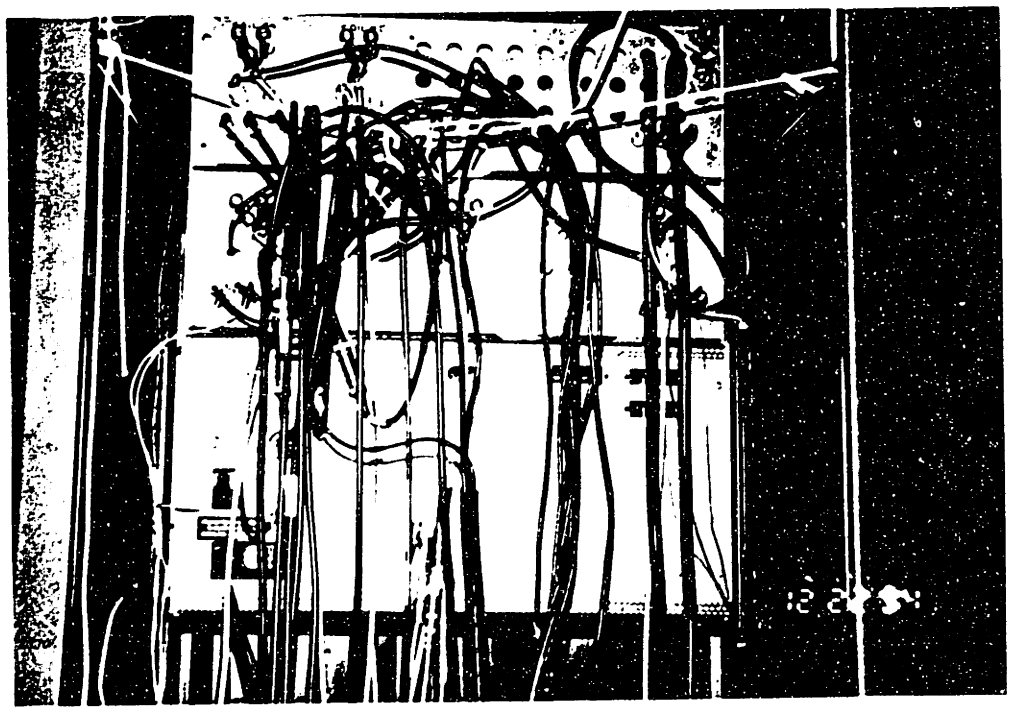

Figure 9.7 The electronic cabinet

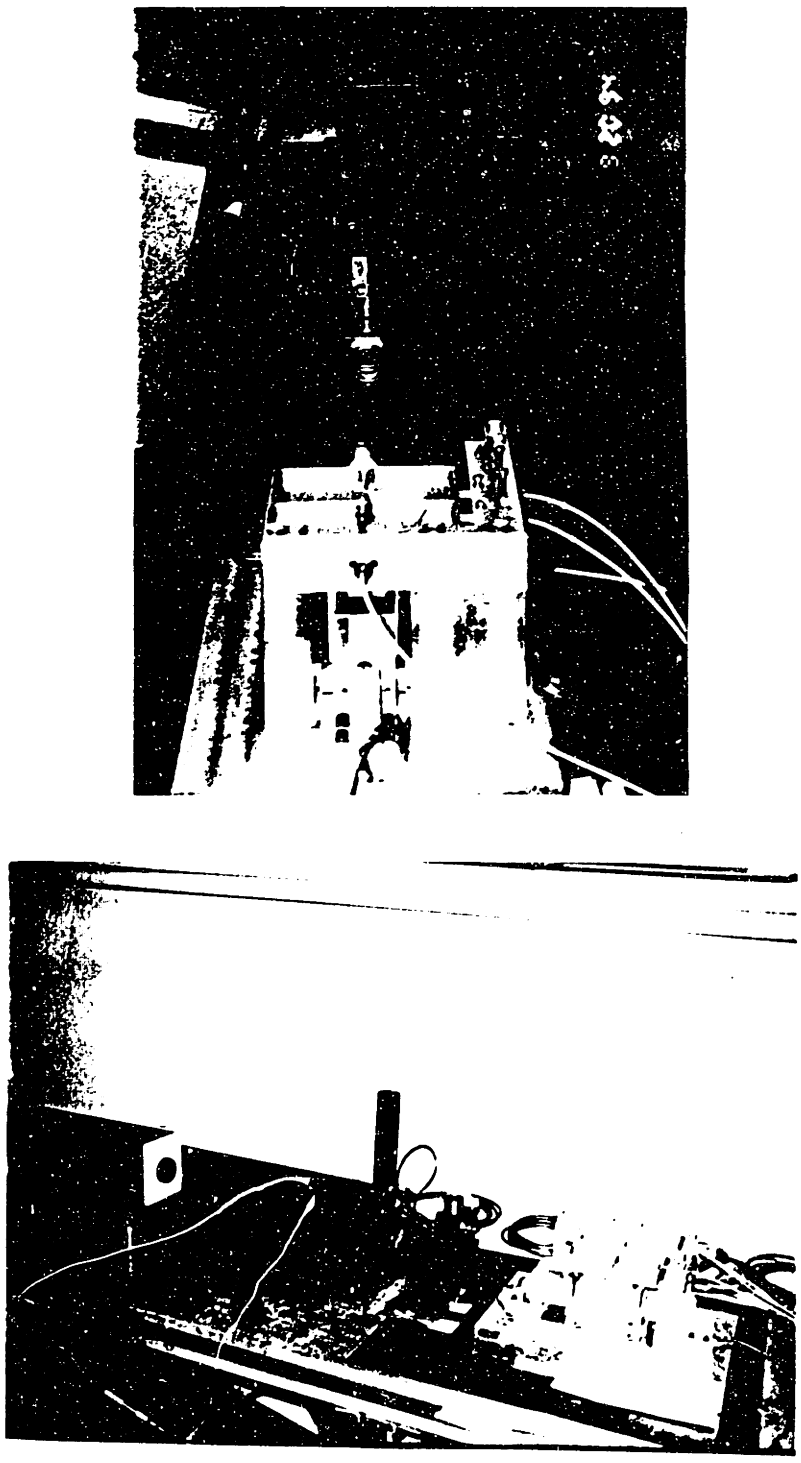

Figure 9.8 The stage under laser calibration

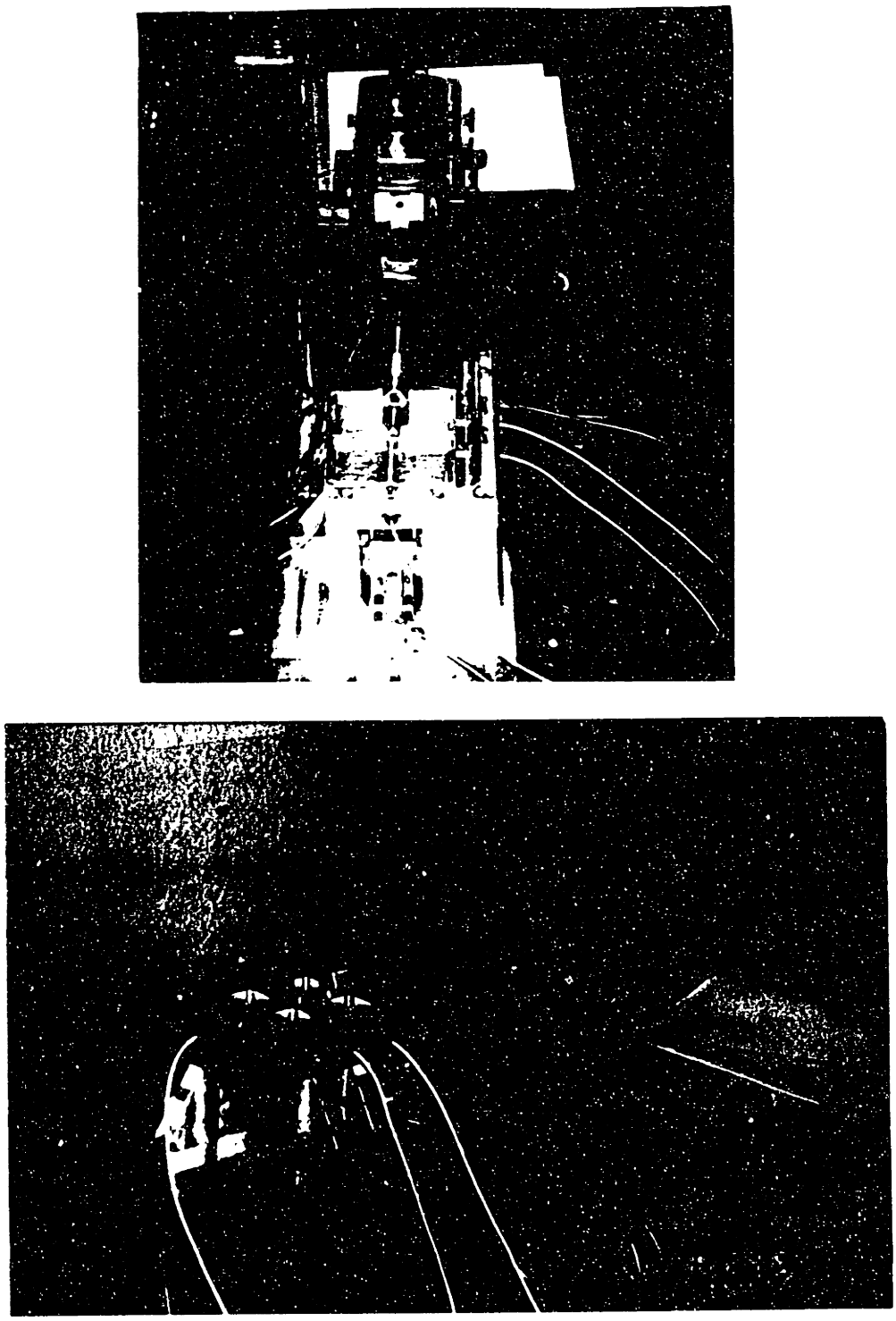

Figure 9.9 The surface roughness measurement machine

CHAPTER 10

ERROR MOTION ANALYSIS

This chapter mentions possible error sources of the implementation, and discusses their influence on the stage response. We also present computer simulations and experimental data to examine the significance of these influences.

10.1 Overview of System Error Sources

Up to this point, all modeling and designs have been based on the ideal case, i.e., we assume that the system parameters are exact, the probes are perfectly aligned, the rectelinearity and surface flatness of the sample holder are perfect, the assembly of the stage has no defect, the gaps between the actuators are all equal to the nominal value, and the electromagnetic force constant C does not vary.

System parameters are not hard to find by theoretical formulation and through experiment. The noise level is also easy to find. However, the assumption of perfect manufacturing and assembling will be a challenge. It may cause some undesirable results. [ASM90], [ASM92] are two standards for evaluating the performance of precision machines. They list possible errors in a machine system. The following are some error sources due to manufacturing and assembling process.

1. The effect of tilt on capacitive sensor alignment. (Sec. 10.2)
2. The influences of the electromagnets force constant modeling error. (Sec. 10.3)
3. The effect of the assembling error in actuators. (Sec. 10.4)
4. Thermal error (Sec. 10.5)
5. Manufacturing error. (Sec. 10.6)

These will be discussed in detail in the following sections. The final goal of error analysis is to find out the possible error sources and their influence, then correct them by hardware or software. A lot of software correction papers can be found in [Sof93].

10.2 Capacitive Sensor Alignment Error

The capacitive sensor alignment error is analyzed by Harb et al [HCS91]. Referring to Figure 10.1, the circular flat plate capacitor, the lower, or target, electrode is modeled as an infinite horizontal plane. The upper, or probe, electrode is separated from it by a distance d_0 at its center and inclined at an angle θ. Assume that the gap has a homogeneous permittivity ε, and the fringing fields can be ignored, the capacitance, C, is obtained by integrating over elemental parallel plates of width dx and separation y to give

$$C = \frac{2\pi r^2 \cos\theta}{d_0}\left[\frac{1-(1-k^2)^{1/2}}{k^2}\right] \text{ where } k = \frac{r\sin(2\theta)}{2d_0}. \qquad (10.1)$$

Figure 10.2 shows various electrode gaps d_0 using a round capacitor of 20 mm diameter. One way to eliminate the tilt effect is by performing on-line calibration of the sensors. As mentioned in chapter 6, this work can be done by introducing a laser module to get the sensor gain. Since the tilt effect changes the capacitance, it changes the gain of sensors. However, the result of on line calibration is to find the sensor gain under such alignment regardless the tilt situation.

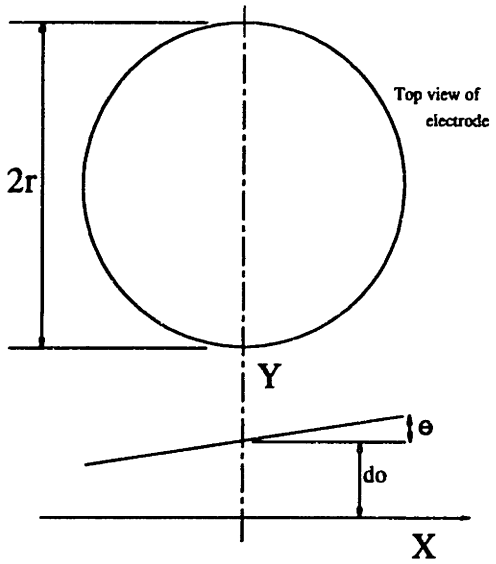

Figure 10.1 Model for parallel plate capacitor

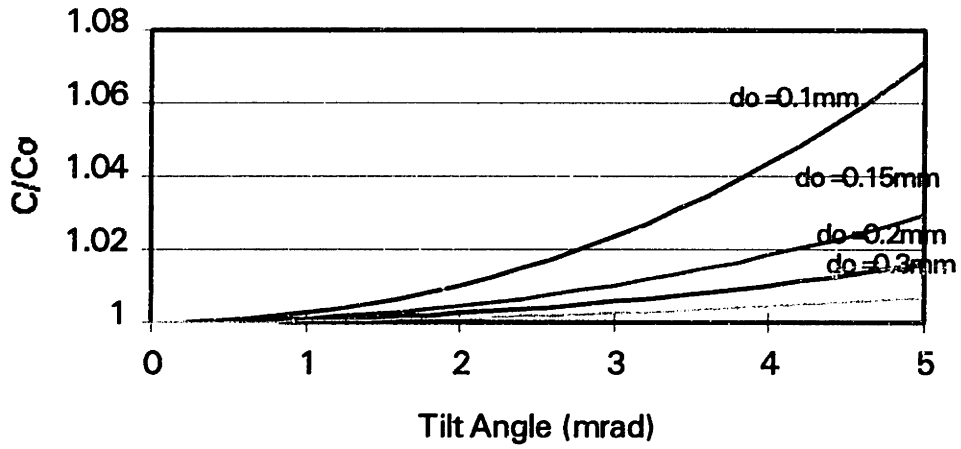

Figure 10.2 Normalized ratio of capacitance values as a function of tilt for a round electrode of 20 mm in diameter separated from the ground plate by different gaps d_0.

10.3 Electromagnets Force Constant Modeling Error

There are several kind errors under this article. In this section, two most significant sources will be discussed.

The effect of the calibration error

As discussed on Chapter 8, the design of feedback linearization depends on the correctness of electromagnet calibration. A perfect modeling, neglecting the time delay of position feedback, can linearize the nonlinear actuators. However, as shown in Chapter 5, the electromagnetic force constant C in $f = Ci^2 / x^2$ is a function of gap, current, force, and its value are far below the theoretical calculation due to the leakage flux. In application, one decides a nominal air gap first, then, finds the nominal C in this gap. However, it may have some deviations when the gap and current change. We would like to find the effect of inexact compensation of feedback linearization.

The feedback linearization law is

$$i = x\sqrt{\frac{f_{desire}}{C_c}} \quad \text{or} \qquad f = \frac{C}{C_c} f_{desire}. \tag{10.2}$$

Where C_c is the force constant we used in feedback linearization and C is the actual value of force constant. If C_c =C, then, the compensation will be exact. A difference between C_c and C will caused a difference between f and f_{desire}., and thus a change in proportional gain K_p.

A SIMULINK simulation for this effect has been done and the result is shown in Figure 9.3. In this simulation, assume the exact electromagnetic force constant C = $4.1 \times 10^{-6}\ Nm^2 Amp^{-2}$ and we use C_c from 2×10^{-6} to 6×10^{-6} and see the effect on step response. We see the smaller the C_c, the faster the step response, and eventually, may drive system to unstable.

The effect of unequal EM constant in actuator pair

The stage moves back and forth by an actuator pair since the actuators can only exert attraction. Unequal force constant in actuator pair causes unequal proportional gain on both sides. The sinusoid output has a suddenly change in the equilibrium position (i.e., x=0) since the proportional gain is changed. We expect the amplitude will be different between the positive side and negative side at high frequency, since the higher the K_p, the higher the bandwidth will be. Once K_p is different, the bandwidth will be different. However, the difference of force constant in the same type actuator will not be

significant. This effect can be neglected compared with the effect of unequal gap error which will be discussed in section 10.4.

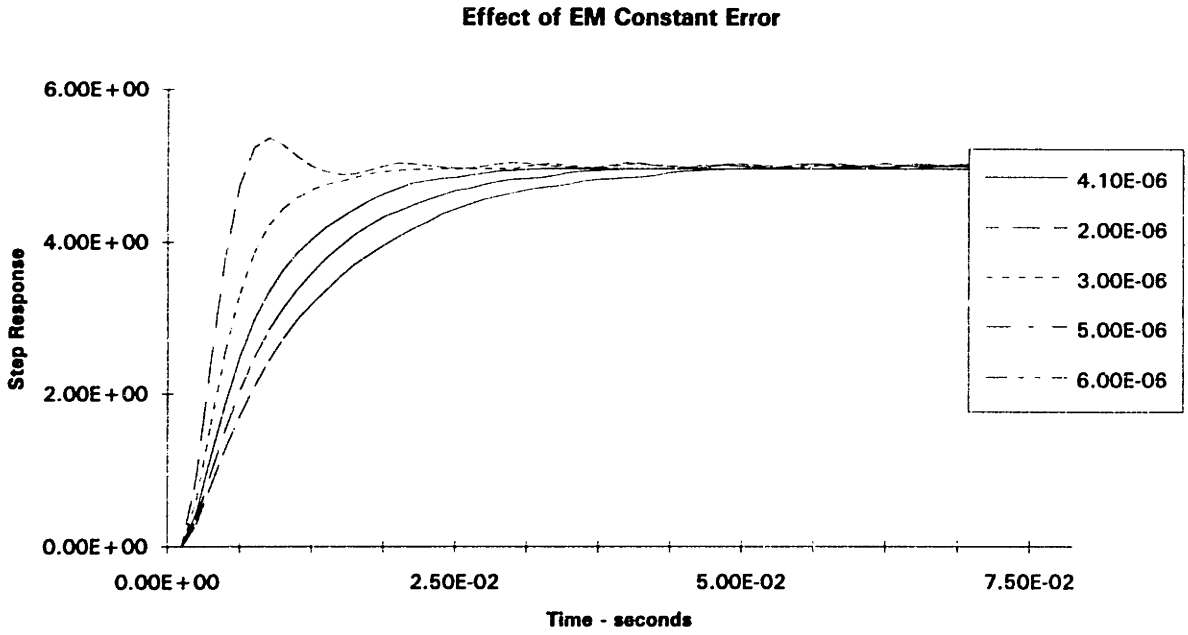

Figure 10.3 The effect of EM constant error in feedback linearization

10.4 Assembling Error

The effect of gap setting error

Assume the electromagnet force constant is perfect by modeled in the feedback linearization process. In this time, just consider the gap setting error between real value x and the value we used in feedback linearization x_f. For performing feedback linearization to linearize the system, one need the correct information on the air gap. The air gap will be a desired nominal air gap g_0 minus the displacement x_m as measured by the capacitive sensor. That is

$$x_f = g_0 - x_m. \tag{10.3a}$$

However, assume we failed to set the g_0 to the desired value, that is

$$x = g_* - x_m \tag{10.3b}$$

where g_* is the actual nominal air gap.

The feedback rule tell us that

$$i = x_f \sqrt{\frac{f_{dsire}}{C}} \quad \text{and} \quad f = \frac{x_f^{\,2}}{x^2} f_{desire}. \qquad (10.4)$$

If x and x_f are equal, f will equal f_{desire}. However, there may exist some difference between these two values. Then, again, their ratio will cause a change in proportional gain and add nonlinearity into systems. Consider Figure 10.4. It's the simulation result by SIMULINK. In this case, the desired air gap g_0 is 300μm. However, due to the assembly error, the real air gap may not equal to the desired one. Here, we run the real gap g_* from 200μm to 400μm and see the step response. As our prediction, in both extreme, the system either tends to strong oscillation or very slow response.

The effect of unequal gap setting in actuator pair

This effect is similar to the case of section 10.3. The net effect is a difference in proportional gain between actuator pair. Unlike the effect of unequal force constant in actuator pair, which is small, it is difficult to get the same nominal air gap between actuator pairs under such small scales (~ 300 μm). Figure 10.5 is a SIMULINK simulation result and same thing happened in doing experiments. The nominal air gap g_* of left actuator which commands the motion when input is negative, is 200 μm. The right actuator, doing the remaining work, has a gap of g_0 = 300 μm. The command input is a 5 Hz sinusoid wave. From Figure 10.5a,b, a phase shift happens between input and output signal. A sudden change also occurs when the stage is at neutral position. And a small oscillation happens when stage moves to the region which close to the left actuator. The unequaled gaps cause unequal control gain and even cause the system to be stable on one side and unstable on the other side if the difference is too large. The input versus output plot (Figure 10.5b) shows a distorted ellipse. If the gaps are equal, the elipse will be without distortion. The higher the difference in gap between actuator pair, the higher the distortion will be.

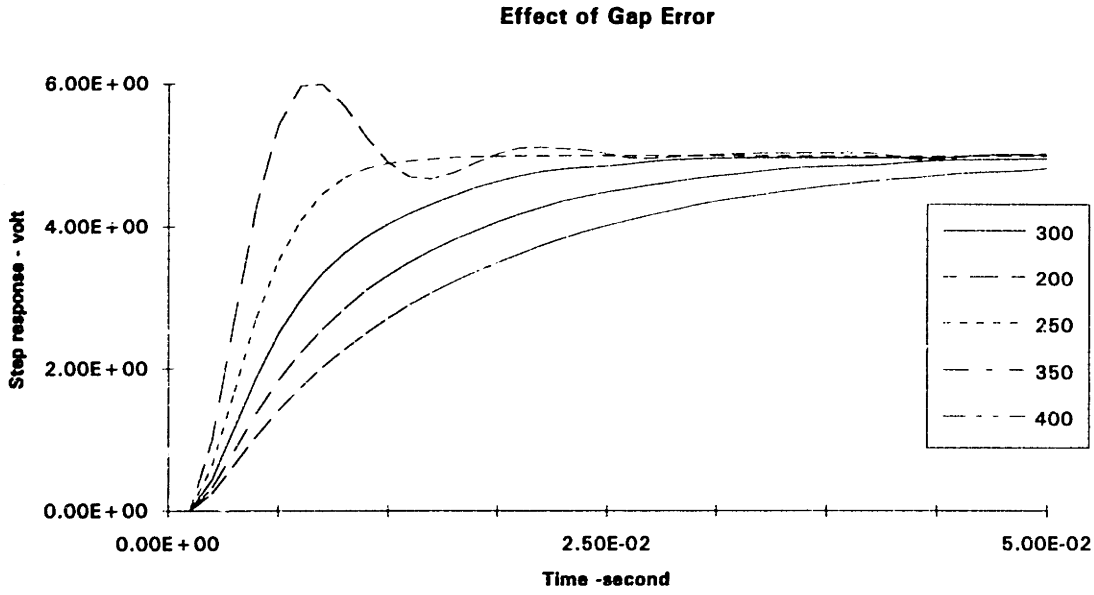

Figure 10.4 The effect of gap setting error in step response

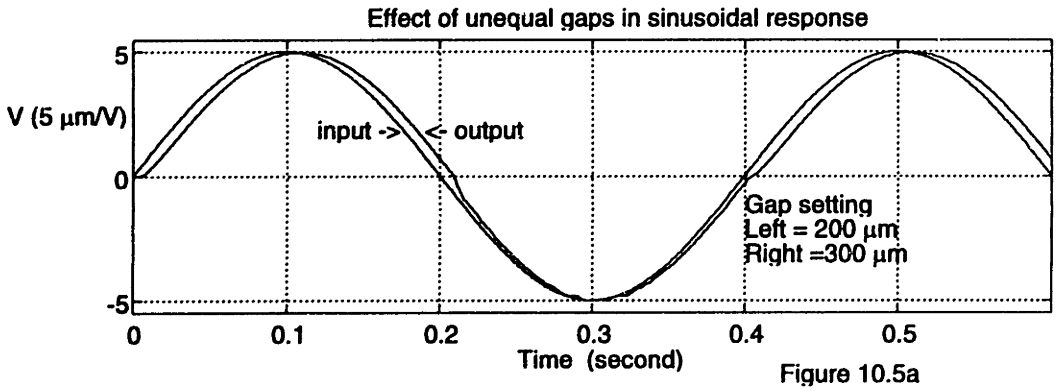

Figure 10.5a

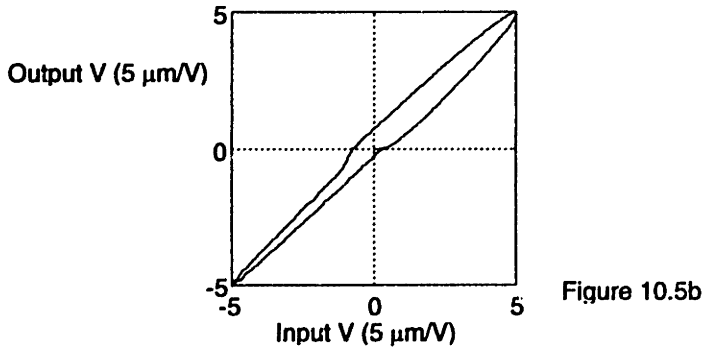

Figure 10.5b

Figure 10.5 The effect of unequal gap setting in actuator pair

10.5 Thermal Error

Thermal errors limit the system accuracy. One can find a detail discussion in the relationship between temperature and dimensional measurement in [ASM73]. In our design, the thermal error source comes from the power input of actuators. Power amplifiers drive a current into actuators. Those coils have certain resistance value. The input power can be calculated by the product of average of the input current squared and the coil resistance. This power, in steady state, will be the heat transfer of actuator to air. Therefore

$$P = I^2 R. \tag{10.5}$$

and

$$\dot{Q} = UA(T - T_\infty). \tag{10.6}$$

Where $\dot{Q}$ is the heat transfer rate. A is the surface area of actuator. T is the temperature of actuator, T_∞ is the ambient air temperature, and U is the overall heat transfer coefficient.

$$\frac{1}{U} = \frac{1}{h} + \frac{l}{k}. \tag{10.7}$$

Where h is the heat transfer coefficient in convective heat transfer, k is the thermal conductivity of actuator in conduction heat transfer, and l is the characteristic length of conductive heat transfer.

In this design, l is 0.005m, surface area A is 0.013 m^2. From heat transfer book [Cha85], the thermal conductivity of aluminum can be found as 204 W/mK. Regarding h, it is more complicated, the order of h under such a natural convection environment is about 5 W/m^2K [Cha85]. Therefore, U is dominated by h and roughly equals h. From experiment, the coil resistance is 1.1 Ω and the average input current is 0.3 Amp. Setting Eq.(10.6) and Eq.(10.7) equal in steady state, the temperature rise can be found as

$$T - T_\infty = 1.2° \text{ C}. \tag{10.8}$$

This temperature rise causes thermal expansion of actuators In the general situation, this expansion will be not uniform. It tends to distort the actuator and sample holder and degrades the degree of parallelism between actuator and target face and more seriously, the parallelism between sensor and sample holder. It is difficult to do an exact analysis of this situation. However, from Eq.(10.8), the temperature rising of actuator is small and it's reasonable to assume the ambient temperature is unchanged during operation. Therefore, the distortion of sample holder can be neglected. Now, just consider the thermal expansion of actuators. This expansion will reduce the air gap between pole and target face. By the thermal expansion equation

$$\frac{\Delta V}{V} = (\frac{\Delta L}{L})^3 = \alpha(T - T_\infty). \qquad (10.9)$$

Where V is the volume of actuator, α is the volume thermal expansion coefficient of aluminum, which is 23μm/m°C. Therefore, combine (10.8) and (10.9). The change in air gap will be the order of 1 μm. Comparing this amount and the normal operation gap 300 μm, it is small and within the tolerance of air gap setting error.

10.6 Manufacturing Error

In the previous discussion, we always assume that the stage is dimensionally perfect. However, there are a number of issues we need to consider when we do the error analysis. These include the tiny difference in dimension of the four steel bars, the accuracy of centering, the degree of squareness and parallelism of sample holder, and the perpendicularity of three holes in L-shape support which are used for mounting probes. The combination of these factors will cause the coupling of the three degree of freedom.

Assume the force exerted in X-axis is F and the eccentricity is δ. Due to the manufacturing error, this F will not act on the X-axis perfectly. It can be decomposed to F_x and F_y, which act on X and Y direction respectively. The F_y will cause the stage move in Y direction. Then the moment will be $M = F_x\delta - F_y g$. Here g is the distance of actuator to center of the stage. This moment will cause the stage to rotate in X-Y plane and cause on unequal reading of two lateral probes.

Figure 10.6 shows the location of each lateral sensor and the model of system coupling. It is not easy to find δ and g accurately then to get a precise model. Instead of finding these parameter, we like to find the significance of these coupling and eliminate it by feedback control. An experiment is set up for finding the coupling between major translation modes. The experiment setup is shown in Figure 7.8. The actuator is commanded to exert force and move the stage. Collecting the reading of laser card & three capacitive probes simultaneously then send to analysis. If the stage were perfect, the reading of two lateral probes should have no change. However, we find that the gap changes with a very slow rate. This means that the X-axis actuator also causes Y direction motion, and due to force that does not act on the center of mass, a small torque is generated. This moment rotates the stage. It can be found from the unequal amount of reading change of two lateral probes. Figure 10.7 shows the measurement result.

As shown in Figure 10.7, the result is not changed smoothly. However, for a range of 100 μm, there are roughly 0.03V change in probe #1 readout, equivalent to 0.15 μm change in position and 0.2V, or 1μm change in probe #2 readout. For simplicity in analysis, this error can be treated as two parts.

The probe #1 output is modeled as induced Y-direction motion. In this design, the maximum amount of induced Y-motion , 0.15 μm, will be easy to compensated by the 4 Y-direction actuators. The probe #2 output is modeled as the sum of induced Y and θ direction motion. The maximum error by induced θ motion will be around 0.9 μm. It's equal to 0.04 milliradian. Since the maximum angular motion in this design is ±2.2 milliradian, therefore, the stage can compensate this angular motion error under properly closed loop control. To compensate the induced motion error mutually is an advantage of this design.

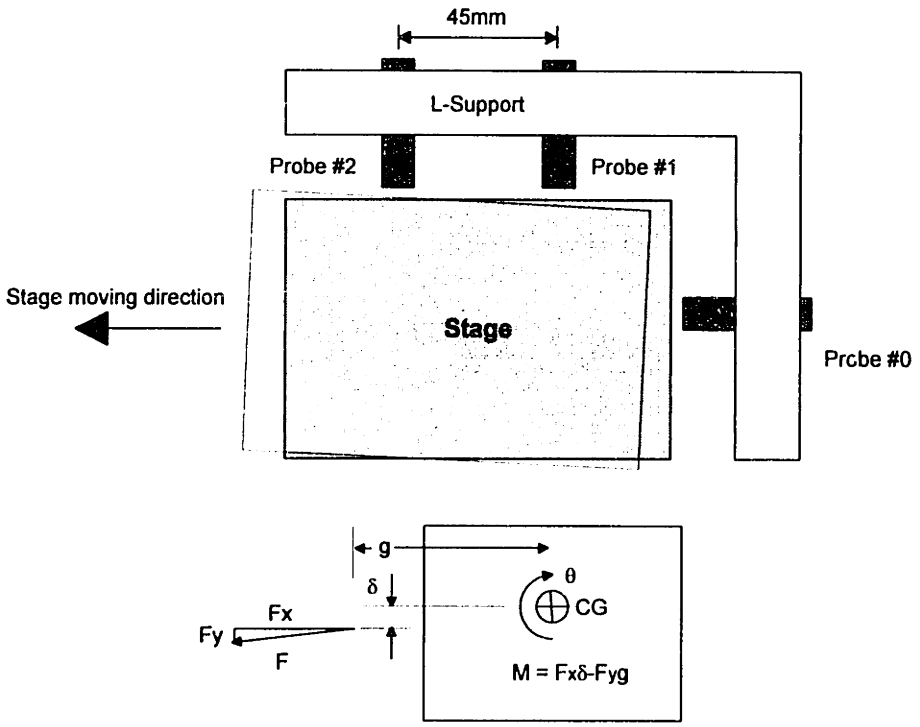

Figure 10.6 Experiment setup for finding manufacturing error and the modeling of system coupling

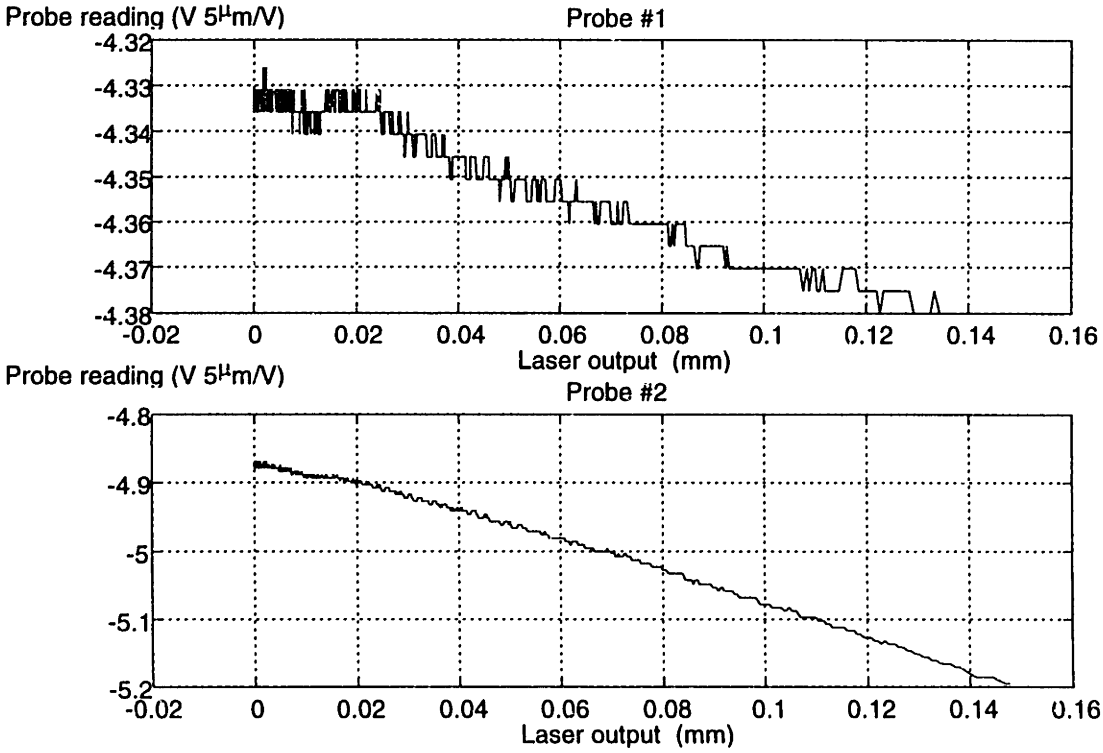

Figure 10.7 The Experiment result on stage coupling

CHAPTER 11

CONTROL RESULT

We examine the stage performance in this chapter under several kinds of command inputs. We also discuss some reasons which cause inconsistency between simulation and the experimental result in this chapter.

11.1 Practical Control Issues

Based on the control system analysis from chapter 8, the controller has been implemented on a Pentium 5/90 MHz computer. The maximum sampling rate is 3 KHz, or the sampling period is 0.33ms equivalently. The control program is written in Microsoft C. The core of the program is a discrete-time control algorithm which is implemented by a backward difference approach for performing PI control in translation and PID control in rotation mode. In series with the discrete controller, a discrete-time lead compensator is connected for canceling the dynamics of the anti-alias filters. After the digital controller, a procedure is used to distribute the control efforts to six actuators. These control efforts are processed by another procedure called the *feedback linearizer* for feedback linearization. Finally, the desired comments are outputted from six DAC channels to the actuators. Figure 11.1 shows the block diagram of the real control system. The control results are obtained from experiments using the above control structure. The following several sections are the resulting data of step and sinusoidal response of single or multi-degrees of freedom control. In the following results, if no particular air gap mentioned, the air gap settings are all 250 μm. The scaling factor has been adjusted such that the proportional gain in rotation mode is 3% or 1/33 of proportional gain of translation mode. For the following results, except for θ step

responses, all K_ps are based on translation mode. For finding the proportional gain of rotation mode, one just needs to include the scaling factor.

For simplicity, the system output will be taken as signal voltage. The conversion factors are 1V equals to 5 μm in translation mode and 0.22 milliradius in rotation mode.

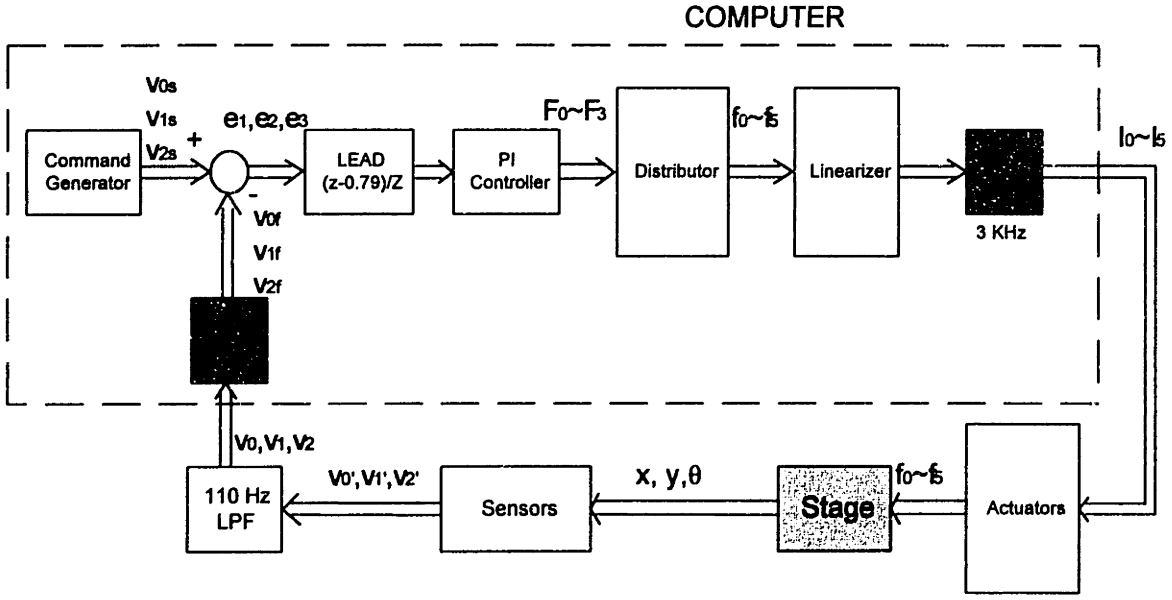

Figure 11.1 The block diagram of stage control algorithm

11.2 Step Response

Step response of X degree of freedom

Figure 11.2 shows the 5V step response of the X degree of freedom. It shows that the higher the K_p and T_i, the shorter the rise time and the higher the overshoot. The rising time of the X degree of freedom is about 30 samples or 10 ms for K_p=2.5 and T_i=0.0035. Note that a typical step response (not only in X, but also in Y which are shown later) consists of several periods. From time t =0 to about 10 samples shows a nearly no action response. Starting from t = 10 samples, it shows a faster response. If K_p is higher, it will have a certain degree of overshoot. After passing this period, a slower response appears again and causes a long settling time. The frequency dependent viscosity of Viscasil plays

the major role in this difference between experiment and simulation result. The detailed explanation is in section 11.3.

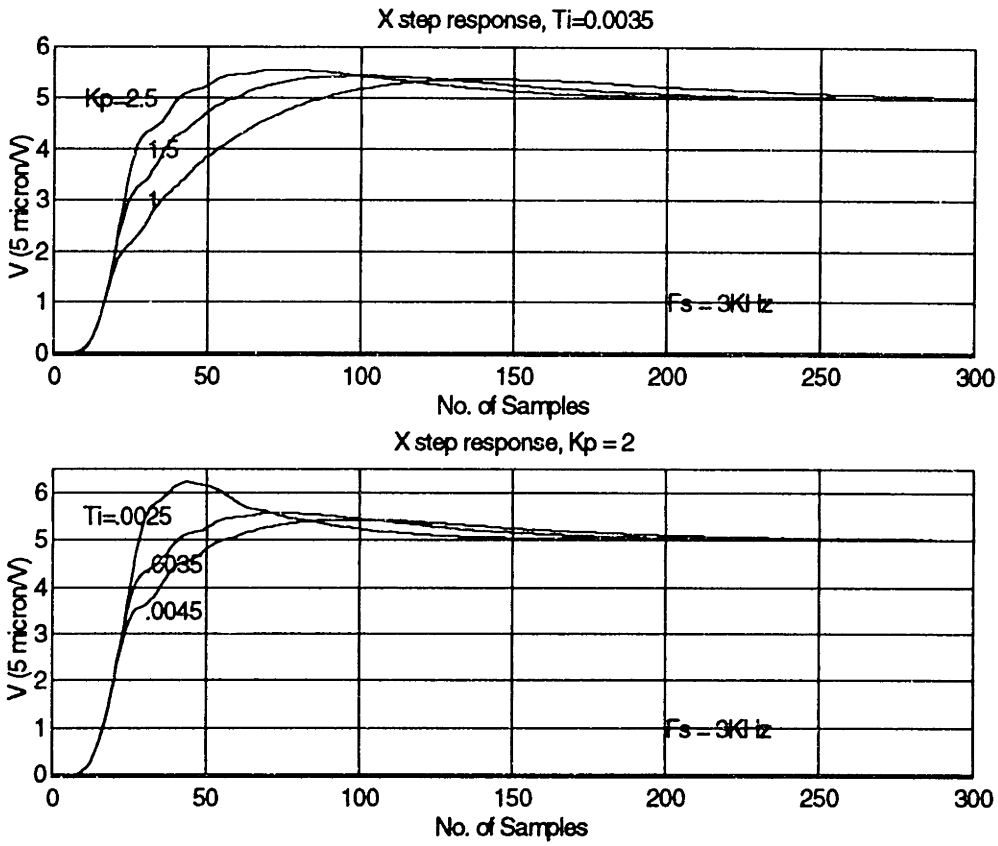

Figure 11.2 +5V X step response (Y and θ are turned off)

Figure 11.3 shows the -5V step response of the X degree of freedom. The rise time is a little bit faster and the overshoot is a little bit higher than the +5V corresponding response. This may be because of the effect of the unequal gap which has been discussed in Chapter 10.

Figure 11.4 shows different amplitudes of the step response under the control gain (K_p=2.5, T_i=0.003). The control effort and the actuators current histories are also shown in Figure 11.4. One can see that when the command is 5V, the control effort is saturated initially. The power amplifier, although its response is much faster than the stage, also shows a considerable period of saturation here. The saturation of controller output and the power amplifier dynamics, combining with the PI law, cause the overshoot in the step

response. One can see the smaller the command amplitude, the smaller the degree of overshoot.

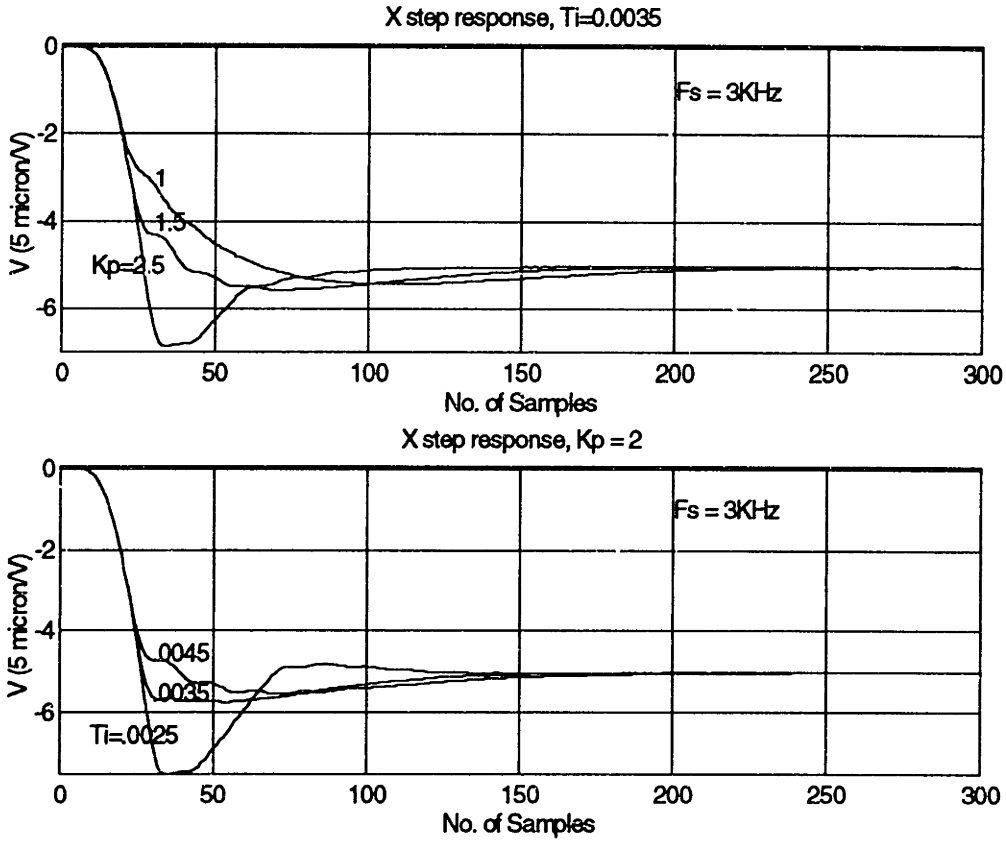

Figure 11.3 -5V X step response (Y and θ are turned off)

Step response of multi-degree of freedom

Since Y and θ are coupled, one cannot get Y or θ responses individually. Figure 11.5 is the response in which Y command is 5V , θ command is 0, and X is turned off. The Y direction response shows a rising time of 40 samples or 13 ms for K_p=2.5 and T_i=0.0035. From θ response, one can see the coupling between these two degrees of freedom. The proportional gain of θ mode is only 3% of Y's K_p. It shows very slow response. Figure 11.6 is the response of -5V input in Y direction and zero input in θ mode based on the same gain sets.

Figure 11.7 is a 1V step of θ mode, in this experiment, the set point of Y is zero and X is turned off.. For appropriate gain, the rising time is about 60 samples or 2 ms and no overshoot. Once the proportional gain is too large, it results in a strong oscillation.

Figure 11.8 is a -1V step of θ mode based on the same situations of Figure 11.6 but the air gap is larger than the above case. As the analysis of Chapter 10, the responses are much slower than the corresponding case in Figure 11.7 due to larger air gap.

In Figure 11.9, the command is a 5V step for both X and Y direction and 0 for θ. The X mode shows faster response and higher overshoot than Y. And due to the low proportional gain, θ mode shows slower response again.

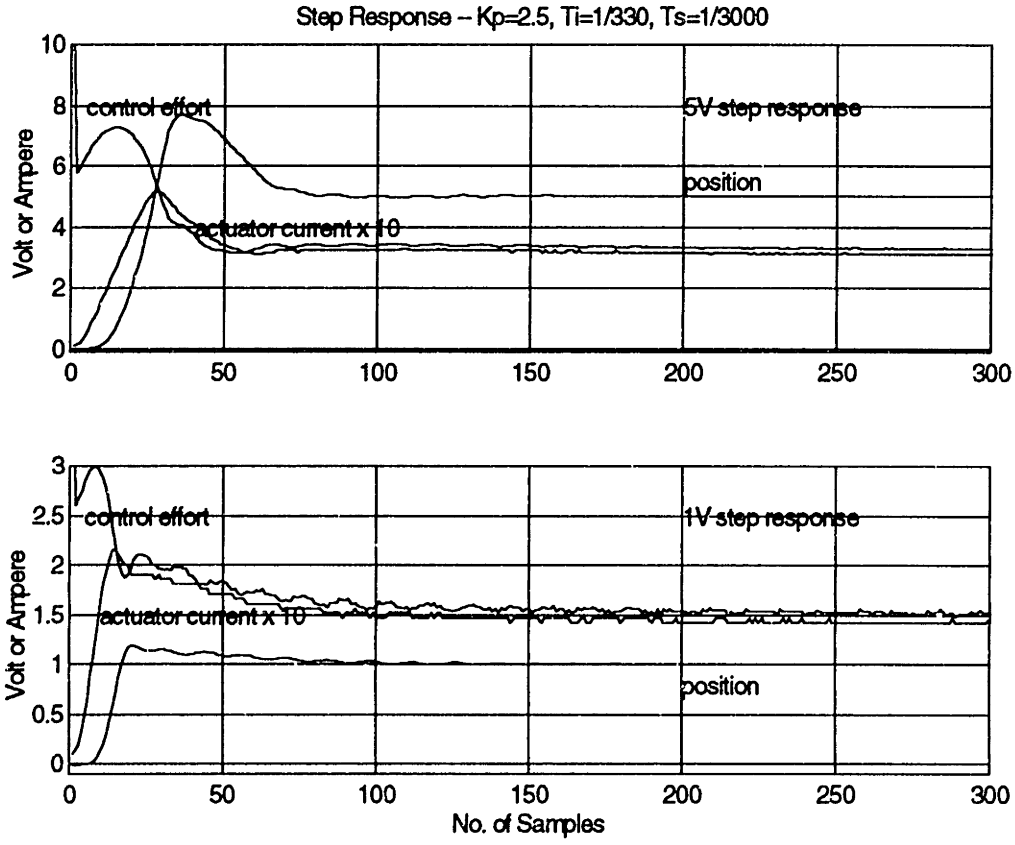

Figure 11.4a Position, control effort, and actuator current in 25 μm and 5μm X step responses

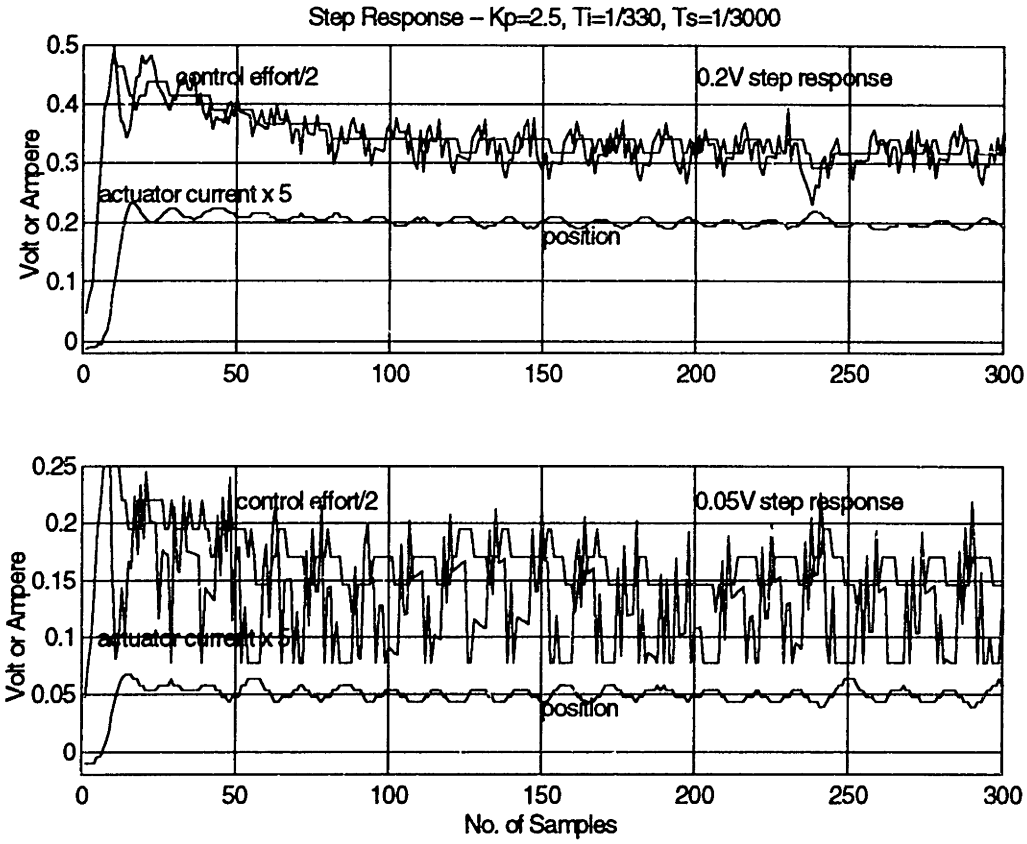

Figure 11.4b Position, control effort, and actuator current in 1μm and 250 nm X step responses

Steady state response

Figure 11.10 is the steady state response of the X, Y and θ step response. Most of the steady state noise is within 2 ADC counts and the peak to peak noise is about 3 ADC units and the standard deviation is within 1 ADC unit. 1 ADC unit is equal to 25 nm. Therefore, the steady state noise is about 75 nm peak-to peak.

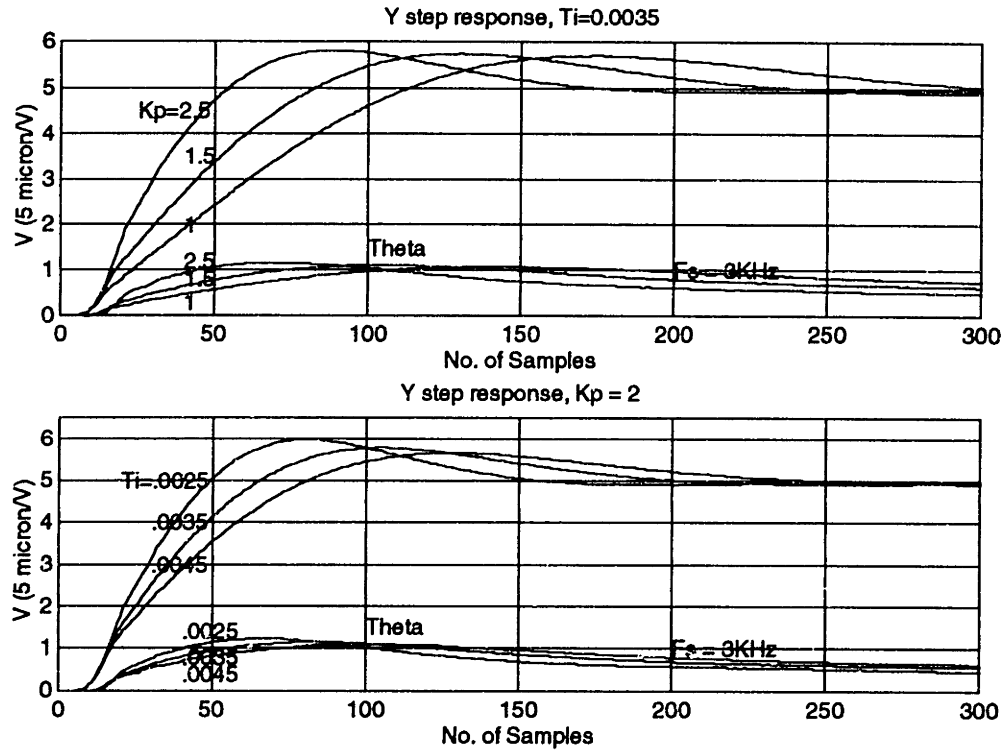

Figure 11.5 +5V Y step response (θ =0, X turned off)

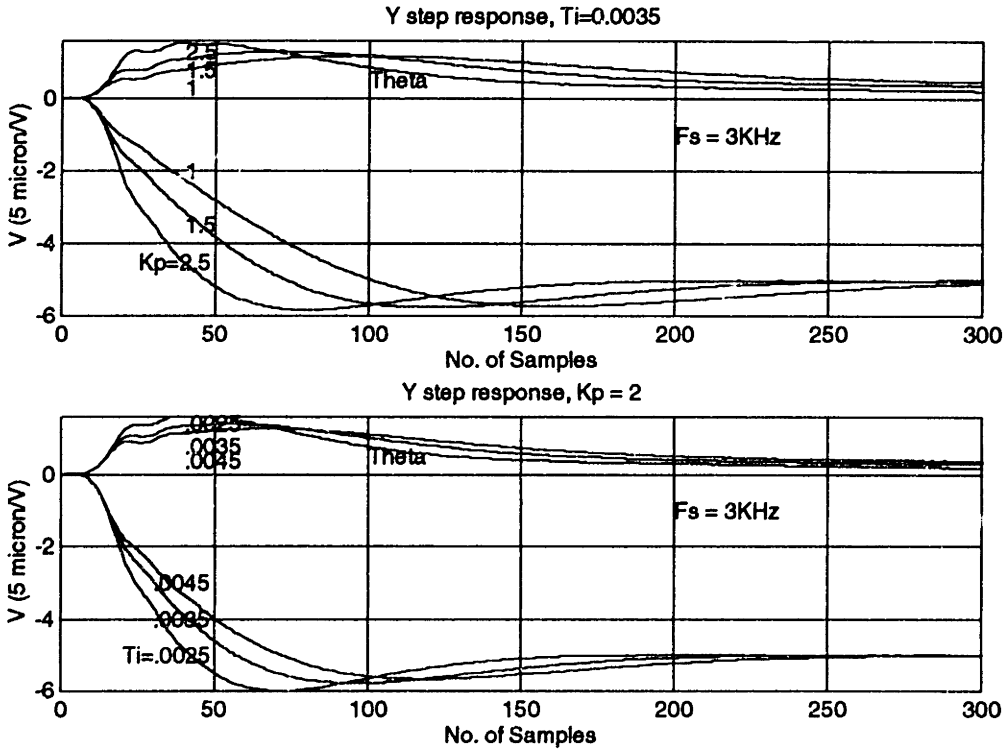

Figure 11.6 -5V Y step response (θ =0, X turned off)

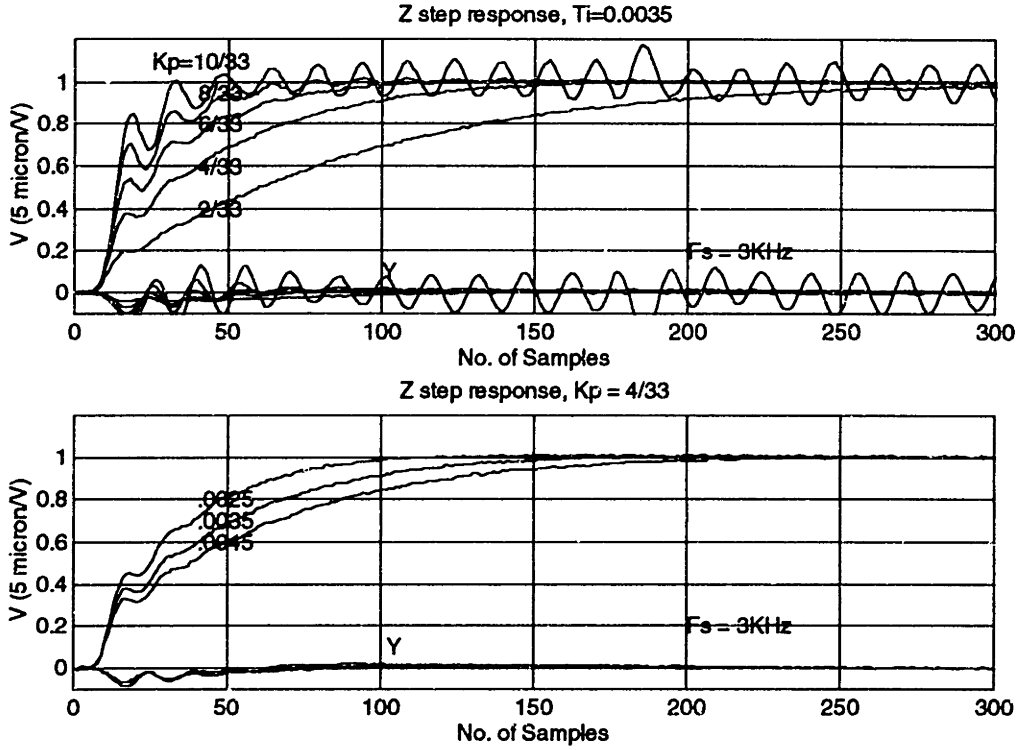

Figure 11.7 1V θ Response (Y =0, X turned off)

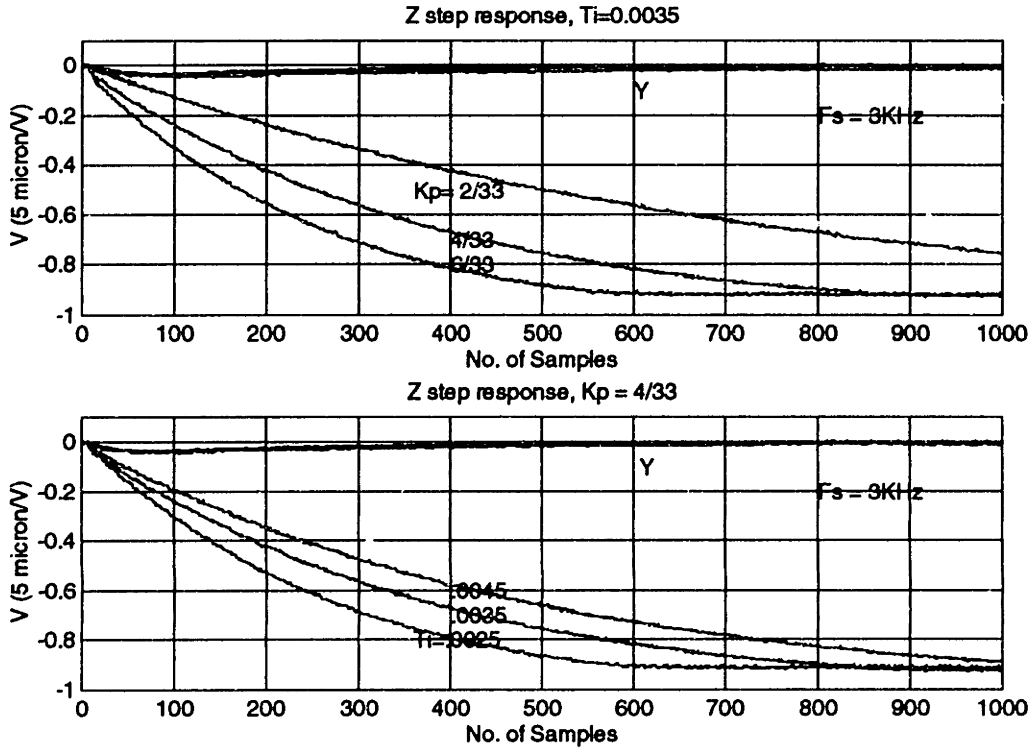

Figure 11.8 -1V θ Response (Y =0, X turned off)

Ti=.0025

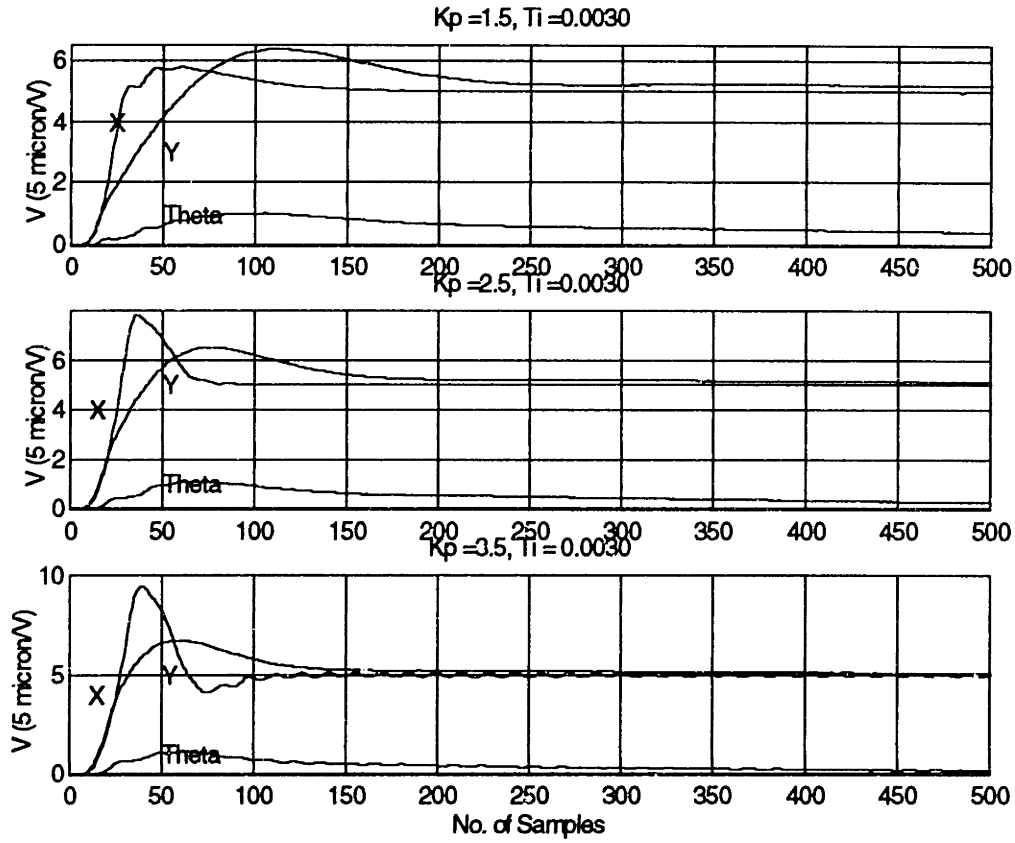

Figure 11.9 A +5V X and Y step response (θ =0)

11.3 Sinusoidal Response

Sinusoidal response of X degree of freedom

As mentioned in [Ols94], the control algorithm which is based on linearizing the nonlinear system will exhibit output distortion and instability when the operation point is changed or the amplitude of command signal has been increased. On the other hand, the use of feedback linearization can avoid such problems. For examining the effect, the Y and Z degrees of freedom are turned off. A 5 Hz sinusoidal signal serves as the X command input. Figure 11.11 shows the stage response to several input amplitudes. The results show there is no signal distortion due to high amplitude.

Sinusoidal response of multi-degree of freedom

One important issue is that what bandwidth the stage can reach? To find the result, a 4V sinusoidal signal is used as the X command input. The command input of Y and θ modes are zero (That is, the Y and θ modes are used for regulator for command input ≡ 0). Figure 11.12 is the test result. One can see that the output amplitude is roughly 70% of command when the frequency of command input is 90 Hz. In this time, K_p=4 and T_i=0.003. Therefore, the bandwidth which stage can reach is about 90 Hz.

Figure 11.13 shows the case where the X command is a 5V sine wave, the Y command is a 2 V sinusoidal wave, and the θ command is zero. The command frequencies are 0.5 and 1 Hz respectively. The X and Y output track the command pretty well but there is a small fluctuation in the θ mode.

Figure 11.14 shows a combination of step and sinusoidal commands. A 5V sinusoidal signal (0.5 Hz and 1 Hz) serves as the X command input. A 5V step signal serves as the Y mode input, and the command of the θ mode is still kept in zero. This mode has its practical application. In chapter 12, this stage will be applied on surface scanning work and this kind of motion will be used to generate surface scans.

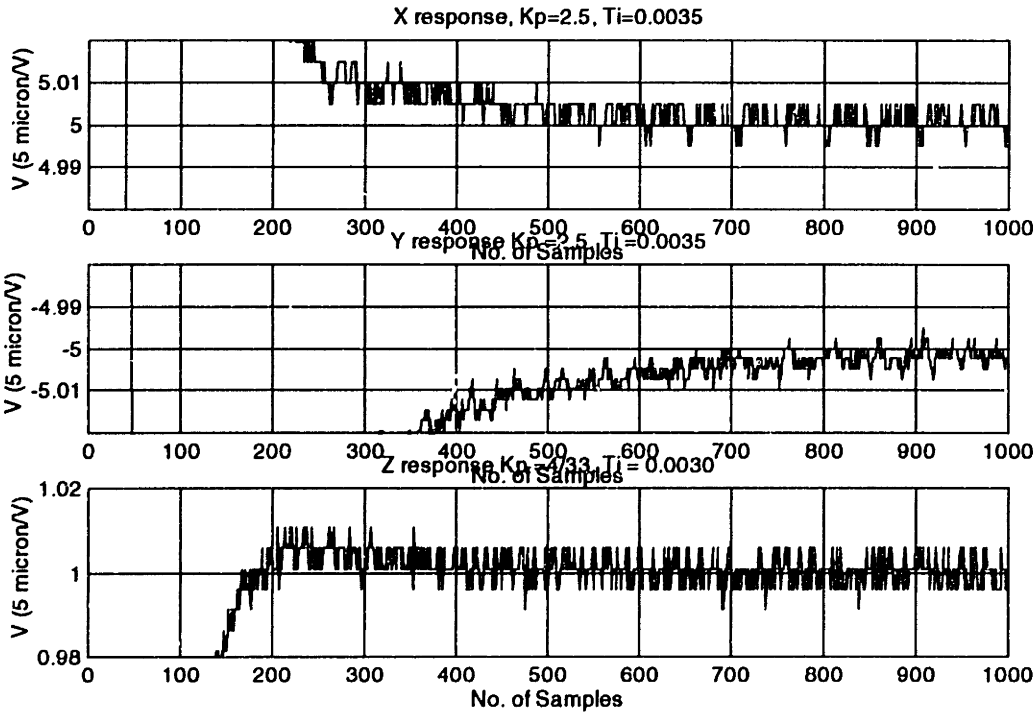

Figure 11.10 Steady state in step responses

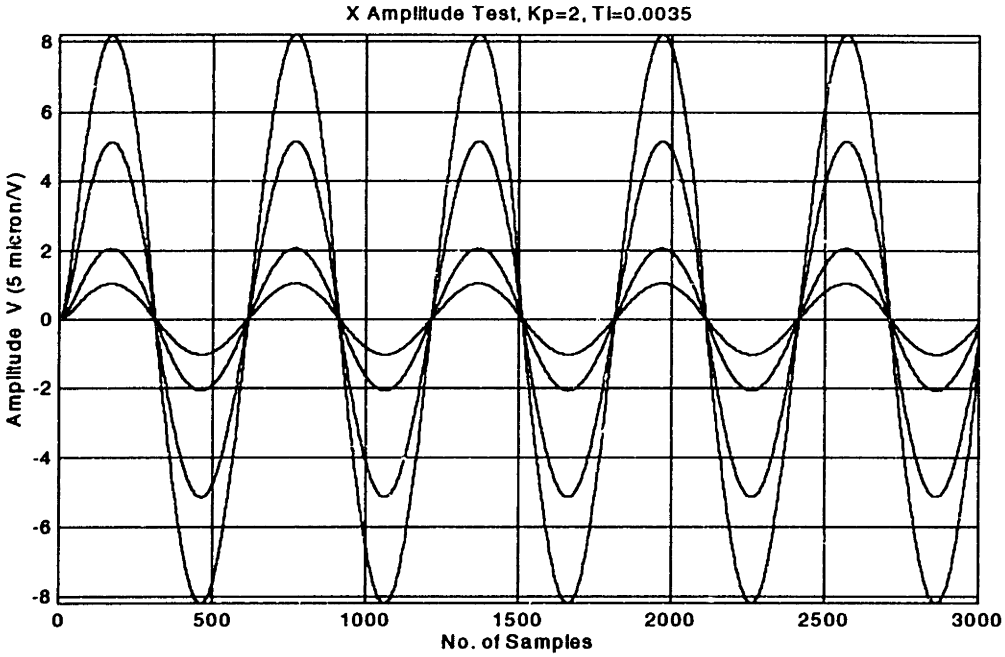

Figure 11.11 Amplitude test on X mode (Y and θ are turned off)

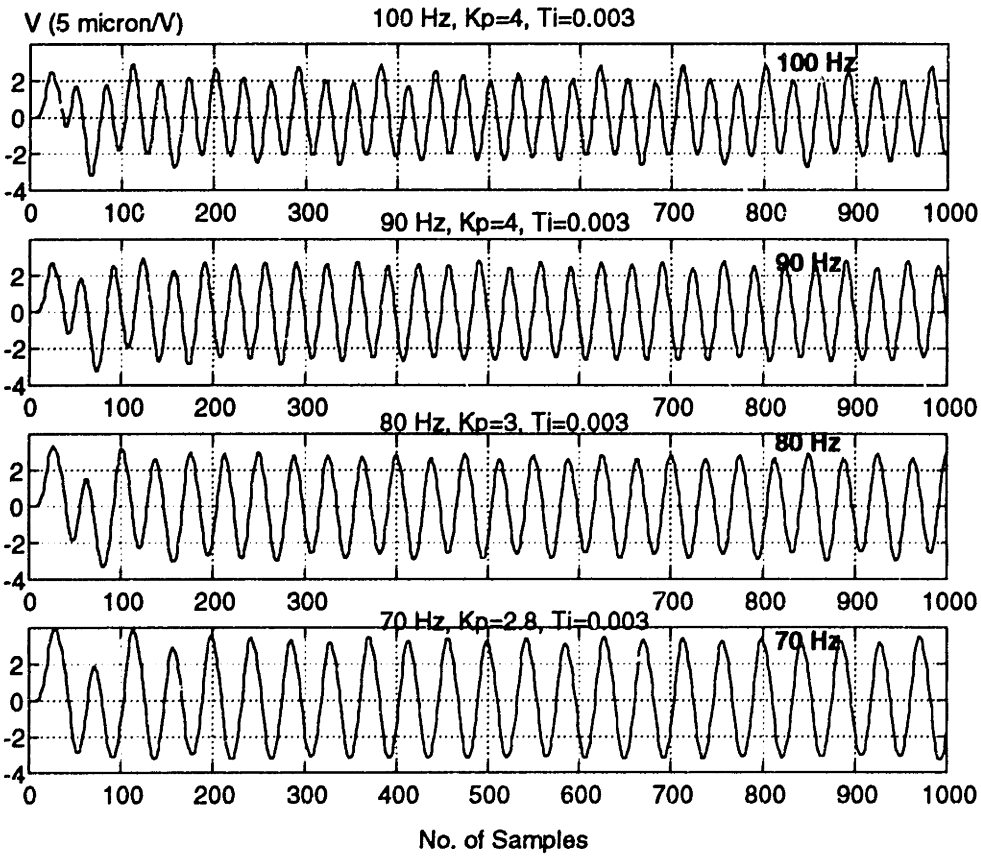

Figure 11.12 X mode bandwidth test (Y, θ =0)

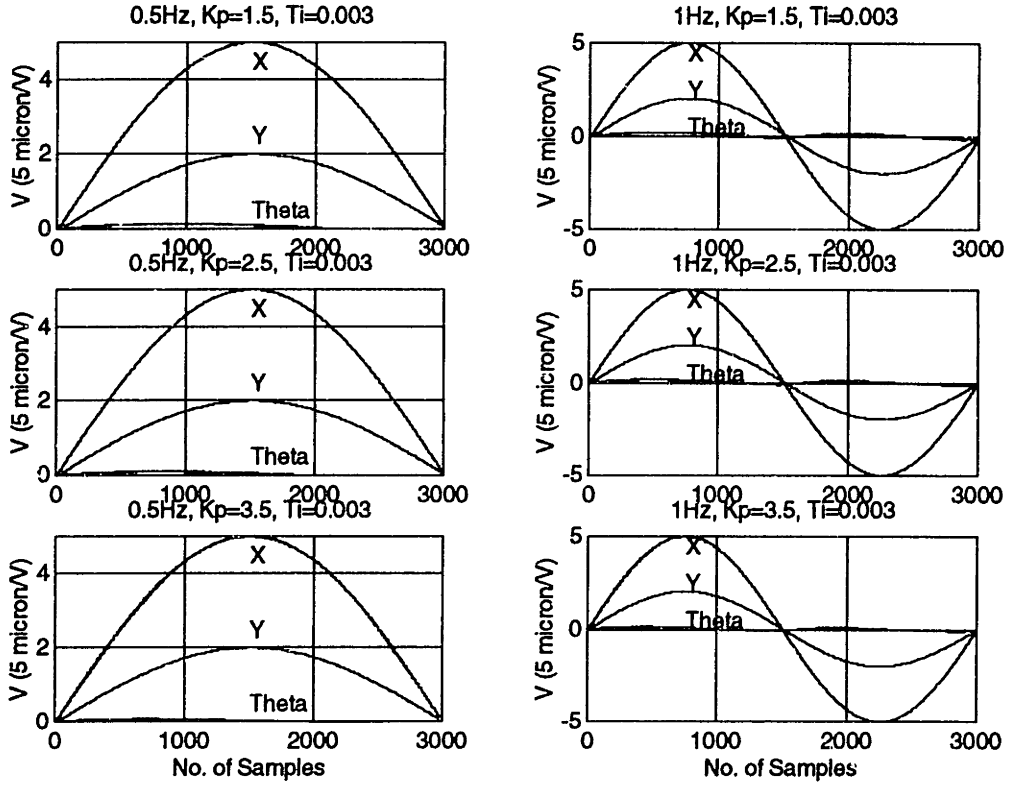

Figure 11.13 Sinusoidal response in X (5V) and Y(2V) mode (θ =0)

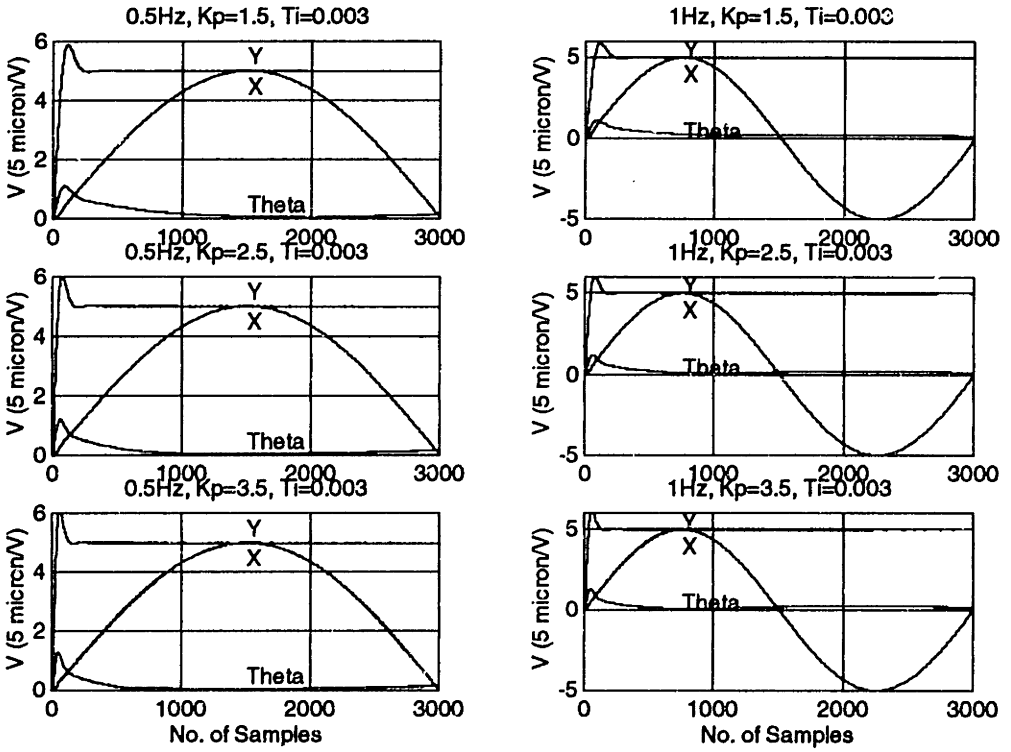

Figure 11.14 Response for combining sinusoidal (X 5V), step (Y 5V) command (θ = 0)

11.4 Conclusion on Stage Control

11.4.1 Further explanation on some phenomena

Step response of translation mode

As discussed in section 11.1, and shown in Figure 4.3, there are several periods in a typical step response.

The first period is about 10 samples. During this period, the stage just starts to move. The Viscasil then passes a transition for transforming its viscosity from its nominal value to the value under a certain rate of shear. As the consequence, the viscosity of Viscasil is very high at this time. Basically, during this period, the system damping is based on the nominal viscosity of Viscasil. The damping ratio is around 22-24. This saturates the controller and power amplifier.

After passing this period, the Viscasil viscosity decreases a lot, which results in a much faster response. However, due to the past accumulation of error, the control effort is too large at this time and it results a certain amount overshoot. After passing this period, the control effort does not change too much. The rate of shear decreases, and therefore, the viscosity increases again, resulting a large damping ratio and slower response.

Step response of rotation mode

The response of rotation mode shows a different story from translation mode. Again, a period of 10 samples shown the system is moving under extreme high damping ratio. After passing this period, the viscosity has been decreased to the viscosity under the rate of shear of rotation mode. This damping ratio is further decreased by the control gain. Once the proportional gain is too high, the system will tend to undamped and eventually, goes to unstable. It does not show any overshoot since the effective damping ratio is not so high as translation mode. From the result of Figure 11.7, when K_p = 10/33, the rotation mode will be excited. It shows a first harmonic of about 210 Hz. This matches the previous analysis on system mode.

Bandwidth Test

The result of bandwidth test, is shown in Figure 11.12. Again, a 10 samples dead zone period appears in the beginning of each plot, it comes from the transient of oil. Transient responses also appear in sinusoidal responses during the first 100 samples. That should be the overall system transient combined with the properties of Viscasil.

Coupling between Y and θ

From the experiment results, one can see that when either Y or θ is commanded to move but the remainder is commanded to stay i.e., 0, one can always find that that one which it should stay in zero always has a transient response to positive Y or θ, then gradually back to its command value. That's due to the manufacturing and assembling error. The four actuators are not set in same situation, the center of stiffness does not equal to the center of mass, and there are some differences among the four steel springs. These effects cause such result.

Nonlinear damping modeling

A more detailed modeling based on the characteristic of Viscasil is presented in this section. The system dynamics is modeled as a mass, linear spring, and a nonlinear damper. The damping force is proportional to $V^{0.6}$. In addition, we use several time delays to modeling the overall behavior during the first 10 samples. Basically, the response of this period is dominated by the transient properties of fluid. The viscosity information in Figure 4.3 is obtained under steady state. There are no available data to understand its transient behavior. This makes things more complicated. For simplicity, we just model this period with several time delays. The system block diagram is shown in Figure 11.15.

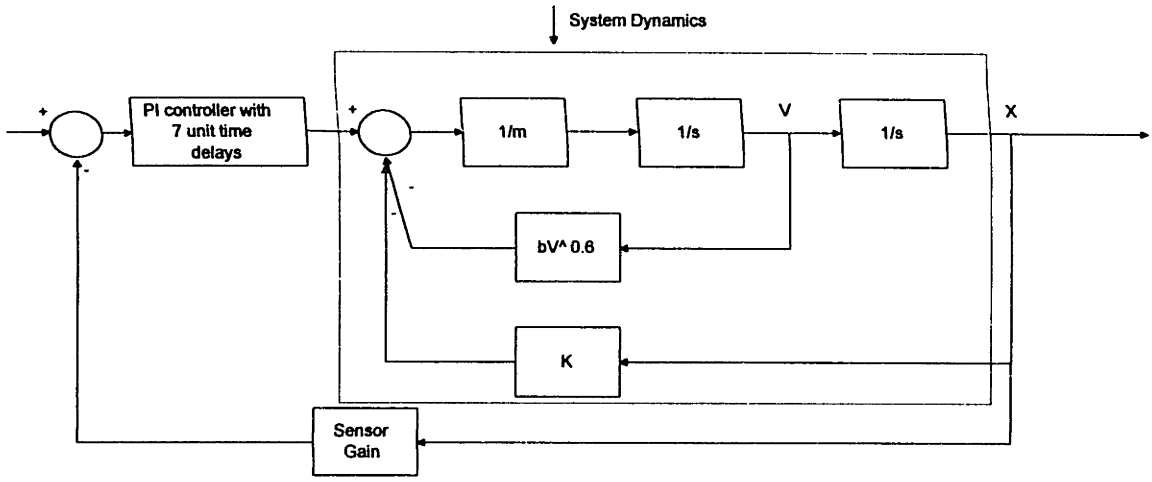

Figure 11.15 The block diagram for nonlinear damping analysis

Figure 11.16 shows the linear damping, nonlinear damping, and the experiment data. The nonlinear simulation result is much closer to the experiment data. However, the simulation shows a long period of small oscillation. It has a small oscillation around the steady state with a long period. This cannot be found in experiment result. It shows that this damper model cannot represent the real behavior of Viscasil at very low rate of shear.

11.4.2 Conclusion

The result shows some differences between experiment results and simulation. There are two main reasons which make contributions. One is the characteristics of damping fluid. After re-modeling by nonlinear damping, the simulation results are much closer to the experiment data. The other reason is the manufacturing error. It causes coupling among the three modes.

The rise time and overshoot can be reduced to under 10 ms and 10% respectively, at the same time in both the X and the Y modes under suitable control gains. However, in the θ mode, as shown in Figure 11.7, the rise time is lower. A 20 ms rise time is nearly the best result. Once the control gain increases again, the output will be tend to oscillate although the response will be faster.

The result also shows some difference between the positive and negative step response. The reason is that there are some differences in the gaps between stage and the

actuator pairs. A 10 microns difference may cause 4% change in proportional gain, and change in all control performances.

The steady state response shows fluctuation with a pick-to-pick value of three bits. This is due to a limit cycle driven by the quantization of the digital device. This result matches the previous analysis and shows the system is really good in vibration rejection.

The X mode can reach 90 Hz bandwidth. The Y mode, however, coupled with θ mode and cannot get response as fast as X mode. For rising the overall system performance, a re-design on the damping of θ mode is the best way. For surface scan, the stage is usually operated in slow frequency (f < 1 Hz). For this purpose, the stage can work very well.

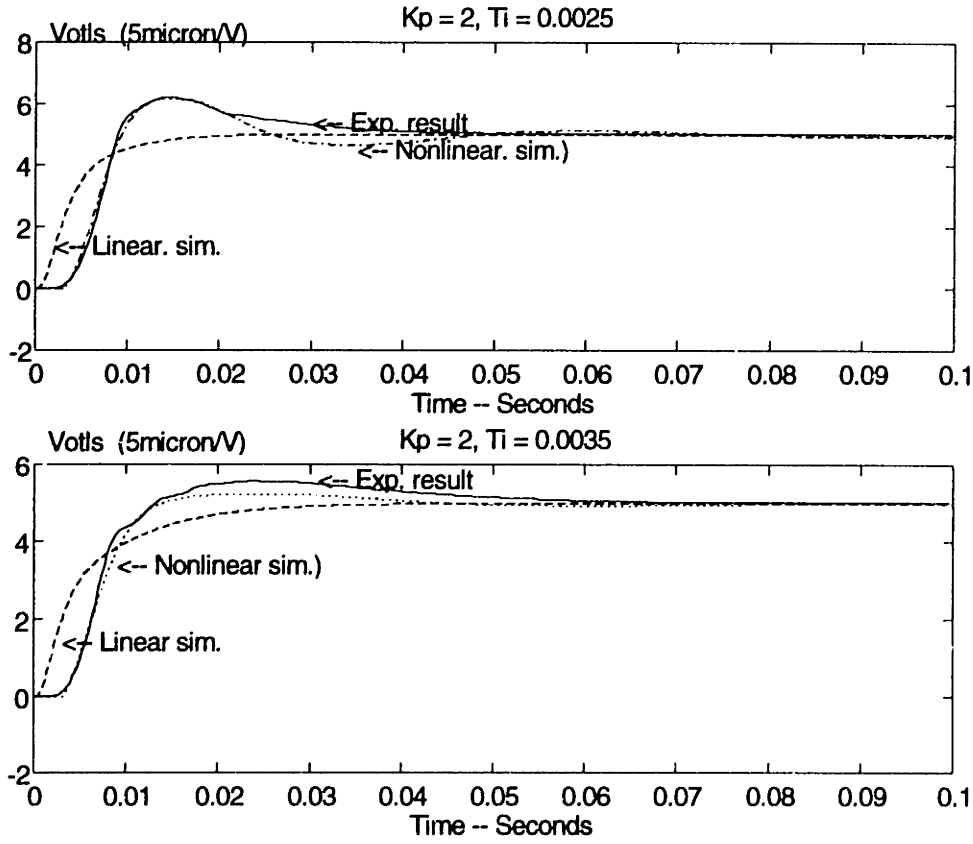

Figure 11.16 The result of nonlinear damping simulation

CHAPTER 12

SURFACE MEASUREMENT

In this chapter, the stage is applied for surface scanning, by combining it with a TALYSURF surface profiler head. Section 12.1 presents the basic principles of surface styli, calibration, and system setup. Section 12.2 discusses some issues in scanning. Section 12.3 shows the results of surface scans.

12.1 System Setup

A direct application of the stage is for surface scanning. For the scanning task, an old TALYSURF 4 surface profiler was modified to work with our system. Its diamond stylus has a tip dimension of 0.001 inch or 25.4 μm. The contact force between the stylus and the specimen is about 0.1 gram. There is a half bridge type LVDT in it. However, since the machine is old, except LVDT and mechanical structure, we discarded its electronics and built our own. For more details on the specification of the stylus, see [Tal65].

LVDT

The term LVDT is the abbreviation for Linear Variable Differential Transformer. It is based on the principle of a differential transformer with variable coupling between primary and secondary coils. There are two kinds of LVDT. The first one is the series opposed LVDT. As shown in figure 12.1a, it consists one primary and two secondary coils. The three windings are situated on a cylindrical bobbin, in which a movable soft magnetic core is located. The motion of the core causes a change of voltage between the two secondary windings. In a certain region, the difference between these two windings

is proportional to the displacement of core. Theoretically, the output is zero when the core is located at the center of LVDT.

The other kind LVDT, as shown in Figure 12.1b, called Half-Bridge type LVDT. There are only three ends. The output of this kind LVDT is also proportional to the core displacement, however, unlike the series opposed one, it has an offset since the output is not the difference of two coils. The half-bridge LVDT is driven by an AC voltage from one end as shown in Figure 12.1b.

The inputs and outputs of both kinds LVDT are all AC signal. For practical application, one should demodulate the output AC signal to a DC one whose magnitude is proportional to the amplitude of AC signal.

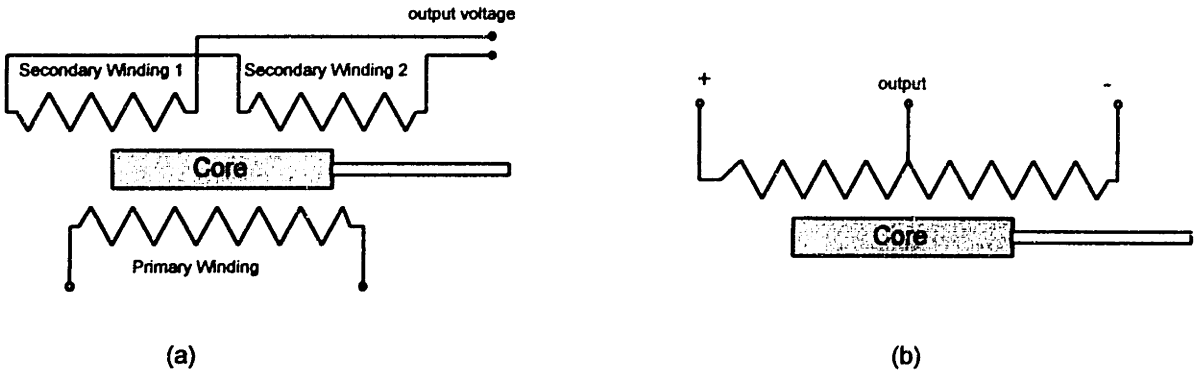

Figure 12.1 a,b Basic structure of LVDT. (a) Series Opposed type, (b) Half-Bridge type.

Demodulator[1]

The LVDT demodulator which is used in this task is prototyped by author. The core part of this demodulator is a AD698 chip obtained from ANALOG DEVICES Corp. The functions of the demodulator are to supply an oscillation signal to LVDT, sense the output, and produce a DC output which is proportional to the core position. The circuit diagram is shown in Figure 12.2 and the functional block diagram is shown in Figure 12.3. The maximum peak to peak output signal is 7 volts.

[1] ANALOG DEVICES Corp. supplied four AD698 and four ADS298 chips for this work. The author wishes to acknowledge ANALOG DEVICES's assistance here.

A Tektronix® AM 502 differential amplifier is connected to the output of the demodulator box. The main purposes of this differential amplifier are for further increasing the system gain and reducing the noise.

LVDT calibration

One should get the relationship between displacement and LVDT voltage output at the beginning. The micrometer which is used to make primarily calibration of capacitive probes again is applied on LVDT calibration.

In this calibration, both of the data of micrometer displacement and LVDT plus demodulator(without differential amplifier) output are recorded. The result is shown in Figure 12.4. The gain is about 1V/250 μm. This value serves as the reference gain. However, in most applications, the surface roughness is on the order of several microns. An additional amplification is thus necessary. It can be achieved by the differential amplifier.

The amplitude of signal noise is also important. The static test result is shown in Figure 12.5. From Figure 12.5a, one can find that the maximum peak to peak noise is around 2 mV or 0.5 μm. And from Figure 12.5b, the major noise source is the 60 Hz AC noise.

System setup

The surface scanning system is shown in Figure 12.6 The LVDT is contacted with the testing sample. The testing sample is attached on the sample holder of stage. The stage performs a certain motion. As the stage moves, the output of the LVDT will be changed by the target surface roughness and the error motion of stage. The output of LVDT is an AC signal, after demodulated and amplified. This roughness and its corresponded position are acquired by our data acquisition system.

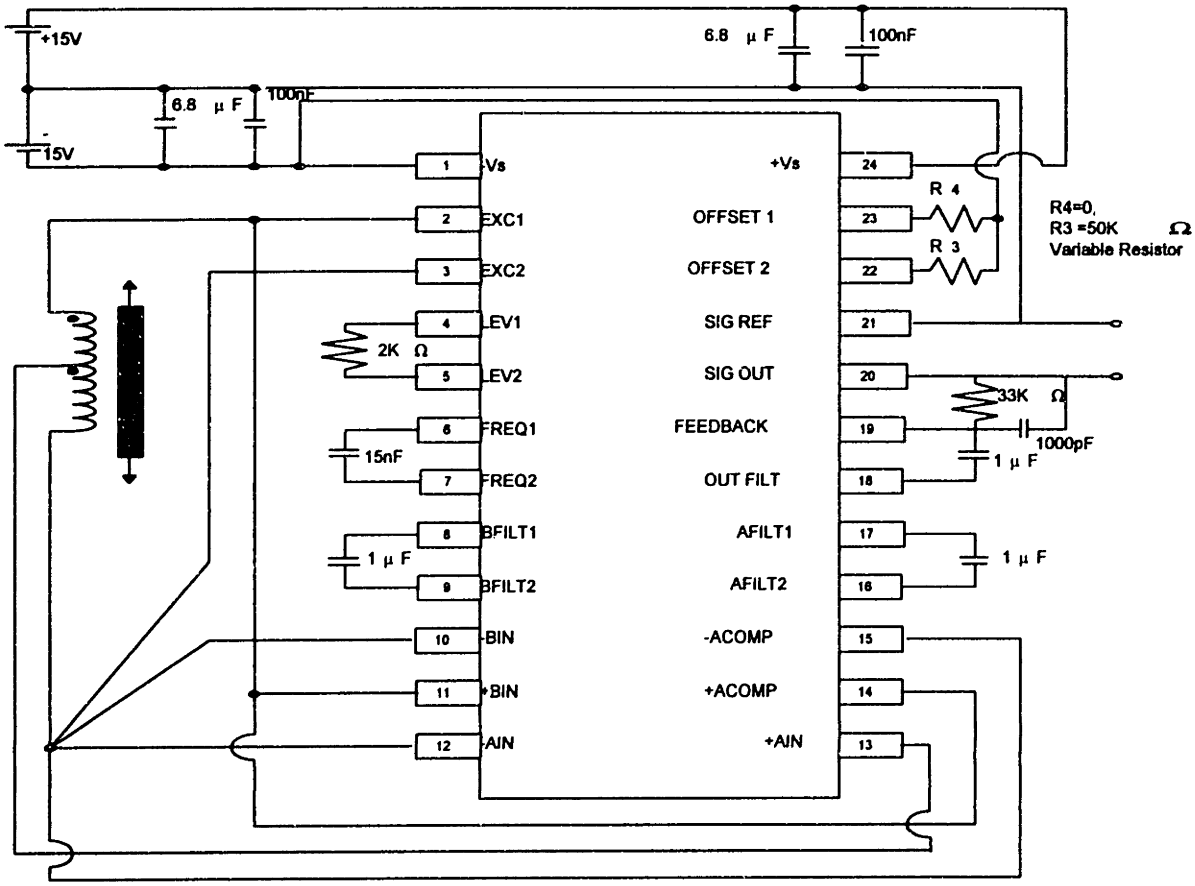

Figure 12.2 The circuit diagram of LVDT demodulator

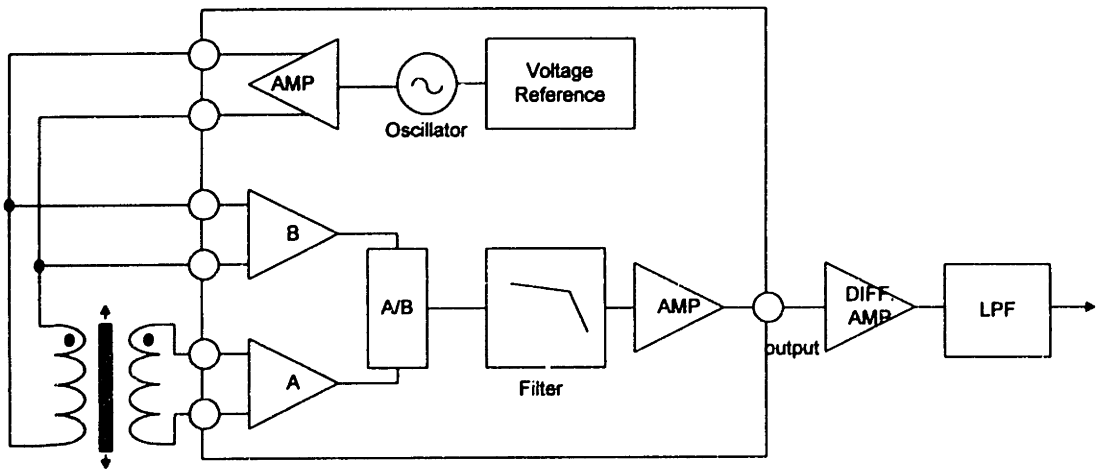

Figure 12.3 Functional block diagram of demodulation system

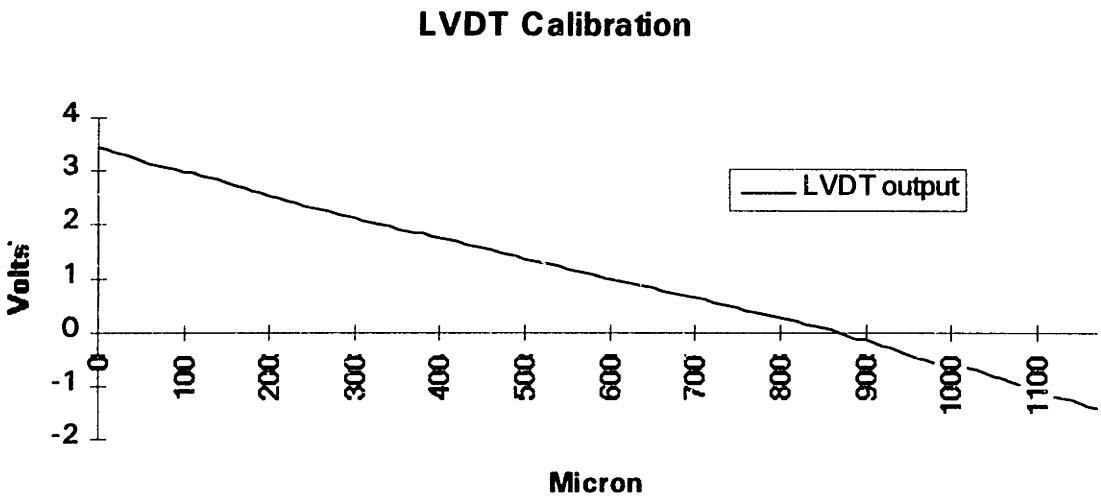

Figure 12.4 LVDT calibration result

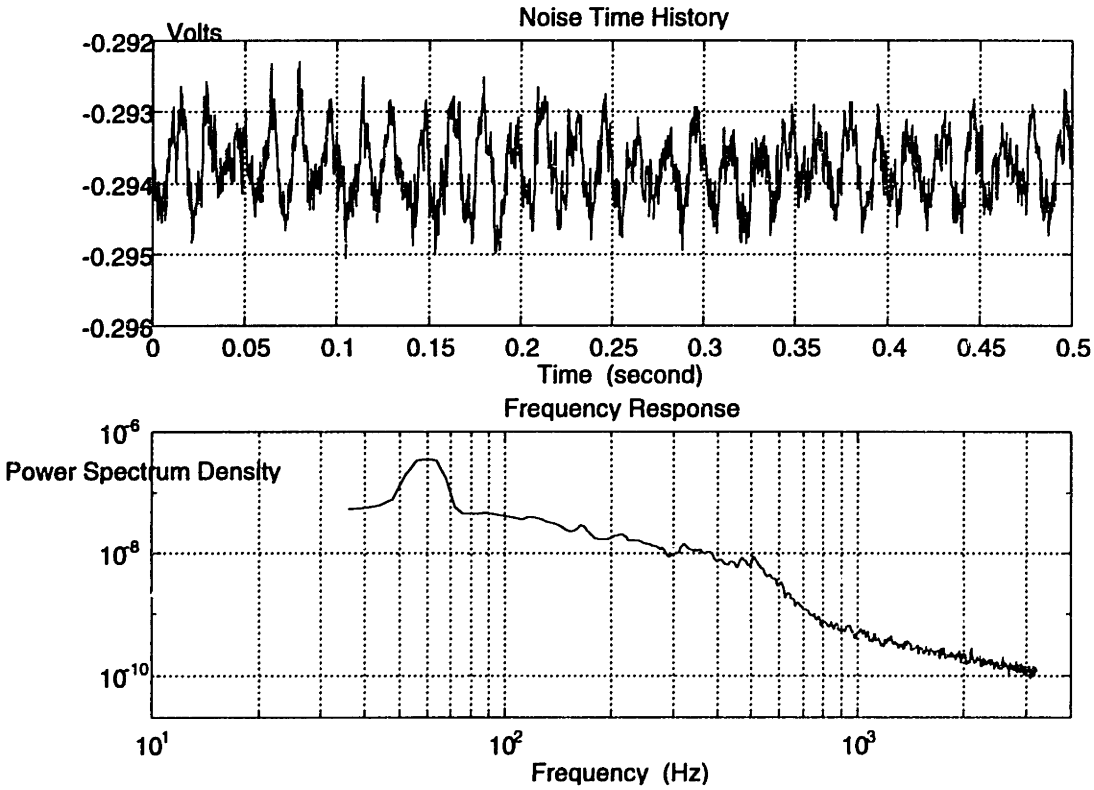

Figure 12.5 The static test result of LVDT signal

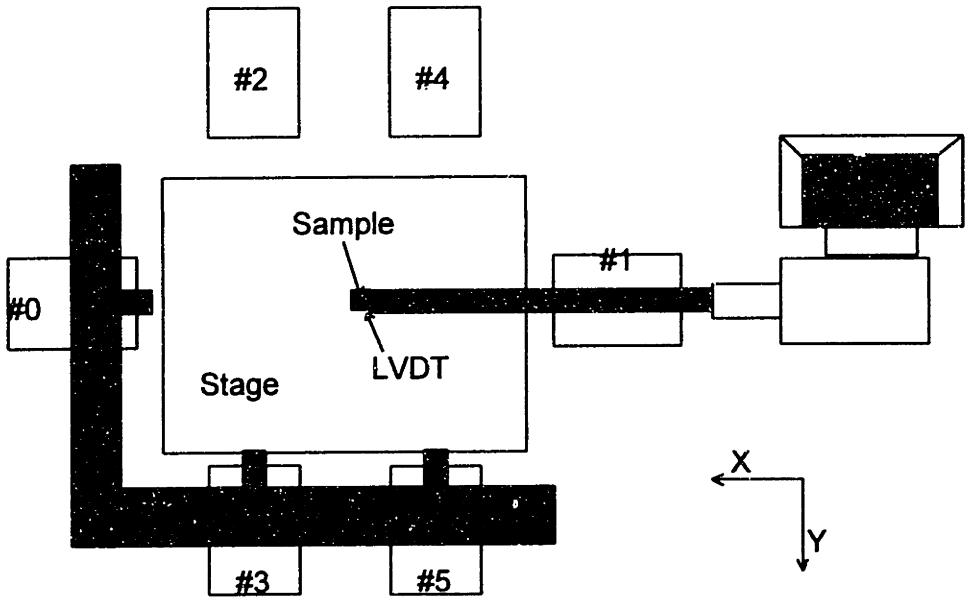

Figure 12.6 The experiment setup of surface scanning

12.2 Practical Consideration Issues

Measurement and force loops

The notion of measurement loops and force loops is fundamental in the design of instruments for surface metrology. In equilibrium state, balanced force must follow a continuous closed path which often involves the machine base. This closed path is the force loops. The measurement loops come as a direct consequence of linking the object via a detector to the reference with which it is being compared.

Since the force loop is necessary under load it is therefore strained, so the dimensional stability is important if it is small. By the similarly reason, the metrology loop is better if smaller because it can reduce noise influence.

The rules concerning loops are therefore[Whi94]:

1. Any changes that occur to a part or parts within a measurement loop but not all of it will result in measured results that are not distinguishable from the measurement.

2. What is of importance is that "force ioops should be kept as far as possible away from the measurement loops". And if possible the force loop should not be allowed to cross into or out of a measurement loop.

So the primary consideration in any design is to determine where the metrology and force loops interact and if possible to separate them. Usually the best that can be achieved is that they are coincident in just one branch of the measurement loop. This makes sense since any strain in a metrology loop will cause a distortion which is an error.

The structural loop, as shown on Figure 12.7, is from diamond styli tip to LVDT core. The length is about 10 cm. By structural testing, the resonance frequency is about 10 Hz and the damping ratio is about 0.1 ~ 0.2. If the metrology loop is follow this way, it will never get any useful information. The idea to minimize the metrology loop is by adding a flat part before the stylus. This part has five degrees of freedom and it is attached on the target surface. Without constraining the movement of stylus probe, it provides a support of the structure of the measurement system. After introducing this part, the metrology loop has reduced to a small loop.

Hysteresis of LVDT styli

Since LVDT is an inductance based measurement instrument, by the basic electromagnetic theory, it will have a certain amount hysteresis loop. As shown in Figure 12.8, the stage moves back and forth at the same axis, the scan result of two different ways. They form a closed loop. To avoid this effect, it is better to use uni-directional scan instead of a back and forth scan.

Scanning rate

Too slow scanning rate will be time consuming and easy to be disturbed by environment (since the scanning period is longer). However, if the scanning rate is too fast, it may excite the LVDT structural dynamics.

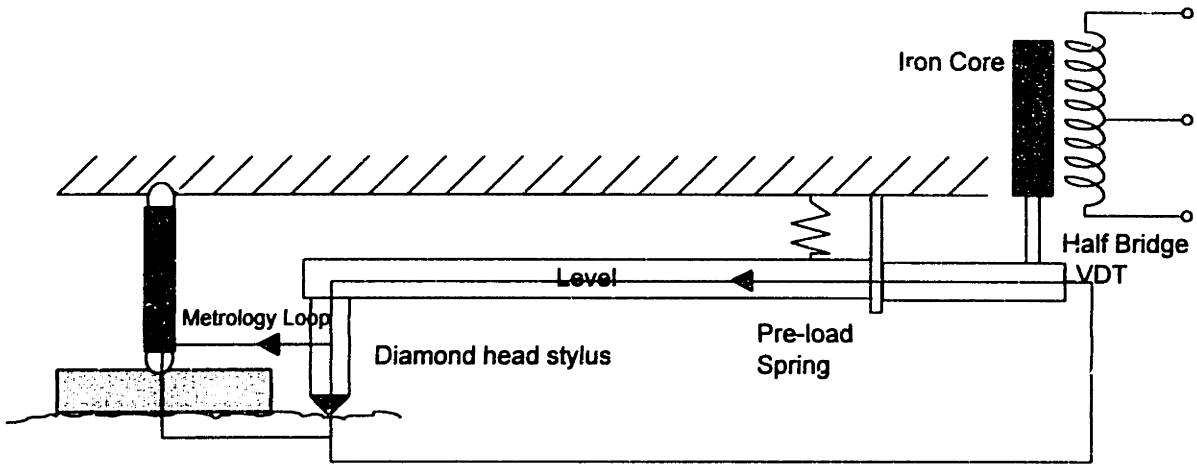

Figure 12.7 The force and metrology loops of surface scanning

Transient response of stage

To get a better result, one should eliminate the influence of the stage transient response to the whole surface scanner. For long travel mode, one should select a sinusoidal motion rather than ramp motion since the latter will introduce high frequency harmonic excitation into system. For lateral step motion, it is better to delay the data acquisition until after the transient dies out.

Error motion and off-line data processing

In general, the target will not be horizontal. Therefore, when it moves with stage, the LVDT actually measures two kinds of information. One is the surface roughness and the other is the elevation change which caused by the surface configuration of target and the mounting condition. The latter one should be extracted out from the source data.

11.3 Surface Scanning Result

Figure 12.9 is the flowchart in surface scanning. For surface scan purpose, the command in X direction is a low frequency sinusoidal signal, a constant value in Y

direction, and zero in θ direction to correct the error motion. The stage moves to a starting point in the beginning and delays a period of time to clear the transient response. Then, the X direction performs a sinusoidal motion for just a period. During the lower half period, the system acquires the surface data by a constant rate with respect to time. During this period, the Y direction is kept equal to a value Y* and θ is kept as zero. After one period, the system moves to next starting point and follows the above procedure until the task has been finished. The data density of the following figures are all 80 data in 80 microns. The area of scan is 80μm × 25μm. But the maximum area that can be scanned is 100μm × 100μm.

Figure 12.10 and 12.11 are the surface of a standard TALYSURF sample. Figure 12.10 is the result when the stylus passes through a scratch on the surface of the sample. Figure 12.11 is the result without scratch. It shows that the average roughness is about 0.7μm for this sample and the depth of the scratch is about 1.5μm. Figure 12.12 is the surface of the stage sample holder. The scratch is a mark made during the fabrication. The surface roughness of this aluminum plate is about 6 μm.

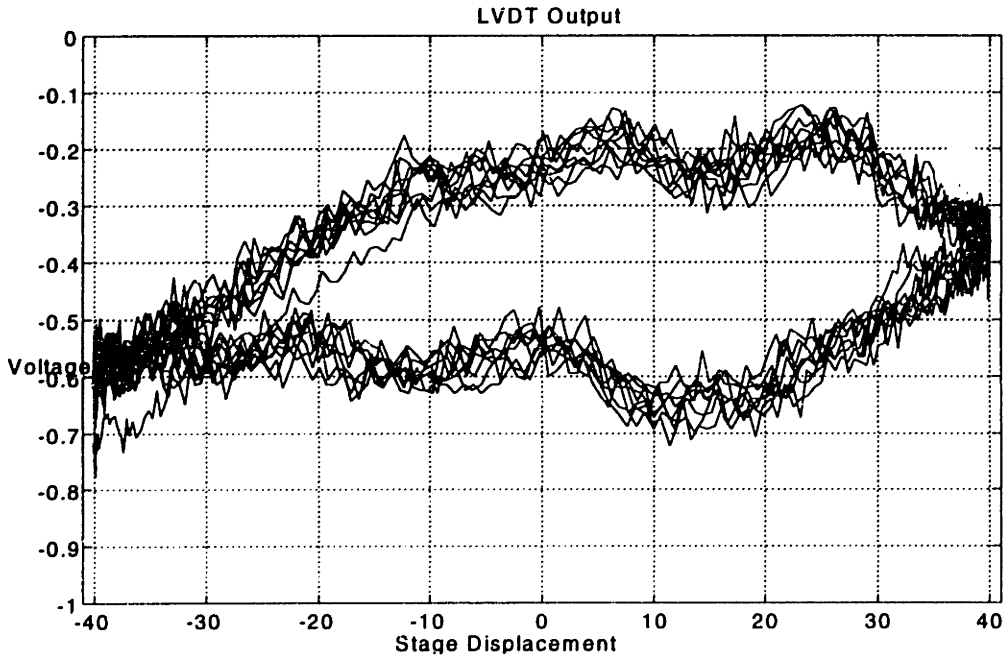

Figure 12.8 The hysteresis loop of LVDT measurement

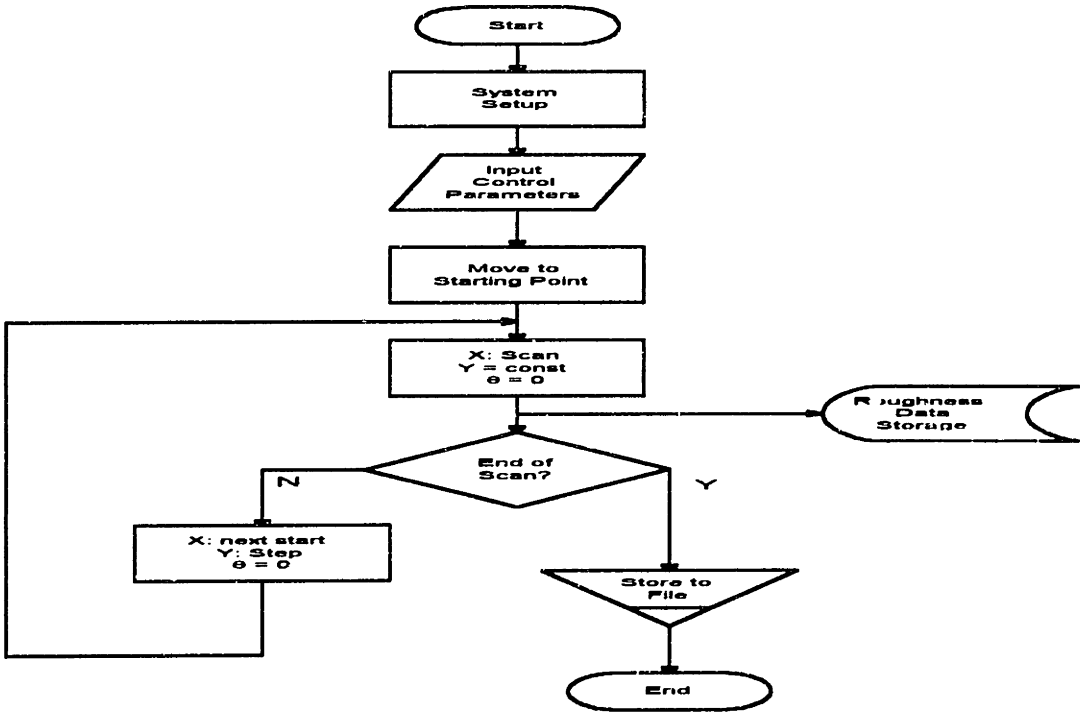

Figure 12.9 The flowchart of surface scan

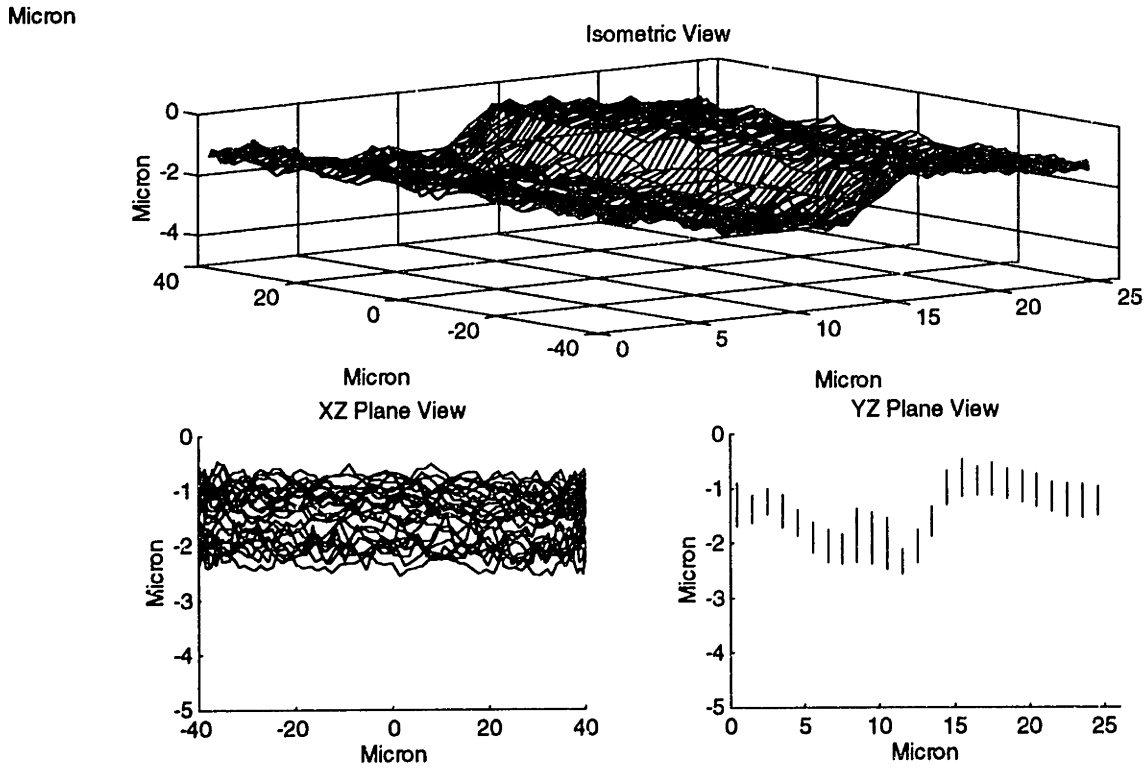

Figure 12.10 The surface scan result of a TALYSURF sample with a scratch

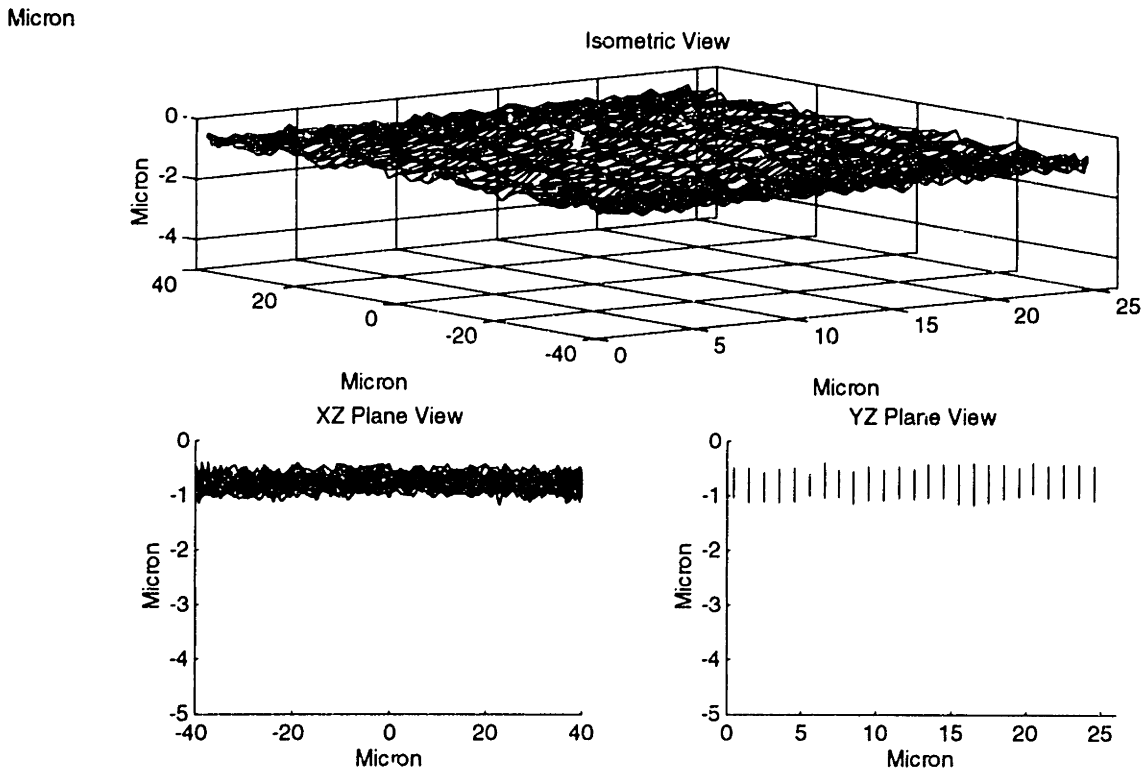

Figure 12.11 The surface scan result of a TALYSURF sample without a scratch

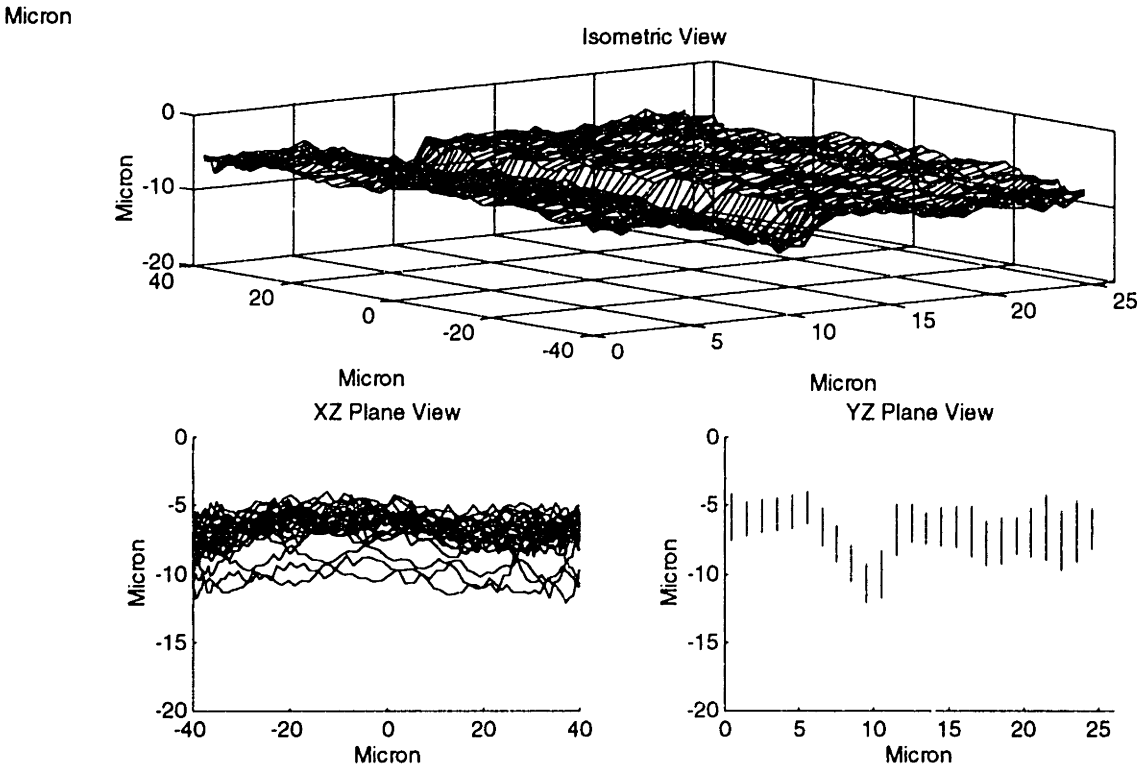

Figure 12.12 The surface scan result of the stage sample holder surface

CHAPTER 13

CONCLUSION

13.1 Summary

This thesis has provided a completed development of the spring-dominated regime stage design and control. The high stiffness of the stage provides the basis of stiffness dominated regime design. As a consequence, it reduces the influence of environmental disturbance. A Y and θ coupled design provides the margin for eliminating the crosstalk between two major axes X and Y. The maximum motion range of the stage is 100 microns in two translation modes and ±2.2 miliradians in rotation mode. The peak to peak noise in steady state is 3 ADC units or about 75 nanometers and the maximum bandwidth can reach is about 90 Hz. It's suitable for using as a micro-positioner. However, due to the manufacturing errors and the damping ratio of rotation mode, we can not get responses in rotation mode as well as translation modes. The rotation mode degrades the overall system performance. However, when the system does not need high bandwidth, this effect is not important. Combining with surface stylus probe, at low scanning rate, this stage can serve as a surface scanner with 10,000 μm^2 scanning area and an accuracy of 0.3μm surface roughness.

13.2 Future Works

This stage design gives us a right design rule and it can achieve more better performance actually. For a further design, if we change the position sensors to get a larger measurement range, the travel range of stage may be increased to 200 ~ 300 μm easily. If we replace the A/D C by a 14 or 16-bit one, the resolution will be increased significantly. However, there are still a few issues should be modified in the future stage design in order to get the optimum performance in the stage control.

1. Modify the stage design There are several defects on current stage design and these defects influence the overall performance a lot. First, either of the stationary or moving plate for performing shear damping should be made to satisfy both translation and rotation mode. The damping force in rotation mode is proportional to Ar^2, and it is proportional to A in translation mode. Every contact element makes the same contribution to damping force of translation mode but this is not true in the rotation mode. One may modify the center portion of either stationary or moving plate to increase the gap a little bit, then, increase the total area or decease overall fluid gap. As shown in Figure 13.1, since the center portion is almost useless in rotation mode damping, it is really important to get a high damping ratio in rotation mode. For adjusting purpose, the rotation mode should have faster response than translation mode. This is the reason why its crossover frequency needs to be higher than the translation modes. However, low damping restricts the magnitude of control gains and therefore, closed loop bandwidth.

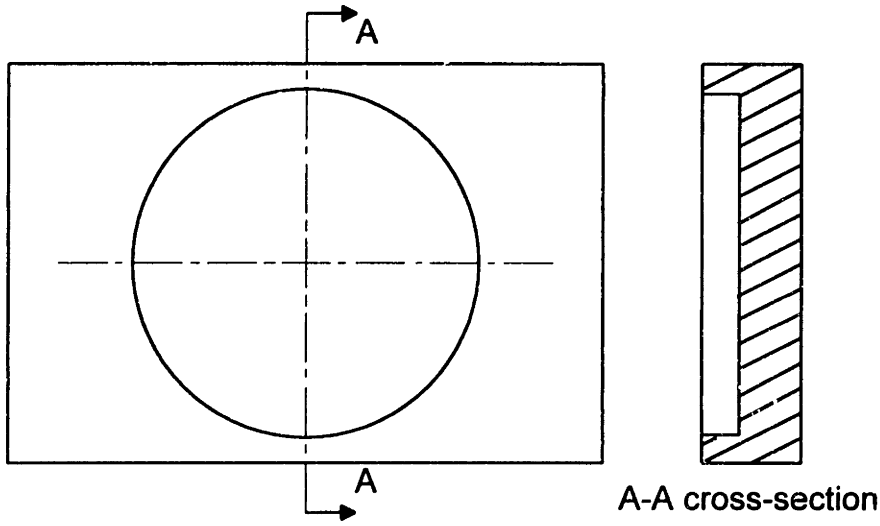

Figure 13.1 The schematic plot of modified base plate

The double H structure should be modified too. It causes a major difficulty in setting the air gaps of four lateral actuators. As a consequence, it changes the effective control gain and final result.

2. Improvement on damping mechanism: The characteristic of Viscasil causes a major difficulty on system modeling and deviation between modeling and experiment result. Since damping ratio is very important in system dynamics. We should use a fluid which has same order of viscosity but its behavior is much close to Newtonian, the damping fluid should be changed.

3. More detailed system modeling: The more accuracy in system modeling, the better results in control one will get. A mass-spring-damper system modeling is simple and has good result in certain degree. However, it is a distributed mass system with numerous joints. For getting more understanding on the system characteristic, one may discard the basic idea on 'translation' and 'rotation' modes and use system identification to get the exact information.

4. Air gaps setting: Currently, we use shims to get the desired air gaps. It performs well in X axis. For Y axis, there is enough room for adjusting by shim. One spends a lot of time to set up the six air gap and the result is not very good. Therefore, a precision air gap setting mechanism will be necessary for getting a more accurate result.

BIBLIOGRAPHY

[ASM73] **ANSI/ASME B89.6.2 (1973):** "Temperature and Humidity Environment for Dimensional Measurement", ASME, N. Y., 1973 (Rev. 1988).

[ASM90] **ANSI/ASME B89.1.12M (1990):** "Methods for Performance Evaluation of Coordinate Measuring Machines", ASME, N. Y., 1990

[ASM92] **ANSI/ASME B5.54 (1992):** "Methods for Performance Evaluaton of Computer Numerically Controlled Machining Centers", ASME, N.Y., 1992

[BeP71] **Bendat, J. S., and Piersol, A. G., (1971):** *Random Data: Analysis and Measurement Procedures,* John Wiley & Sons Inc., 1971.

[BiS86] **Binnig, G., and Smith, D. P. E. (1986):** "Single-Tube-Dimensional Scanner for Scanning Tunneling Microscopy", *Review of Scientificc Instrument* 57(8), Aug., 1986.

[Cha85] **Chapman, A. J. (1985):** *Heat Transfer,* 4th edition, MacMillian Publishing Co., N. Y., 1985.

[CYS92] **Clark, S. M., Youngquuit, M. G., Spence, C. F., and Baldeschwieler, J. D. (1992):** "Hardware for Digitally Controlled Scanned Probe Microscope", *Review of Scientific Instrument* 63(10), Oct., 1992.

[Dow86] **Downer, J. R., (1986):** *"Design of Large-Angle Magnetic Suspensions,"* Sc.D. Thesis, M. I. T., Cambridge, Massachusetts, 1986.

[FPE86] **Franklin, G. F., Powell, J. D., and Emami-Naeini, A. (1986):** *Feedback Control of Dynamic System,* Addison-Wesley Publishing Co., Reading, MA, 1986.

[FPW90] **Franklin, G. F., Powell, J. D., and Workman, M. L. (1990):** *Digital Control of Dynamic System,* 2nd edition. Addison-Wesley Publish Co., Reading, MA, 1986.

[HCS91] **Harb S., Chetwynd D. G., Smith S. T., (1991):** Application and Performance of Capacitance Micrometry as a Super Precision Transfer Standard, *Proceedings of ASPE,* 6, 17-20, Oct. 1991.

[HiY93] **Higuchi, T., and Yamaguchi, T. (1993):** "Development of a New High Speed Positioning Servomechanism by Electromagnetic Attractive Force", *JSPE-59-10,* pp. 37-42, 1993.

[Hol94] **Holmes, M. L. (1994):** *Analysis and Design of a Magnetically-Suspended Precision Motion Control Stage*, Master Thesis, Department of Electrical Engineering, University of North Carolina at Charlotte, 1994.

[KaR75] **Karnopp, D., and Rosenberg, R., (1975):** *System Dynamics: A unified Approach,* John Wiley & Sons Inc., 1975.

[KoN94] **Kobayashi, I., and Numasato, H., (1994):** "Development of Stage Mechanism with High Damping Capacity for High-Precision Positioning", *JSPE-60-2*, Feb., 1994.

[KoN94] **Kobayashi, I., and Numasato, H., (1994):** "Optimizing Mechanical Damping Factor and Improvement of the positioning Control Performance Using Viscous-Elastic Guide", *JSPE-60-2,* Feb., 1994.

[Mar94] **Marsh, E. R., (1994):** *An Integrated Approach to Structural Damping*, Ph.D thesis, Department of Mechanical Engineering, Massachusetts Institute of Technology, Cambridge, MA, 1994.

[McR87] **McRae D. J., (1987):** Non-Contact Dimensional Gaging Using Capacitive Sensing, *Sensors Expo.* 1987

[MoS91] **Morgan, B. A., and Stupian, G. W. (1991):** "Digital Feedback Control Loop for Scanning Tunneling Microscopes" , *Review of Scientific Instrument* 62(12), Dec., 1991.

[Mor86] **Morrison, R. (1986):** *Grounding and Shielding Techniques in Instrumentation,* 3rd edition, John Wiley & Sons, 1986.

[Ols94] **Olson, S. M. (1994):** *Nonlinear Compensation of a Single Degree of Freedom Magnetic Suspension System*, Master Thesis, Department of Mechanical Engineering, Massachusetts Institute of Technology, Cambridge, MA, 1994.

[OAI90] **Ota, M., Andoh, S., and Inoue, H. (1990):** "MAG-LEV Semiconductor Wafer Transporter for Ultra-High-Vacuum Environment", *2nd Intl.' Symposium on Magnetic Bearing,* pp. 109-114, Tokyo, Japan, 1990.

[OpS89] **Oppenheim, A. V., Schafer, R. W. (1989):** *"Discrete Time Signal Processing"*, Prentice Hall Inc., Englewood Cliffs, N.J., 1989.

[Ott76] **Ott, H. W. (1976):** *Noise Reduction Techniques in Electronic Systems,* John Willey & Sons, New York, 1976.

[Pla56] **Plainevaux, J. E. (1956):** Mouvement de tangage d'une suspension elementaire surlames elastiques, *Nuovo Cimento*, 4(5), 1133-1141.

[PHT94] **Poovey, T., Holmes, M., and Trumper, D. (1994):** "A kinematically Coupled Magnetic Bearing Calibration Fixture", *Precision Engineering*, Vol 16, No. 2, Apr., 1994.

[Rao85] **Rao, S. S., (1985):** *Mechanical Vibrations,* Addison-Wesley Publishing Company, Reading MA, 1985.

[Slo92] **Slocum, A. H. (1992):** *Precision Machine Design,* Prentice-Hall Inc., Englewood Cliffs, NJ, 1992.

[SlL91] **Slotine, J. J. E., and Li, W., (1991):** *Applied Nonlinear Control,* Prentice-Hall Inc., Englewood Cliffs, NJ, 1991.

[SCH94] **Smith, S. T., Chetwynd, D. G., and Harb, S. (1994):** A Simple Two-Axis Ultraprecision Actuator, *Rev. Sci. Instrum.*, 65(4), 910-917.

[Sin87] **Sinha, P. K. (1987):** *Electromagnetic Suspension -- Dynamics and Control.* Peter Peregrinus Ltd., London, England, 1987.

[SmC91] **Smith, S. T., and Chetwynd, D. G. (1991):** *Fundamental of Ultraprecision Mechanism Design,* Gordon and Breach Science Publishers, U. K., 1991.

[Sof93] *Software Correction of Precision Machines,* report to NIST contract No. NIST-60NANB2D1214, Precision Engineering Laboratory, University of North Carolina at Charlotte, July, 1993.

[SpV89] **Spong, M., and Vidyasagar, M. (1989):** *Robot Dynamics and Control,* John Wiley & Sons Inc., New York, NY, 1989.

[Tal65] *Talysurf Surface Measuring Instrument User's Manual.* Talyor & Hobson LTD., Leicester, England, U. K. 1965.

[TiG72] **Timoshenko, S., and Gere (1972):** *Mechanics of Materials,* 2nd edition, McGraw Hill Book Co., New York, NY, 1972.

[TiG70] **Timoshenko, S., and Goodier, J. N. (1970):** *Theory of Elasticity,* 3rd edition, McGraw-Hill Book Company, New York, NY, 1970.

[Tru90] **Trumper, D. L., (1990):** *"Magnetic Suspension Techniques for Precision Motion Control,"* Ph. D. Thesis, M. I. T., Cambridge, Massachusetts, 1990.

[TSN91] **Trumper, D. L., Sanders, J. C., Nguyen, T. H., and Queen, M. A. (1991):** "Experimental Result in Nonlinear Compensation of a One Degree-of-Freedom Magnetic Suspension", presented at the NASA International Symposium on Magnetic Suspension Technology, Hampton, VA, August 19-23, 1991.

[Tzo91] **Tzou, H. S. (1991):** "Design of a Piezoelectric Exciter/Actuator for Micro-Displacement Control: Theory and Experiment", *Precision Engineering,* Vol. 13, No. 2, pp. 104-110, Apr., 1991.

[Whi94] **Whitehouse, D. J. (1994):** *"Handbook of Surface Metrology"*, Institute of Physics Publishing, Bristol, U. K., 1994.

[WiT93] **Williams, M.E. and Trumper, D. L. (1993):** "Materials for Efficient High-Flux Magnetic Bearing Actuators", 2nd International Symposium on Magnetic Suspension Technology, Seattle, WA 1993.

[WoM68] **Woodson, H. H., and Melcher, J. R. (1968):** *Electromechanical Dynamics-Part I, II,* John Wiley & Sons Co., 1968.

[Yeh92] **Yeh, T. J. (1992):** *Dynamics and Control of High Precision Magnetically Levitated Vibration Isolation System,* Master Thesis, Department of Mechanical Engineering, Massachusetts Institute of Technology, Cambridge, MA, 1992.

[Zor89] **Zorbas D., (1989):** *Electric Machines, Principles, Applications, and Control Schematics*, West Publishing Company, 1989.

[Zyg91] Zygo AXIOM 2/20 Laser Measurement System Operation and Reference Manual, Zygo Corp. Middlefield CT , 1991.

APPENDIX

Appendix I: The Mechanical Drawing of Stage

Appendix II: The Simulink Blocks for Simulation

Appendix III: Control Code

Appendix I: The Mechanical Drawings of Stage

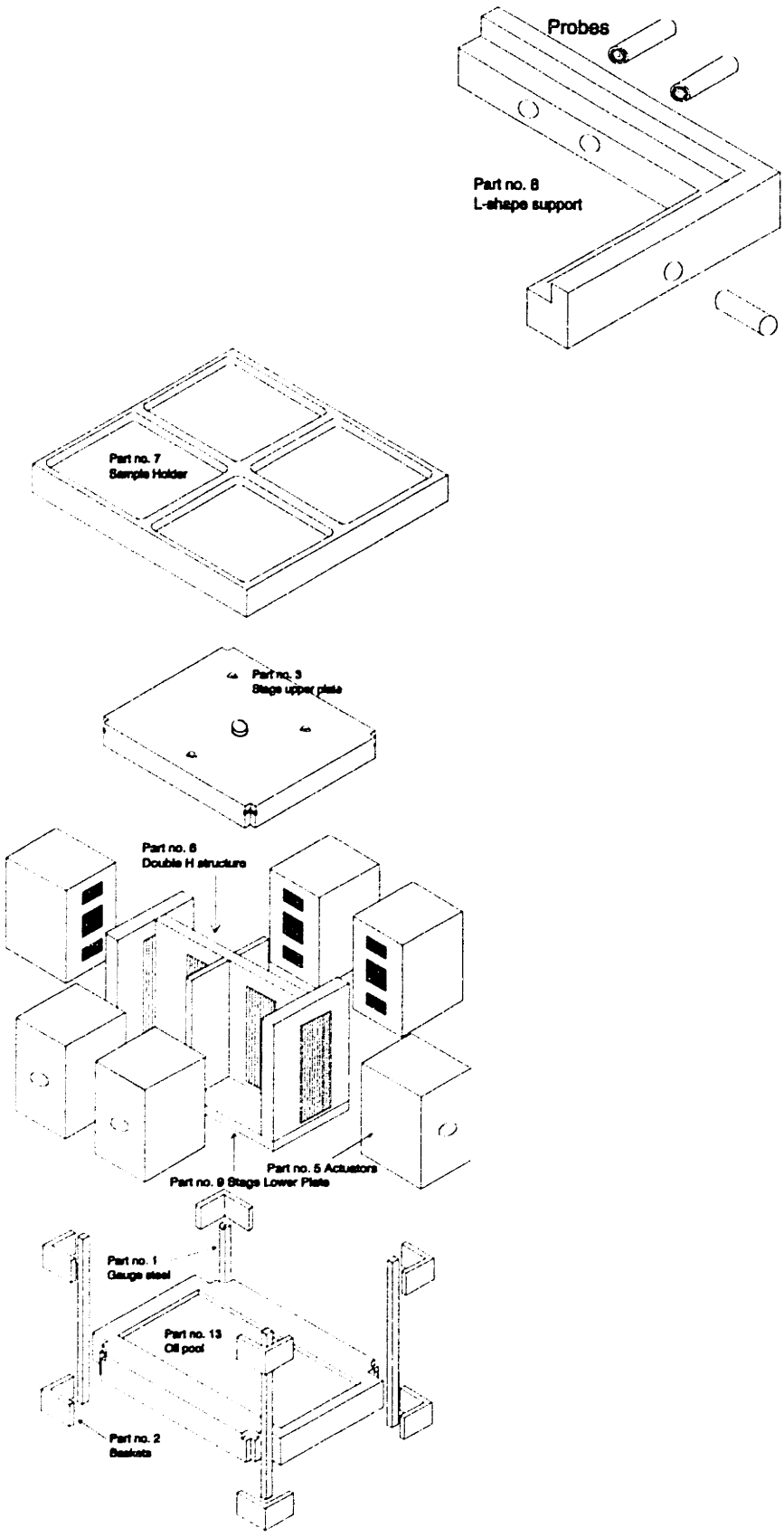

Figure A1.1 The exploded diagram of stage

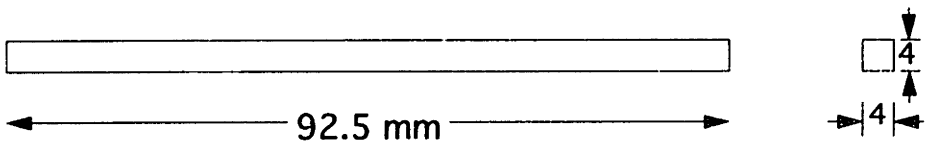

Part no. 1 (4 off)

Gauge steel

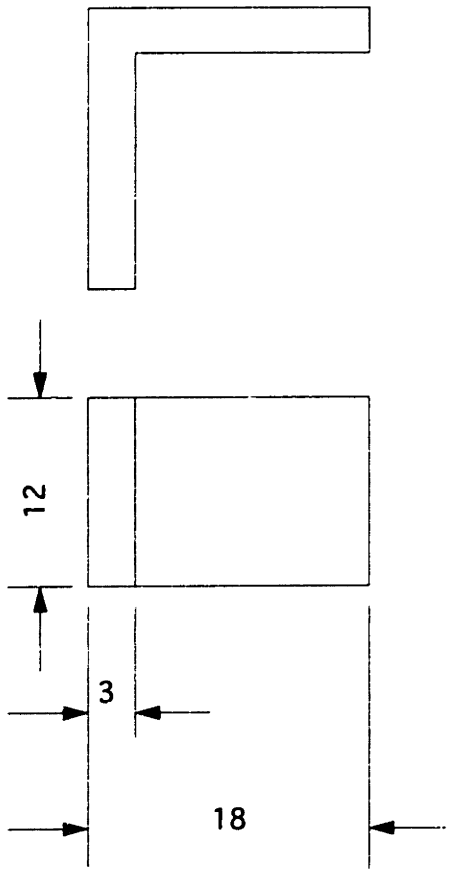

Part no. 2 (8 off)

Aluminum

Figure A1.2 Part no. 1 and part no. 2

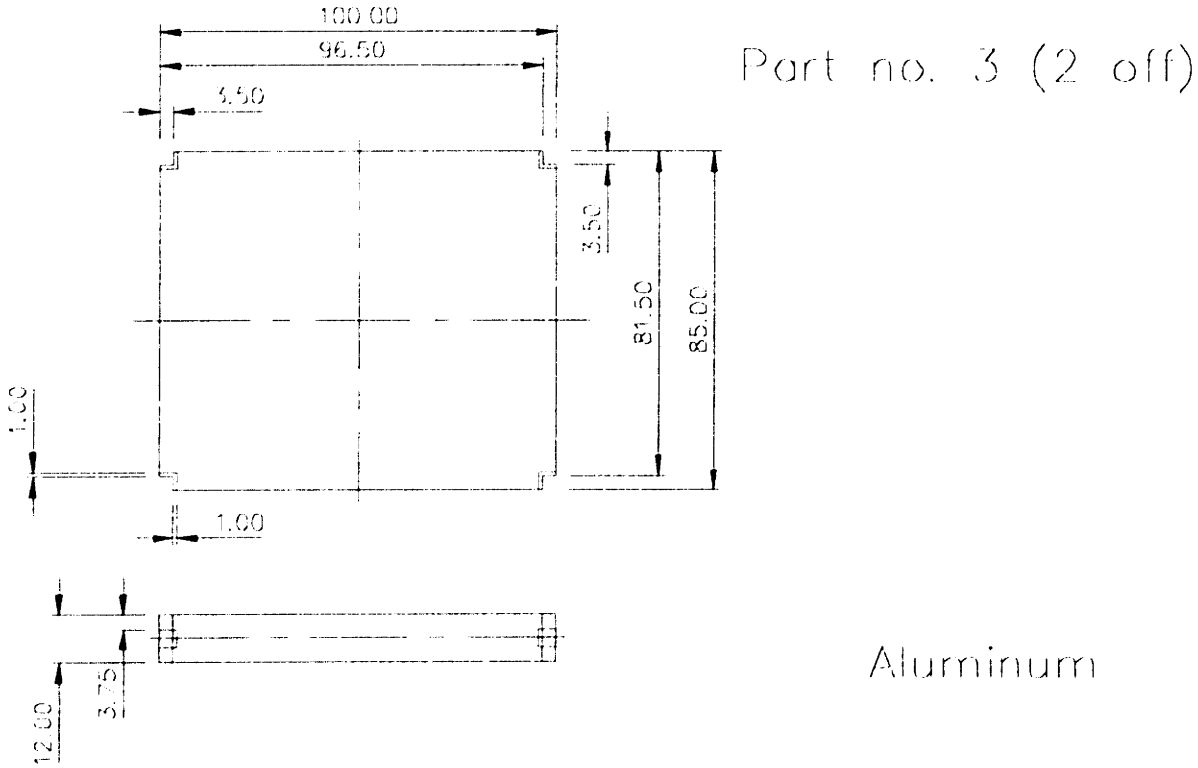

Figure A1.3 Part no. 3.

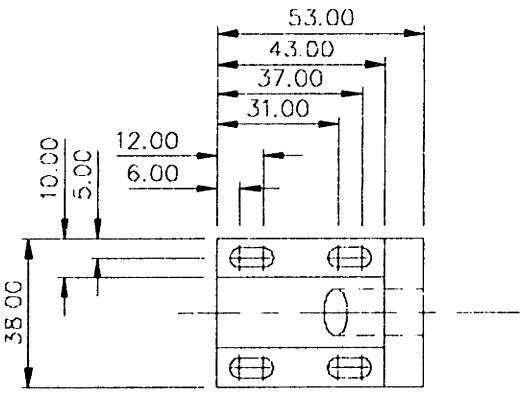

Part no. 4 (6 off)

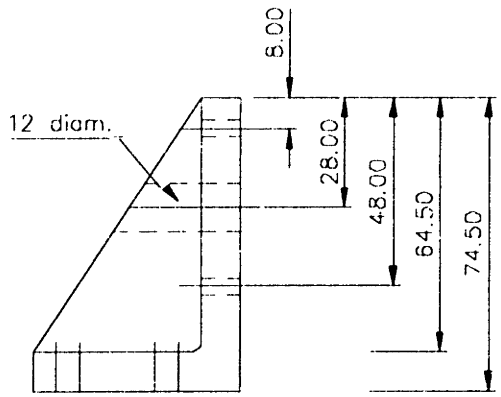

Aluminum

Figure A1.4 Part no. 4.

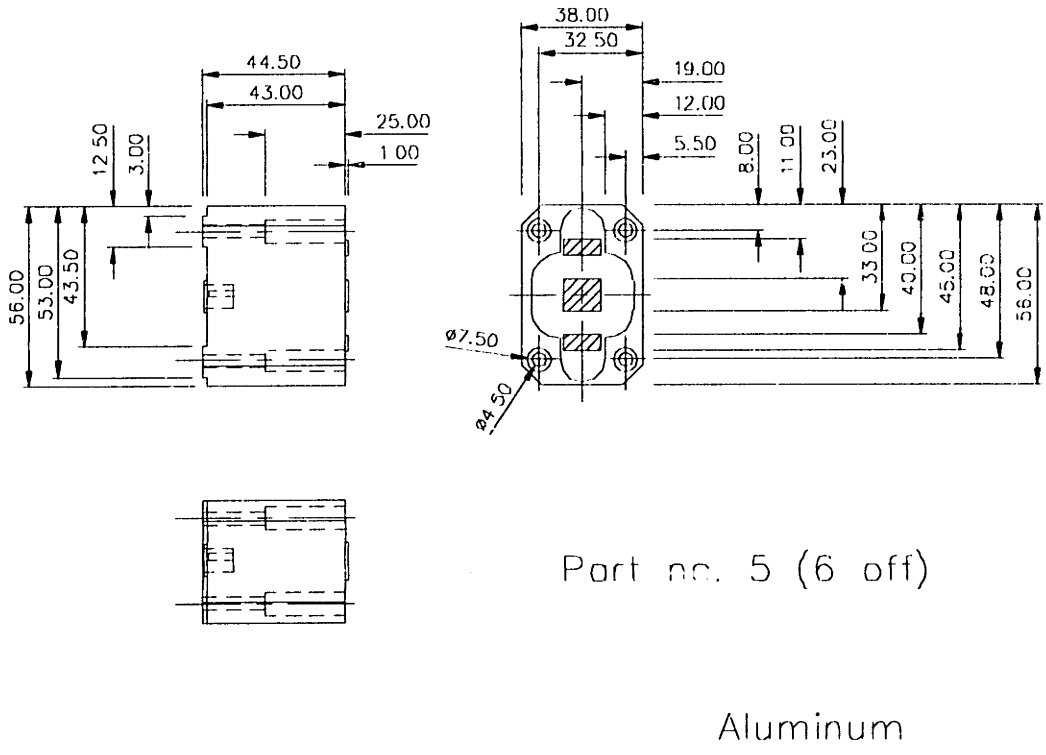

Figure A1.5 Part no. 5

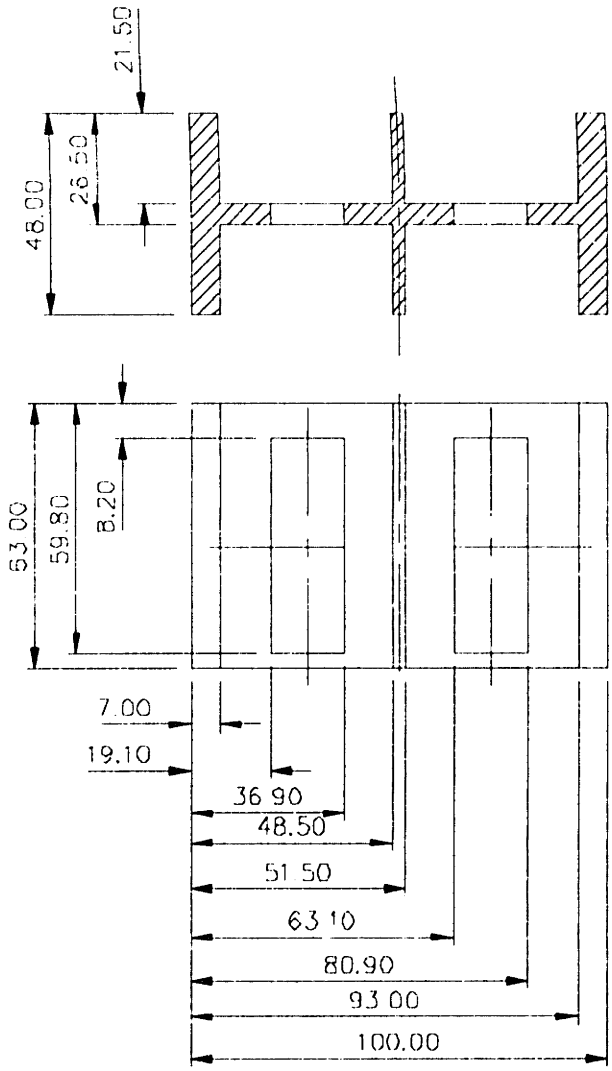

Figure A1.6 Part no. 6

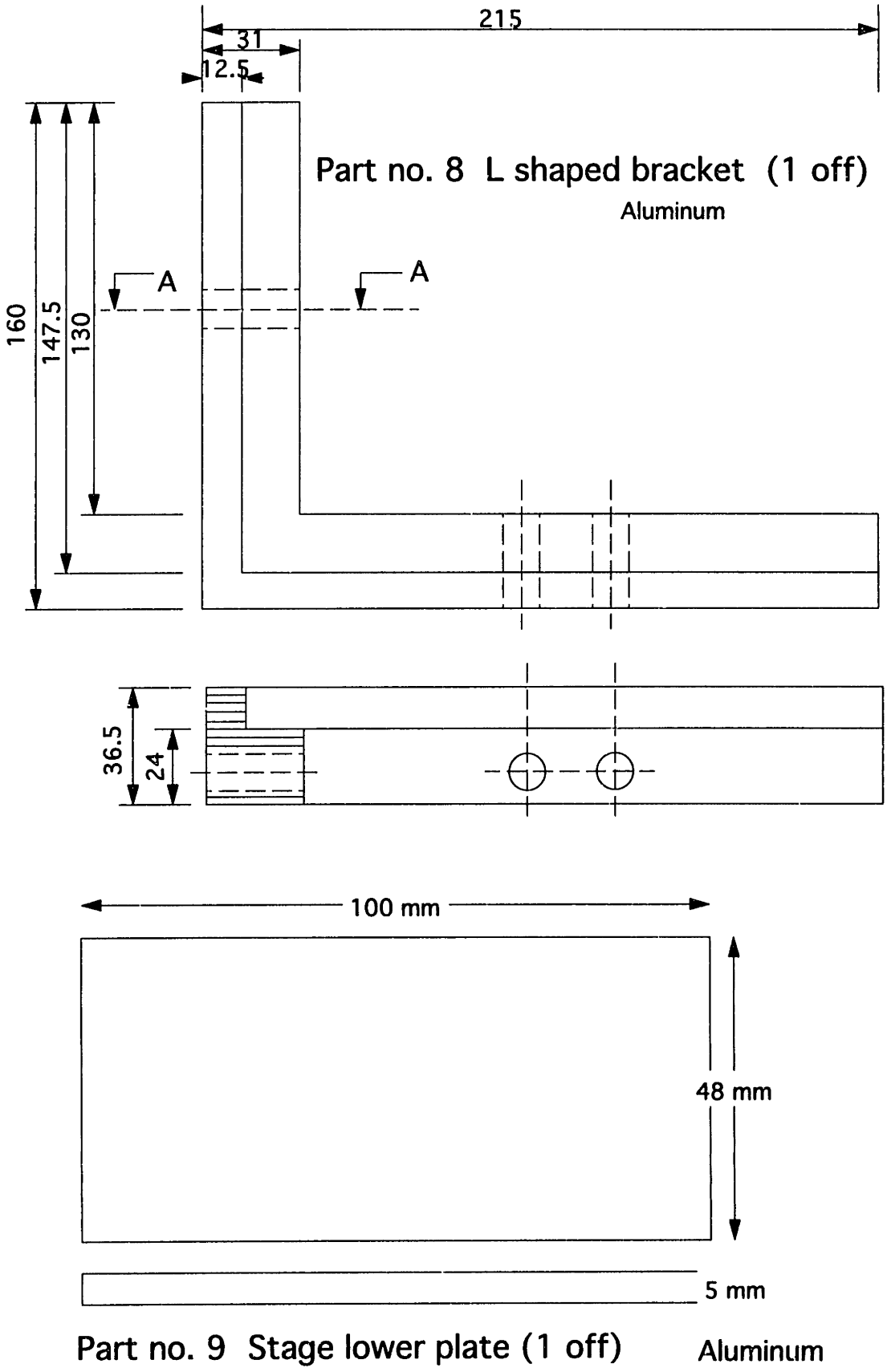

Figure A1.7 Part no. 8 and part no. 9.

Part no. 10, 11, 12 Sensor barket support block Aluminum

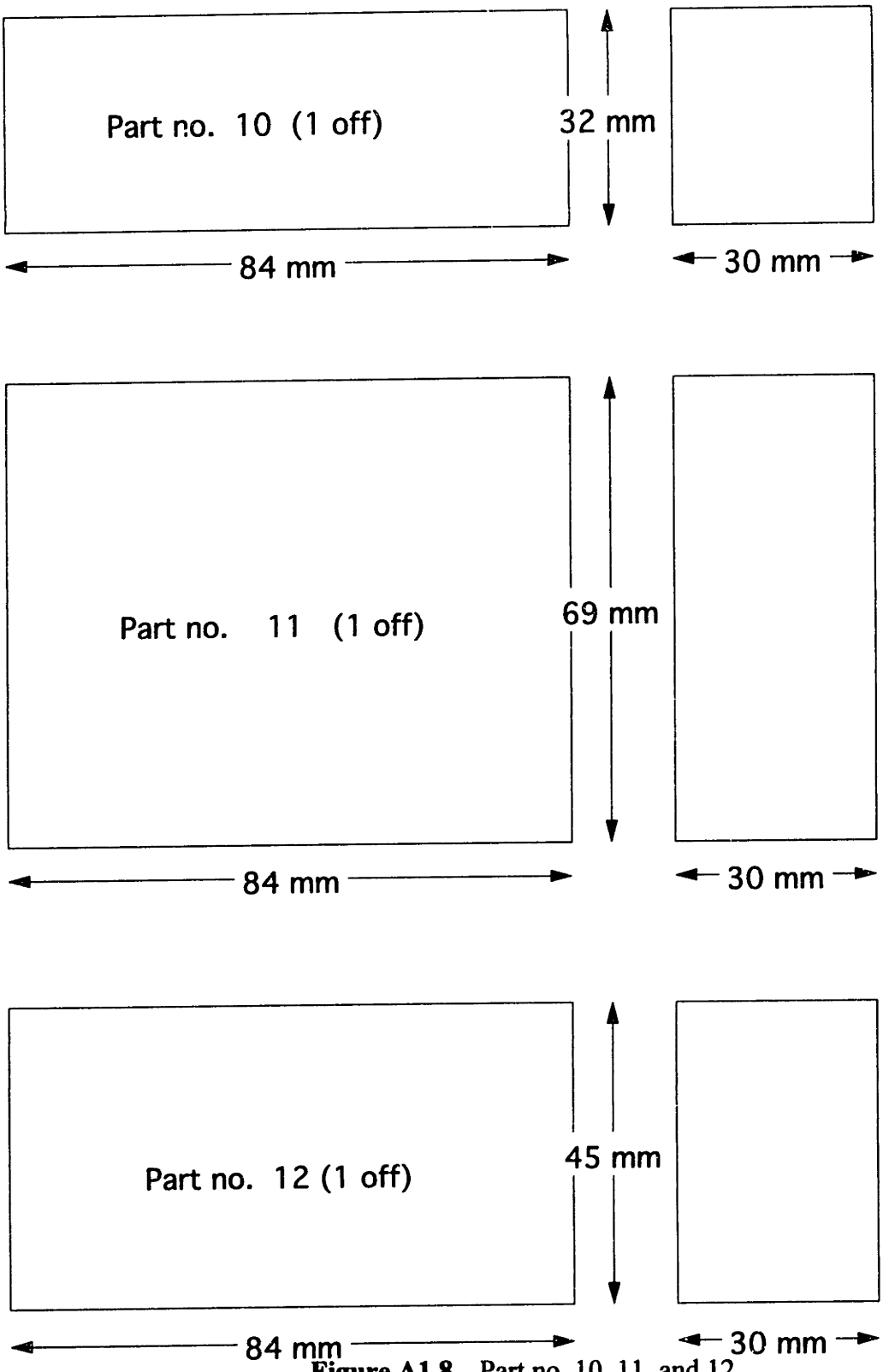

Figure A1.8 Part no. 10, 11, and 12.

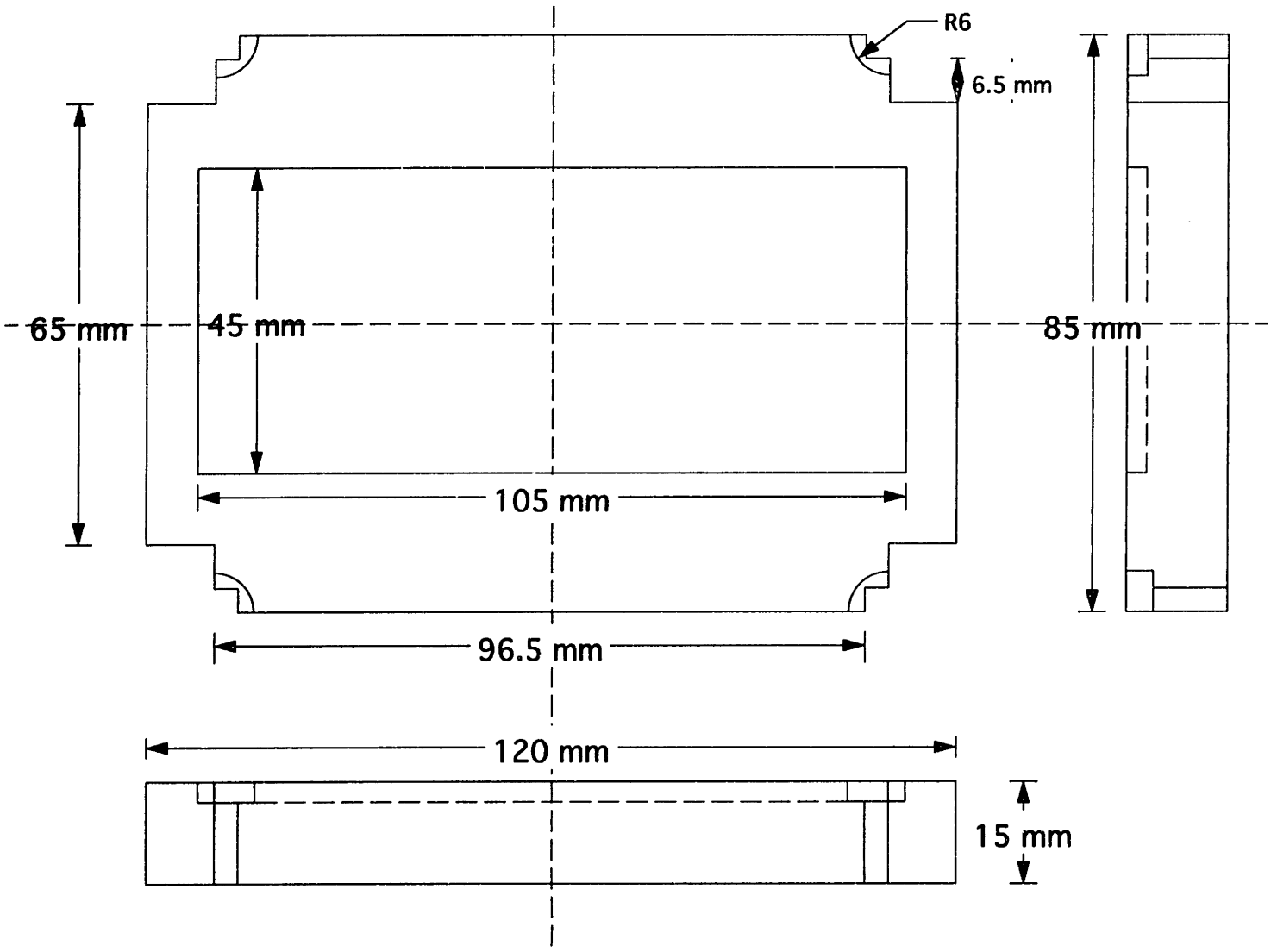

Part no. 13 The Pool for Viscasil (1 off) **Aluminum**

Figure A1.9 Part no. 13

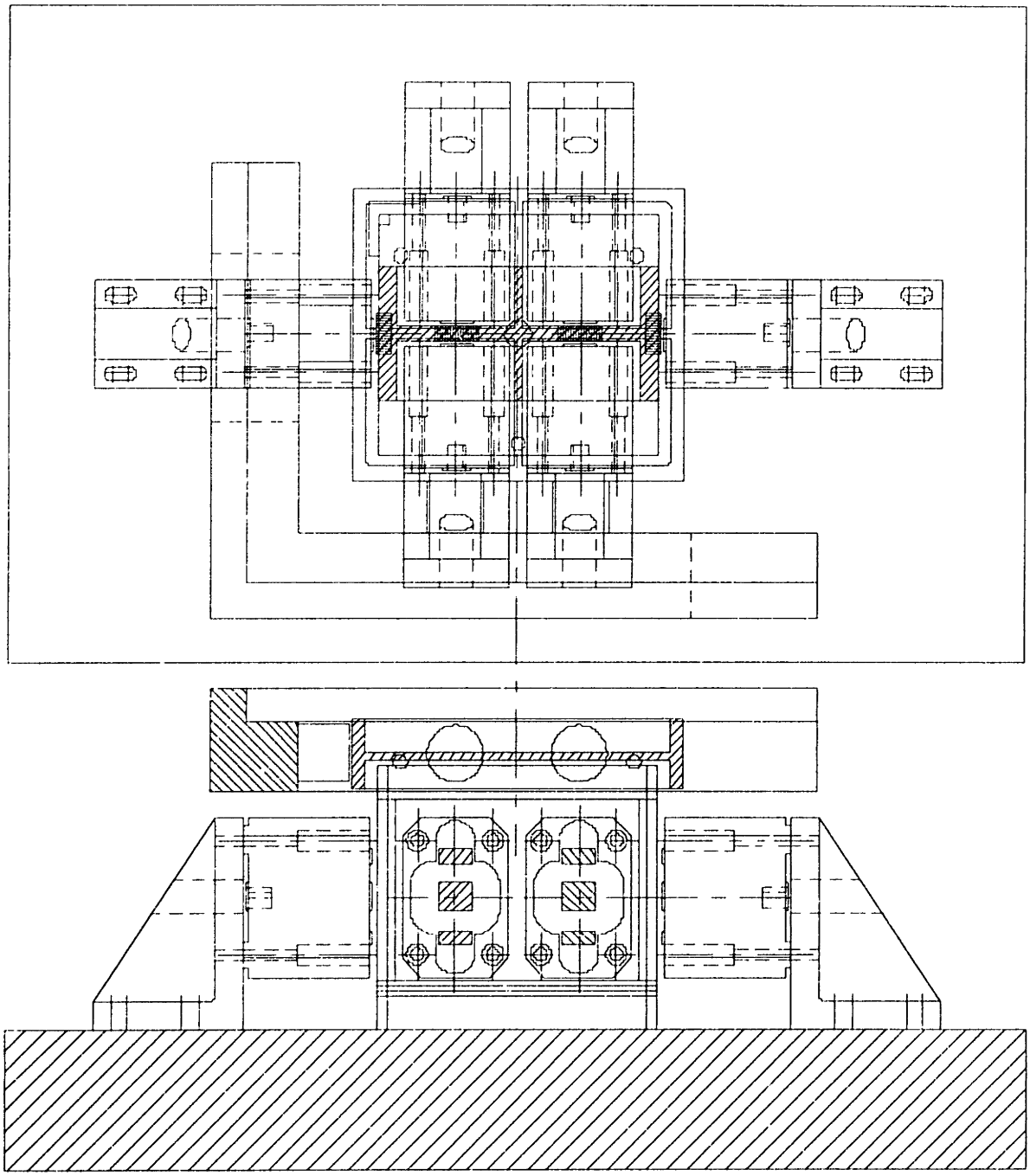

Figure A1.10 Overall assembly of stage and actuators.

Appendix II: Simulink Blocks for Simulation

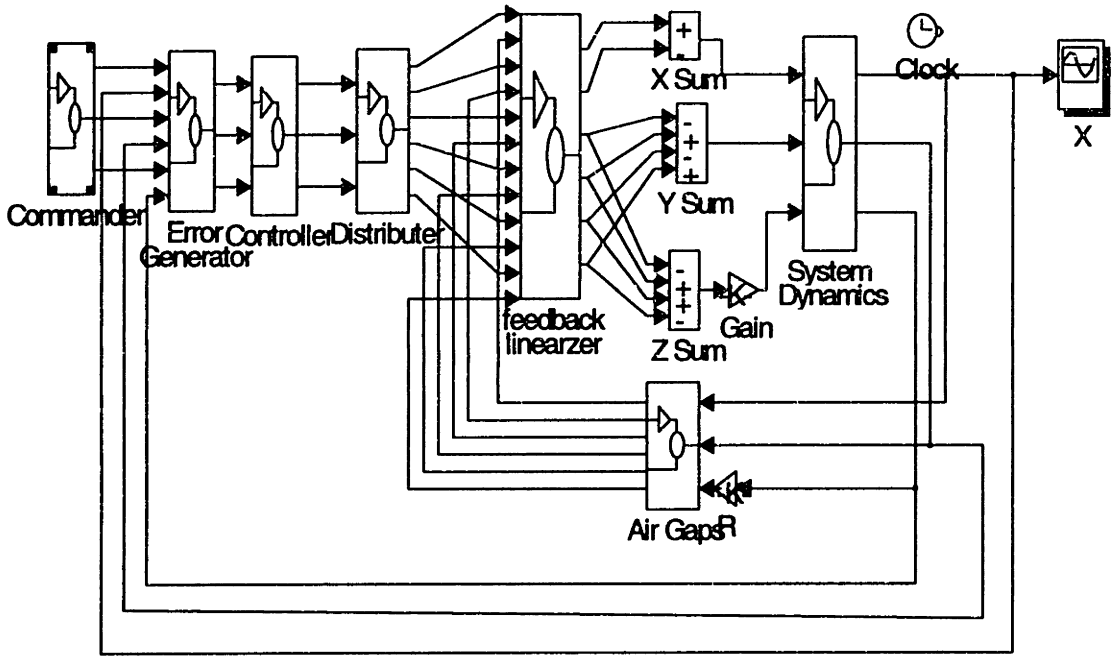

Figure A2.1 The overall Stage Simulation Block Diagram

This simulation block diagram contains several subgroups. They will be shown in the following pages.

commander: generating the desired motion command.
error generator: generating the motion errors by comparing the command and real signals.
controller: performing PI control.
distributor: distributing three control efforts to six actuators.
feedback linearizer: performing feedback linearization.
system dynamics: the plant dynamics for control.
air gaps: calculating the real air gaps for feedback linearization.

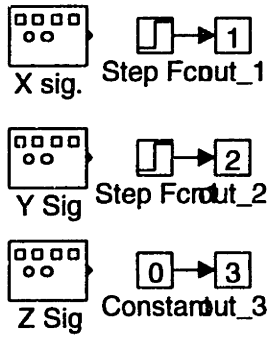

Figure A2.2 The command generator

The command generator is constituted by three function generators for generating different command for three degrees of freedom. They can be replaced by step command blocks or constant input.

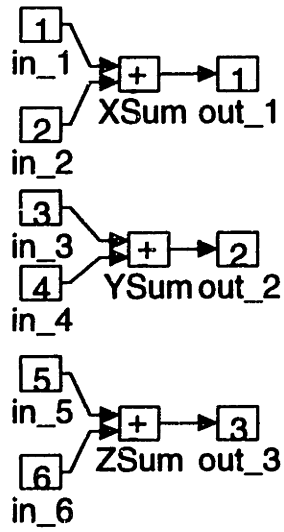

Figure A2.3 The error generator

Three summation blocks constitute this group. The inputs are command positions and real positions. After comparing them, the block outputs position errors.

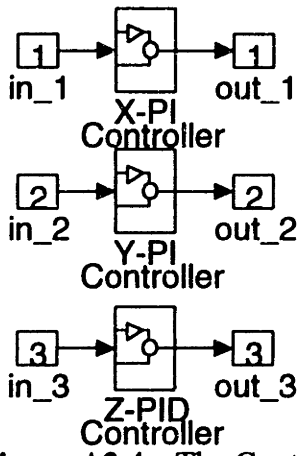

Figure A2.4 The Controller

The controller group is made of three PI controllers. Each PI controller has the same form but different parameters. It is shown in Figure A2.5.

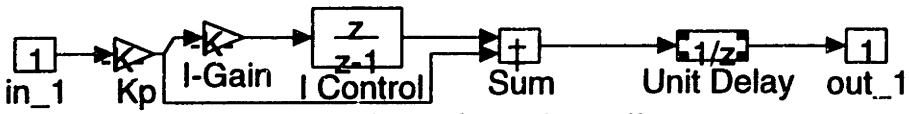

Figure A2.5 The PI Controller

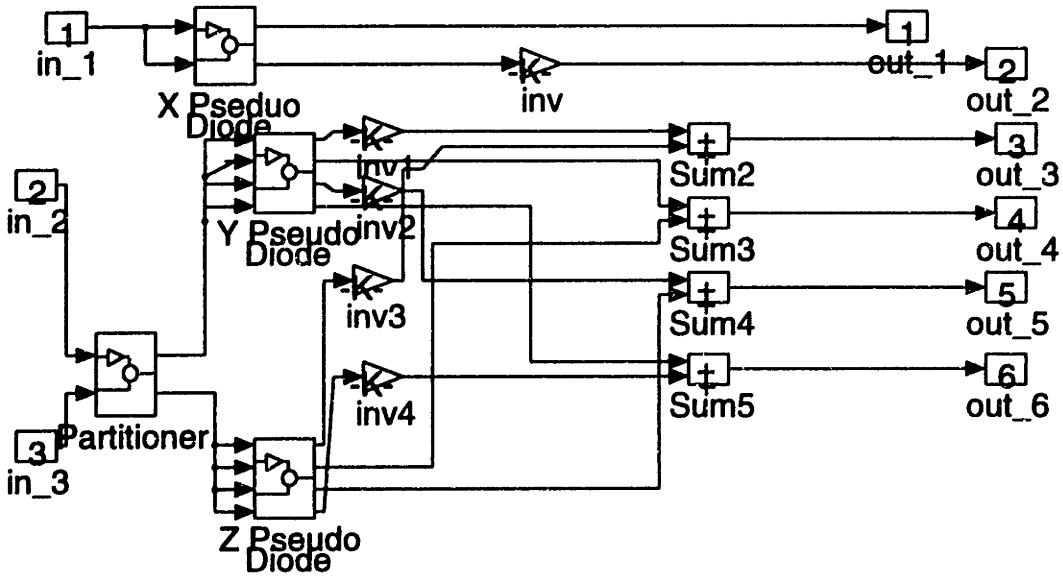

Figure A2.6 The Distributor

The main functions of distributor are to distribute the three control efforts to six actuators. There are several subgroups in it for simplification the representation. There are *The Partitioner*(Figure A2.7), and three *Pseudo Diodes*(Figure A2.8).

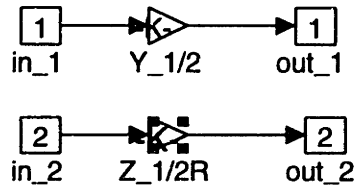

Figure A2.7 The Partitioner

The main function for this block is to divide the control effort by two since in Y or θ mode, there are two actuators in operation at the same time .

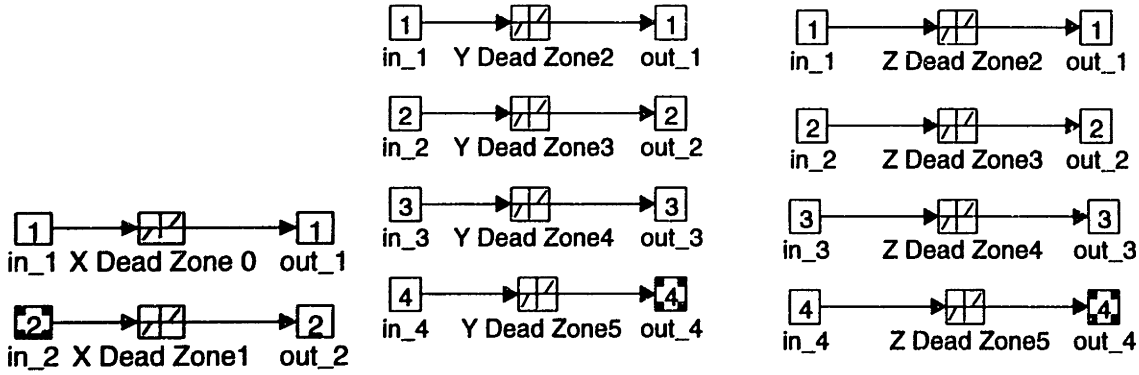

Figure A2.8 The Pseduo Diodes

Since the actuators can only exert attractive force, they only accept the positive command. For negative command, one need to convert it to a positive command for the opposite actuator. This is the reason why we need this block.

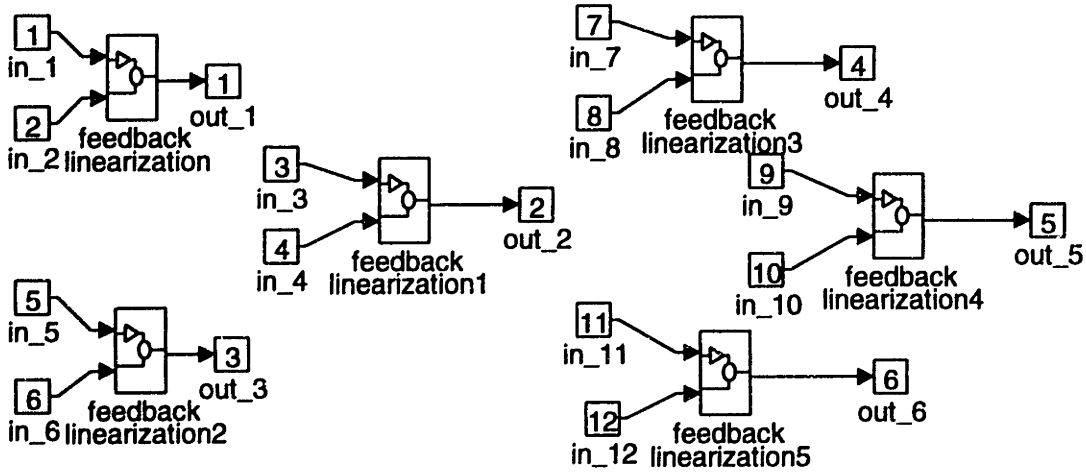

Figure A2.9 The Feedback Linearizer

This block is used for nonlinear compensation of electromagnetic actuators. It is constituted by six feedback linearization blocks. (Figure A2.10)

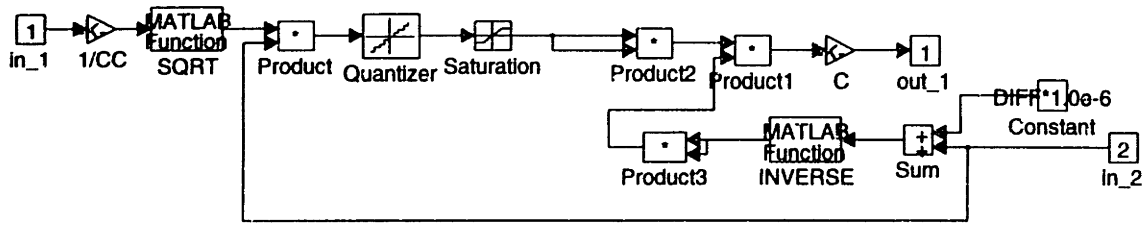

Figure A2.10 The Feedback Linearization

This block performs the normal procedures for feedback linearization. Moreover, the real and calibrated electromagnetic constants can be set to two different values for investigating the error motion. The nominal gaps of two actuators may set to two values for simulating the unequal gap effect here too.

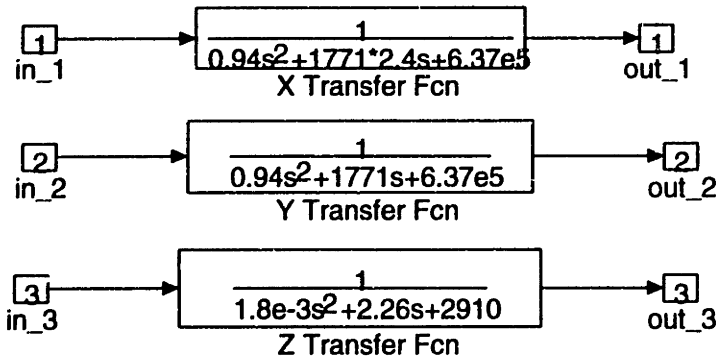

Figure A2.11 The System Dynamics

There are three transfer functions in this block to represent the dynamics of three modes.

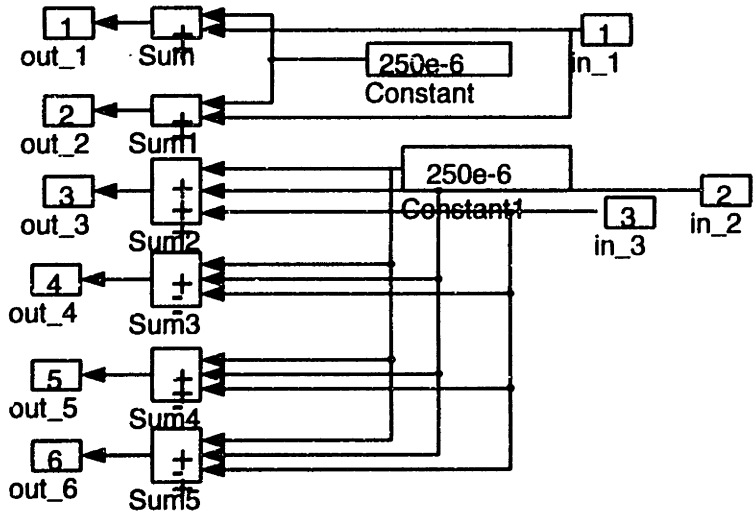

Figure A2.12 The Air Gaps

This block decides the real air gaps between the stage and six actuators.

Appendix III: The Control Code

```
/*************************************/
/*                                   */
/*        Conpid3.c                  */
/*                                   */
/*    This program do the control for the   */
/*    magnectic actuators for X-Y stage.    */
/*    D/A board:    DATEL 422               */
/*    A/D board:    NI-ATMIO-16L            */
/*************************************/

/* June 2, 1994                      */
/* Rev Sep 26, 1994                  */
/* Rev Oct 04, 1994                  */
/* Rev Nov 10, 1994                  */
/* Use instaneous AD & DA conv.      */
/* Rev. Nov 24, 1994                 */
/* Add a LEAD Work on controller     */

#include <c:\c600\include\stdio.h>
#include <c:\c600\include\conio.h>
#include <c:\c600\include\math.h>
#include <c:\c600\include\malloc.h>
#include <c:\c600\include\utility.h>
#include <c:\c600\include\stdlib.h>


/*    A/D Register Address Definition    */

#define AD_BASE_addr          0x220
                /*addr. of MIO-16 */
#define AD_comm_reg_1
                AD_BASE_addr
#define AD_comm_reg_2
                AD_BASE_addr + 0x02
#define AD_stat_reg          AD_BASE_addr
#define AD_start_conv
                AD_BASE_addr + 0x08
#define AD_start_daq
                AD_BASE_addr + 0x0a
#define AD_clear
                AD_BASE_addr + 0x0c
#define ext_strobe
                AD_BASE_addr +0x0e
#define int2clr
                AD_BASE_addr + 0x14
#define mux_cntr
                AD_BASE_addr + 0x04
#define mux_gain
                AD_BASE_addr + 0x06
#define FIFO
                AD_BASE_addr + 0x16
#define RTSIswtch
                AD_BASE_addr + 0x1E
#define RTSIstrbe
                AD_BASE_addr + 0x1f
#define CONVERSION          (4096.0/20)
#define AD_gain_val          0x00
                /* Here we define gain = 1
                 if 0x40, gain = 10,
                 if 0x80, gain = 100,
                 if 0xC0, gain = 500.
                */

/*    AM9513 counter/timer register define   */

#define AD_counter_dreg
                AD_BASE_addr + 0x18
#define AD_counter_creg
                AD_BASE_addr + 0x1A
#define AD_counter_sreg
                AD_BASE_addr + 0x1A


/*    DATEL D/A 422 define              */

#define DA_BASE              0x300
#define DA_command_reg
                        DA_BASE
#define DA_counter0_reg
                        DA_BASE + 0x08
#define DA_counter1_reg
                        DA_BASE + 0x0A
#define DA_control_reg
                        DA_BASE + 0x0E
#define DA_channel_reg
                        DA_BASE + 0x02
#define DA_dac_reg          DA_BASE + 0x04
#define DA_status_reg       DA_BASE
#define DA_sim_up_reg
                        DA_BASE + 0x06


/*    Stage Paramete· define            */

#define S_x       637000     /* X-direction EM
compliance */
#define S_y       637000     /* Y-direction EM
compliance */
#define G         500        /* Torsional Stiffness of
stage */
#define R         0.0225     /* the arm of force
couple */
```

```
#define CC1        0.0000041
        /* EM force constant for 2 X-forcer*/
#define CC2        0.000009
        /* EM force constant for 4 Y-forcer */
#define g_x        0.000300
        /* initial gap of X-dir. mag */
#define g_y        0.000300
        /* initial gap of Y-dir. mag */
#define AMP        0.095
        /* Current amplifier gain, i = AMP*v */
#define f_offset   0.01
        /* Software bias force */

/*     Discrete PI control definition        */

#define KP_def     2.5  /* Proportional gain */
#define TS_def     (3.0)     /*Sampling period */
#define TI_def     (1.0/333.3)
                   /*Integral Const. */
#define KD_def     (0.0)
                   /*Deravtive Const. */
#define SENSOR_gain      200000.0       /* A/D
A scaling factor that position = SF2 * volt */
#define RATIO   1.5    /* Ratio of Kp between
linear & Angular motio */

#define NPOINTS 3000
#define PI     3.14159625
#define SAT_0  40.0
#define SAT_1  40.0
#define SAT_2  50.0


/*     Define Procedure       */

void set_timer(void);
void init9513();
void AD_set();
void DA_set();
void change();
float  input(float x_out[]);
        /* Read position from A/D */
float  command_gen(float x_c[]);
        /* Generate Path */
float  LEAD(float error_in[], float x_lead[], float
x_prev[]);
float   PID_control(float lead_in[], float now[],
float prev[], float accu[]);
                        /* Discrete PI control */
float        force_distb(float    pid__in[],    float
force_act[]);
            /* Distribute 3 forces to 6 actuators */
float   fback_linza(float f_desire[], float x_p[],
float current[]);
                        /* Feedback Linearization */
void    output(float vcurrent[]);       /* write data
to D/A port */


/*     Global Variable declaration     */

float  Ts,Kp,Ti,Kd,
      x_c[3],       /* command position */
      volt[3],      /* AD READ out */
      f_c[3],       /* command force */
      err[3],       /* position error */
      x_f[3],
/* positions which determined by sensor */
      x_pi[3],      /* output of PI controller */
      force[6],
/* command force in 6 actuators */
      out[6],       /* output of 6 D/A channel */
      prev[3],
/* The last set of values in PID control */
      x_prev[3],
/* The last set of values in Lead Compensation
*/
      x_lead[3],
/* Result of Lead compensation */
      accu[3],
 /* The past accumulate of error */
      Sature[3],
/* 3 Maximum forces in system,    */
      ibias[6],
 /* Bias current set for actuators */
      freq,         /* Sinusoidal frequency (Hz) */
      CC[6],
      ioutput[6],
      offset[3],
      aa[3], bb[3], cc[3],
/* Convinent Way to reduce the math cal in
control loop */
      gain_1, gain_2, gain_3,
      hertz;

int    gain;         /* gain of AT-MIO-16 */
unsigned long     index;          /* an index to
dealing the global clock */
int    AD_channel[3]; /* AD_channel number */
int    chan_no;
long   count;        /* cycle counter */
char menutext[]={"\n\
      r----Run controller\n\
      t----Change Sampling period\n\
      p----Change P gain\n\
      d----Change D gain\n\
      i----Change I gain\n\
      enter selection:>"} ;
```

```
void main()
{
    int i,j,k;
    int choice;
    float temp, *pos, *com, *tim;
    char ans[10],filename[20], dec[10];
    FILE *fout;
    int done;
    Ts = TS_def;
    Kp = KP_def;
    Ti = TI_def;
    Kd = KD_def;
    done = 1;
     printf(" Please adjust cap. probe in which
the read out is between 0 & -2\n");
      printf(" Please input command sinusoidal
frequency Hz\n");
    scanf("%f", &freq);
    printf("%f\n",freq);

    while(done == 1) {
   /* clearscreen();
    setcursorpos(4,0);  */
       printf("PID control- Current parameter
values:\n\n");
      printf("\tSample period (KHz): %.2f\n",
Ts);
    printf("\tProportional gain: %.2f\n",Kp);
    printf("\tDerivative gain: %.2f\n",Kd);
    printf("\tIntegrator gain: %.4f\n",Ti);


    printf("\n\nOption Menu:\n");
    printf("%s",menutext);
    scanf("%s",ans);
    choice = ans[0];
    switch(choice){
        case 'r':  /* run controller */
            done = 0;
            break;
        case 't':  /* new sampling time */
              printf("Enter sample period in
KHz:\n");
            scanf("%f",&temp);
            Ts = temp;
             /* Ts = queryfloat("Enter sample
period in KHz:>");  */
            break;
        case 'p':  /* new P gain */
                printf("Enter Position gain,
Kp:\n");
            scanf("%f",&temp);
            Kp = temp;
           /*  Kp = queryfloat("Enter position
gain, Kp :>");  */
            break;
        case 'd':  /* new D gain */
                printf("Enter derivative gain,
Kd:\n");
            scanf("%f",&temp);
            Kd = temp;

                /*  Kd = queryfloat("Enter
derivative gain, Kd :>");  */
            break;
        case 'i':  /* new I gain */
                 printf("Enter integral gain,
Ti:\n");
            scanf("%f",&temp);
            Ti = temp;

                 /* Ti = queryfloat("Enter
integrator gain , Ti :>");  */
            break;

        default:
        break;  }
    }
                        if((pos = (float
*)malloc(NPOINTS*sizeof(float)))==NULL){
        printf("Cannot allocate memory for
arrays!\n");
        exit(1);
    }
                        if((com = (float
*)malloc(NPOINTS*sizeof(float)))==NULL){
        printf("Cannot allocate memory for
arrays!\n");
        exit(1);
    }
                        if((tim = (float
*)malloc(NPOINTS*sizeof(float)))==NULL){
        printf("Cannot allocate memory for
arrays!\n");
        exit(1);
    }

    for(i=0;i<3;i++)
    {
        accu[i] =0;
        prev[i] =0;
        x_prev[i] =0;
        AD_channel[i] =i;
    }
    index = 0;
```

```
                /* Here we select channel 0,1, &2
as
                    our input channel   */
      Sature[0] = SAT_0;       /* Maximum X-dir
force */
      Sature[1] = SAT_1;       /* Maximum Y-dir
force */
      Sature[2] = SAT_2;       /* Maximum Z-rir
torque */

      CC[0] = CC1;
      CC[1] = CC[0];
      CC[2] = CC2;
      CC[3] = CC[2];
      CC[4] = CC[2];
      CC[5] = CC[2];

      Ts = 1/(1000*Ts);
      aa[0] = Kp*(1+Ts/Ti);
      aa[1] = aa[0];
      aa[2] = Kp*(1+Ts/Ti +Kd/Ts)/RATIO;
      bb[0] = Kp*Ts/Ti;
      bb[1] = bb[0];
      bb[2] = bb[0]/RATIO;
      cc[0] = 0;
      cc[1] = cc[0];
      cc[2] = Kp*Kd/(Ts*RATIO);
         /* Kp for angular motion is Kp(linear
motion)/Ratio */
      gain_1 =S_x/SENSOR_gain;
      gain_2 =S_y/(2*SENSOR_gain);
      gain_3 =S_y/(2*SENSOR_gain);
      hertz = 2*PI*freq*Ts;

      AD_set();
      DA_set();
      for (i=0;i<6;i++)
           ioutput[i]=0;
      output(ioutput);
      for(i=0; i<100; i++)
           input(volt);
      for(i=0;i<3;i++)
           offset[i] = volt[i];
             printf("\nOffset Value is %f, %f,
%f\n",offset[0],offset[1],offset[2]);
      printf("\nPress any key to continue.\n");
      while(!kbhit());
      getch();
        printf("Begining Computer control.  Press
any key to quit.\n");
      while(!kbhit())

      {
        input(volt);       /* Read Data from A/D
board */
      x_f[0] = volt[0] - offset[0];
           x_f[1] = (volt[1]+volt[2] - offset[1]-
offset[2])/2;
                x_f[2] = (volt[1]-volt[2] -
offset[1]+offset[2]);

              command_gen(x_c);   /* Generate
command trajectory */

      for(i=0;i<3;i++)
           err[i] = x_c[i] - x_f[i];
           LEAD(err,x_lead,x_prev);
           PID_control(x_lead,x_pi,prev,accu);
           force_distb(x_pi, force);  /* Generate
command force in 6 actuators */
            fback_linza(force, x_f, ioutput);  /*
Perform feedback linearization */
      output(ioutput);

      if(index < NPOINTS){
           pos[index] = volt[0]-offset[0];
           com[index] = volt[1]-offset[1];
           tim[index] = volt[2]-offset[2];
           } /* If */
      index ++;
      }    /* while loop! */
      for (i=0;i<6;i++)
           ioutput[i]=0;
      output(ioutput);
      printf("Store data to Disk <y/n>?\n");
      scanf("%s", &dec);
      if (dec[0] == 'y') {
           printf("please input filename *.asc...");
           scanf("%s", &filename);
           printf("%s\n",filename);
           fout = fopen(filename, "w");
           printf(
                    "Storing to file %s in current
directry...",filename);
           for (i=0;i<NPOINTS;i++)
                              fprintf(fout,"%f %f
%f\n",pos[i],com[i],tim[i]);
           printf("Done\n");
           fclose(fout);
           }


} /* End of MAIN PROGRAM !  */
```

```
void AD_set()
{
      int CR1_copy;          /* software copy of
mux_gain_r */
     int st_bin;          /* set binary format */
     int i;
     int samp_count, samp_int;

/* Initialize the AT-MIO-16 board          */
/* disable DMA and interrupts, initialize     */
/* A/D circuitry, clear FIFO, input chan 0    */
/* gain = 1, RTSI pins reset               */


}  /* AD_set */


void DA_set()
{
     int yy;
/* To initial DA board and generate a certain rate
clock */

unsigned timer0_count, timer1_count, lsb, msb,
lsb_1, msb_1;

     outpw(DA_command_reg, 0x40);

/* To get  Sampling rate */
     yy = 8000/(1000*Ts);
      timer0_count = 1000;   /* Divide by 1000
in counter 0 */
      timer1_count = yy;      /* Divide by 4 in
counter 1 */

      lsb = timer0_count % 256;      /* 8-bit lsb
using modulo operator */
     msb = timer0_count/256;       /* 8-bit msb
using integer division */
        outpw(DA_command_reg, 0x40);    /*
Trigger update mode, no channel increment */

     outp(DA_control_reg, 0x34);    /* Counter
0, load lsb then msb, Mode 2 */
       outp(DA_counter0_reg, lsb);     /* write
counter 0 lsb */
      outp(DA_counter0_reg, msb);     /* write
counter 0 msb */

     outp(DA_control_reg, 0x74);    /* Counter
1, load lsb then msb, Mode 2 */
     if (timer1_count < 256)
     {
                    outp(DA_counter1_reg,
timer1_count); /*write counter 1 lsb */
          outp(DA_counter1_reg, 0);          /*
write counter 1 msb */
     }
     else
     {
          lsb_1 = timer1_count % 256;    /* 8-
bit lsb using modulo operator */
           msb_1 = timer1_count / 256;    /* 8-
bit msb using integer division */
            outp(DA_counter1_reg, lsb_1);   /*
write counter1 lsb */
           outp(DA_counter1_reg, msb_1);   /*
WRITE COUNTER1 MSB */
     }  /* If */

     outpw(DA_dac_reg, 0x800); /*initialize */
     outpw(DA_sim_up_reg, 0x10);  /* to set bit
15 = 1 in Status register */

}  /* DA_set */


float command_gen( float x_c[])
{
      /* j: trajectory frequency, k: amplitude */
     x_c[0] = 5*sin(hertz*index);
     x_c[1] = 5; /*2*sin(hertz*index);*/
     x_c[2] = 0;
}




float input(float volta[])
/*      Here we use AT-MIO-16 as the A/D and
we use channel 0,1,2
                    by   its   differential   mode
*/

{


     int j,k;

      for(j=0;j<3;j++)
      {
       chan_no = j;
       change();
       outpw(AD_start_conv, 0x00);
```

```
            while((inpw(AD_stat_reg)& 0x2000)
!=0x2000);
            k = inpw(FIFO);
            volta[j] = (k+1.0)/204.8;

            /*  printf("volta[%d] = %f\n",j,volt[j]);
*/
            outpw(AD_clear, 0x00);

      } /* for j */
                        /*      printf("%f,    %f,
%f\n",volt[0],volt[1],volt[2]); */

} /* input */


void change()
{
      int i;
     /*  CR1_copy = 0x00;  */
      outpw(AD_comm_reg_1, 0x00);
      outpw(AD_comm_reg_2, 0x00);

      outpw(mux_gain, chan_no);
      outpw(AD_clear, 0x00);
      outpw(int2clr, 0x00);
  /*    for (i=0; i<56 ; i++)
            outp(RTSIswtch, 0);
      outp(RTSIstrbe, 0);       */



      init9513();
      outpw(mux_gain, chan_no);
      outpw(AD_comm_reg_1, 0x00);
}


void init9513()
{
      int i;

       outpw(AD_counter_creg, 0xFFFF);      /*
master reset */
       outpw(AD_counter_creg, 0xFFEF);      /*
set up 16-bit mode */
       outpw(AD_counter_creg, 0xFF17);      /*
point to m. mode reg */
       outpw(AD_counter_dreg, 0xF000);      /*
load m.m value */

      for(i=1; i<6; i++)
      {
            outpw(AD_counter_creg, 0xFF00+i);
/* select CMR  */
            outpw(AD_counter_dreg, 0x0004);  /*
store mode val */
            outpw(AD_counter_creg, 0xFF08+i);
/* select load reg */
            outpw(AD_counter_dreg, 0x0003);  /*
load l.r. value */
      }  /* for loop */

            outpw(AD_counter_creg,  0xFF5F);
/* load reg values  */

}  /* int9513 */


float LEAD(float error_in[], float x_lead[], float
x_prev[])
{
      int i;
      for(i=0; i<3; i++)
      {
                        x_lead[i]  =  error_in[i]  -
0.79*x_prev[i];
            x_prev[i] = error_in[i];
      }
}



float    PID_control(float x_lead[],float now[],
float prev[], float accu[])
/*  Perform Discrete PI control  with anti-windup
*/
{
 int i;
    /*  bb = Kp*Ts/Ti;    */
    /*  aa = Kp*(1+Ts/Ti + Kd/Ts);  */
    /*  cc = Kp*Kd/Ts;  */
  for(i=0; i<3; i++)
      {
            now[i] = accu[i] + x_lead[i]*aa[i] -
 cc[i]*prev[i];
            accu[i] = bb[i]*x_lead[i]+ accu[i];
            if (accu[i] >= Sature[i])
                  accu[i] = Sature[i];
            if (now[i] >= Sature[i])
                  now[i] = Sature[i];
            if (accu[i] <= -Sature[i])
                  accu[i] = -Sature[i];
            if (now[i] <= -Sature[i])
                  now[i] = -Sature[i];
```

```
            /*  printf("now[2]= %f\n",now[2]);
*/
        prev[i] = now[i];
    }           /* for loop */
 } /* PID_control */


float force_distb( float pid_in[], float
force_act[])
/* To distribution 3 desired position inputs to 6
actuators */
/* due to the fact that the actuator can only exert
*/
/* attractive force.                          */

{
    float fact_31, fact_32, fact_41, fact_42;
    float fact_51, fact_52, fact_61, fact_62;

    if(pid_in[0] > 0)
        {
            force_act[0] = pid_in[0]*gain_1
+ f_offset;
            force_act[1] = f_offset;
        }
    else
        {
            force_act[0] = f_offset;
            force_act[1] = -pid_in[0]*gain_1;
        };

    if(pid_in[1] < 0)
        {
            fact_31 = -pid_in[1]*gain_2 +
f_offset;
            fact_51 = fact_31;
            fact_41 = f_offset;
            fact_61 = f_offset;
        }
    else
        {
            fact_41 = pid_in[1]*gain_2 +
f_offset;
            fact_61 = fact_41;
            fact_31 = f_offset;
            fact_51 = f_offset;
        };

    if(pid_in[2] < 0)
        {
            fact_32 = -pid_in[2]*gain_3 +
f_offset;
            fact_62 = fact_32;
            fact_42 = f_offset;
        }
    else
        {
            fact_42 = pid_in[2]*gain_3 +
f_offset;
            fact_52 = fact_42;
            fact_32 = f_offset;
            fact_62 = f_offset;
        };

    force_act[2] = fact_31 + fact_32;
    force_act[3] = fact_41 + fact_42;
    force_act[4] = fact_51 + fact_52;
    force_act[5] = fact_61 + fact_62;
   /*  printf("f32= = %f\n",fact_32);       */

} /* force_distrb */


float fback_linza(float f_desire[], float x_p[],
float current[])
/* Using feedback linearization method to
linearize the output */
/* Input: desired force, actual position, output:
desired voltage */
/*    I    =    X    *    SQRT(F_desired/CC)
*/
{
    float dist[6];
    int i;

    x_p[0] = x_p[0]/SENSOR_gain;
    x_p[1] = x_p[1]/SENSOR_gain;
    x_p[2] = x_p[2]/(2*R*SENSOR_gain);
    dist[0] = g_x - x_p[0] ;
    dist[1] = g_x + x_p[0] ;
    dist[2] = g_y - x_p[1] - R*x_p[2];
    dist[3] = g_y + x_p[1] + R*x_p[2];
    dist[4] = g_y - x_p[1] + R*x_p[2];
    dist[5] = g_y + x_p[1] - R*x_p[2];

    for(i=0; i<6; i++)
                                    current[i] =
(dist[i]*sqrt(f_desire[i]/CC[i]))/AMP;
            /*  printf("Currnet out = %f,
%f\n",current[0],current[1]); */


} /* fback_linza */


void output(float vcurrent[])
```

```
/* Here we are waiting the system timer, once
the right time comes */
/*   , we send the valuees to 6 output ports
*/
{
     int outvalue[6];       /* The binary data for
input to DA */
     int i;
     /* printf("vcurrent[0] = %f\n",vcurrent[0]);
*/
     for(i=0; i<6; i++)
     {
          outvalue[i] = ( vcurrent[i] )* 204.8 +
2048;
                /*          printf("outvalue[0] =
%d\n",outvalue[0]);
                            printf("outvalue[1] =
%d\n",outvalue[1]);    */
          if(outvalue[i] >= 4095)
               outvalue[i] = 4095;
                                  /* (real number
+10)/20*4096 */
                        /* To convert vlotage to
straight binary */
          outpw(DA_channel_reg, i);
          outpw(DA_dac_reg, outvalue[i]);

while((inpw(DA_status_reg)&0x8000)==0x800
0);
          outpw(DA_sim_up_reg,0x10);
     } /* for loop */

      /* if((inpw(DA_status_reg) & 0x4000) ==
0x4000)     */
                              /* Check bit 14 of
Status register */
                        /* if over run error */



} /* output */
```